Spacecraft Power Systems

SECOND EDITION

Mukund R. Patel
and Omid Beik

CRC Press
Taylor & Francis Group

Spacecraft Power Systems

This second edition of *Spacecraft Power Systems* is a comprehensive coverage of the fundamentals, design trades, components, controls, and operations of spacecraft power systems based on the real-world design and operations of spacecraft that have successfully flown for decades. It also includes emerging high-voltage, high-power systems for in-space propulsion for interplanetary travel.

With new and updated chapters, sections, and discussions, the second edition covers up-to-date high-voltage, MW-scale electric propulsion, updated PV and battery systems, spacecraft power components, power electronics, and their architectures and operations. This book also presents the latest in spacecraft design processes and trades, controls, operations, and protection.

This book is intended for senior undergraduate and graduate students in mechanical, aerospace, and electrical engineering taking courses in Space Systems, Space Engineering, and Spacecraft Power Systems, as well as for practicing aerospace and power engineers and managers who are designing, developing, and operating spacecraft power systems.

Spacecraft Power Systems

Second Edition

Mukund R. Patel and Omid Beik

CRC Press
Taylor & Francis Group
Boca Raton London New York

CRC Press is an imprint of the
Taylor & Francis Group, an **informa** business

Cover image: Shutterstock

Second edition published 2024
by CRC Press
2385 NW Executive Center Drive, Suite 320, Boca Raton FL 33431

and by CRC Press
4 Park Square, Milton Park, Abingdon, Oxon, OX14 4RN

CRC Press is an imprint of Taylor & Francis Group, LLC

First edition published by CRC Press 2004

Library of Congress Cataloging-in-Publication Data
Names: Patel, Mukund R., 1942- author. | Beik, Omid, author.
Title: Spacecraft power systems / Mukund R. Patel and Omid Beik.
Description: Second edition. | Boca Raton : CRC Press, [2024] |
Includes bibliographical references and index.
Identifiers: LCCN 2023027255 (print) | LCCN 2023027256 (eBook) |
ISBN 9781032383484 (hbk) | ISBN 9781032383521 (pbk) | ISBN 9781003344605 (ebk)
Subjects: LCSH: Space vehicles—Auxiliary power supply.
Classification: LCC TL1100 .P38 2023 (print) | LCC TL1100 (ebook) |
DDC 629.47/445—dc23/eng/20230703
LC record available at https://lccn.loc.gov/2023027255
LC ebook record available at https://lccn.loc.gov/2023027256

ISBN: 978-1-032-38348-4 (hbk)
ISBN: 978-1-032-38352-1 (pbk)
ISBN: 978-1-003-34460-5 (ebk)

DOI: 10.1201/9781003344605

Typeset in Times
by codeMantra

Dedication

Dedicated to my mother Shakariba
and my grandmother Joitiba
for their immense love for me
Mukund Patel

Dedicated to my family
Omid Beik

Contents

Acknowledgment xvii
About the Book xviii
Authors xx

PART A Power System Fundamentals

Chapter 1 Satellite Overview 3

1.1 Introduction 3
1.2 Satellite Systems 4
1.2.1 Communications and Data Handling System 4
1.2.2 Attitude and Orbit Control System 4
1.2.3 Tracking, Telemetry, and Command System 4
1.2.4 Electrical Power System 5
1.2.5 Thermal Control System 5
1.2.6 Structure and Mechanisms System 5
1.2.7 Propulsion System 5
1.3 Earth Orbit Classification 6
1.3.1 Geostationary Orbit 7
1.3.2 Geosynchronous Orbit 9
1.3.3 Highly Elliptical Orbit 10
1.3.4 Low Earth Orbit 10
1.3.5 Sunsynchronous Orbit 10
1.4 Orbit Mechanics 10
1.5 Satellite Stabilization Methods 12
1.5.1 Gravity Gradient Method 12
1.5.2 Magnetic Damping 12
1.5.3 Spin Stabilization 12
1.5.4 Three-Axis Stabilization 13
1.6 Launch and Transfer Orbits 14
1.7 Operational Orbit 14
1.8 Eclipse Due to Earth and Moon 14
1.8.1 Beta Angle 17
1.9 Solar Flux 17
1.10 Spacecraft Mass 18
Reference 19
Further Readings 19

Chapter 2 Near-Earth Space Environment 20

2.1 Introduction 20
2.2 Launch and Transfer Orbit Environment 20
2.3 On-Orbit Environment 20
2.3.1 Lack of Gravity and Atmosphere 21
2.3.2 Magnetic Field 21
2.3.3 Meteoroids and Debris 22
2.3.4 Atomic Oxygen 23
2.4 Van Allen Belts 23
2.5 Solar Wind and Solar Flare 26
2.6 Geomagnetic Storm 28
2.7 Nuclear Threat 28
References 28
Further Readings 29

Chapter 3 Power System Options 30

3.1 Introduction 30
3.2 Primary Battery 30
3.3 Fuel Cell 32
3.4 Solar PV Battery 33
3.5 Solar Concentrator-Dynamic Power System 35
3.6 Nuclear–Thermoelectric 36
3.7 Nuclear Electric and Chemical-Dynamic 37
3.8 Other Systems 37
3.8.1 Thermo-Photovoltaic 38
3.8.2 Solar–Thermoelectric 38
3.8.3 Thermionic 38
3.8.4 Alkaline Metal Thermal-to-Electric Converter 39
3.9 System Voltage Options 39
References 40
Further Readings 40

Chapter 4 Photovoltaic–Battery System 41

4.1 Introduction 41
4.1.1 Solar Array 41
4.1.2 Battery 42
4.1.3 Power Regulation 42
4.2 Power System Architectures 43
4.2.1 Direct Energy Transfer 44
4.2.2 Max Power Point Tracking (Peak Power Tracker) 47
4.3 Typical PV–Battery Power System 47
4.3.1 Solar Array 47
4.3.2 Battery 48

4.3.3 DC Bus 48
4.3.4 DC–DC Converter for Solar PV 49
4.3.5 DC–DC Converter for Batteries 49
4.3.6 Loads 50
4.3.7 Power Distribution Unit 50
4.3.8 Supervisor Controller and Power and Energy Management Software 51
4.3.9 Battery Bus 51
4.3.10 Ground Power Cord 51
4.4 The International Space Station 51
4.5 Communications and Science Satellite Buses 52
Reference 55
Further Readings 55

Chapter 5 Design Process and Trades 57

5.1 Introduction 57
5.2 Power System Requirements 57
5.3 Environmental Effects on Design 58
5.4 Spacecraft-Level Trades 59
5.5 Power System-Level Trades 60
5.5.1 Solar Array Design Trades 62
5.5.2 Battery Design Trades 62
5.5.3 Bus Voltage Trades 62
5.6 Load Power Profile 63
5.7 Solar Array Sizing 66
5.8 Battery Sizing 68
5.9 Power Flow Analysis 68
5.10 Design Analysis List 70
5.11 Design Process Phases 71
5.12 Factory-to-Orbit Events 71
5.13 Power System Functions Over Life 72
Further Readings 73

PART B PV–Battery System

Chapter 6 Solar Array 77

6.1 Introduction 77
6.2 Photovoltaic Cell 77
6.3 PV Technologies 78
6.4 Equivalent Electrical Circuit 80
6.5 *I–V* and *P–V* Characteristics 81
6.6 Array Construction 83

6.6.1 Rigid Panels 83
6.6.2 Body-Mounted Array 84
6.6.3 Three or More Wings 85
6.6.4 Flexible Array 85
6.7 Array Performance 86
6.7.1 Sun Intensity 86
6.7.2 Sun Angle 86
6.7.3 Temperature Effect 87
6.7.4 Sun Acquisition 90
6.7.5 Shadow Effect 92
6.8 Array Design 93
6.8.1 Degradation Factors 94
6.8.2 Radiation Damage 94
6.8.3 Offsetting from Sun 94
6.8.4 Magnetic Moment 95
6.9 Concentrator Array 96
Reference 97
Further Readings 97

Chapter 7 Battery 99

7.1 Introduction 99
7.2 Battery Cell 99
7.3 Types of Rechargeable Batteries 101
7.3.1 Nickel Cadmium (NiCd) 101
7.3.2 Nickel Hydrogen (NiH_2) 101
7.3.3 Nickel Metal Hydride (NiMH) 102
7.3.4 Lithium-Ion 102
7.3.5 Lithium Polymer 106
7.3.6 Lithium Iron Phosphate (LFP) 106
7.4 Electrical Circuit Model 107
7.5 Properties and Performance 108
7.5.1 Charge (Coulombic) Efficiency 108
7.5.2 Charge/Discharge Ratio 109
7.5.3 Round-Trip Energy Efficiency 109
7.5.4 Internal Impedance 110
7.5.5 Self-Discharge 110
7.5.6 Self-Heating 110
7.6 Cycle Life 110
7.7 Burst Power Capability 112
7.8 Battery Design 112
7.9 Launch and Ascent Power 115
7.10 Charge Regulation 115
7.10.1 Multiple Charge Rates 117
7.10.2 Single Charge Rate 117
7.10.3 Unregulated Charging 117

7.11 Battery Management 118
7.12 Dynamic Model 119
7.13 Battery Cycle Life Model 122
7.14 Alternative Energy Storage 124
References 125
Further Readings 125

Chapter 8 Power Electronics 127

8.1 Introduction 127
8.2 Switching Devices 127
8.3 Shunt Regulator 128
8.3.1 Full and Partial Shunts 129
8.3.2 Linear and PWM Shunts 130
8.3.3 Sequential Linear Shunt 131
8.3.4 Multistage PWM Shunt 132
8.3.5 Polyphase PWM Shunt 132
8.3.6 Calibrated Step Shunt 133
8.4 Shunt Circuit Design 133
8.5 Bus Ripple Filter Design 134
8.6 Power Converters 135
8.6.1 DC–DC Buck Converter 136
8.6.2 DC–DC Boost Converter 139
8.6.3 DC–DC Buck–Boost Converter 140
8.6.4 Flyback Buck–Boost Converter 141
8.6.5 Transformer-Coupled Forward Converter 141
8.6.6 Push–Pull Converter 142
8.6.7 Inductor-Coupled Buck Converter 143
8.6.8 DC–DC Resonant Converter 143
8.6.9 DC–AC Converters 143
8.6.10 DC–AC Converters SPWM Control 145
8.6.11 DC–AC Converters Square-Wave Control 146
8.6.12 Multilevel Converters for High Voltage 147
8.7 Magnetics 149
References 149
Further Readings 149

Chapter 9 Distribution Harness and Protection 151

9.1 Introduction 151
9.2 Ampacity of Wire 151
9.3 *R-L-C* Parameters 151
9.4 Conductor Materials 155
9.5 Wire Insulation and Cable Shield 156
9.6 Connectors 156
9.7 Harness Mass Minimization 158

9.8 Harness Design Process 160
9.9 Flexible Harness 162
9.10 Fuse Protection 162
9.10.1 Fuse Rating 164
9.10.2 Types of Fuse 166
9.10.3 Fuse Characteristics 167
9.10.4 Fuse Derating 168
9.10.5 Fuse Selection Criteria 169
9.10.6 Redundant and Parallel Fuses 170
9.10.7 Fuse Testing 171
9.10.8 Unfused Loads 171
9.11 Remote Power Controllers 171
9.12 Early Fault Detection 172
Further Readings 172

Chapter 10 Ancillary Components 173

10.1 Introduction 173
10.2 Solar Array Drive 173
10.3 Deployment Devices 174
10.3.1 Electro-Explosive Device 174
10.3.2 Laser-Initiated Deployment 175
10.3.3 Shape Memory Metal 175
10.4 Deployment Controller 176
10.5 Thermal Controller 177
10.5.1 Thermocouple 177
10.5.2 Metallic Resistance Wire 177
10.5.3 Thermistor 178
10.6 Relays 178
10.7 BPM and BCVM 180
10.8 Battery Letdown Unit 180
10.9 Current Meters 181
10.10 Capacitors 182
10.11 Filters 183
10.12 Telemetry and Commands 184
10.13 Electronic Packaging 186
10.14 Radiation Shield 187
10.15 EMI Shield 189
Further Readings 192

PART C Power System Performance

Chapter 11 Energy Balance and Power Management 195

11.1 Introduction 195
11.2 Energy Balance Analysis 197

11.3 Computer Program Structure 197
11.3.1 Battery Module 198
11.3.2 Solar Array Module 199
11.3.3 Bus Module 199
11.3.4 Input Variables 200
11.3.5 Output Format 201
11.3.6 Program Verification 201
11.4 Energy Balance Simulation Runs 201
11.4.1 On-Orbit Simulation 202
11.4.2 Transfer Orbit Simulation 202
11.4.3 Transfer Orbit Load Budget 203
11.4.4 Launch and Ascent Simulation 204
11.5 Battery State of Health Monitoring 205
11.6 Battery Latch-up in a Sun-Regulated Bus 207
References 208
Further Readings 209

Chapter 12 Dynamic Performance and Stability 210

12.1 Introduction 210
12.2 Bus Impedance and System Stiffness 210
12.3 Voltage Regulation and Transients 213
12.4 High-Frequency Ripples 215
12.5 Ripple Measurement 217
12.6 Minor Fuse-Blow Cross-Talk 218
12.7 Major Fuse Blow Transient 220
12.8 Stability and Bus Impedance 221
12.9 The Dynamic Stability of a Control System 225
12.10 Dynamic Simulation Model 227
12.10.1 Solar Array Model 228
12.10.2 Other Component Models 229
12.11 Simulation Runs 229
References 230
Further Readings 230

Chapter 13 Electromagnetic Interference and Compatibility, and Electrostatic Discharge 231

13.1 Introduction 231
13.2 Sources of EMI 232
13.3 Modes of Coupling 233
13.4 EMI/EMC Specifications 236
13.5 EMI Suppression Methods 236
13.5.1 Twisting Wires 236
13.5.2 Grounding 237
13.5.3 Cable Shielding 237
13.5.4 Bonding 237

13.6 Common-Mode EMI 238
13.7 Broadband EMI 238
13.8 Electromagnetic Pulse/Nuclear Threat 238
13.9 ESD in Spacecraft in GEO and LEO 239
13.10 Dielectric Breakdown 239
13.11 Effects of ESD 240
13.12 ESD Mitigation 240
13.13 ESD Control in a Solar Array 241
13.14 Part Sensitivity 242
References 243
Further Readings 243

PART D Special Power Systems

Chapter 14 Interplanetary and Deep Space Missions 247

14.1 Introduction 247
14.2 Temperature in Deep Space 249
14.3 Lunar Mission 250
14.4 Near-Sun Mission 251
14.5 Mars Mission 252
14.6 Missions to Jupiter and Saturn 253
14.7 Deep Space Missions 255
References 256
Further Readings 256

Chapter 15 Radioisotope Thermoelectric Generator 257

15.1 Introduction 257
15.2 Thermoelectric Fundamentals 258
15.2.1 Single-Stage Unicouple 260
15.2.2 Single-Stage Multicouple 260
15.2.3 Multistage, Multicouple 261
15.2.4 RTG Assembly 261
15.3 Electrical Model of the RTG 263
15.4 Maximum Power Transfer 264
15.5 The Effect of Temperature and Aging 265
15.6 Flight History of RTGs 267
15.7 Segmented TECs 267
15.8 Advanced RTGs 268
15.9 Thermoelectric Cooler 269
Reference 269
Further Readings 269

Chapter 16 High-Power, High-Voltage Systems 270

16.1 Introduction 270
16.2 High-Voltage PV Array 271
16.3 Nuclear Reactor TEC System 271
16.4 High-Voltage Design Issues 273
16.4.1 Paschen Breakdown Voltage 273
16.4.2 Dielectric Stress Concentration 274
16.4.3 Corona Degradation 275
16.4.4 Atomic Oxygen 277
16.4.5 Plasma and Charged Particles 278
16.4.6 Temperature Extremes 282
16.4.7 Design Guidelines 282
16.5 High-Voltage DC and AC Systems 283
16.6 Very High-Voltage System 284
16.7 Repetitive Pulse Power 287
16.8 Multimegawatt Burst Power 288
16.9 High-Temperature Components 292
References 295
Further Readings 296

Chapter 17 In-Space Electric Propulsion 297

17.1 Introduction 297
17.2 In-Space Propulsion 297
17.3 Specific Impulse 300
17.4 Types of EP Based on Thrust 302
17.4.1 Electrothermal Hydrazine Thruster (EHT) 302
17.4.2 Hydrazine Arcjet (HAJ) 302
17.4.3 Ion Thruster 303
17.4.4 Stationary Plasma/Hall-Effect Thruster 306
17.4.5 Magneto-Hydrodynamic/Electro-Hydrodynamic 307
17.4.6 Pulsed Plasma Thruster 307
17.5 Performance Comparison 308
17.6 EP Based on Solar PV 309
17.7 EP Based on Nuclear Power 311
17.7.1 Nuclear Thermal Propulsion 312
17.7.2 Nuclear Electric Propulsion 312
17.8 Microwave Beam Propulsion 320
17.9 Tether Power Propulsion 321
17.9.1 Space Debris Cleanup 323
17.9.2 Orbit Transfer Vehicle 324
17.9.3 Keeping the Space Station Afloat 324
17.9.4 Exploring the Outer Planets 324
References 324
Further Readings 325

Chapter 18 Fuel Cell Power 326

18.1 Introduction 326
18.2 Electrochemistry of a Fuel Cell 326
18.3 Electrical Performance 328
18.4 Types of Fuel Cells 330
18.5 Regenerative Fuel Cells 332
18.6 RFCs for Space Colonies 333
18.7 RFCs for Satellites 334
References 335
Further Readings 336

Index 337

Acknowledgment

Many colleges have contributed toward updating the successful first edition of this book on spacecraft power systems, without which a book on such emerging technologies cannot possibly be brought to the second edition. We have been extremely fortunate to receive full support from many organizations and expert individuals in the field. This book is also a direct result of teaching a continuing education course to engineers working at many prime contractors and NASA centers. The principal author is grateful to Marshall Kaplan, president of Launchspace Inc., for inviting him to develop and teach a course on space power under the initial sponsorship of the U.S. Space Foundation.

Several organizations provided current data and reports on the space power technologies. They are NASA, the European Space Agency, the U.S. Department of Energy, and spacecraft manufacturers worldwide. Many expert individuals at those organizations gladly provided all the help I asked for. Our special gratitude goes to Jim Haines, former head of the Power Systems Section at the European Space Agency, and Professor Steve Lapen at the University of Southern California for reviewing the book chapters and providing valuable comments.

Professional engineers attending our courses often knew more about their specialties than we did. Their stimulating discussions have continuously sharpened our knowledge on space power. Several of them were not only encouraged to update this book to the second edition with expanded coverage on high-voltage, high-power, megawatts-scale electric prolusion but also provided valuable suggestions and comments during the development of this book.

Dr. Patel is grateful to his wife Sarla and grandchildren Mira, Viveka, Naiya, Sevina, Dhruv, and Rayna, who contributed the time they would have otherwise cheerfully spent with him.

We heart-fully acknowledge the valuable support and encouragement from all.

Mukund R. Patel
Omid Beik

About the Book

The second edition of this book is an expanded, revised, and updated version of the first edition, with new and updated chapters, sections, and discussions on topics such as electric propulsion, PV and battery systems, spacecraft power system components and architecture, power electronics, and high-voltage systems.

This book is designed and tested to serve as (i) a textbook for university undergraduates in electrical, mechanical, and space engineering fields, and (ii) a reference for graduate students, researchers, and engineers where they will get detailed treatment of this rapidly growing segment of space power systems. This book is divided into four parts, Parts A, B, C, and D, in 18 chapters.

Part A covers the fundamentals of spacecraft power systems and consists of Chapters 1–5. It provides an overview of satellite systems, their propulsion, and their general operational characteristics. Environmental effects around the satellite are reviewed, and operations of spacecraft power system are discussed. Different options for satellite power systems are provided, and PV battery is discussed in detail. Requirements for the power systems and design tradeoffs are also addressed in Part A of this book. These discussions are arranged in five different chapters.

Part B is dedicated to PV battery power systems and consists of Chapters 6–10. It starts with a chapter on solar array, providing details of photovoltaic cells, PV technologies, I-V and P-V characteristics, and the construction of PVs for spacecraft and their performance. A chapter is dedicated to battery systems, providing in-depth discussions on the battery technologies, their charge and discharge, their dynamic model, battery management systems, and futuristic options for batteries in space. Power electronics play a vital role in the conversion and processing of power within the spacecraft's power systems. A chapter is dedicated to power electronics systems and magnetics. Switching devices, shunt circuits, filters, and magnetics are covered in detail. Harnesses for electrical power system distribution in the spacecraft are discussed in a chapter. Details of wires, their ampacity, conductors, and their parameters, as well as the protection of the power system, are addressed in this chapter. The last chapter in Part B is dedicated to ancillary components, where controllers, meters, capacitors, packaging, EMI, and thermal matters are addressed.

Part C covers performance of spacecraft power systems and consists of Chapters 11–13. Power management is discussed in a chapter where energy balance, battery health monitoring, and computer programming structure are addressed. Stability of power system in spacecraft is of vital importance and is discussed in detail in a chapter. Stiffness of bus, voltage and frequency transients, ripple, and quality of power are discussed. Dynamic stability of control and simulation models is also discussed in this section. The last chapter in Part C is dedicated to EMI/EMC and electrostatic discharge.

Part D covers special power systems in spacecraft and consists of Chapters 14–18. Interplanetary and deep space missions are discussed in a chapter. A chapter is dedicated to radioisotope thermoelectric generators, providing details of their operation, control, and structure. High-voltage systems are discussed in one chapter, where

pulse power and multi-megawatt burst power are also addressed. An entire chapter is dedicated to electric propulsion systems. This chapter provides the fundamentals of electric propulsion, including their design, structure, control, and performance. Different solutions for in-space electric propulsion systems are addressed. The final chapter in Part D is dedicated to fuel cell power systems.

Mukund R. Patel
Yardley, Pennsylvania

Omid Beik
Denver, Colorado

Authors

Mukund R. Patel, PhD, PE, is Professor Emeritus at the U.S. Merchant Marine Academy in Kings Point, NY. He has served as Principal Engineer at General Electric Space Division in Valley Forge, PA; Fellow Engineer at Westinghouse Research Center in Pittsburgh, PA; Senior Staff Engineer at Lockheed Martin in Princeton, NJ; Development Manager at Bharat Bijlee (Siemens) in Mumbai, India; and 3M McKnight Distinguished Visiting Professor at the University of Minnesota, Duluth. He has over 50 years of internationally recognized experience in research, development, design, and education of the state-of-the-art electrical power equipment and systems.

Dr. Patel obtained his Ph.D. degree in Electrical Power from the Rensselaer Polytechnic Institute, Troy, NY; M.S. in Engineering Management from the University of Pittsburgh; M.E. in Electrical Machine Design with Distinction from Gujarat University; and B.E. with Distinction from Sardar University, India. He is a Fellow of the Institution of Mechanical Engineers (UK), Associate Fellow of the American Institute of Aeronautics and Astronautics, Senior Life Member of IEEE, Registered Professional Engineer in Pennsylvania, Chartered Mechanical Engineer in the UK, and a member of Eta Kappa Nu, Tau Beta Pi, Sigma Xi, and Omega Rho.

Dr. Patel is an Associate Editor of *Solar Energy*, the journal of the International Solar Energy Society. He has presented and published over 50 research papers at national and international conferences and journals, holds several patents, has earned NASA recognition for his exceptional contribution to the power system design for the UAR Satellite, and was nominated by NASA for an IR-100 award. He has authored five textbooks published by CRC Press and major chapters on electrical power in handbooks such as the *International Handbook on Space Technologies* published by Praxis and Springer, *Energy Storage in Technology, Humans, and Society towards a Sustainable World*, and *Solar Power in Marine Engineering Handbook* published by SNAME in 2022.

Omid Beik, Ph.D., received his Ph.D. degree in Electrical and Computer Engineering from McMaster University, Hamilton, Ontario, Canada, in 2016. He was a Postgraduate Researcher at the University of Manchester, UK (2011–2012), a Postdoctoral Research Fellow at McMaster University, Hamilton, Ontario, Canada (2016–2017), a Senior Engineer with Magna Powertrain Inc., Concord, Ontario, Canada (2017–2018), a Lead R&D Engineer with Mirus International Inc., Brampton, Ontario, Canada (2018–2019), a Senior Manager with Forte Mobility Co. Ltd., Aurora, Ontario, Canada (2020–2021), and an Assistant Professor (tenure-track) with the Department of Electrical and Computer Engineering at North Dakota State University (2021–2023), Fargo, ND, USA. He is currently an Assistant Professor (tenure-track) with the Department of Electrical Engineering at the Colorado School of Mines, Golden, CO, USA. He founded Enercs Inc., an early-stage technology startup in Toronto, Canada that specialized in the research and development of state-of-the-art technologies in power electronics, electric machines, and drives for applications in renewable energy systems and electrification. Enercs Inc. held exclusive rights to a portfolio of patents and related inventions. Dr. Beik has authored the book *DC Wind Generation Systems, Design, Analysis, and Multiphase Turbine Technology*, Springer, 2020, and co-authored the books *Wind and Solar Power Systems: Design, Analysis, and Operation*, CRC Press, 2021, *Multiphase Hybrid Electric Machines: Applications for Electrified Powertrains*, Springer, 2021, and *Spacecraft Power Systems*, CRC Press, 2024. He has authored/co-authored a portfolio of peer-reviewed journal and conference papers and patents. Dr. Beik is a Senior Member of IEEE and has served as an Editor for IEEE Transactions on Energy Conversion and IEEE Power Engineering Letters, and as an Associate Editor for IEEE Transactions on Transportation Electrification and the IEEE Electrification eNewsletter. Dr. Beik has served in various roles in the organizing committee of IEEE/International conferences.

Part A

Power System Fundamentals

1 Satellite Overview

1.1 INTRODUCTION

A satellite consists of various systems designed to meet mission-specific requirements. All but the simplest satellites require a common set of systems, as shown by the solid lines in Figure 1.1. Complex satellites require additional systems, as shown by the dotted lines. The systems are classified into two groups: the payload and the bus. The payload consists of the communications equipment in commercial satellites, science instruments in research satellites, or weapons in defense satellites. The bus consists of all remaining equipment grouped into several functional systems that support the payload. The power system is one of the bus systems. It consists of the solar array, battery, power electronics, distribution harness, and controls. Other essential bus systems are the communications and data handling systems to receive commands and return information, telemetry sensors to gage the satellite state, and a central computer to coordinate and control activities of all the systems. Satellites with complex missions also require systems to determine the spacecraft's attitude and orbit orientation, and a propulsion system to control both.

Satellite design is generally optimized to the fullest extent, such that any change would result in a higher cost. The total mission cost, however, is a complex function of many variables, and so is the power system cost. The cost, C, in dollars per watt of power generated can be expressed as a function of four major variables as follows:

$$C = f(X_1, X_2, X_3, X_4) \tag{1.1}$$

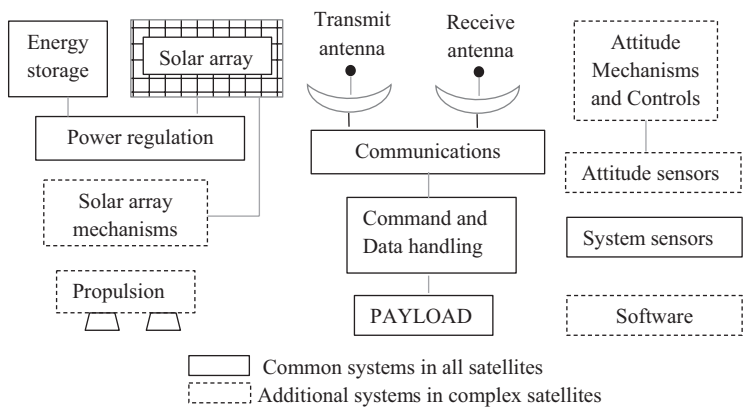

FIGURE 1.1 Various systems in satellites.

DOI: 10.1201/9781003344605-2

where

X_1 = cost per kg of the power system mass launched,
X_2 = cost per liter of the power system volume launched,
X_3 = cost per watt of the power system's generation capacity, and
X_4 = cost of altitude control related to power system components.

1.2 SATELLITE SYSTEMS

The typical communications satellite bus consists of the following systems.

1.2.1 Communications and Data Handling System

The communications and data handling system performs three independent functions: (i) It receives and demodulates information transmitted to the satellite from the ground station via command links; (ii) It transmits data, both recorded (remote) and real-time, from the satellite to the ground station via data links; and (iii) It transmits bus equipment and other telemetry data from the satellite to the ground station via telemetry links.

1.2.2 Attitude and Orbit Control System

The attitude and orbit control system determines the exact position of the satellite with respect to the local vertical, thus providing precise pointing of the communications antennas, imaging sensors, and any other mission sensors. The attitude control function accepts error signals, from which the basic or precision attitude determination function provides 3-axis attitude control using three reaction wheels. The basic attitude determination function obtains pitch and roll data from the Earth sensor and yaw data from the gyroscopes with updates from the sun sensor to provide a basic 3-axis pointing within 0.1° accuracy. The precise attitude determination function uses three gyroscopes with updates from a star sensor to provide a 3-axis pointing within 0.01° accuracy.

1.2.3 Tracking, Telemetry, and Command System

The tracking, telemetry, and command system accepts analog, discrete, and digital data from various systems of the spacecraft and processes them into a continuous data stream for direct transmission to the ground or for on-board storage for later transmission. These data are analyzed and evaluated on the ground to determine the spacecraft's state of health and its operational configuration. The command and control functions are all digital. It provides ascent guidance from booster separation through transfer orbit and controls the satellite's attitude and operating modes on orbit. The control is exercised in accordance with commands and data received from the ground station, supplemented by signals and data supplied by other systems of the satellite. This system also provides error correction coding, a key function of the system.

1.2.4 Electrical Power System

The electrical power system generates, stores, conditions, controls, and distributes power within the specified voltage band to all bus and payload equipment. The protection of the power system components in case of credible faults is also included. The basic components of the power system are the solar array, solar array drive, battery, battery charge and discharge regulators, bus voltage regulator, load switching, fuses, and the distribution harness. The harness consists of conducting wires and connectors that connect various components together.

In the Earth-orbiting satellite, the solar array is rotated once per orbit by the solar array drive to track the sun at or near a normal angle. The rotation is rate-servo-controlled. The body information and position errors are computed by the satellite computer to derive rate control signals. The nominal rate of rotation is 0.06° per second. Using slip rings and carbon brushes is one way of providing the rotary joint between the rotating array and the satellite body. The control signals for the required rotation rate come from the tracking, telemetry, and command system, which also selects the rotation direction.

1.2.5 Thermal Control System

The thermal control system maintains the temperature of all equipment within the specified limits during normal and abnormal operations. It provides both passive and active cooling as needed. Typical components of this system are fixed radiators, louvers, multilayer blankets, coatings, tapes, heaters, thermostats, temperature sensors, and control electronics. Thermistors are widely used as temperature sensors. The components are sized for the average electrical power dissipation, the external heat input from the sun, the Earth's reflected sunlight (albedo), and the long-wavelength (infrared) heat radiated from the Earth.

1.2.6 Structure and Mechanisms System

The structure and mechanisms system primarily provides a frame for mounting and linking various mechanical components together. Mechanisms for deploying the booms, the solar array, and other components after orbit injection are often included in this system. The deployment power circuits and devices are well shielded for electromagnetic interference to prevent unspecified deployment. The deployment motion is derived by spring-loaded rotary mechanisms. A rotary vane damper filled with viscous silicone fluid governs the deployment rate. The solar array deployment generally involves cable cutting and/or rod cutting. Structures are often made of magnesium and aluminum. Composites are also common. Some steel and occasionally beryllium are used where needed.

1.2.7 Propulsion System

Once the spacecraft is in space, a propulsion power, sometimes referred to as in-space propulsion, propels the spacecraft for various reasons, including:

i. For the spacecraft to maintain its orbit, power is required to generate a force along the orbit $\left(f_{pm}\right)$ as shown schematically in Figure 1.2. This force acts against the force of gravity $\left(f_g\right)$ at an angle.

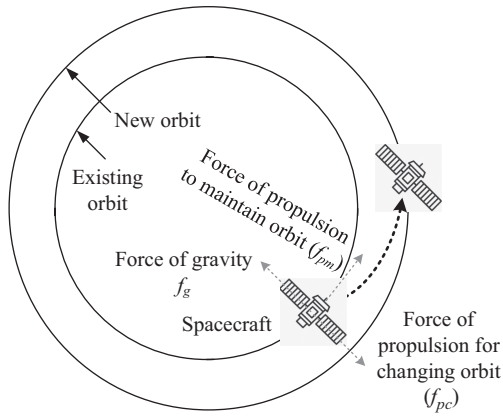

FIGURE 1.2 Spacecraft transitioning from an existing orbit to a new orbit.

ii. For the spacecraft to change its orbit and transition to a new orbit, power is required to generate a force $\left(f_{pc}\right)$ that overcomes the force of gravity. This power is often much greater than the power required to maintain a spacecraft's orbit because it is acting directly against gravity.

In addition to propulsion power, electrical power is needed for maintaining various spacecraft equipment such as antennas, receivers, radios, sensors, lights, control, and other services. The power for these is sometimes provided by the propulsion source through a power system structure, which will be addressed in later chapters. In-space propulsion can be provided by different sources. One common method uses a mixed system of high-pressure regulated helium or nitrogen and liquid hydrazine. The gaseous helium or nitrogen, and hydrazine are carried in high-pressure cylindrical titanium alloy tanks. The propulsion system may also be based on solid fuels, nuclear energy, or electric sources. Common electric propulsion for small to mid-size spacecraft uses photovoltaic solar panels and battery systems. An electric propulsion system based on rotating electric machines driven by a heat source has been studied for larger spacecraft.

1.3 EARTH ORBIT CLASSIFICATION

The Earth is a sphere with a slight flatness at the top. Its diameter is 12,713.54 km at the poles and 12,756.32 km at the equator, the difference being 42.78 km. Air surrounds the Earth and extends up to 160 km above the surface, beyond which the atmosphere gradually fades into space. The satellites orbiting the Earth are classified into several groups, with their typical parameters listed in Table 1.1. The orbits are often described by the following abbreviations:

GEO: geosynchronous Earth orbit, circular at 35,786 km altitude
MEO: mid-Earth orbit, circular at 2000–20,000 km altitude

TABLE 1.1
Classification of the Earth's Orbits

Orbit Type	Apogee (km)[a]	Perigee (km)[b]	Eccentricity[c]	Inclination[d]	Period[e]
Geostationary	35,786	35,786	0	0	1 sidereal day
Geosynchronous	35,786	35,786	Near 0	0°–90°	1 sidereal day
Elliptical Molniya	39,400	1000	High	62.9°	½ sidereal day
Low Earth	Various	Various	0 to high	0°–90°	>90 min

[a] Closest distance from the Earth surface.
[b] Farthest distance from the Earth surface.
[c] Ratio of difference to sum of apogee and perigee radii.
[d] Angle between orbit plane and equatorial plane.
[e] One sidereal day is 23 h, 56 min, 4.09 s.

LEO: low Earth orbit, generally circular at 200–2000 km altitude
HEO: highly elliptical orbit, such as Molniya

A communications satellite provides interconnectivity over a large area for point-to-point, point-to-multipoint, and broadcast communications. It can serve fixed as well as mobile terminals anywhere—on land, on the sea, in the air, or in space. A typical satellite transponder receives an uplink signal from a ground station, frequency converts it, amplifies it, and retransmits it to the ground.

In the case of LEO and MEO, the orbit parameters are chosen to avoid the radiation belts that surround the Earth at altitudes of 1.3–1.7 and 3.1–4.1 Earth radii, respectively. A typical LEO satellite has an altitude of 500–1500 km, an orbit period of 1.5–2 h, and is visible to a given Earth station for only a few minutes in every orbit period. A typical MEO satellite is between 5000 and 12,000 km altitude, with an orbit period of several hours. In a highly elliptical inclined orbit, it can see the polar regions for a large fraction of its orbit period.

A GEO satellite moving west to east at an altitude of 35,786 km (22,237 miles) results in a nominal orbit period of 24 h and remains stationary with respect to the Earth. Three such satellites spaced 120° apart in the equatorial plane can provide continuous coverage of the globe except near the poles. The launch vehicle booster and its upper stages deliver the satellite into the transfer orbit, which is an elliptical orbit with the Earth at one of its foci and the apogee at the geosynchronous orbit. An apogee kick motor is then fired to circularize the orbit at the geosynchronous height. The primary features of various orbits are described below.

1.3.1 Geostationary Orbit

The geostationary orbit is a very special geosynchronous orbit and, in fact, is unique. It is exactly circular, with a radius of 42,164 km, in the Earth's equatorial plane, with zero degree inclination and zero eccentricity. A satellite placed in this orbit is synchronized with the Earth's rotation rate and direction (eastward). It does not move

with respect to the Earth, and sees the same object on the Earth steadily. The orbit period is the same as that of the Earth's rotation, i.e., 23 h 56 m 4.09 s. As a result, the satellite's beam-to-Earth and the ground station's beam-to-satellite are steady in position. This simplifies the design and operating requirements of both the satellite and the ground station. However, it takes more fuel to reach and maintain the geostationary orbit than any other orbit around the Earth at that altitude. Numerous satellites already placed there make it difficult to get a desirable location in this orbit that would avoid radio frequency interference from neighboring satellites. The Tracking and Data Relay Satellite (TDRS) of the US Department of Defense was an example of a geostationary satellite. A satellite placed in this orbit tends to drift away from its assigned station. Hence, a periodic station-keeping operation is required.

The time in space is kept in sidereal time, which measures the rotation of the Earth in relation to a fixed star. Solar time is used on Earth to measure the Earth's rotation in relation to the sun. The same star is not in the same place at the same solar time but is in the same place at the same sidereal time from day to day. A sidereal day consisting of 24 sidereal hours is the time the Earth takes to rotate once on its axis past an imaginary line from the Earth's center to any star. Thus, the sidereal time is measured from a point in the sky called the vernal equinox, although no bright star marks this point.

The geostationary orbit period is exactly 1 sidereal day. It is slightly shorter than the mean solar day of 24 h because of the sun's apparent motion resulting from the Earth's rotation around the sun, which is 360° in 365.24 days, i.e., 0.9856° per day. By the time the Earth has rotated once in relation to a distant star, it has moved westward along its orbit, as depicted in Figure 1.3. The sun is then 0.9856° east of its position at the start of the Earth's rotation. The Earth needs additional time to rotate eastward to come back in line with the sun. The Earth must thus rotate a total of 360.9856° in 1 mean solar day so that the meridian will align itself with the sun from one noon

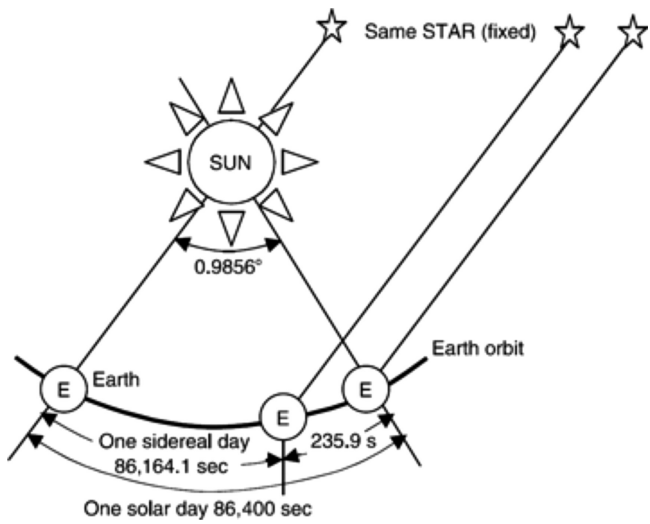

FIGURE 1.3 Sidereal day and mean solar day for Earth.

to the next in exactly 24 h (86,400 s). The time for the Earth to rotate 0.9856° past one rotation is 86,400/(0.9856/360.9856) = 235.91 s. The sidereal period of rotation is therefore 86,400 − 235.91 = 86,164.09 s, or 23 h, 56 m, 4.09 s, which is shorter by 3 m and 55.91 s than the mean solar day.

1.3.2 Geosynchronous Orbit

Most commercial communications satellites operate in numerous geosynchronous orbits. The geostationary orbit described above is one unique orbit in the entire class of geosynchronous orbits. The distinction between the two is minor and fine, but it is important. The geosynchronous orbit is similar to the geostationary orbit, except that its inclination can be any value between 0 and 90°. Inclinations other than 0° require ground-station tracking antennas. Sometimes, that may not be a disadvantage because the ground stations require tracking antennas for other reasons. Mobile platforms, such as planes and ships, also require tracking antennas. The geosynchronous orbit is chosen for fuel-efficient launch and orbit maintenance. If a satellite is placed in $i°$ inclination orbit, the point directly below the satellite oscillates between $i°$ north and $i°$ south every day, and appears to drift to the north and south in a figure eight, as shown in Figure 1.4. The angular height of this figure is just the magnitude of $\pm\pi i°/180$ radians. This motion away from the equator induces a longitudinal difference between the ideal and actual satellite points. The difference appears as the satellite moves toward the equator. The maximum longitudinal deviation is $(\pi i°/180)^{2/4}$. The variation in distance is $\pm(\pi i°/180)R_o$, where R_o is the orbit radius. The ground stations must be aligned with the north–south (N–S) motion of the satellite in an inclined orbit.

When the sun and the moon are not in the equatorial plane, the N–S components of their combined gravity force change the orbit inclination of the geostationary and geosynchronous satellites at a rate of about 0.85° per year. Station-keeping maneuvers are required to compensate for such orbit drift. This consumes some fuel, which

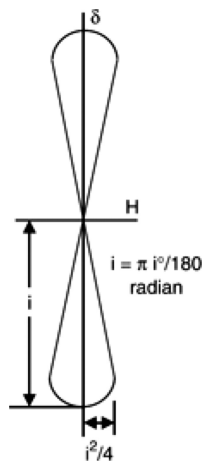

FIGURE 1.4 Satellite motion orbit with $i°$ inclination.

must be carried on board to last for the duration of the mission. The use of arc jets minimizes the fuel requirement by increasing the propulsion efficiency. The arc jets and station-keeping fuel requirement can be eliminated if 0.85° drift per year is acceptable or can be accommodated in the mission design, as was the case in TDRS. In exchange, the satellite would require several degrees of yaw maneuvering on a daily basis to remain pointed at the ground station.

1.3.3 Highly Elliptical Orbit

Among highly elliptical orbits, Molniya is one specific orbit named after a Russian communications satellite with a 1000 km perigee and a 39,400 km apogee. With the period of ½ sidereal day in this orbit, the satellite comes to the same longitude on every other apogee. The advantage of the Molniya orbit is good coverage of the entire northern hemisphere. The disadvantage is that there is no coverage over the southern hemisphere. Moreover, it requires more satellites and two tracking antennas at each ground station. GPS, although not in a Molniya orbit, has an orbit period of ½ sidereal day because of its selected MEO location in a circular orbit. Some US military satellites have used the elliptical Molniya orbit with 63.4° inclination to cover Russia for 10 h out of a 12 h period.

1.3.4 Low Earth Orbit

This is approximately a circular orbit at low altitude. The International Space Station and NASA's space shuttle orbiter operate in low Earth orbit. Most communications satellites operate in GEO, but some newer constellations are planned and/or placed in LEO between 500 and 2000 km altitudes and 30°–90° (polar) inclinations. Being closer to the Earth, smaller and simpler satellites—such as Starlink satellites—can be used in this orbit. Also, two-way communications introduce a time delay of only 0.02 s versus 0.5 s in geosynchronous orbits. On the negative side, LEO communications satellites require tracking of omni-directional antennas, and many satellites are needed for wide coverage. For example, Starlink currently consists of over 4000 mass-produced small satellites that communicate with designated ground transceivers. In total, nearly 12,000 satellites are planned to be deployed, with a possible extension to 42,000 in a later stage. Starlink is a satellite constellation in LEO at about 550 km altitude. It is operated by SpaceX to provide internet coverage to over 60 countries at present, and it was very valuable in the Ukraine war. It further aims to provide global mobile phone service after 2023.

1.3.5 Sunsynchronous Orbit

A satellite in this orbit maintains a constant angle between the sun's direction and the orbit plane, and always sees the sun at the same angle. It is used for special applications.

1.4 ORBIT MECHANICS

Kepler's three laws of planetary motion, based on Newton's laws, apply to a satellite orbiting a planet. They are as follows:

First law: The satellite orbit is an ellipse with the planet at one focal point.

Second law: The line joining the planet and the satellite sweeps equal areas in equal times. If the time intervals Δt_1 and Δt_2 in Figure 1.5 are equal, then the swept areas A_1 and A_2 are also equal.

Third law: The square of the orbit period is proportional to the cube of the semimajor axis, i.e.,

$$T_o^2 = \frac{4\pi^2 a^3}{\mu} \tag{1.2}$$

where a is the semimajor axis of the orbit, and μ is the gravity constant of the planet. For the Earth, μ is $3.986 \times 10^{14}\,\text{m}^3/\text{s}^2$ or $3.986 \times 10^5\,\text{km}^3/\text{s}^2$.

For circular orbits, the third law gives the orbit period T_o in terms of the orbit radius R_o,

$$T = \frac{2\pi R_o^{1.5}}{\sqrt{398{,}600}}\,\text{s}, \quad \text{or} \quad T_o = 2.7644 \times 10^{-6} R_o^{1.5}\,\text{h} \tag{1.3}$$

For the orbit period to be 1 sidereal day of 86,164.09 s, the orbit radius must be 42,164 km. Deducting the mean radius of the Earth's surface 6,378 km, we get the geosynchronous satellite altitude of 35,786 km above the Earth's surface. This altitude is about six times the Earth's radius.

The satellite velocity in a circular orbit is given by

$$\upsilon = \frac{2\pi R_o}{T_o} \tag{1.4}$$

which is 3.075 km/s in GEO orbit. In comparison, the Earth travels in its orbit around the sun at a speed of 30 km/s, about ten times faster.

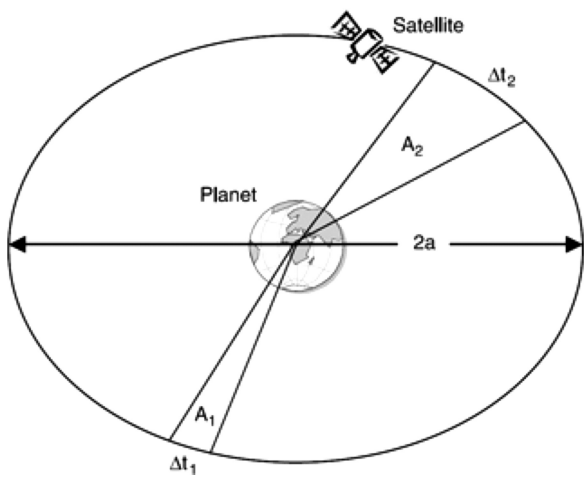

FIGURE 1.5 Kepler's second law of planetary motion.

1.5 SATELLITE STABILIZATION METHODS

The satellite's stabilization in orbit is achieved by either an active or passive method described below.

1.5.1 Gravity Gradient Method

Gravity gradient is a passive method, sometimes used in small LEO satellites. The difference in the attractive force of gravity on the parts closest and farthest from the Earth creates a moment that maintains the satellite aligned with the local vertical. This method requires long booms in order to have adequate moment, and it does not work in geosynchronous orbits because of the near-zero gravity there.

1.5.2 Magnetic Damping

Magnetic damping is another passive method. It uses long booms with magnets that interact with the Earth's magnetic dipole field to produce the stabilization moment.

1.5.3 Spin Stabilization

Spin stabilization is an active method that has been commonly used on most satellites until recently. It is still used for small satellites. The spinning bicycle wheel and the spinning top are stable above a certain minimum spin rate. The satellite's stability can be similarly maintained by storing angular momentum in a spinning body on board the satellite. For spin stabilization, the moment of inertia about the desired spin axis must be greater than that about any orthogonal axis. Small satellites are spun in entirety. Large satellites using complex antennas are split into two sections: the despun antenna section and a spinning cylindrical body. The solar cells are mounted on the spinning body, as shown in Figure 1.6. A typical spin rate is 30–60 revolutions per minute. Heavier satellites require higher spin rates for stability. Spin-stabilized satellites are also called dual-spin or gyrostat satellites.

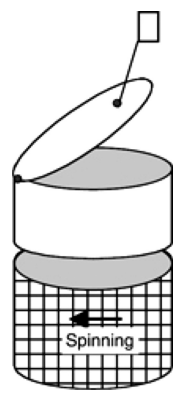

FIGURE 1.6 Spin-stabilized gyrostat satellite.

1.5.4 Three-Axis Stabilization

Three-axis or body stabilization is another active method commonly used in modern satellites. In this method, the satellite uses several spinning momentum wheels located inside the body, as shown in Figure 1.7. The orientation is automatically maintained by a servo-control system that adds or subtracts momentum from the spinning momentum wheels. Thrusters are used periodically to maintain the orientation as necessary. The satellite usually has a box-shaped body with flat solar panels (wings) extending from the north and south faces. Table 1.2 compares key features of the spin-stabilized and 3-axis-stabilized satellites. The 3-axis stabilization generally results in lower dry mass for satellites with solar array power exceeding a few hundred watts. For this reason, it is widely used in modern large, high-power satellites.

All spacecraft, once disturbed from their stable position, may oscillate for a long time in characteristic modes that may be close to being unstable. It is important that these modes are identified and suitable damping is introduced by the attitude and/

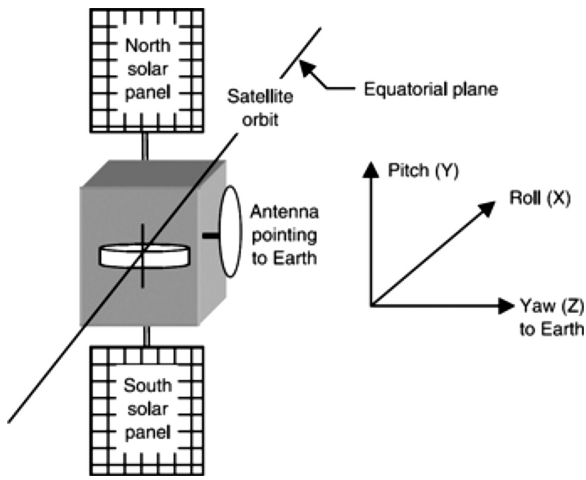

FIGURE 1.7 Three-axis body-stabilized satellite with definition of attitude axes.

TABLE 1.2
Key Features of Spin-Stabilized and 3-Axis Stabilized Satellites

Spin-Stabilized	3-Axis Stabilized
Inherently stiff due to rotational inertia	Bias or zero momentum maintains the stability
Simple mechanical structure	Complex attitude control
Only one-third of the solar array generate power at any time	Full solar array generates power all the time
Power limited by body size that fits the launch vehicle	Can have high power by adding solar panels
Less flexibility in design	Great flexibility in design
Suitable for small satellites	Suitable for large satellites

or orbit control systems to restore the vehicle to a stable position. Fuel movement in the tanks may also contribute to the oscillations, but it is normally controlled by baffles. There are five points within the reference frame in space at which a stationary body will be in equilibrium. All these points are in the plane in which the dominant masses rotate. They are referred to as the Lagrangian or Libration points, and are of potential use for spacecraft in Earth–Moon type systems.

1.6 LAUNCH AND TRANSFER ORBITS

The communications satellite is placed in a geosynchronous orbit in two main steps. The launch vehicle places the satellite first into a low Earth circular orbit, called the parking orbit. Then, the so-called Hohmann transfer takes the satellite to the final orbit using minimum fuel. The first velocity increment changes the low circular orbit into a highly elliptical transfer orbit with perigee that of the final circular orbit. The second velocity increment at the apogee of transfer orbit places the satellite in the final circular orbit. When the perigee and apogee kick motors are fired, some sort of stabilization is needed because the thrust would tumble the satellite and cause incorrect orbit injection.

The fully deployed satellite, which is 3-axis stabilized in the operational orbit, can use spin stabilization in the transfer orbit when the solar panels are stowed into a box-shaped body. The satellite is despun by applying reaction wheel torque to bring it to a nonspinning state at the end of transfer orbit. The de-spinning operation takes about 10 min. Until the solar array is fully deployed, the sunlit panel radiates heat from the front face only, as opposed to both the front and back faces after deployment. Moreover, the exposed panel is oriented normal to the sun to maximize power generation except during maneuvering. To keep the temperature of the sun-side panel from rising above the tolerance limit, the satellite is spun at a low rate, such as $1/10^{th}$ to 1 revolution per minute. Spinning at such a slow barbecue rate is merely for thermal reasons, even when the spinning is not required for stability. The spin rate is gyro-controlled. One can deploy the array in the transfer orbit, but it adds a mechanism and structural complexity, resulting in added mass, low reliability, and difficult transfer orbit maneuvers.

1.7 OPERATIONAL ORBIT

As the satellite revolves around the Earth in operational orbit at inclination θ measured from the equatorial plane, it changes its orientation with respect to the sun with seasons, as depicted in Figure 1.8.

The north of the Earth's rotation axis is inclined 23.45° toward the sun on the summer solstice day and 23.45° away on the winter solstice day. On the autumnal and vernal equinox days, the axis inclination is zero, resulting in equal day and night.

1.8 ECLIPSE DUE TO EARTH AND MOON

Since the ecliptic and equatorial planes are inclined to each other by 23.45°, the angle of incidence of the sunlight on the solar arrays varies from 66.55° to 90°. The corresponding incident solar flux varies from 91.75% on a solstice day to 100% on an

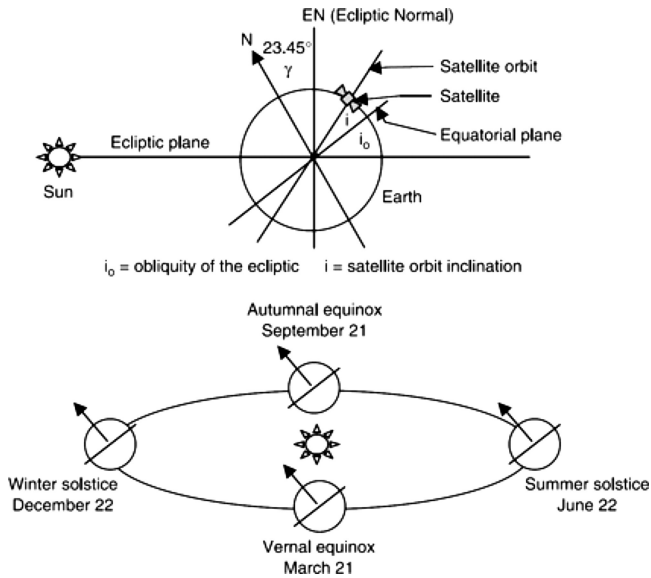

FIGURE 1.8 Satellite in Earth's orbit with seasonal variations.

equinox day. However, on equinox days, the satellite encounters the longest eclipse once per day when the Earth blocks the sunlight from illuminating the satellite.

When the satellite is in shadow of the Earth, the solar array's power generation ceases, and its temperature drops sharply. Predicting the eclipse duration is, therefore, important for the spacecraft's power system design. For the geosynchronous satellite, the longest eclipse occurs on the vernal and autumnal equinoxes when the sun is in the equatorial plane, as shown in Figure 1.9. The duration for which the entire sun is blocked is called the umbra (total eclipse marked by a dotted arc). The total arc when the sun is fully or partially blocked is called the penumbra (arc *a–b*). It is proportional to the mean solar day, accounting for the Earth's orbital motion during the eclipse. The umbra duration varies with the seasons, with the longest being 69.4 min occurring around March 21 and September 21. From the geometrical considerations of the geosynchronous orbit in Figure 1.9, the penumbra duration is 73.7 min (1.228 h)

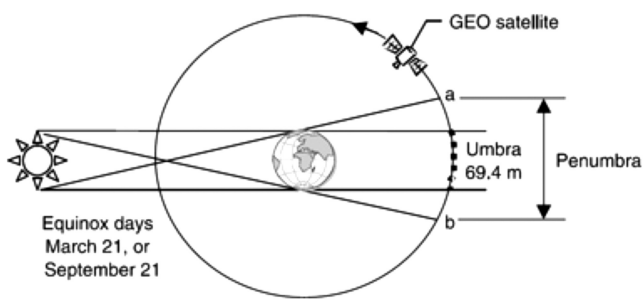

FIGURE 1.9 Eclipse in geosynchronous orbit—umbra and penumbra.

and the umbra is 4.3 min shorter than the penumbra. Since the solar array output voltage and current during this 4.3 min would not meet the requirements for the power system operation, the penumbra is taken as the eclipse duration for the power system design.

As the sun moves above or below the equator after an equinox, the duration of the eclipse becomes shorter and shorter, and finally becomes zero when the inclination of the sun becomes high enough. The eclipse onset time on a particular day is of interest to the satellite design engineer because it determines the required services and the battery requirements onboard the satellite.

In near-equatorial, circular, low Earth orbits, eclipses of approximately equal duration occur once every orbit period. The duration of the eclipse depends on the orbit altitude, inclination, and the sunlight incidence angle on the orbit plane. It can vary by a factor of two in LEO. Figure 1.10 shows the eclipse duration and orbit period vs. circular orbit altitude.

For a circular orbit, the eclipse duration (in h) is given by

$$T_e = \frac{1}{2} + \frac{1}{\pi}\sin^{-1}\left\{\frac{\left(1-\left(\frac{R_{\text{Earth}}}{R_{\text{orbit}}}\right)^2\right)^{1/2}}{\cos(\beta)}\right\} \tag{1.5}$$

In addition to eclipses due to the Earth's shadow on the satellite, the moon can also obstruct the sun as seen by the satellite. Such eclipses are irregular in occurrence, varying from 0 to 4 per year, with an average of two. Usually they are spaced far apart, but in the worst case, two eclipses can occur in 24 h. The duration can vary from several minutes to more than 2 h, with an average of 40 min. The satellite may experience additional battery depth of discharge and fall in temperature in the case

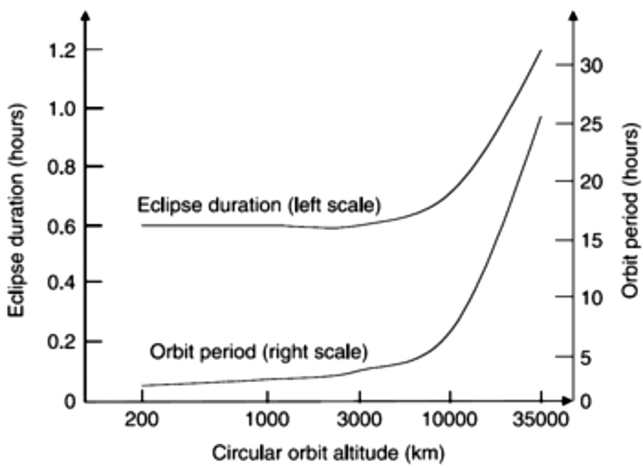

FIGURE 1.10 Eclipse duration and orbit period vs. circular orbit altitude.

where an eclipse due to the moon occurs adjacent to an eclipse due to the Earth. In most missions, however, eclipses due to the moon impose no additional design requirement, but that has to be ascertained. Otherwise, shedding a noncritical load temporarily during the worst moon eclipse often circumvents the situation.

1.8.1 Beta Angle

The beta angle, β, is defined as the angle between the Earth–Sun line and the orbit plane when the spacecraft is closest to the sun (orbit noon). It varies seasonally between 0° and $(i + i_o)$°, where i = orbit inclination and i_o = angle between equator and ecliptic plane, which is 23.45°.

The value of $\beta = 90°$ results in the greatest solar flux on the satellite body, and $\beta = 0°$ gives zero flux. In most satellites, with the array always pointed to the sun by the solar array drive motor, the β angle has an insignificant effect on the generation of electric power. However, the thermal control system is impacted by the β angle. Low β may require additional heaters, while high β may require additional cooling. The β angle impacts the solar array temperature, which in turn has a small secondary effect on power generation. The most significant effect of the β angle on the power system design comes from the eclipse duration, as given by Equation 1.5. As β increases, the eclipse duration decreases, which consequently requires a smaller battery and less charging power during sunlight. The β angle is not to be confused with the sun angle, θ, often used to define the sunlight incidence angle on the solar array, which could be canted to catch the sun normally if β is not 90°. The sun angle is defined as the angle between the solar array plane and the sun-pointing vector. The power generation is proportional to $\cos\theta$, so θ of 90° results in the maximum power generation, and 0° gives zero power. The power system engineer starts with the orbit parameters specified by the customer, which primarily set the orbit period, eclipse duration, and the β angle. These parameters, in turn, have the greatest impact on the power system design.

1.9 SOLAR FLUX

The energy received from the sun in space varies with the distance squared. The Earth's orbit around the sun is approximately circular, with a slight eccentricity of 0.01672. The distance, therefore, varies within ±0.01672 times the average distance between the sun and the Earth, which is 149.6 million km, defined as one astronomical unit (AU) of distance. Thus, the solar flux varies over $(1 \pm 0.01672)^2$ or 1 ± 0.034 of the yearly average. Within these small variations, the Earth is closest to the sun around January 2 (perihelion) and farthest around July 2 (aphelion). For many years, the average solar radiation in the Earth's orbit has been taken as $1358 \pm 5\ \text{W/m}^2$ on the surface normal to the sun. Measurements reported by Frohlich[1] show a higher average value of $1377 \pm 5\ \text{W/m}^2$, which is now generally accepted. However, the conservative number of $1358 - 5 = 1353\ \text{W/m}^2$ continues to be widely used. Table 1.3 shows the ratio of the seasonal flux over the yearly average flux on the equinox and solstice days. It also shows the seasonal variations in the orbit's inclination.

Satellites using solar arrays with single-axis tracking gimbals generate less power in accordance with the cosine of the sun's angle. The last column gives the combined

TABLE 1.3
Variation of Solar Flux and Angle of Incidence with the Seasons

Day of the Year	Seasonal Flux/ Yearly Average	Angle of Incidence with Single-Axis Tracking Gimbals	Flux on Array/Yearly Average on Suntracking Surface
Vernal equinox, March 21	1.001	0°	1.001
Summer solstice, June 22	0.967	23.45°	0.887
Autumn equinox, September 21	0.995	0°	0.995
Winter solstice, December 22	1.034	23.45°	0.949

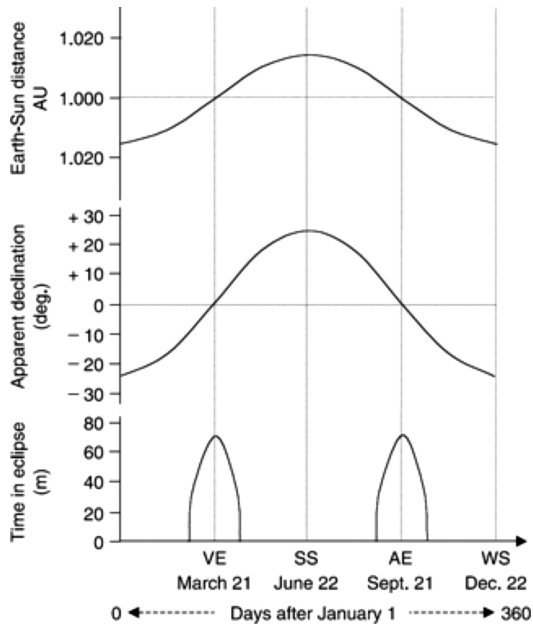

FIGURE 1.11 Seasonal variations in solar parameters over 1 year in geosynchronous orbit.

effect of the cosine and the flux variation due to eccentricity on the solar array output power. The output on the summer solstice day is 11% lower than that on the vernal equinox day. The seasonal variations in solar parameters in geosynchronous orbit are collectively depicted in Figure 1.11.

1.10 SPACECRAFT MASS

Hundreds of small spin-stabilized and large 3-axis-stabilized satellites have been built and deployed in various orbits. The spacecraft's dry mass and the corresponding

electrical power requirements for GEO satellites have been steadily rising. The new technological developments in solar cells and evolutionary design improvements have jointly contributed to the higher solar array output power per kilogram for modern communications satellites. For large 3-axis body-stabilized GEO satellites with a total eclipse load of 5–10 kW, the electrical power system (EPS) mass is about 30% of the total spacecraft dry mass, the payload mass is also about 30%, and the remaining 40% is in the structure and all other spacecraft systems.

REFERENCE

1. Frohlich, R.C., *Contemporary Measures of the Solar Constant: The Solar Output and its Variations*, Colorado Associated University Press, Boulder, CO, 1977, pp. 93–109.

FURTHER READINGS

Beik, O. and Emadi, A. "Toward integrated digital aircraft control systems: For electrified-system optimized size, cost, and efficiency," *IEEE Electrification Magazine*, 5(4), 46–52, 2017.

Beik, O., Patel, M. R. and Talebzadeh, S. Large spacecraft electric propulsion using multiphase generator, in *2023 IEEE Aerospace Conference*, Big Sky, MT, USA, pp. 1–8, 2023.

Saude, B., LaSart, N., Blair, J. and Beik, O. "Microgrid-based wind and solar power generation on moon and mars," *IEEE Transactions on Smart Grid*, 14(2), 1329–1332, 2023.

2 Near-Earth Space Environment

2.1 INTRODUCTION

The near-Earth space environment, i.e., thermosphere and ionosphere, presents a substantial risk to space systems. The sun continuously radiates energy in several forms—visible light, invisible infrared, ultraviolet A, B, and C, X-rays, gamma rays, radio waves, electrons, protons, and plasma (electrically charged hot gas). The abundance of charged particles that come with the sun's radiation makes space a hostile environment. The energy in these particles impinging on the surface causes damage, which accumulates over a period of time.

The spacecraft power system must withstand the space environment and meet full performance specifications over the entire mission life, starting from the launch phase to disposal at the end of life. General design criteria required for this purpose are studied and documented by space research organizations such as NASA.[1] As the solar array is directly exposed to the space environment, it is particularly vulnerable to damage. In fact, the rate of damage to a solar array determines the spacecraft's life in many cases. Environmental factors also affect the overall design of all other components of the power system.

2.2 LAUNCH AND TRANSFER ORBIT ENVIRONMENT

High levels of acceleration, shock, and vibration are present during lift-off and during pyro-driven deployments at various stages. The resulting stress levels, which vary with the launch vehicle, have effects on the power system design, particularly on the solar panels. For example, the solar panels may be required to withstand the launch acceleration of about 3*g* on the *Orbiter*-type space shuttle and about 10*g* on the launch vehicle *Saturn*, where *g* is the acceleration due to gravity on the Earth's surface. The pyroshock levels during deployments can be extremely high for a few milliseconds. The shock spectrum is generally characterized by high-frequency components. The peak shock level in *Ariane* during payload separation, for example, could be about 2000*g* at frequencies above 1.5 kHz. In transfer orbit, the solar panel is still folded but must withstand the accelerating force at perigee and the braking force at apogee. Thermally, the outer solar panels must withstand the Earth's heat radiation and albedo, in addition to the solar radiation, without exceeding the specified temperature limit.

2.3 ON-ORBIT ENVIRONMENT

The power system design is influenced primarily by the following on-orbit environmental factors.

 DOI: 10.1201/9781003344605-3

2.3.1 Lack of Gravity and Atmosphere

The lack of gravity and atmosphere in space has significant effects on the design of power systems. Zero gravity and vacuum jointly deprive all spacecraft equipment from the natural convection cooling that is normal on Earth. The internal thermal design in space, therefore, depends primarily on conduction cooling and, to some extent, on radiation cooling. The heat rejection to the outer space, however, must depend only on radiation cooling.

The vacuum causes sublimation and outgassing, more so in some materials than others. The subsequent condensation of the sublimed vapor on cold surfaces can cause short circuits in electrical parts. Since zinc has a high sublimation rate, and some polymers have high outgassing rates, their use in space is restricted. The solar array's current-collecting slip rings and brushes can experience cold welding under high contact pressure in a vacuum. The use of lubricants with low sublimation rates or keeping them in sealed, pressurized enclosures is therefore important.

2.3.2 Magnetic Field

The interaction of the Earth's magnetic field B, and the magnetic dipole moment M, created by an electrical current loop, produces torque $\boldsymbol{T}$ on the spacecraft. The cross-vector product of M and B gives this torque (in Nm), i.e.,

$$T = M \times B \tag{2.1}$$

where M is expressed in A·m^2 and B in tesla. The magnetic moment is produced by current loops in the spacecraft's power circuits. The moment (in A·m^2) is defined as the vector product of the current and the loop area, i.e., $M = I \times A$. Its direction is perpendicular to the loop area, as shown in Figure 2.1.

In the geostationary orbit, the normal component of B is constant around 0.104 μT, and the radial component varies between ±0.042 μT as the satellite revolves around the Earth. In orbits at other altitudes, the magnetic field varies inversely with the orbit radius cubed. The normal component of B produces a torque in the equatorial plane, averaging to zero over the orbit period. Both components of the torque affect the satellite's attitude. The power system's contribution to the magnetic torque comes from the solar panel, battery, and wires connecting various system components.

The magnetic moment of the spacecraft is minimized by design and compensation in the following ways:

- Lay out the current-carrying conductors such that they form the smallest possible loops.

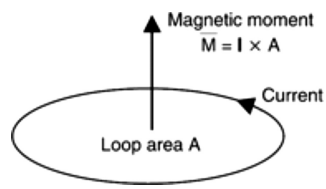

FIGURE 2.1 Definition of magnetic moment.

- Make two adjacent loops in opposite directions so that they compensate for each other.
- Twist wires wherever possible to neutralize the moments of adjacent twists.

After using one or more of the above design, the net residual magnetic moment is determined by tests after the satellite is assembled. A moment that would limit the resulting torque below 100 μNm in the operational orbit is generally considered acceptable.

2.3.3 Meteoroids and Debris

Impacts of solid objects can cause damage to the solar array. Small particles not large enough to cause immediate damage can cause gradual degradation in output power over time. The particle mass and the hit rate (flux) depend on the orbit. Several NASA studies conducted to predict the meteoroid flux in the Earth's orbit have given consistent results. They show that the average number varies inversely with the meteoroid mass, as given by the following simple expression:

$$\text{meteoroid flux} = \frac{1}{m} \tag{2.2}$$

where the flux is measured in the number of particles of mass greater than m grams per square kilometer per year. The most common meteoroids are small, having masses between 0.1 and 100 mg and are generally called micrometeoroids. The probability of having n impacts with particles of mass between m_1 and m_2 on a given surface area during y years is estimated using Poisson's probability distribution function. In the absence of accurate information, their mass density is assumed to be 0.5 g/cm^3 with a mean impact speed of 20 km/s. The actual fluency varies with the orbit. For example, in the geostationary orbit of Tracking and Data Relay Satellite (TDRS), the estimated meteoroid flux for a 15-year mission is shown in Figure 2.2. The yearly fluence rate in other orbits is shown in Figure 2.3.

In addition to the natural micrometeoroids, man-made debris, an increasing concern now more than ever before, can vary from 1 μm to 10 mm in diameter. They have an average density equal to that of aluminum, the most widely used material for satellite and launch vehicle components. Their relative velocity with respect to the spacecraft varies from zero to twice the orbital velocity, with an average around

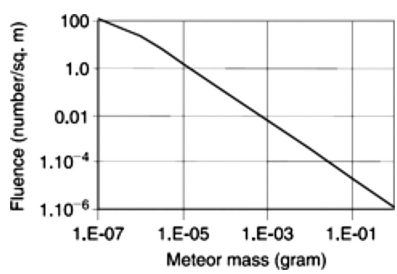

FIGURE 2.2 TDRS meteoroid environment fluence over 15 years.

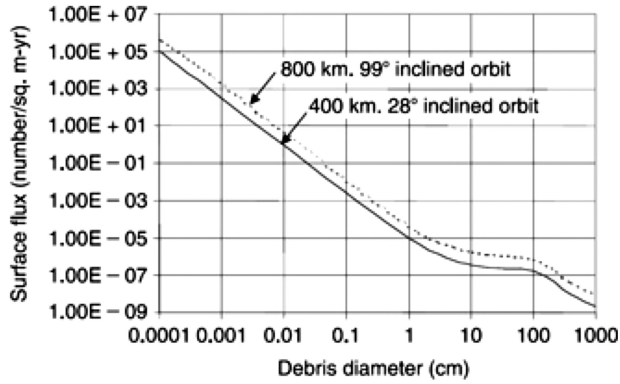

FIGURE 2.3 Debris flux rate estimate in various orbits.

10 km/s. The impact energy of large meteoroids can instantly damage the solar array's protective glass and cells. Micrometeoroids, on the other hand, erode the glass surface gradually, with subsequent degradation in the power output over time.

2.3.4 Atomic Oxygen

Atomic oxygen is present in low Earth orbit. It severely erodes some materials, such as silver, which is extensively used in the solar array construction. Similar erosion is also seen in some electrical insulation, such as Kapton™ and silicon rubber. The erosion comes not only from the chemical activity but also, in large part, from the atoms traveling at several km/s velocity relative to the spacecraft. In addition to the erosion (surface recession), atomic oxygen can also form stable oxides on the metal surface. For these reasons, exposed bare silver in solar arrays and silicon or Kapton insulation on electrical wires are undesirable. This topic is dealt with in Chapter 5.

2.4 VAN ALLEN BELTS

The Earth's magnetic field covers the magnetosphere, a doughnut-shaped region of space influenced by the Earth's magnetic field. It acts on the electrons and protons coming from space. The Van Allen radiation belts are parts of the magnetosphere that contain a large number of particles. The magnetosphere normally shields the Earth from these particles. However, when a disturbance on the sun radiates an abundance of particles, some reach the Earth's atmosphere near the magnetic poles and cause a glow known as an aurora, popularly known as the northern lights (or the southern lights, in the southern hemisphere).

The Earth's magnetic field, varying with the radius cubed, has a radial gradient, and it converges near the magnetic poles, as shown in Figure 2.4. The solar wind brings charged particles into the Earth's magnetic field. These particles are deflected by the Lorentz force F, given by the following cross-vector product:

$$\boldsymbol{F} = q\boldsymbol{V} \times \boldsymbol{B} \tag{2.3}$$

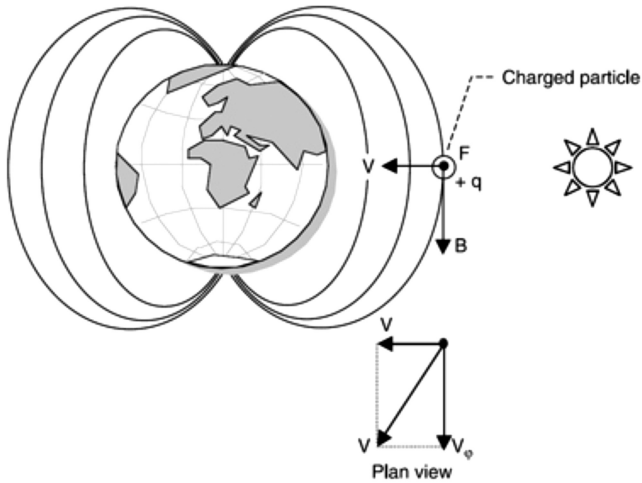

FIGURE 2.4 Lorentz force on a charged particle moving in Earth's magnetic field.

where q is the particle charge, V is the particle velocity, and B is the Earth's magnetic field intensity. The particle moving radially toward the Earth at velocity V generates a circumferential force that will impart velocity V_θ. The resultant velocity is then V_R, as shown in the plan view. The radial gradient in the field imparts a spiral motion to the particle. The spiraling particle comes to rest once all the energy is absorbed and then springs back and forth, as explained below.

A particle moving in a converging magnetic field generates a force that pushes the particle into a weak magnetic field (Figure 2.5), causing it to drift at a velocity V_z. The V_z decreases as the particle moves toward the equatorial plane of a weak magnetic field, and the V_θ increases to keep the kinetic energy constant. The particle eventually comes to a stop in the z-direction and is reflected back into the weaker field. Since the field is again converging on the other side, the particle is reflected back again. Thus, the converging field confines the charge particle between two magnetic mirrors. This way, most particles remain trapped in a certain belt all the time. However, particles with sufficiently high axial kinetic energy do not get reflected and escape the confinement belt.

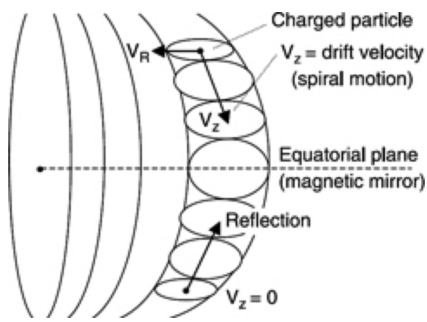

FIGURE 2.5 Charged particles moving in a convergent magnetic field.

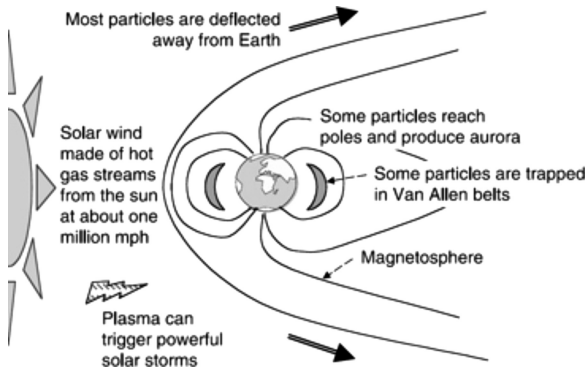

FIGURE 2.6 Van Allen radiation belts.

Most particles become trapped in two doughnut-shaped radiation belts known as the Van Allen Belts, which are part of the magnetosphere. The belts are stronger on the sun's side than on the side away from the sun, as shown in Figure 2.6. The trapping is concentrated in two belts shown in Figure 2.7. The electrons get trapped in a belt spanning 2–5 Earth radii, with a heavy concentration between 3 and 4 Earth radii. The high-energy protons penetrate closer to the Earth and get trapped in another belt spanning around 1–2 Earth radii with a heavy concentration around 1.5 Earth radii. Since the charged particle flux varies over the satellite orbit, the integrated radiation flux (fluence) is used in the power system design.

The solar array, in particular, requires protection against radiation damage. The geosynchronous satellites orbiting at 6.6 times the Earth's radius are way outside the inner proton belt and at the outer edge of the outer electron belt. Therefore, they are exposed to only a small part of the outer electron belt. However, they are more vulnerable to high-energy protons generated by solar flares.

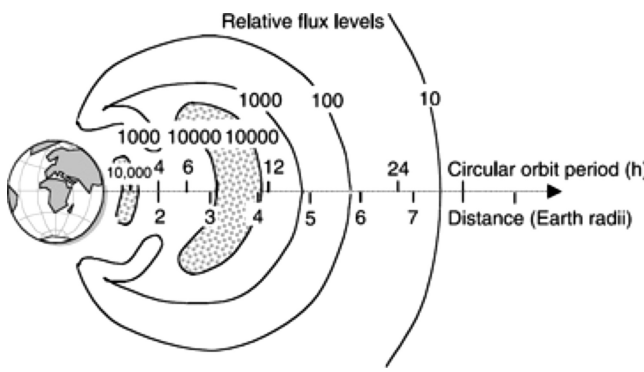

FIGURE 2.7 Extent of Van Allen radiation belts around Earth per NASA's AP-8 Environment Model.

2.5 SOLAR WIND AND SOLAR FLARE

A continuous stream of protons, electrons, and ionized gas leaving the sun and sweeping the solar system is called the solar wind. It is very thin, containing about 5 charged particles per cubic centimeter of space. The solar wind streams constantly, but not evenly. These particles travel past the Earth at speeds of about 480 km/s. In comparison, the Earth travels in its orbit at 30 km/s. When these particles flow past the Earth, some get trapped in the Earth's magnetosphere.

A solar flare is a gush of ionized gas with charged particles spewed out by the corona, the sun's glowing outer shell. It is associated with dark sunspots bounded by intense magnetic fields that come and go in 11-year cycles. The flare can cause auroras and disturb radio signals on Earth. The ionized gas is extremely hot (>1 million °C), such that atoms of hydrogen and helium are homogenized into dilute plasma, composed mainly of negatively charged electrons and positively charged protons. Although this constitutes a million tons of matter moving at a million miles per hour, its density is so low that it is still considered a vacuum. However, its effects can be devastating, as depicted in Figure 2.8.

Solar flares occur in 11-year cycles. One major period was November and December 2000. Several flares occur during each solar cycle, in which 7 years are active and 4 are inactive. The intensity levels of the flares vary over a wide range. Therefore, their energy levels and the corresponding probabilities that must be considered in designing the power system are mutually agreed upon by the

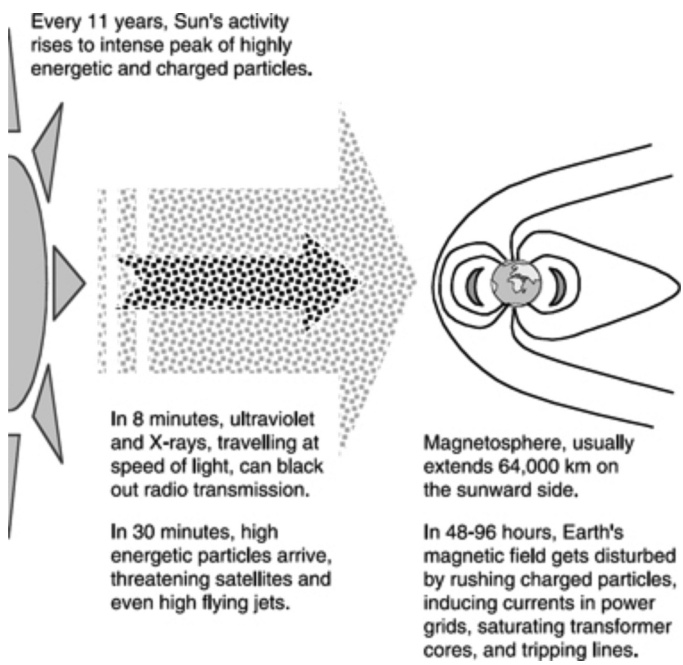

FIGURE 2.8 Solar flare and effects on Earth.

satellite customer and the manufacturer. The relatively strong 1989–1990 flares were extensively analyzed by spacecraft engineers because of the quantity and quality of data obtained and their impact on many spacecraft in orbit at the time. The newly developed model suggests that the proton fluences below 10 MeV were significantly underestimated in the past. This causes more degradation of the photovoltaic cells short circuit current I_{sc}, although not much in the open circuit voltage V_{oc}. From this study, it is estimated that a solar array design based on the old King model[2] of 1974 would have about a 20% probability of missing the power output requirements by a few percent compared to the new Feynman model[3] of 1989–1990 flares.

Table 2.1 gives the total annual flux in a typical geosynchronous orbit. The integrated flux of solar flare protons per 11-year cycle based on the new NASA/JPL model with an 80% confidence level is given in Table 2.2.

Spacecraft going beyond the solar system, such as *Pioneer* and *Voyager*, experience the so-called termination shock wave at the edge of the solar system. The termination shock wave is a zone around the solar system where the solar wind crashes into the tenuous gas and dust that fill interstellar space.

TABLE 2.1
Total Annual Fluence in a Typical Geosynchronous Orbit (number/cm^2)[a]

Particle Type	Normal Solar Flares	Intense Solar Flares
Trapped electrons	~10^{14}	~10^{14}
Trapped protons	Negligible	Negligible
High-energy solar flare protons	~10^{7}	~10^{10}

[a] Energy level of the electrons varies from a few keV to several MeV, and that of protons in several hundred MeV range.

TABLE 2.2
Integrated Flux of Solar Flare Protons per 11-Year Solar Cycle[a]

Energy (>MeV)	Solar Protons (number/cm^2)
1	5.3×10^{11}
5	2.0×10^{11}
10	1.0×10^{11}
30	2.3×10^{10}
50	9.7×10^{9}
70	6.6×10^{9}
100	2.5×10^{9}

[a] Based on new NASA/JPL model with 80% confidence level.

2.6 GEOMAGNETIC STORM

There is a well-recognized link between solar activity, disturbances in the geomagnetic field, and disruptions to man-made systems such as satellites, communications networks, defense systems, and even the sturdy power grids on Earth. Analysis suggests that these vulnerabilities to magnetic disturbances will continue and perhaps even increase as these systems continue to evolve and grow.

Under such storms, the magnetic field of the Earth is disturbed, causing induced currents in the overhead transmission lines of the power grid. The high-voltage lines, due to their long length and large loop area with the Earth's surface, can induce a high current. This low-frequency, d.c.-like geomagnetically induced current then enters the high-voltage transformers, driving them into deep magnetic saturation, causing the voltage to collapse and severe overheating. To protect airline passengers against the charged particles, the US Federal Aviation Administration warned pilots to stay below 25,000 feet when flying near the poles in order to avoid excess radiation.

The major effects of solar flares and geomagnetic storms on spacecraft power systems are:

i. Rapid degradation of the solar array's power generation due to high radiation dose. This is a life-shortening, not a life-threatening, effect.
ii. Common-mode EMI noise entering the electrical power system components through exposed cables, possibly latching some power electronics switches and relays, upsetting and permanently losing the power system's performance.
iii. Electrostatic discharge and sparking caused by a geomagnetic storm may permanently shorten out connections between the solar panels and other parts.

2.7 NUCLEAR THREAT

Some defense satellites are required to withstand a man-made threat of nuclear detonation of a specified intensity. The energetic particles released during a nuclear event are fission electrons, neutrons, gamma rays, and X-rays. Their energy levels depend solely on the destructive power of the nuclear device deployed. The threat level specified for the design is determined from the probability and consequence considerations. The level of nuclear threat, however, is always a classified number under the US Department of Defense's (DoD) secret classification system.

REFERENCES

1. NASA, "Space Vehicle Design Criteria (Environment)," Technical Report No. SP-8005, 1980.
2. King, J.H., "Solar proton fluence for 1977–1983 space missions," *Journal of Spacecraft and Rockets*, 11, 401–407, 1974.
3. Feynman, J., "New interplanetary proton fluence model," *Journal of Spacecraft*, 27(4), 403–408, 1990.

FURTHER READINGS

Beik, O., Patel, M.R. and Talebzadeh, S., Large spacecraft electric propulsion using multiphase generator, in *2023 IEEE Aerospace Conference*, Big Sky, MT, USA, pp. 1–8, 2023.

Saude, B., LaSart, N., Blair, J. and Beik, O., "Microgrid-based wind and solar power generation on moon and mars," *IEEE Transactions on Smart Grid*, 14(2), 1329–1332, March 2023.

Stassinopoulos, J.M., Barth, J.M., and Smith, R.L., "METSAT Charged Particle Environment Study, Revised Edition, Method 2," NASA Report No. GSFC X-600-87-11, 1987.

3 Power System Options

3.1 INTRODUCTION

Power requirements for very early satellites were several watts. In today's mid-size communications satellites, it is several kilowatts and is growing. Some strategic defense spacecraft power requirements are estimated to be in hundreds of kilowatts, and some defense spacecraft concepts require hundreds of megawatts of burst power. Solar radiation is the only external source of energy available in space. Any power system not using solar energy must carry its own source of energy on board, such as the primary battery, fuel cell, nuclear fuel, or chemical fuel. The basic components of the spacecraft power system are shown in Figure 3.1. They are the primary energy source, energy conversion, power regulator, rechargeable energy storage, power distribution and protection, and power utilization by the user's equipment (loads). Candidates for the primary energy source include solar radiation, radioisotopes, nuclear reactors, and electrochemical and/or chemical fuel. The energy conversion may be photovoltaic (PV), thermoelectric, dynamic alternator, fuel cell, or thermionic. Energy storage has been primarily electrochemical, although flywheel technology[1–4] has been developed at NASA Glenn Research Center but not utilized in space so far. From the available options that are compatible with a given mission and its environment, the satellite-level optimization study is conducted to select the best combination of energy source, energy conversion, and energy storage technologies. The final selection must meet multiple criteria, but the primary criteria are always low mass and low life-cycle cost. Such selection is largely influenced by the product of the power level and the mission duration, as shown in Figure 3.2. The dividing lines among various options are only approximate and have large overlaps. The following sections briefly describe these options and their optimum application ranges. The detailed description and performance of often-used options are covered in separate chapters.

3.2 PRIMARY BATTERY

A primary battery can economically power a small elementary spacecraft, requiring only several watts over several days. Early short mission spacecraft flew with

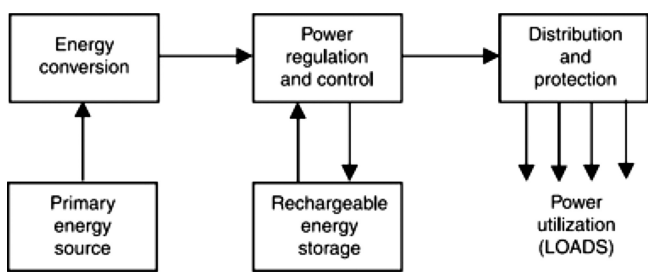

FIGURE 3.1 Basic components of a spacecraft power system.

DOI: 10.1201/9781003344605-4

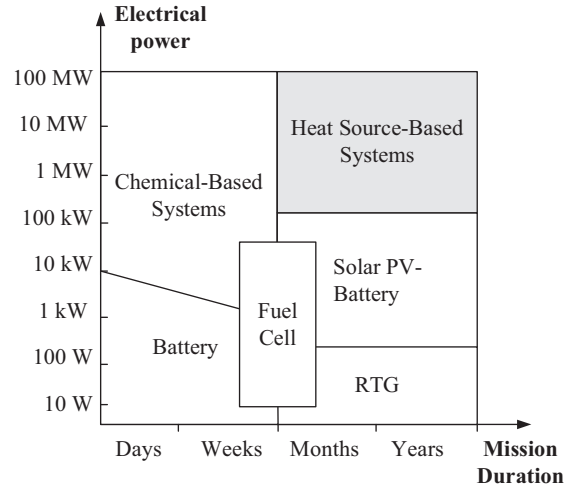

FIGURE 3.2 Optimum energy sources for various power levels and mission durations.

primary batteries such as AgZn and NaS. Even today, low-power, short-lived satellites carrying instruments with a low duty ratio may be designed using a primary battery such as LiCFx as the only power source, thus eliminating the solar panel and battery-charge electronics.

The battery cell consists of two electrode plates submerged in an electrolyte, as shown in Figure 3.3a. The electrochemistry of the cell generates an electrical potential difference between the electrodes, which can drive electrical current through an external load circuit. Thus, the battery converts the stored chemical energy between the electrode plates into direct-current electricity. The cell can deliver only a certain amount of charge, measured in ampere-hours (Ah), before all of its energy is depleted. The cell voltage decays with the Ah discharged, as shown in Figure 3.3b.

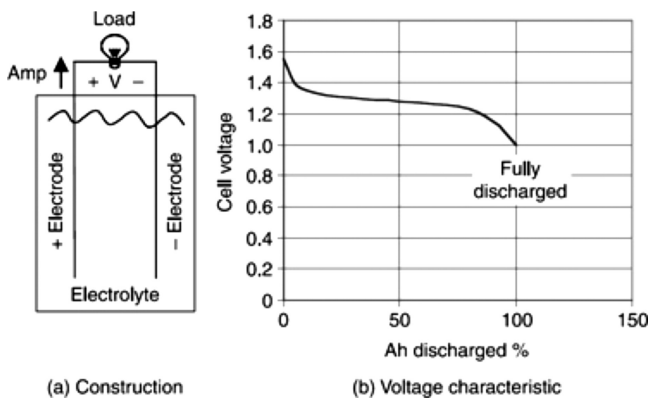

FIGURE 3.3 Battery cell construction and voltage characteristics. (a) Construction. (b) Voltage characteristic.

The primary battery has nonreversible electrochemistry. It cannot be recharged once its Ah capacity has been drained. It is then discarded, often jettisoned from the spacecraft, to shed mass and fuel for the forward mission.

3.3 FUEL CELL

Powering loads greater than several watts for more than a few days or a few weeks is not practical using a battery, but it is easily done with a fuel cell. The fuel cell, developed as an intermediate-term power source for space applications, was first used in a moon buggy and continued to be used to power NASA's space shuttles until their retirement. It also has other niche applications at present. A fuel cell converts chemical energy in the fuel, such as hydrogen and oxygen, into electricity (Figure 3.4a). Since the fuel continuously replenishes the energy, the cell does not run out of energy. Hence, the fuel cell is not rated in terms of the Ah capacity but in terms of the power generation rate. The cell voltage is maintained (Figure 3.4b) as long as the fuel is supplied at the required rate. Therefore, the fuel cell can be an optimal choice for supplying hundreds or thousands of watts over a few weeks using the onboard fuel.

A fuel cell is a static electrochemical device that generates direct-current electricity by a chemical reaction without altering the electrodes or the electrolyte materials. In concept, hydrogen and oxygen are combined to produce electricity and water, which is the reverse of the electrolysis of water. The crew in manned missions can use this water. The fuel does not burn as in an internal combustion (IC) engine. Thus, the fuel cell operates differently from both the electrochemical battery and the IC engine. The conversion efficiency of the fuel cell is not limited to that of the Carnot cycle because the fuel cell bypasses the thermal-to-mechanical conversion and its operation is isothermal. That is why its efficiency can be, in principle, much greater than that of the IC engine. The efficiencies of some commercial fuel cells approach 70%–80%, about twice the combustion engine efficiency. The space qualified fuel cell efficiency, however, is around 10%–15% at present but has the potential for a significant increase.

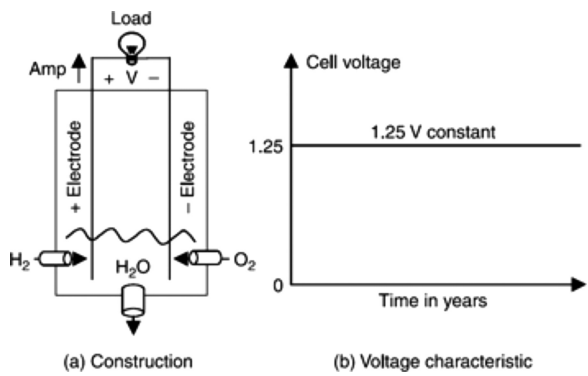

FIGURE 3.4 Fuel cell construction and voltage characteristics. (a) Construction. (b) Voltage characteristic.

3.4 SOLAR PV BATTERY

One of the most valuable breakthroughs in the space industry was probably the PV cell used to convert sunlight into electricity for Earth-orbiting satellites. Today, it is the most widely used energy conversion technology in the industry and has fueled the information revolution using high-power communications satellites. Power requirements ranging from tens of watts to several kilowatts over a life ranging from a few months to 15–20 years can be met with an array of PV cells. Satellites requiring continuous load power even during an eclipse must use a rechargeable battery along with the PV array. The battery is charged during sunlight and discharged to power the load during an eclipse. A power regulator and control circuits are used as required for the mission.

The general layout of the PV-battery power system is shown in Figure 3.5. All components other than the solar array are generally located inside the satellite body. The orientations of the core body and the solar array are maintained relative to the sun and the Earth. The core body is normally maintained in a near constant orientation relative to the Earth, while the α drive and the β gimbals orient the solar array to the sun. The α drive rotates 360° once per orbit as the satellite revolves around the Earth. The β gimbals rotate $\pm\beta°$ to compensate for the variation in the solar β angle and also to prevent array shadowing, if applicable. Not all satellites have β gimbals, but almost all that use the solar energy for power generation have an α drive. The most common form of α drive is a slip ring assembly with a solar array drive in 3-axis stabilized satellites and a rotary power transfer assembly in gyrostats. Angular errors induced by the structural distortions are often compensated by the α and/or β drive settings.

The seasonal variations of the β angle and the eclipse duration over 1 year for the International Space Station in a 400 km (220 n.m.) altitude and 51.6° inclination orbit are shown in Figure 3.6.[5] For a given system design, the power available to the load varies over the year due to seasonal variation in the β angle. At high $\pm\beta$ when the eclipse duration is zero, the load capability of the electrical power system would be the greatest, as no battery-charge power is required. For the soon-retiring ISS, there is no eclipse at all for $\beta > 71°$, making the orbit sun-synchronous.

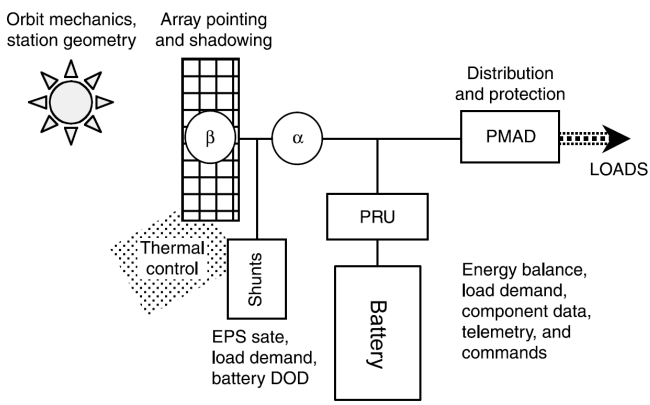

FIGURE 3.5 Solar photovoltaic–battery power system configuration.

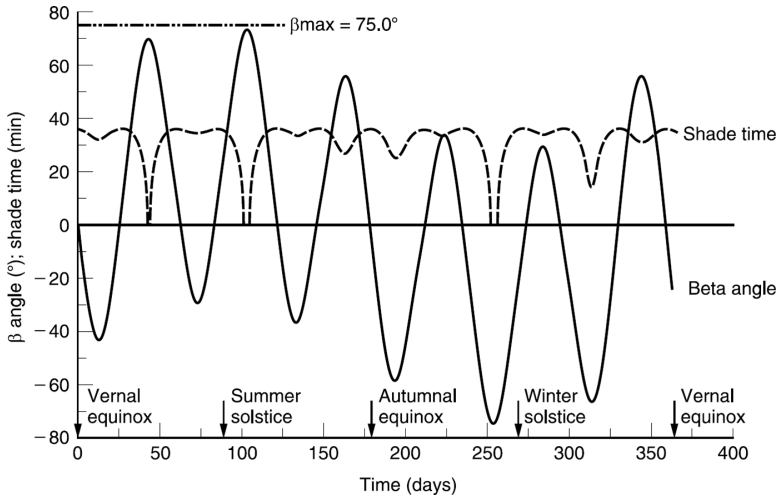

FIGURE 3.6 Beta angle and eclipse duration variation with season for the International Space Station.

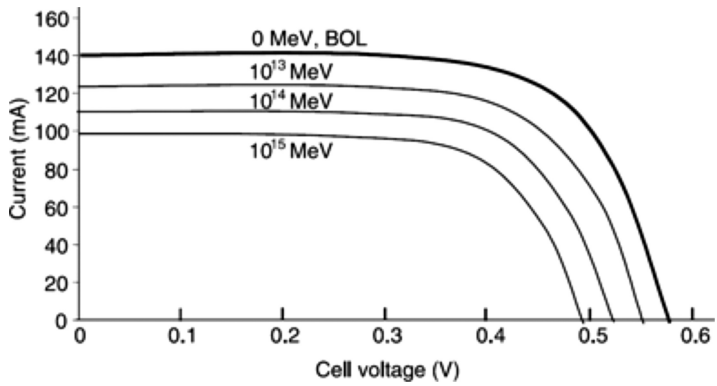

FIGURE 3.7 Degradation in *I–V* characteristics of a typical photovoltaic cell under radiation.

The PV cell has been a building block of space power systems since the beginning. The cell is a diode-type junction of two crystalline semiconductors that generates electricity under sunlight. Its performance at the beginning of life (BOL) is characterized by the output voltage and current at its terminals, as shown by the heavy line in Figure 3.7. The two extreme points on this curve, namely the open circuit voltage V_{oc} and the short circuit current I_{sc}, are often used as performance indicators. The maximum power a cell can generate is the product of V_{oc}, I_{sc}, and a factor that is approximately constant for a given junction. The *I–V* characteristic of the PV cell degrades, as shown by thin lines, with the increasing fluence of charged particles on the solar array in the space environment. Such degradation results in decreasing power generation

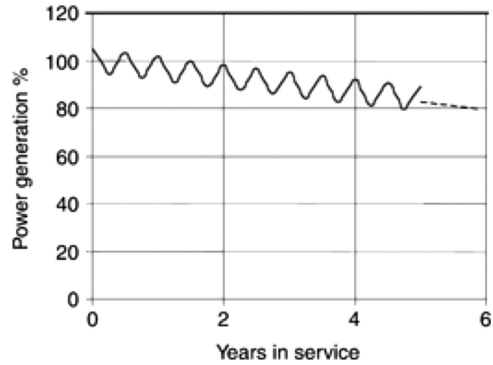

FIGURE 3.8 Degradation of solar array output power versus service years.

with time. With the combination of seasonal variations of β angle and yearly degradation of charged particles, the power generation of the solar array over the mission life varies as shown in Figure 3.8.

3.5 SOLAR CONCENTRATOR-DYNAMIC POWER SYSTEM

Solar energy can be used in systems other than PV cells. For example, the sun's energy is collected in the form of heat using a concentrator. The heat, in turn, is used to generate steam and drive a rotating turbo-generator or a reciprocating alternator; either way, it uses a thermodynamic energy converter.

The dynamic power system was a primary candidate for early space station design, having an estimated power requirement of 300 kW. The system configuration is shown in Figure 3.9. A parabolic concentrator focuses the sun's heat on a receiver, which boils a fluid. The fluid can be a suitable liquid or even a liquid metal, such as potassium chloride. High-pressure steam produced in the receiver drives a steam turbine based on the Rankine cycle. The fluid can also be a gas, such as a mixture of helium and xenon, with a molecular weight around 40. The heated gas drives a turbine working on the Brayton cycle. The gas-based system, however, minimizes erosion and the problem of sloshing when transporting a liquid. In either case, the high-pressure, high-temperature fluid drives the turbine, which in turn drives an electrical generator. The energy conversion efficiency is about twice that of the PV system. This minimizes the deployed collector area and the aerodynamic drag in low Earth orbit. An indirect advantage is that the energy storage is interwoven into the system at no extra cost. It primarily resides in the form of latent heat, with a phase change at high temperatures around 1000 K.

The dynamic power system incorporates thermal energy storage for hours with no degradation in performance or for longer durations with some degradation. This feature makes the technology capable of producing high-value electricity to meet peak demands. Moreover, compared to the solar PV system, the solar–thermal system is more economical as it eliminates the costly PV cells and battery. The solar concentrator-dynamic system with a turbo-alternator also offers a significant advantage in efficiency and weight, and hence the overall cost, over solar PV technology.

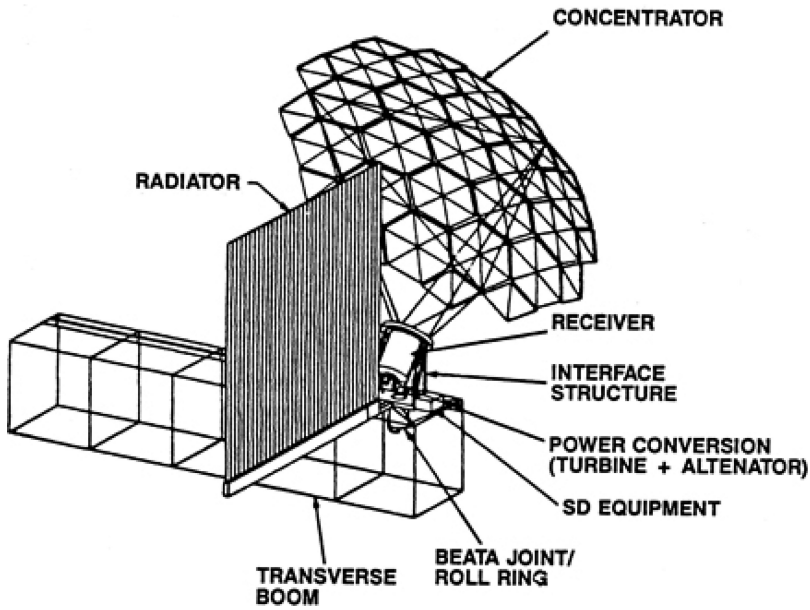

FIGURE 3.9 Solar concentrator-dynamic system.

Source: NASA.

3.6 NUCLEAR–THERMOELECTRIC

Interplanetary and deep space missions far away from the sun cannot be effectively designed using PV power generation due to reduced solar intensity. The spacecraft must therefore carry on board a primary energy source, such as a radioactive isotope or a nuclear reactor. In the first alternative, the radioisotope heats a thermoelectric (TE) material such as lead telluride, which generates electrical potential (Figure 3.10). The principle is similar to that in a thermocouple, only with higher conversion efficiency. The radioisotope thermoelectric generator (RTG) is routinely used for interplanetary missions requiring power levels of several hundred watts. The reactor, on the other hand, has been considered for high power in the 30–300 kW range. Both power sources have the advantage of supplying power all the time, thus eliminating the need for a battery in base-load systems with no peak power requirement. The obvious disadvantage is the heavy radiation shielding required around the electronic components. Also, the nuclear fuels that are safe and easy to handle with little shielding, such as curium-244 and plutonium, are expensive. Inexpensive, easily available fuels, such as strontium-90, are unsafe.

High-energy particles emitted from the radioactive isotope material are the primary energy source, which heats the absorbing material. The thermal power radiation decreases proportionally with the remaining mass. The mass of the isotope material decays exponentially at a rate characterized by the half-life $T_{½}$, which is long. Therefore, power generation is essentially maintained for decades. This makes the nuclear energy source ideal for long-life interplanetary missions; many of them

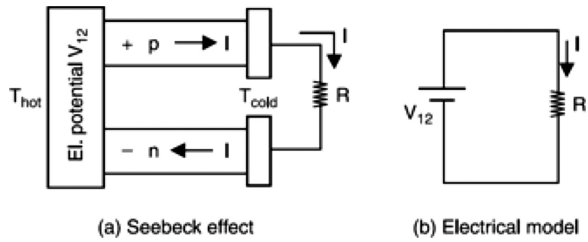

FIGURE 3.10 Thermoelectric converter. (a) Seebeck effect. (b) Electrical model.

require several hundred watts of power. For high-power defense spacecraft, a nuclear reactor with a TE converter had been funded and a prototype developed during the 1990s in the Space Power-100 (SP-100) program for some defense missions, requiring a high degree of radiation hardness under nuclear threat and power requirements ranging from 30 to 300 kW.

3.7 NUCLEAR ELECTRIC AND CHEMICAL-DYNAMIC

For large spacecraft, such as those intended for space travel, hundreds of kilowatts or multimegawatts of electrical power are required for propulsion. This can be supplied by (i) A nuclear reactor that rotates a turbine, which in turn spins an electric generator, or (ii) A chemical source, i.e., solid or liquid fuel. A short-life burst power mission may consider carrying onboard chemical fuel. On the other hand, a long-life mission may require a nuclear reactor. The primary source of power in such a reactor is nuclear fission, just like that in a ground-based nuclear power plant, only much smaller in scale. A variety of concepts using a nuclear–dynamic system were considered for the strategic defense initiative programs in the late 1980s and early 1990s. The strategic defense initiative conceptual design power levels were in the multimegawatt range between 30 and 300 MW. The basic requirement for such missions is to generate high power in the pulse or burst mode for a short duration of time, such as engagement at full power for about 15 min a few times over the mission's life. For the remaining time during the entire mission, the system needs to coast while consuming minimum power. The design driver for such a power system is large-scale energy storage with a slow charge rate and energy discharge at a high rate. For energy storage, both the flywheel and the superconducting magnet have been considered, along with other options.

3.8 OTHER SYSTEMS

There are other power system options in various stages of development. They may find applications in some special niche missions. In evaluating potential applications of any new technology, the prime considerations are always mass, cost, reliability, and technology risk. For example, a system using any fluid has the potential for leakage and sloshing. On the other hand, a system with no moving parts has three inherent advantages: high reliability, no vibration, and no torque on the platform.

3.8.1 Thermo-Photovoltaic

In the thermo-photovoltaic scheme, the radioisotope or solar heat is directed at the PV cells. It has a significantly higher conversion efficiency for generating electricity as opposed to the present use of RTGs. Therefore, it may find applications as a mission-enabling technology where its high cost is acceptable. The system can have a cylindrical or a flat configuration, as shown in Figure 3.11. A heated surface radiates infrared heat onto an array of PV cells sensitive to the infrared range. A part of the energy is converted into d.c. electricity, and some is reflected back and dissipated as heat. The energy conversion process is different compared to that in a conventional PV cell.

3.8.2 Solar–Thermoelectric

The power system for a near-sun probe operating at high temperatures cannot effectively use PV cells because of severe temperature degradation in performance. In such a mission, the collected solar heat can be directed at a pile of thermoelectric converters. The only difference between the RTG and the solar–TE is the source of heat. The RTG heat source is a suitable nuclear radioisotope, while heat in the solar–TE scheme comes from the sun.

3.8.3 Thermionic

In this conversion process, the thermal energy is converted into electricity by using the electrons released from a hot body, known as thermionic emission, or the Edison effect. The electrons released from the cathode are collected at the anode, and a closed path through a load is established to complete the circuit back to the cathode. It has no moving parts. The concept is an old one but may attract new interest due to advances made in high-temperature materials. The thermionic converter is basically a heat engine with electrons as the working fluid and is subject to the Carnot efficiency limitation. For this reason, it operates at much higher temperatures, with a hot side around 1800–2000 K and heat rejection around 800–1000 K. This imposes limits on candidate materials and life. Also, the thermionic converter produces a very low voltage, requiring extensive power conversion and large power conditioning losses. A typical example of this development is the thermionic fuel element that integrates the converter and nuclear fuel for space power in the kilowatt-to-megawatt range for long missions. Converters filled with ionized gas, such as cesium vapor, in the inter-electrode space yield higher specific power due to space charge neutralization.

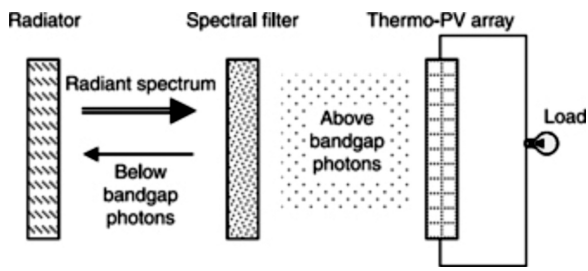

FIGURE 3.11 Thermo-photovoltaic converter.

3.8.4 Alkaline Metal Thermal-to-Electric Converter

The alkaline metal thermal-to-electric converter is a direct thermal-to-electric energy conversion system. It operates at temperatures around 1000 K on the high side and 600 K on the low side and yields an efficiency of 18%–20%. It is a static system suitable for power levels below 100 W. It uses a unique characteristic of the alkali metal conducting ceramic β-alumina.[6] It is a solid electrolyte that conducts sodium ions but is an electron insulator. An electrochemical potential is generated when sodium is present at two different pressures separated by an electrolyte. The sodium is circulated through the converter using a porous stainless steel wick that uses capillary forces to transport the sodium from the low-pressure region to the high-pressure region. It has no moving parts and develops low voltage, requiring a high level of power conditioning. A commercial version of this technology with titanium nitride electrodes is used for small downhole instruments in the oil industry.

3.9 SYSTEM VOLTAGE OPTIONS

The bus voltage for early spacecraft with loads of a few hundred watts was 28 V d.c., primarily based on the product specifications readily available for the power system at the time. Since then, the power levels have increased significantly. As power, at its simplest form, is the product of voltage and current, high power requires a high-voltage bus in order to keep the current at a reasonable level. Otherwise, the excessive power loss in switching devices and the I^2R loss in conductors reduce the system efficiency considerably. Today's small to mid-size spacecraft bus voltages, somewhat standardized by the product lines of various manufacturers and government agencies, are 28, 50, 70, 100, 120, and 160 V, as shown in Figure 3.12. However, for large-scale multihundred or MW-scale spacecraft, the voltage levels need to be increased; a potential voltage of 1000 V and higher has been considered for these spacecraft.

High-voltage design, however, impacts component selection. Moreover, space environment considerations also limit the voltage to a certain level for a given mission. The factors that influence the voltage selections are:

- Power level being the primary driver
- Space environment, space plasma, and potential electrostatic discharge leading to sparking

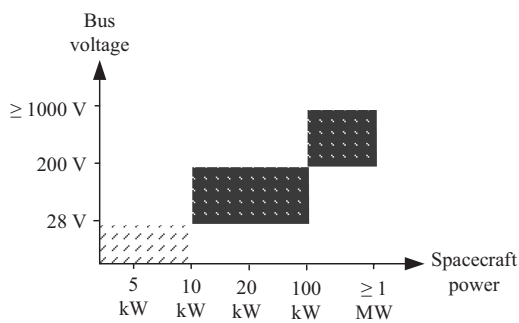

FIGURE 3.12 Optimum voltage for various power levels.

- Paschen's minimum breakdown voltage between bare conductors to avoid sparking
- Availability of components, such as semiconductor devices, power distribution and protection devices, tantalum capacitors, etc.
- Human safety

REFERENCES

1. Beik, O. and Emadi, A., "Toward integrated digital aircraft control systems: For electrified-system optimized size, cost, and efficiency," *IEEE Electrification Magazine*, 5(4), 46–52, Dec. 2017.
2. McLallin, K.L., Fausz, J., Jansoen, R.H., and Bauer, R.D., Aerospace flywheel development for IPACS applications, in *Proceedings of the 36th Intersociety Energy Conversion Engineering Conference*, ASME, 2001, vol. I, 2001, pp. 105–110.
3. Patel, M.R., Flywheel energy storage for spacecraft power system, in *Proceedings of the 34th Intersociety Energy Conversion Engineering Conference*, SAE, 1999, Paper Number 183.
4. Patel, M.R., Integrated Energy-momentum wheel for satellite power and attitude control systems, in *Proceedings of the 35th Intersociety Energy Conversion Engineering Conference*, AIAA, 2002, Paper No. 196.
5. Hojnicki, J.S. et al., "Space Station Freedom Electrical Performance Model," NASA Glenn Research Center, Report No. TM-106395, 1993.
6. Pantalin, J.E. et al., Advanced AMTEC converter development, in *Proceedings of the 35th Intersociety Energy Conversion Engineering Conference*, ASME, 2001, pp. 519–524.

FURTHER READINGS

Aghamohammadi, M.R. and Khormizi, A.B. Small signal stability constrained rescheduling using sensitivities analysis by neural network as a preventive tool, in *2010 Asia-Pacific Power and Energy Engineering Conference*, March 2010, pp. 1–5.

Aghamohammadi, M.R., Beik Khormizi, A., and Rezaee, M., Effect of generator parameters inaccuracy on transient stability performance, in *Proceedings of the 2010 Asia-Pacific Power and Energy Engineering Conference*, Chengdu, China, 28–31 March 2010, pp. 1–5.

Beik, O., Patel, M.R. and Talebzadeh, S., Large spacecraft electric propulsion using multiphase generator, in *2023 IEEE Aerospace Conference*, Big Sky, MT, USA, 2023, pp. 1–8.

Brown, E.J. et al., Measurements of conversion efficiency for a flat plate thermo-photovoltaic system using a photonic cavity test system, in *Proceedings of the 35th Intersociety Energy Conversion Engineering Conference*, AIAA, 2000, Paper No. 3029.

Hyder, A.K. et al., *Spacecraft Power Technologies*, Imperial College Press/World Scientific Publishing Co, London, 2003.

Marshall, C.G. et al., Example of a prototype lightweight solar array and the three promising technologies it incorporates, in *Proceedings of the 35th Intersociety Energy Conversion Engineering Conference*, SAE, 1999, Paper No. 01-2550.

Patel, M.R., *Spacecraft Power Systems*, 1st Edition, Chapter 25, Flywheel Energy Storage. CRC Press, Boca Raton, FL, 2004.

Saude, B., LaSart, N., Blair, J. and Beik, O., "Microgrid-based wind and solar power generation on moon and mars," *IEEE Transactions on Smart Grid*, 14(2), 1329–1332, March 2023.

4 Photovoltaic–Battery System

4.1 INTRODUCTION

Photovoltaic (PV) conversion of the sun's energy is the most common source of electrical power in space. An array of PV cells powers the load and charges a battery during sunlight. The battery powers the load during an eclipse. The solar array's output voltage is higher at the beginning of life and when the array is cold for several minutes after each eclipse. Also, the battery has a lower voltage during discharge than during charge. Since the system is required to provide power to the load at a voltage regulated within specified limits, a voltage regulator provided through a conventional regulator using power electronics-based converters is always needed to match the voltages of various power components during the entire orbit period.

The PV power system, therefore, primarily consists of a solar array (SA), a rechargeable battery, and a power regulator, which regulates power flows between various components to control the bus voltage. Other components, such as various sensors, are also required to make the array and the battery work together. The total power system is thus coordinated internally as well as externally through interfaces with other systems on the spacecraft. The top-level performance characteristics of the basic PV–battery system are described in this chapter, leaving the component-level details for later chapters.

4.1.1 Solar Array

The SA is made of numerous PV cells stacked in series–parallel connections to obtain the desired voltage and current from the assembly. It converts the incident photon energy into dc voltage, which drives current through the external load circuit. The SA works more like a constant-current source over its normal operating range. Its terminal voltage versus current characteristic, referred to as the *I–V* curve, is shown in Figure 4.1. The end-of-life curve must meet the performance requirement. The characteristic curve changes significantly with temperature and the radiation dose of charged particles, as shown in the figure. The power, being the product of the voltage and current, varies as shown in Figure 4.2. The power output of an array is maximum at the knee-point voltage. The system produces less power when operating at any other voltage. Also, the power output gradually degrades with accumulated radiation dose. At the end of life, the array generates less power than at the beginning of life.

DOI: 10.1201/9781003344605-5

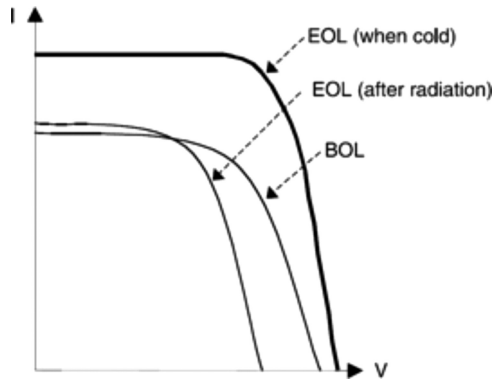

FIGURE 4.1 Current versus voltage characteristics of a photovoltaic cell.

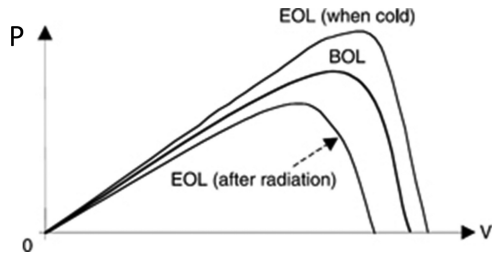

FIGURE 4.2 Power versus voltage characteristics of a photovoltaic cell.

4.1.2 Battery

The battery is made of rechargeable electrochemical cells connected in a series–parallel combination to obtain the desired voltage and current. Its terminal voltage depends primarily on the state of charge (SOC) and, to some extent, on the operating temperature. The battery charge is measured in terms of the ampere-hours stored between the positive and negative plates. The voltage is highest when the battery is fully charged and lowest when it is fully discharged. Since the battery works more like a constant voltage source over the normal operating range, its terminal characteristics are generally expressed in terms of the battery voltage versus the SOC. Figure 4.3 depicts the voltage of one fully charged cell as it discharges and then gets recharged. The voltage scale in the figure represents both the NiCd and the NiH_2 cells. The battery voltage drops significantly with increasing discharge, and then rises during charging. The average voltage during charge is higher than that during discharge.

4.1.3 Power Regulation

In a spacecraft power system, power regulation is primarily accomplished by battery charge and discharge power electronics-based converters, shunt dissipators, and the mode controller with related control systems. The shunt dissipator is

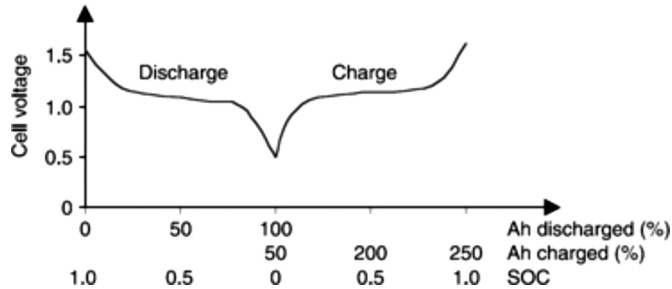

FIGURE 4.3 Battery cell voltage versus SOC in one complete cycle.

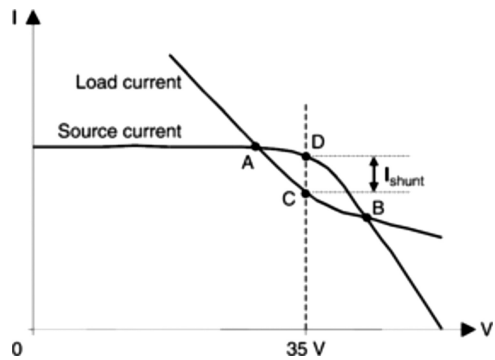

FIGURE 4.4 Stability of the operating point and shunt control during sunlight.

necessary to control the bus voltage during sunlight, as described hereafter. The SA (source) and the constant power load have their own *I–V* characteristics, as shown in Figure 4.4. The system can operate at either of the two intersection points, A or B. However, point A is inherently unstable because the load slope is less than the source slope. Point B, on the other hand, is inherently stable. Without a shunt control, the system would operate at point B, producing lower power. With shunts designed to regulate the sunlight voltage at, say, 35 V, the system will pull back from point B to point C by shunting the excess current to the ground. The shunt current in this operating mode would be I_{shunt}, the difference between the source current at D and the load current at C.

4.2 POWER SYSTEM ARCHITECTURES

The SA, battery, and shunt characteristics described above, along with the load voltage requirement, are extremely important in selecting the power system architecture that is most suitable for the mission. The mission-imposed or self-derived requirements on the power system also have bearings on the architecture selection. The PV–battery system is configured in one of the following architectures that would optimize the system's performance for a given mission.

4.2.1 Direct Energy Transfer

Direct energy transfer (DET), in which the solar power is transferred to the loads with no series component in between. The necessary exceptions are: (i) the slip rings to provide a rotary joint between the Earth-facing spacecraft body and the sun-facing SA and (ii) the power distribution unit (PDU) consisting of load switching relays and fuses to protect the power system from faults in the load circuits. The DET can be further subdivided into two classes: (i) the fully regulated bus and (ii) the sunlight-regulated bus. The components and operation of these two buses are similar, except that the latter has no battery discharge converter in the power regulator unit (PRU).

In a fully regulated DET bus, commonly known as the *regulated bus*, the bus voltage is controlled within a few percent during the entire orbit period. The typical bus voltage variation is ±2% to 5% of the nominal voltage. The architecture of this bus is shown in Figure 4.5. It has the following components:

Solar array: The SA is an array of PV cells that convert sunlight into electricity. The large array is generally divided into many parallel circuits (strings), each with isolation diodes, so that a failed string would not draw power from the healthy ones. The ungrounded end of each section and individual string is isolated from the main bus and battery by diodes. These diodes may be located inside the PRU for protection or on the back of the SA, exposed to the environment. In one case, the slip rings are involved, but not in the other. The electrostatic discharge-induced transient voltage suppressing snubber capacitors may be located inside or outside. The array's negative terminal is usually grounded. If the positive were grounded, the power system would work just as well, except that we must use p–n–p semiconductors instead of traditional n–p–n devices in the PRU. The power converter design would change accordingly. One advantage of the positive ground is that the structure becomes negatively charged and

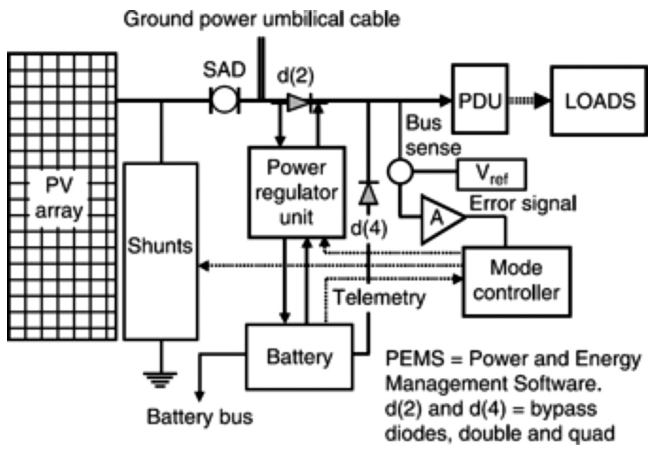

FIGURE 4.5 Fully regulated direct energy transfer architecture.

attracts atomic oxygen ions at a lower speed, causing less sputtering of the anodized aluminum commonly used in the spacecraft structure. The bus diode pair d(2), typically Schottky diodes, prevents loss of the bus voltage in case the battery charger gets an internal fault, which may clear after some time. Such diodes—appropriately called the DET diodes—have been used in many defense meteorological satellites. They are not absolutely needed and would reduce efficiency. In its absence, adequate fusing should be used to protect the bus from faults in the battery charger. The current required to clear a charger fault would come from the SA, whether or not d(2) diodes are present.

Solar array drive: The solar array drive (SAD) consists of slip rings, a motor, and motor drive electronics. It continuously orients the SA to face the sun to generate the maximum possible power during the entire sunlight period of the orbit.

Shunt dissipator: During sunlight, particularly in the beginning of life, this component dissipates power that is unwanted after meeting the load power and the battery charge power requirements.

Battery: The battery stores energy in an electrochemical form to supply power to the loads during eclipse periods over the entire mission life. NiCd secondary batteries were extensively used in satellites until the mid-1980s. Beginning in the 1990s, NiCd was replaced by NiH_2 for better performance and lower mass. In modern designs, however, Li-ion is used in most satellites for their overall superior performance and longer cycle life.

Power regulator unit: The PRU provides an interface between the SA bus and the battery. The battery voltage varies widely, with the cell voltage varying from low when fully discharged to high when fully charged. The discharge converter in the PRU boosts the battery voltage to the bus voltage during an eclipse, and the charge converter boots the array voltage to the battery voltage during sunlight. For GEO missions, the charge converter rating is much smaller than the discharge converter rating. In such situations, designing the charge and discharge converters separately would be beneficial, as their individual designs could be better tuned to their own ratings and requirements. On the other hand, for LEO missions, a bidirectional converter may be beneficial, as the charge converter and the discharge converter ratings are comparable. The following approximations may help trade various options in conceptual designs. A 1 kW battery discharge converter may weigh 2–3 kg. A 1 kW PRU designed to operate between −25°C and 60°C with a reliability of 0.99975 may weigh 6–7 kg, including the battery charge converter and dedicated support electronics.

Power distribution unit: The PDU ensures that all loads, except critical and essential loads, are powered through switches and fuses. The fuses are not to protect the loads as much as they are to protect the power system from faults in the user equipment.

Bus voltage controller (Mode controller): The mode controller controls the bus voltage. It consists of the bus voltage sensor, the reference voltage, and

the error signal amplifier. The amplified error signal output of the bus controller enters the mode controller, which in turn sends command signals needed to regulate the bus voltage within the required limits. The operating mode of electric power system (EPS) automatically changes in response to the error signal, as described below. The mode selector switch is typically a magnetic latching relay.

The mode controller sets the system's operating mode in response to the error signal, which is the difference between the actual bus voltage and the reference voltage representing the required bus voltage. Depending on the error signal value and its polarity (positive or negative), the mode controller sends a control signal to either the shunt regulator, the battery charge regulator, or the battery discharge regulator (Figure 4.6). One of these three sub-regulators, in turn, maintains the bus voltage within the specified limits.

Battery bus: The battery bus is essentially a tap point directly off the battery. During the launch and ascent phases of the mission, the PV array is not deployed, and the battery meets all the energy needs. For example, all electro-explosive devices for spacecraft deployment are powered directly from the battery bus for high reliability and low bus impedance (as there is nothing between the power source and the load). The battery diodes d(4) in Figure 4.5 provide an inrush of current to clear the fuse of any load branch in case of an internal fault in it, thus protecting the power system at large.

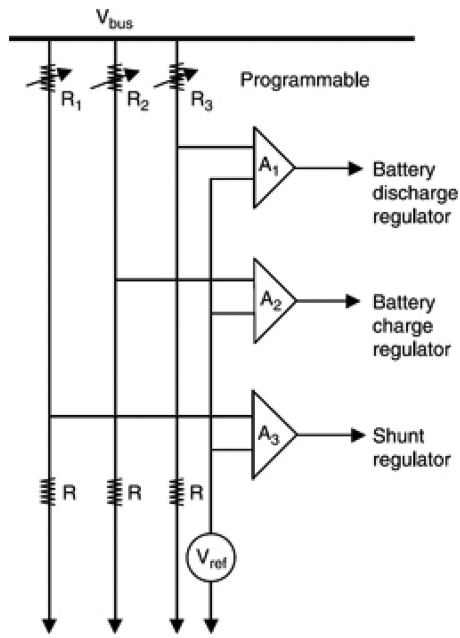

FIGURE 4.6 Mode controller error signal routing concept.

4.2.2 Max Power Point Tracking (Peak Power Tracker)

The process of extracting maximum power from the solar panel is referred to as the maximum power point tracking or peak power tracking (PPT). It sets the SA output voltage at the value that always results in the maximum power transfer from the array to the load under varying operating conditions, such as daily or seasonal variations in the array temperature, sun angle, solar flux, etc. The array voltage is then converted by a series dc–dc switch-mode regulator between the array and the load to match the load voltage requirement and the array output voltage (Figure 4.7). The concept uses the "maximum power transfer theorem" taught in the Electrical Circuits course. Essentially, the PPT transforms the load impedance with the source by varying the dc–dc converter voltage ratio and the duty ratio to extract the maximum power from the array. For PPT architecture to be cost-effective, the power loss in the PPT converter must be less than the gain in operating the system at the peak power point all the time.

4.3 TYPICAL PV–BATTERY POWER SYSTEM

The architecture of a spacecraft power system based on PV batteries is shown in Figure 4.8, with its key components described below.

4.3.1 Solar Array

The SA is an array of PV cells that convert sunlight into electricity. The large array is generally divided into many parallel circuits (strings), each with isolation diodes, so that a weak or failed string would not draw power from the healthy ones. The ungrounded end of each section and individual string is isolated from the main bus and battery by diodes (called the bus diodes). These diodes may be located inside the PRU for protection or on the back of the SA, exposed to the environment. In one case, the slip rings are involved, but not in the other. The electrostatic discharge-induced transient voltage suppressing snubber capacitors may be located inside or outside. The array's negative terminal is usually grounded. If the positive were grounded, the power system would work just as well, except that we must use p–n–p semiconductors instead of traditional n–p–n devices in the PRU. The power converter design

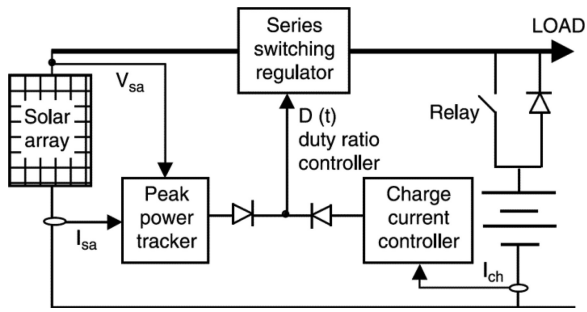

FIGURE 4.7 Peak power tracker (dc–dc switching regulator) in series with the photovoltaic array and the load.

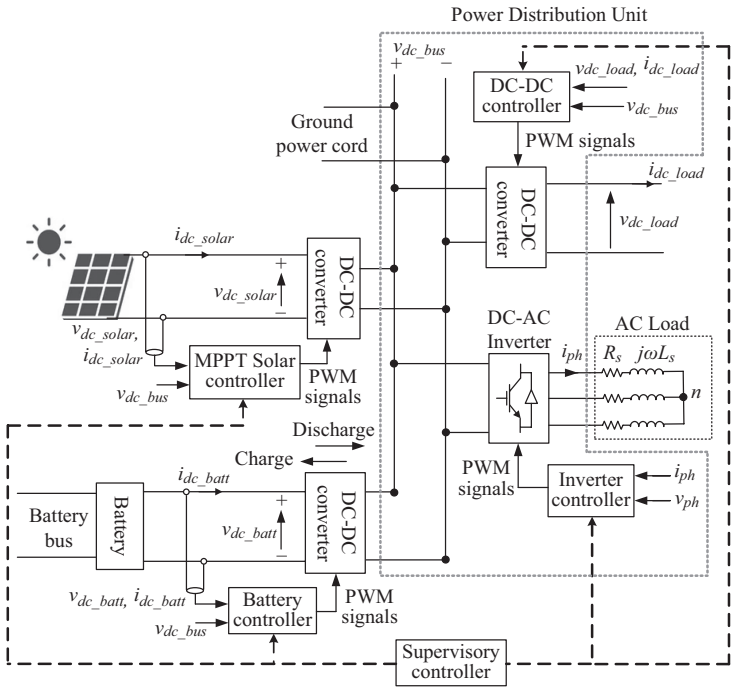

FIGURE 4.8 PV–battery power system architecture.

would change accordingly. One advantage of the positive ground is that the structure becomes negatively charged and attracts atomic oxygen ions at a lower speed, causing less sputtering of the anodized aluminum commonly used in the spacecraft structure.

4.3.2 Battery

The battery stores energy in an electrochemical form to supply power to the loads during eclipse periods over the entire mission life. NiCd secondary batteries were extensively used in satellites until the mid-1980s. These batteries were replaced by NiH_2 for better performance and lower mass, and more recently with Li-ion batteries. As battery technology improves, the batteries in the spacecraft will continue to be replaced with newer generations.

4.3.3 DC Bus

The dc bus is the main electrical component in the spacecraft power system, where all the sources (PV and battery in this architecture) and loads (dc and ac loads) are interfaced. The bus collects the power from the sources and distributes it to the loads. Bus voltage is an important parameter in the design of the electrical power system for the spacecraft. As the spacecraft become larger and hence more powerful, the bus voltage needs to be increased to reduce losses and enhance efficiency.

4.3.4 DC–DC Converter for Solar PV

Each source is connected to the dc bus through a dc–dc converter. In the case of solar panels, their output voltage varies with the solar flux intensity. The dc–dc converter takes this variable solar output voltage and steps it up or down to the fixed dc bus voltage. A dc–dc converter for PV solar, such as shown in Figure 4.9, needs to have the following features:

1. Isolation via a transformer that separates the ground on the PV solar panel side from the ground on the dc bus and load side and presents unwanted dc faults to pass through
2. Step-up or step-down via transformer. The transformer allows stepping the PV solar to a high-voltage dc bus as the power levels continue to increase for spacecraft
3. Unidirectional power flow from PV to dc bus to prevent damage to the PV panels
4. Fully controllable

The topology in Figure 4.9 has all the above features; this topology is commonly referred to as a flyback dc–dc converter. The diode on the secondary prevents power from flowing from the dc bus to the solar panel, while the switch allows for controlling the output voltage and power of the converter to the dc bus. As shown in Figure 4.8, the dc–dc converter controls the maximum power point tracking for the solar panel. To perform this, the voltage and current output of the PV panel and the dc bus voltage are measured, which are used for comparing with reference values. A control system that is designed based on the system parameters generates switch control signals using the pulse width modulation technique. The switch signal is applied to the switch (*S*).

4.3.5 DC–DC Converter for Batteries

The battery systems in a spacecraft can be used as follows:

1. Secondary battery for PV solar systems. In this case, the battery plays the role of a backup or complementary source of energy for the spacecraft.
2. Primary battery. In this case, the battery is the main source of energy for the spacecraft, while other sources, such as solar or RTG, are used as backup or secondary.

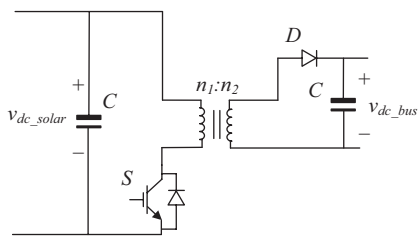

FIGURE 4.9 Isolated dc–dc converter for photovoltaic solar (Flyback topology).

In both primary and secondary battery systems, a controller needs to manage the charge and discharge of the battery. The battery is usually charged if its SOC is below full charge and when the power from the PV panels exceeds the demand power of the loads. If the load exceeds the power generated from the PV panels and the battery SOC is above its minimum, the battery discharges and provides the remaining load power. A dc–dc converter manages the battery charge and discharge and its interface to the dc bus. The dc–dc converter for the battery system is required to have the following features: (i) Bidirectional capability to allow charge and discharge, (ii) Isolation via a transformer, and (iii) Step-down or step-up via a transformer.

Figure 4.10 shows a full bridge topology for the dc–dc converter for the battery system. This topology satisfies all the features listed above. For control, the battery voltage, current, and dc bus voltage are measured and compared with reference values in a battery controller, as shown in Figure 4.8. The controller generates the required pulse width modulation signals for the switches.

4.3.6 Loads

In a spacecraft, the term *load* includes all loads, i.e., the payloads (transmitters, receivers, science instruments, etc.), as well as the housekeeping bus system loads. For all loads, the orbital average power requirement is taken into account in sizing the PV array and the battery. The loads may be constant or have a variable nature. Some loads may have their own converter that directly connects to the dc bus and provides the required voltage and current for the load.

4.3.7 Power Distribution Unit

The PDU ensures that all loads, except critical and essential loads, are powered through switches and fuses. The fuses are not to protect the loads as much as they are to protect the power system from faults in the user equipment. As seen from Figure 4.8, the PDU also includes:

1. dc–dc converters that connect to the dc bus on one side and provide different dc voltages and current on the output for loads. There are as many dc outputs from the dc converters as the loads require.
2. dc–ac inverters to provide ac output for the ac loads, if any. The inverters may be single-phase or three-phase, depending on the nature of the ac loads.

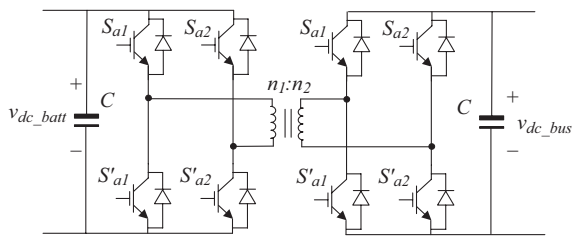

FIGURE 4.10 Isolated bidirectional dc–dc converter for battery (Full bridge topology).

The controls for the converters that interface the loads to the dc bus are done via individual controllers for each converter, as seen in Figure 4.8. For this, the dc bus voltage and the voltage and current measurements at the output of each converter are measured and used as feedback.

4.3.8 Supervisor Controller and Power and Energy Management Software

The supervisory controller performs power and energy management. It is designed for the spacecraft power system, as shown in Figure 4.8. The supervisory controller "talks" to each individual controller and receives and sends command signals based on the status of the load, generation, dc bus voltage, and PDU. Although the power and energy management software is part of the software system, it is dedicated to EPS performance, health monitoring, control, and protection. In case of emergencies or during planned mission operations, power and energy management software (PEMS) sheds loads in a preset sequence if and when the battery SOC cannot support all loads. The battery telemetry consists of the battery voltage, current, temperature, individual cell voltages, and internal pressures of selected cells. Some of these telemetry readings also go to PEMS.

4.3.9 Battery Bus

The spacecraft power system usually has a battery bus, as shown in Figure 4.8. The battery bus is a tap point directly off the battery on the left-hand side. During the launch and ascent phases of the mission, the PV array is not deployed, and the battery meets all the energy needs. For example, all electro-explosive devices for deployment are powered directly from the battery bus for high reliability and low bus impedance (as there is nothing between the power source and the load).

4.3.10 Ground Power Cord

As shown in Figure 4.8, the spacecraft power system has a ground power cord that is connected to the dc bus. To preserve battery power during pre-launch testing and final checks before lift-off, the on-board system uses external ground power via an umbilical cord. To further preserve the battery, power transfer is scheduled as late as possible in the countdown.

4.4 THE INTERNATIONAL SPACE STATION

As of 2023, the International Space Station (ISS) is set to decommission and deorbit by 2031. Figure 4.11 shows the ISS in its present configuration. The ISS is the largest space structure to date, measures 357 feet, or 108 m from end to end, and weighs about one million pounds. The ISS is maintained in a nearly circular orbit with a minimum mean altitude of 370 km (230 mi) and a maximum of 460 km (290 mi) in the center of the thermosphere, at an inclination of 51.6° to Earth's equator and an eccentricity of 0.007.

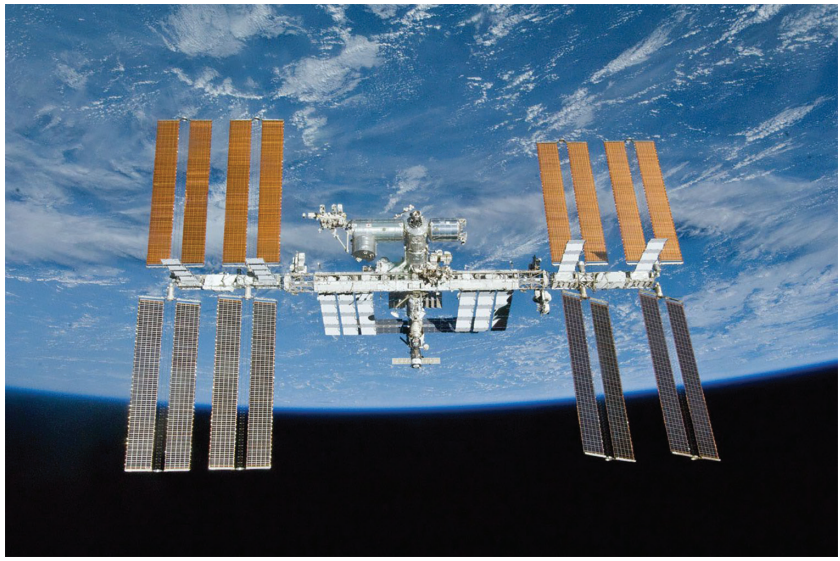

FIGURE 4.11 International Space Station with its solar array and other modules in view. (Source: NASA.)

The ISS electric power system consists of a hybrid mix of two main segments: a 160–120 V US-built portion and a 28–120 V Russian-built portion. The 120 V is the distribution voltage, while the 160 V is the US section solar panel output voltage. Each ISS SA wing (often abbreviated "SAW") consists of two retractable "blankets" of solar cells with a mast between them. Two SA wings make up a set of SAs. The two wings are deployed in opposite directions. Altogether, the four sets of arrays can generate 84–120 kW of electricity. The original Ni-H2 batteries have been replaced by 3 Li-ion batteries per 8 channels, totaling 24 Li-ion batteries on the ISS. Table 4.1 lists ISS's solar panel specifications, while Table 4.2 lists batteries.

4.5 COMMUNICATIONS AND SCIENCE SATELLITE BUSES

In view of reducing cost and delivery time, all prime manufacturers develop standard buses that can meet various power requirements without making many changes. The standard bus has a degree of flexibility to be tweaked a little if and when needed to meet a customer's specific requirements. A few such standard buses in communication satellites available in the recent past and in operation now are briefly described below:

100 V Bus: Boeing Satellite Systems' standard fully regulated bus, BSS-702™, is a dual voltage bus, with a primary 100 V dc for high power equipment and a secondary 30 V dc for low-power components. It now uses Li-ion batteries and silicon triple-junction solar cells. A xenon electric ion-propulsion system is used for N–S station keeping, which is powered by the 100 V bus. Loads are either unfused, fuse-protected, or switched by relay or transistor, depending on the current magnitude and the nature of the load.

TABLE 4.1
ISS Solar Panels

Solar Panel Components	Description	Voltage (V)	Power max (kW)	Pavg (kw)	Mass
Blanket	Set of solar cells	160	15	–	1200 lbs
Solar array wings (SAW)/channels	Consist of two retractable "blankets" of solar cells with a mast between them	160	31	–	2400 lbs
Solar array sets/ modules	Two solar array wings make up a set of solar arrays. the two wings are deployed in opposite directions.	160	64	–	4800 lbs
Total Solar Panels	All four sets of solar arrays	160	240	84–120	19,200 lbs or 9.6 ton

TABLE 4.2
ISS Batteries

Type	Voltage per Cell	Number of Cells	Battery Voltage	Average Power	Ampere Hour	Total Ah per Battery	Mass per Battery	Total Number of batts.
Li-Ion	3.2–3.95	30	96–118.5	6.6	30 cells of 134 Ah (cells in Series)	4020	233 lbs	24

70 V Bus: Lockheed Martin Space Systems has sold many A2100™ standard, fully regulated DET buses operating at 70 V. It was made available up to 20 kW using a SA made of flat panels with Si, GaAs, or multijunction PV cells as needed for the required power level. The PV cell coverglass is coated with indium tin oxide (ITO) to eliminate arcing due to electrostatic discharge. The booms and yokes are made from aluminum or graphite. One SAD per SA wing with redundant motor windings provides a large torque margin in case jerking is needed. Power slip rings and signal slip rings are in separate sections.

The main power bus assembly provides load distribution, current sensors, voltage sensors, and a bus filter. The fuse box houses protective fuses and also loads power switches for controlling the bus load when needed. The transient over- and under-voltage following a large load step, such as

turning on an arc jet (>4 kW total), is individually analyzed to ensure meeting the bus ripple requirement.

The bus under-voltage protection under a set limit is provided by commanding and latching the payload power converter off. The shaded loads can be turned on only by a ground command.

A shunt is connected to each solar circuit. The shunt switch is either completely turned on or off. The on-switch shunts the power to the ground, while the off-switch feeds the power to the bus. The desired bus regulation with fine resolution is maintained by using one active shunt. Such a configuration also minimizes the bus voltage ripple.

Under-50 V Buses: British Aerospace's standard 42.5 V fully regulated and 28–42.5 V sun-regulated buses have been used on many small satellites. US manufacturers, on the other hand, offer 28 V fully regulated and 22–35 V sun-regulated buses for small satellites requiring load power under a couple of kilowatts.

Small Satellite Bus: Typical small satellites have: (i) A SA covering a wide range of solar flux and temperature with wide swings in the *I–V* characteristics, (ii) Peak power tracking architecture and no sun-tracking gimbals, (iii) Body-mounted SA or three to four flat panels on a 1–2 mm aluminum substrate with insulation and optimized coverglass, or a flexible SA with a cloth-type substrate weighting about 5% of the rigid substrate, and (iv) One battery, if permissible; otherwise two.

Early small satellites were spin-stabilized, with their drum-like bodies covered with PV cells all around. Such a configuration uses the cells ineffectively because it uses less than one third of the PV cells for power generation at any given time. The PPT is more suitable for being one common architecture for a number of small satellites for a variety of missions. The design can be modular and adaptable without component redesign, thus being cost-effective. The power control unit maximizes the energy delivered to the bus by driving the SAs to operate at their maximum power point over a wide range of temperatures, sun inclination, and illumination intensity. The tracker system, in addition to its flexibility, does not dissipate power associated with the shunt regulation inside the spacecraft. It adjusts the operating point of the SA as needed, thereby leaving excess power on the array.

Microsatellite Bus: Very small satellites with load power requirements in watts can use a simple and lean architecture. The SA, the battery, and the loads are permanently connected in parallel. The battery feeds the loads automatically during an eclipse and recharges itself during sunlight by imposing its drained voltage on the bus. Once fully charged, the battery voltage is relatively constant, and the battery works as a buffer. Any excess current is absorbed by the shunt resistance connected in parallel with the battery by means of a switch.

Low voltages (7–15 V) have been considered for satellites with loads in the tens of watts. However, such a low voltage is likely to end up costing a lot because it requires components other than standard 28 V class components. For example, the

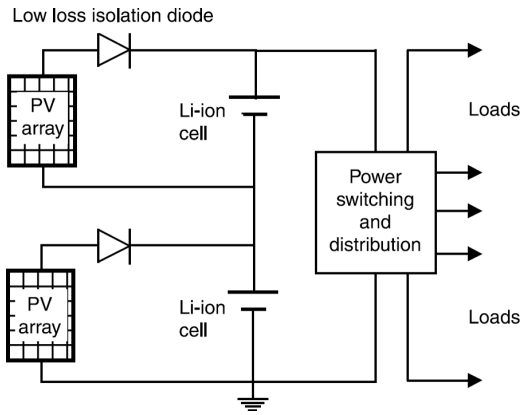

FIGURE 4.12 Microsatellite power system with no regulator.

ST5 spacecraft designed by NASA GSFC[1] for a few watts of load used a battery-dominated low voltage bus depicted in Figure 4.12. To minimize the number of components for high reliability and low mass, it used a body-mounted SA with triple-junction cells, one Li-ion battery, and simple power electronics. The electronics that traditionally provide solar array regulation and battery charge control are eliminated. Low-loss diodes are used in series with a solar array for fault isolation. The bus voltage is the same as the battery voltage, which may vary from 2.7 to 4.0 V per cell. The design can be modular in that, for a higher-power microsat, two modules can be connected in series, as shown in the figure.

REFERENCE

1. Schumacher, D., Beik, O., and Emadi, A., "Standalone integrated power electronics system: Applications for off-grid rural locations," *IEEE Electrification Magazine*, 6(4), 73–82, Dec. 2018.

FURTHER READINGS

Beik, O., Dekka, A., and Narimani, M., A new modular neutral point clamped converter with space vector modulation control, in *Proceedings of the IEEE International Conference on Industrial Technology*, 2018, pp. 591–595.

Castell, K. and Wingard, R., Recent advances in power system design at GSFC, in *Proceedings of the 34th Intersociety Energy Conversion Engineering Conference*, SAE, 1999, Paper No. 01-2534.

Cho, Y.J. and Cho, B.H., A novel battery charge-discharge of the regulated peak power tracking systems, in *Proceedings of the 34th Intersociety Energy Conversion Engineering Conference*, SAE, 1999, Paper No. 01-2445.

Gietl, E.B., Gholdston, E.W., Manners, B.A., and Delventhal, R.A., Electrical power systems of the international space station - A platform for power technology development, In *Proceedings of the 35th Intersociety Energy Conversion Engineering Conference*, AIAA, 2000, Paper No. 35-AP-SS-1. Also NASA Report No. TM-210209, June 2000.

Hill, R., Boeing satellite systems 702 electrical power system, in *Proceedings of the 36th Intersociety Energy Conversion Engineering Conference*, ASME, 2001, Paper No. AT-59.

Salim, A.A., In-orbit performance of lockheed martin's electrical power system for A2100 communication satellite, in *Proceedings of the 35th Intersociety Energy Conversion Engineering Conference*, AIAA, 2000, Paper No. 1-AP-SP-1.

Saude, B., LaSart, N., Blair, J. and Beik, O., "Microgrid-based wind and solar power generation on moon and mars," *IEEE Transactions on Smart Grid*, 14(2), 1329–1332, March 2023.

Veerachary, M., Senjyu, T., and Uezato, K., "Voltage-based maximum power point tracking control of PV system," *IEEE Transactions on Aerospace and Electronics Systems*, 38(1), 262–267, 2002.

5 Design Process and Trades

5.1 INTRODUCTION

Multiple factors play a role in the spacecraft power system design process, which starts with analyzing the orbit parameters, the load power requirement, and heritage data on similar satellites built and flown earlier. The design that meets the mission requirements at minimum mass, volume, and cost at present generally incorporates new technologies as they become available and space-qualified. The design process starts with a top-level trade analyses—formal or informal—in order to select the power system architecture that would lead to an optimized design. The detailed design then follows and continues in several iterations until it is fully optimized. The engineer would know that the design is fully optimized when a small change in any one component would result in a penalty of some sort at the power system level or at the spacecraft level.

5.2 POWER SYSTEM REQUIREMENTS

The customer performance requirement specifies only the launch, transfer orbit, and operational orbit constraints and the payload power demand over the mission life with the specified power margin. This leads to the spacecraft requirements. All systems of the bus derive their requirements from the spacecraft requirements, and all components of a system derive their requirements from the respective system requirements. The spacecraft requirement specifications generally do not specify the power system requirements *per se*. It merely includes a general statement such as "the power system shall generate, condition, distribute, and store electrical power to meet the requirements of the spacecraft payload and bus systems during all phases of the mission." To meet such a broad statement of work, almost all requirements of the power system are self-derived based on the overall mission requirements set by the customer and given to the satellite manufacturer in the form of overall mission specifications and on the design approach taken by the manufacturer based on the heritage designs that have worked well in the past.

The basic satellite-level parameters impacting the electrical power system (EPS) design are the orbit altitude, orbit inclination, and mission duration. These parameters are used to determine the orbit period, sunlight and eclipse durations, and the solar β angle between the orbit plane and the Earth–Sun line. The power system design is then driven by the load power requirement in all phases of the mission, which are launch and ascent, transfer orbit, parking orbit, operational orbit, and disposal orbit. However, the orbit period, the maximum eclipse duration, and the load

DOI: 10.1201/9781003344605-6

power requirement in the operational orbit determine the ratings of the solar array, battery, and other components.

All such requirements on EPS are self-derived from the spacecraft-level requirements and in-house analyses and trade studies, leading to (i) Solar array end-of-life (EOL) power level, (ii) Battery capacity in ampere-hours, (iii) Battery DOD and charge control, (iv) Bus voltage regulation, (v) EMI, EMC, and ESD, and (vi) Interfaces with other spacecraft systems.

5.3 ENVIRONMENTAL EFFECTS ON DESIGN

Solar array power generation diminishes with increasing radiation dose, more so in low and highly elliptical Earth orbits that pass through the Van Allen radiation belts. For a given load power, therefore, the solar array area requirement increases as the mission duration becomes longer. The charged particles impinging on the spacecraft surface slow down through collision and lose their energy. The deposited energy in the material causes damage by atomic excitation in metals and semiconductors and ionization in plastic materials. Various particles lose energy at different rates as they penetrate the surface and cause damage at different rates. The higher the rate, the more damage they produce. The damage is most severe in the Van Allen belts because of the high level of radiation. Although the belt region, which is between the low Earth orbit (LEO) and the crowded geosynchronous orbit, is potentially a valuable piece of orbital real estate, the region has remained relatively unexplored because of the practical and economic difficulties of shielding conventional satellites from charged particles. NASA has measured charged particles in many orbits to develop and validate a computer model. In 2002, nine astronauts aboard the International Space Station each wore a 0.04-inch square silicon chip dosimeter that measured the levels of radiation they were exposed to during space walks. On Earth, similar devices are used in hospitals worldwide to measure the radiation given to cancer patients.

The solar array is the most affected component in the power system by space radiation. The degradations are listed in Table 5.1 in order of their importance. The array's performance degrades with the increasing level of fluency, but not in a linear

TABLE 5.1
Environmental Causes and Effects on Solar Array Performance

Environment	Effect
Ionized particles	Damage to the p–n junction
Micrometeoroids and debris	Damage to cell active area and interconnects Increased cell shunt resistance
Contamination from out-gassing and propulsion plume	Degradation in optical properties of the coverglass
Space plasma	Increased leakage current
Thermo-elastic cycling	Cracks in solder joints of the interconnects
Bypass diode failure	Shorts in cell blocks and reduced string current
Ultraviolet radiation	Degradation in optical properties of the coverglass

relationship. The damage is greater in the initial years than in the latter years. The impinging particles produce defects in the crystalline structure of the photovoltaic (PV) cells. The resulting defects degrade the voltage and current outputs of solar cells. Low-energy particles create damage close to the surface and therefore lower the open circuit voltage. On the other hand, high-energy particles penetrate deeper in the base and lower the lifetime of electron hole pairs, thus decreasing the short circuit current. The power generation capability continues to degrade as the radiation dose accumulates over the years. When it falls below the specified requirement, the solar array is considered to have reached the end of its life.

Radiation damage to spacecraft components can now be predicted fairly accurately. For example, the damage found on the solar array of the Russian space station MIR, when examined in 2000, was as predicted for the effects of radiation, micrometeoroids, thermal absorptivity, and emissivity. The most damaging effects of the environment on the power system occur during solar storms. The damage can be minimized if the intensity of such storms can be predicted in advance.

5.4 SPACECRAFT-LEVEL TRADES

A number of considerations need to be made in designing the spacecraft power system with a web of interfaces with other systems, as shown in Figure 5.1. One of the goals of the spacecraft design program is to minimize mass and cost *at the spacecraft level*. Therefore, while focusing on the power system, the power system engineer keeps a peripheral view of the overall mass and cost of the spacecraft with applicable input from the spacecraft system engineer and/or the chief engineer. Reducing 1 kg of mass in one component while adding less than 1 kg in another component is a winning trade. Such trades are continuously revisited as new spacecraft technologies become available.

The following factors have a large influence on the architecture selection of the PV–battery power system. They are driven primarily by top-level mission

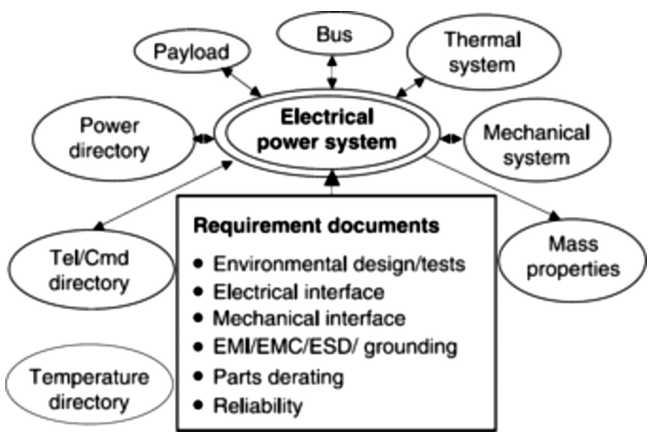

FIGURE 5.1 Power systems interface with other systems on spacecraft.

requirements and do not involve power system-level trades. However, understanding their influence on the power system can quickly lead to the selection of an optimum spacecraft EPS architecture.

1. The spacecraft's operational orbit is an important design consideration. As the satellite altitude increases, the orbit period increases, and the eclipse time, as a fraction of the sunlight time, decreases. The demand on the battery discharge and the charge power therefore decrease.
2. Mission duration and other parameters play a significant role in the power system design.
3. The micrometeoroids and orbital debris are worse in the 50°–55° inclination orbits. The charged particle radiation environment is also worst in this orbit over the South Atlantic Ocean, where the Van Allen belt dips to a low altitude. At higher inclinations in LEO, the Earth's infrared radiation decreases while the albedo (solar radiation reflected from the Earth) increases.
4. The β angle between the Earth–Sun line and the orbit plane varies seasonally. It reaches maximum values on the summer and winter solstice days, which is $\beta_{\max} = i + i_o$, where i = orbit inclination and $i_o = 23.45°$ (the angle between the equator and the ecliptic plane). As β increases, the eclipse time decreases, and the solar array temperature also decreases. At higher β, therefore, the EPS is capable of supplying a greater load, both during eclipse and during sunlight. The eclipse duration is the longest when $\beta = 0$ and the shortest or even zero when β is maximum.
5. The array pointed away from the normal sun line reduces the solar flux, increases the coverglass reflectivity, and changes the view factor to Earth, affecting the array temperature. Typically, a 3° error in the gimbals pointing and a 2° error in the array flatness, for a total of about 5° error, are allowed in the sun's pointing. The cosine law up to 30° governs the power loss. In the 30°–80° range, the loss is greater than that given by the cosine law, and the array generates no power beyond 80°. This has an impact on the transfer orbit maneuvering when the array could be way off-normal.
6. A planner solar array with dual-axis gimbals requires tracking of the sun line to the array normal by no more than $\beta°$. With single-axis gimbals, the array must have a cant angle equal to the annual average β angle. A concentrator array requires two-axis sun tracking to maintain the sun line normal to the array surface.

5.5 POWER SYSTEM-LEVEL TRADES

The EPS design is specific to each spacecraft. In some satellite designs, the mass of the power system as a percentage of the satellite's dry mass may range from 25% in LEO satellites to 45% in geosynchronous Earth orbit (GEO) satellites. This mass must be supported during launch and then transferred to the final orbit. Saving even a few percent of the power system mass can result in appreciable savings at the spacecraft level. For example, the impact of the EPS on the structural system, although not

obvious and direct, is strong. The first task of the power system design engineer is to select the optimum architecture. This includes deciding on the dc bus voltage, type of source (PV solar, battery, or other sources), and power electronics and controls. This task generally starts with understanding the spacecraft mission, e.g., a manned spacecraft for short duration or an unmanned satellite for long duration, the mission parameters, the loads and their nature (variable or fixed), and other considerations. As an example, for a short mission operating over wide orbit parameters, a PV–battery source may be suitable. For an interplanetary or deep space mission, nuclear power sources may be optimum. All these options must be considered for the mission under design in order to arrive at the optimum power system architecture. Next, the bus voltage level and the power generation and energy storage technologies must be jointly selected to optimize the total power. The major driving factors are the payload power level, operating orbit parameters, mission life, and number of satellites in the program. For the self-derived satellite-level load requirement, the trade study is done to select various key components for the power system, such as the PV cell, cover-glass thickness for radiation protection, array substrate, battery cell, power converter topologies, etc. An example of such a trade is displayed in Figure 5.2. As the trade study proceeds from left to right, the selections made are shown by continuing lines. Since the solar array and the battery are two components that primarily contribute to the mass and cost of the power system, they receive more attention and see more rapid technological changes than other components.

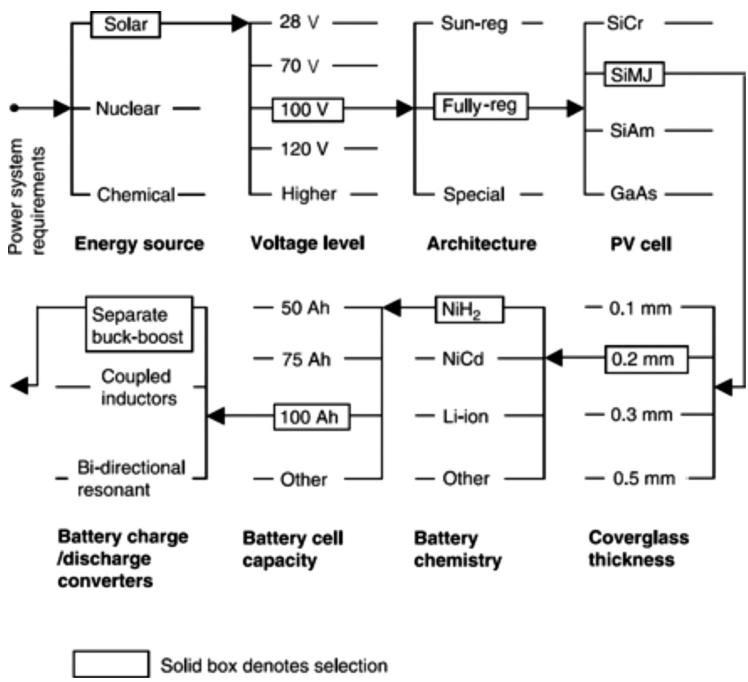

FIGURE 5.2 Power system design flowchart.

5.5.1 Solar Array Design Trades

The mass of the solar array is a design and trade-off factor. A mass reduction in the solar array has multiple benefits at the satellite level, such as reduced drag, inertia, and propellant mass. The solar array area is linearly proportional to the required power generation. At the same time, it also has a significant influence on the propulsion and attitude control systems. A large array increases the drag and moment on the satellite, more so in LEO satellites and in low Earth orbits of geosynchronous satellites. A small array of high-efficiency cells might be worth the added cost, considering that it would allow lower park orbits for the same drag. A lower park orbit allows the launch vehicle to insert more mass into the orbit, resulting in a reduced launch cost per kilogram of payload. A small array may also result in a shorter transfer time from the park orbit to the geosynchronous operational orbit as a result of lower drag in the early part of the transfer orbit. This may yield greater benefit, considering that the transfer from LEO to GEO may take hundreds of days with large arrays. Aligning the center of pressure and center of gravity of the satellite body can minimize the drag.

If a narrow orbit control is required in LEO, a large array may add significant propellant mass to a long-duration mission, probably costing more than the savings from using low-efficiency PV cells. In GEO, a large array causes orbit drift due to solar pressure. Therefore, the satellite requires more propellant fuel to keep the N–S station in operational orbit during its entire mission life. If precision attitude control is required, it is necessary to have a low mechanical natural frequency of the solar array in the first mode of vibration. Small arrays inherently have high frequency. A large array, on the other hand, would require adding structural rigidity and decoupling at an additional cost. The torque compensation hardware must be sized for drag and solar pressure. The torque is generally canceled by changing the reaction wheel speed and then de-spinning the wheels using torque rods over the duration of the orbit. Thus, a large array can increase the size of the torque rods and the reaction wheels.

5.5.2 Battery Design Trades

LEO and GEO satellites differ significantly in their power system requirements. GEO satellites have a high launch cost and require fewer battery charge/discharge cycles. LEO satellites, on the other hand, have a low launch cost, high ionized radiation, and a much greater number of battery charge/discharge cycles. The battery chemistry selection may, therefore, differ significantly for these two classes of satellite. The NiCd battery was the workhorse of the space industry until the mid-1980s, when the NiH_2 battery replaced it for both LEO and GEO missions. The Li-ion battery has recently made inroads into the space industry because of its significantly higher specific energy. As of now, Li-ion batteries are used in almost all spacecraft.

5.5.3 Bus Voltage Trades

The bus voltage is one of the early and main criteria in developing a spacecraft power system. As the power levels increase, the bus voltage needs to be increased to maintain an acceptable current level and power loss in the conductors.

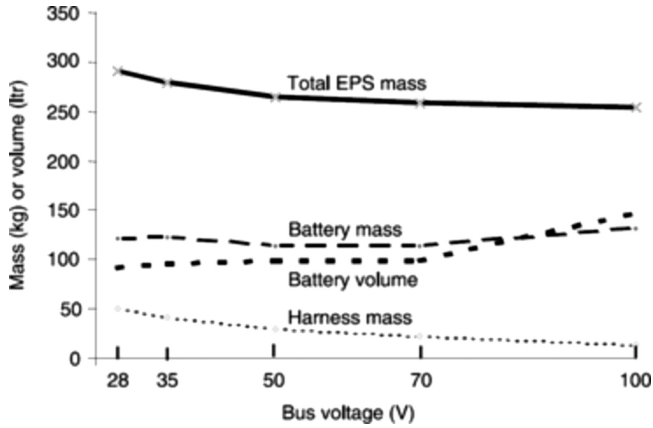

FIGURE 5.3 Bus voltage trade example for a 2000 W GEO satellite.

For communications satellites, selecting one of the standard buses offered by prime contractors may be the most economical option. However, the voltage selection may be open for designing special science, defense, or crewed spacecraft. Even in such cases, the bus voltage is sometimes set by the heritage and the preferred database. One approach to selecting a bus voltage is to develop preliminary designs for various available voltages and arrive at the optimum. The mass of each component is estimated under various bus voltage options and added to the total power system mass and volume. As for the cost, it may be assumed that the cost is proportional to the mass, at least in the first approximation. Figure 5.3 is an example of such a trade for a 2000 W GEO satellite with a 15-year mission life. Notice that the solar array mass is not shown in the chart but is included in the total mass. As it is a series–parallel assembly of numerous PV cells, it is fairly independent of the bus voltage. In a high-voltage bus, more PV cells are connected in series and fewer in parallel, but still, the same number of cells is needed to generate the required power. For this example mission, the figure indicates that a 70 V bus is near optimum. The 100 V bus reduces the harness mass, but it also increases the battery mass and volume significantly. This is because the battery ampere-hour rating in a 100 V bus becomes so small that its energy storage per kilogram of mass and liter of volume falls significantly. As a result, a 100 V bus does not reduce the total mass compared to a 70 V fully regulated bus.

5.6 LOAD POWER PROFILE

Understanding the loads, their nature, and their behavior is a key parameter for selection of source, bus voltage, power electronics converters, and controls. One of the tasks in EPS design is to compile a detailed load power profile for each component to be powered. It is also called the power budget or the power allocation in an early phase of the design. It is a spread sheet of input power drawn by each load of equipment during all operating time durations, e.g., power during on and off time, peak

power, quiescent power when off, and thermal dissipation. The component dissipation may vary significantly during sunlight and eclipses, as well as at the beginning and end of life. Such variations are properly accounted for.

The power versus time curve for each item of load equipment may be condensed into two parameters: the peak power and the duty ratio. For a well-defined load, which is on or off, the duty ratio is the ratio of on-time to the period of repetition, that is, $D = T_{on}/T$.

For a continuously varying load at the other extreme, it is defined as

$$D = \frac{\text{energy consumed in one repetition period}}{\text{peak power} \times \text{repetition period}} = \frac{\int_o^T P(t)\,dt}{P_{pk}T} \tag{5.1}$$

The average power required by any equipment is then $P_{\text{avg}} = D \cdot P_{pk}$. Figure 5.4 is a typical communication load profile for a geosynchronous satellite. The load reaches high peaks of short duration when the transponders are communicating with the ground.

The average power is used to determine the solar array and the battery ratings. On the other hand, a load averaged over five thermal time constants of the equipment is used to determine the equipment power rating, the wire gage, and the fuse size. The peak power and duty ratio of most equipment are significantly different during the launch, the transfer orbit, and the operating orbit. They may also vary seasonally during the operating orbit. The worst-case seasonal power situation is sometimes known from similar satellites designed and flown in the past. When there is no such heritage to draw from, considering 4 key days in the year, as listed in the first column of Table 5.2, may be adequate for a geosynchronous satellite. On these 4 days, both

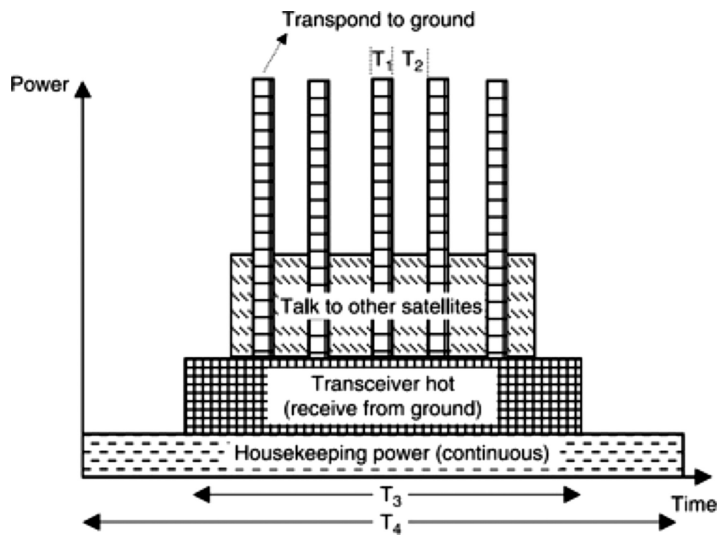

FIGURE 5.4 Typical communications satellite load profile.

TABLE 5.2
Seasonal Variations in Power Generation and Heater Power Requirement

Seasonal Day	Solar Flux[a]	Sun Angle	Power Generation[b]	Heater Load
Vernal equinox	1.001	0°	1.001	High
Summer solstice	0.967	23.5°	0.887	Low
Autumn equinox	0.995	0°	0.995	Low
Winter solstice	1.034	23.5°	0.948	Medium

[a] Normalized with the annual average.
[b] Accounting for seasonal variations in both solar flux and sun angle.

the power generation and the heater power requirements vary. Since the energy balance must be maintained all the time in the operating orbit, any one of these 4 days may most probably be the worst case for setting the power system capability. Because the heater power requirement is low when the power generation is low, it may not be obvious which day is the worst for the power system design. In the absence of some heritage data, it may be necessary to conduct a preliminary design for all 4 days to determine the worst case, and then to focus on the worst case for detail design. The summer solstice is usually the worst day for the load power capability of the GEO communications satellite. After establishing the worst day, the design process focuses on meeting the load power requirement on that day.

The load requirements of each of the bus systems and the payload components are then met during the transfer orbit and the worst-case operating orbit. Tables 5.3 and 5.4 are examples of loads and their characteristics in one satellite during the transfer orbit and operational orbit, respectively. The load power values in these tables are input powers to the components that must be supplied by the power system. In new designs, when the loads are somewhat uncertain, appropriate margins are incorporated in the power estimates. For example, it may be acceptable to the design team to have no margin for heritage components requiring no change at all, 10% margin for components modified from a heritage design, and 30% margin for new components yet to be developed.

TABLE 5.3
Transfer Orbit Load Power Profile for System A

	Component 1	Component 2	Component *n*	System Total
Quantity	X_1	X_2	X_n	X_{TO}
Peak power	Y_1	Y_2	Y_n	Y_{TO}
Peak heat dissipation	Z_1	Z_2	Z_n	Z_{TO}
Duty ratio	D_1	D_2	D_n	D_{TO}
Average power	P_1	P_2	P_n	P_{TO}
Average loss (dissipation)	L_1	L_2	L_n	L_{TO}

TABLE 5.4
Operation Orbit Load Power Profile for System A

	Component 1	Component 2	Component *n*	System Total
Quantity	X_1	X_2	X_n	X_{OP}
Peak power	Y_1	Y_2	Y_n	Y_{OP}
Peak heat dissipation	Z_1	Z_2	Z_n	Z_{OP}
Duty ratio	D_1	D_2	D_n	D_{OP}
Average power	P_1	P_2	P_n	P_{OP}
Average loss (dissipation)	L_1	L_2	L_n	L_{OP}

TABLE 5.5
Total Average Load and Heat Dissipation Budget (Allocation) for Power System

System	Transfer Orbit Power	Operational Orbit Power	Transfer Orbit Heat Dissipation	Operational Orbit Heat Dissipation
System A	P_{TO}	P_{OP}	L_{TO}	L_{OP}
System B	..	..	..	..
System Z	..	..	..	..
Payload	..	..	..	..
Spacecraft total load	$\Omega\, P_{TO}$	$\Omega\, P_{OP}$	$\Omega\, L_{TO}$	$\Omega\, L_{OP}$

Various system loads obtained from Tables 5.3 and 5.4 are then condensed into the total power system load budget, as shown in Table 5.5. All bus systems are to be included in this table, including the payload and the housekeeping load for the EPS itself.

5.7 SOLAR ARRAY SIZING

The load power profile developed above is then used to determine the solar array's output power requirement. For example, for a communications satellite having a 2500 W communication payload power, the solar array power generation requirement is shown in Table 5.6 in two seasons and during an eclipse. The autumnal equinox day, having the longest eclipse, in this case determines the solar array output requirement of 3940 W, which includes a 5% power margin and a 5% reliability margin. The solar array must generate this power at the end of its life. The beginning-of-life power would be greater depending on various degradation factors, which are:

- Environmental degradation due to ionized radiation
- Cell-to-cell current mismatch (assembly loss)

TABLE 5.6
Example of Sizing Solar Array Output Power for a Communications Satellite (Average Watts)

	Autumn Equinox[a]	Summer Solstice[b]	During Longest Eclipse
Communication payload system	2500	2500	2500
Communication system load margin (10%)	250	250	250
Total communication system load	2750	2750	2750
Bus systems			
TT & C	50	50	50
Attitude control	50	50	50
Thermal control	150	100	50
Electrical power	20	20	20
I^2R conduction loss	50	50	60
Battery charging	500	100	0 (disch.)
Total electrical power system load	3570	3150	2980
Power margin (5%)	180	160	150
Reliability margin (5%)[c]	190	170	165
Total solar array power generation required at the end of life	3940[d]	3480	3295

[a] Non-eclipse season near September 21.
[b] Eclipse season near June 22.
[c] Allows one string failure (in a typical 20 circuit solar array).
[d] Solar array output power required = 3940 W minimum.

- Sun angle off-pointing angle (due to array flatness, structural misalignments, and sun-tracking errors)
- All others, such as micrometeoroids, space debris, contamination, plasma, ultraviolet radiation, yellowing of coverglass, and thermal cycling

Considering the values of individual degradation factors, the total degradation is obtained by multiplying all those factors. If the total degradation comes to 33%, as an example, then the solar array must generate a beginning-of-life power of 3940/(1 – 0.33) = 5880 W in order to meet the 3940 W load requirement at the end of life. This is the $P_{\max}$ it must deliver at its knee-point voltage V_{mp} with appropriate margins both in power and in voltage. The $P_{\max}$ is temperature-dependent, so we need to know the array's operating temperature. The temperature is calculated by equating the heat input and output for the front and back of the array. All cells on an array are assumed to operate at the same temperature. The heat input is the solar radiation, albedo, Earth's infrared radiation, and the adjacent solar array. The heat output is the power converted into electricity and the power radiated back into space. If multiple wings connected in parallel operate at different temperatures, the operating voltage is selected to be a few volts less than the V_{mp} of the higher-temperature wing to avoid the colder array operating above V_{mp} where the power output drops rather quickly.

5.8 BATTERY SIZING

For sizing the battery, the functionality of the battery system, primary or secondary energy storage, the percentage load that it supplies, and the duration are primary design factors. At the preliminary design stage, the round-trip energy efficiency approach can be used to derive the approximate rating of the battery. For life considerations, the maximum depth of discharge (DOD) must be below a certain value that depends on the number of charge/discharge cycles the battery is required to deliver during the mission's life. With these considerations, the ampere-hour rating is derived from the expressions below:

- Battery cells in series = minimum permissible battery voltage for pyro or power electronics/minimum cell voltage at the end of discharge at EOL
- Wh discharged = eclipse load in watts × eclipse duration in hours
- Ah discharged = Wh discharged/average cell voltage during discharge × number of cells in series
- Ah capacity = Ah discharged/permissible DOD for required cycle life
- Wh charge = Wh discharged/round-trip energy efficiency (say 0.80)

$$\text{Charge power} = \text{Wh charge/charge time during sunlight} \tag{5.2}$$

5.9 POWER FLOW ANALYSIS

For balanced and continuous operations, the energy collected during sunlight must match the energy required by the loads, plus the energy used to charge the battery and the total power loss. Such a balance must be maintained over the orbit period with the worst-case eclipse duration. In the simplest case with constant load during the orbit (Figure 5.5), the two shaded areas A_1 and A_2 must be equal in each orbit period during the entire mission life. A small deviation from such a stringent requirement in an occasional orbit could be manageable for a short time, but must be thoroughly examined for acceptability from the battery DOD considerations.

The design optimization is done to maximize the power output to the load while maintaining the energy balance. The start point of the energy balance analysis is usually the beginning of the eclipse. The battery state of charge is determined at

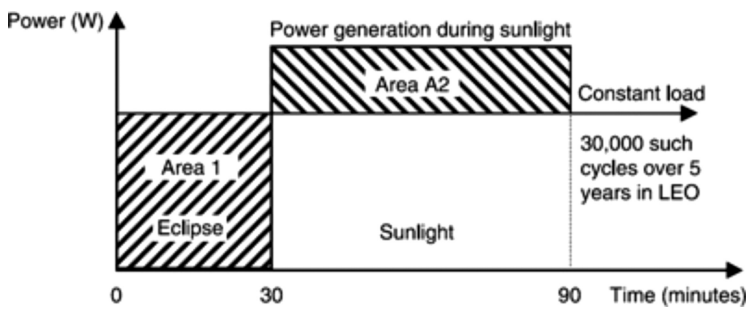

FIGURE 5.5 Energy balance over one orbit period with a constant load.

the end of eclipse based on the load and the power losses. The design engineer then determines the required solar array output to bring the battery back to full state of charge while meeting the load power during sunlight. During the entire orbit period, the engineer also determines the maximum power, voltage, or current handled by each component, which then sets the component power, voltage, and current ratings. The best design is obviously the one that leaves minimum margins in all components and is also acceptable to the program team for the level of uncertainty in the design or the system operation. At the minimum, the system should not be battery or array-limited. Typically, a few percent margin in both the battery and the solar array is considered adequate.

The spreadsheet shown in Figure 5.6 illustrates the power flow necessary to maintain the energy balance for an example satellite requiring 3000 W of constant load during sunlight and also during an eclipse. It may use flywheel energy storage instead of a battery, but that would not change the analysis method. In addition to the power generation (solar array) and energy storage (battery), it includes other components, such as the power electronics and distribution harness. Various power electronic converters are used to change the voltage as needed at various points in the power system. Their efficiencies are accounted for in the systems model. The power consumed in the control electronics, such as the bus voltage controller and bus voltage error amplifier, is included in the efficiency numbers.

The power flow analysis determines the voltage and current throughout the power system and establishes the power handling capability and heat dissipation of various

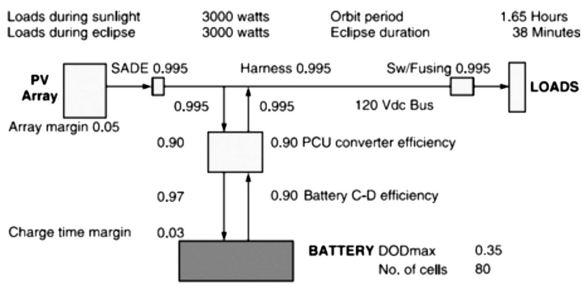

Energy balance analysis key results:

Energy discharged from EW during eclipse	2381.2 Wh
Charging power required from the bus	2779.8 watts
Load at PCU during sunlight (before charging power)	3030.2 watts
Load at PV array during sun (including charge+diode)	5839.2 watts

Required minimum steady state ratings of system components:

PV array EOL capability including margin	6131.2 watts
PCU charge converter rating	2489.3 watts
PCU discharge converter rating	3045.5 watts
Charge power in battery	2414.6 watts
Discharge power out of battery	3383.8 watts
Depth of discharge of energy during longest eclipse	0.350 pu
Energy storage rating of the battery	6803.5 Wh

Summary of Major Component Ratings:

Solar array power output rating	5839.2 watts
Battery Wh energy storage rating	6803.5 Wh
Battery Ah rating with 80 cells	68.90 Ah
PCU charge converter rating	2489.3 watts
PCU discharge converter rating	3045.5 watts

FIGURE 5.6 Power flow and energy balance analysis example for a 3000 W LEO satellite.

components. It computes the power through various components based on the component efficiencies marked on the spreadsheet. The converter efficiency, harness resistance, and diode voltage drops are factored into the computations. The current, voltage, and power loss in the distribution harness are also determined for each segment of the system. For a given EPS design, a spreadsheet is also typically used to perform the following two types of analyses:

- Forward analysis to establish the EPS load capability, assuming that the battery must be fully charged at the end of the sunlight in each orbit
- Backward analysis to verify whether a given load profile can be supported without exceeding the component ratings, assuming that power can be drawn from the solar array and the batteries within the permissible DOD during that time period. This is often done to assess the peak power capability during a planned or contingency operation or when the load profile is not flat during the loading period.

5.10 DESIGN ANALYSIS LIST

Various design analyses are conducted side by side as the design matures. They may confirm or change the design in order to meet the required specifications under all normal and abnormal conditions. Table 5.7 is a list of such analyses that are typically conducted as applicable for a given mission.

TABLE 5.7
Typical Design Analyses Required for the Power System Design

Design analyses performed:

- Launch and ascent power
- Transfer orbit energy balance
- Operational orbit energy balance
- Component dissipations
- Stability and transient analysis
  - Transient due to step load changes (on and off)
  - Transient during fault and recovery (fuse blow)
  - Ripple analysis due to repetitive load pulses
  - Stability margin and sensitivity analyses
- Battery latch-up analysis for sunlight regulated bus

Each of the above analyses is performed at:

Beginning of life with

- Minimum load
- Maximum load
- Nominal and failure conditions

End of life with

- Minimum load
- Maximum loads
- Nominal and failure conditions

5.11 DESIGN PROCESS PHASES

In today's competitive environment, it is not enough to ensure that the system and the equipment are designed to be capable of meeting high standards of performance and reliability. A consideration of manufacturing processes and expected tolerances is part of a good and complete design. A thorough and correct design the first time is of paramount importance for maintaining the program's schedule and cost. The following *Rule of Ten* can be a strong motivator for the design engineer: *Not doing something right the first time costs ten times as much to find and fix each time it escapes to the subsequent stage, from the design to the delivery.* This rule results in the following string of cost multipliers for fixing an error at various phases of the total design and delivery cycle:

Design	Production	Test	Launch Pad
1 (reference cost)	10	100	1,000

The engineer must also detect and correct the design early enough to avoid potential manufacturing and test problems. This would minimize, preferably reduce to zero as a goal, the design changes, test failures, manufacturing disruptions, troubleshooting, and rework. For such cost-effective implementation of the design, all engineers—design, manufacturing, test, and field engineers—work as *a total team on the total satellite*. Only such a concurrent design team can ensure that the design of each system is compatible with all other systems and also with the manufacturing and test procedures. For this purpose, the design process incorporates various reviews as it proceeds from the contract award to delivery. A typical design phase sequence is listed in Table 5.8.

5.12 FACTORY-TO-ORBIT EVENTS

In the entire design process, the engineer stays focused on what the power system is required to do not only in the operational orbit but also during the factory tests, on the launch pad, and during the orbit acquisition. The following are some typical functions and requirements in various phases of the satellite that the power system engineer must incorporate into the design:

- **Storage:** Unforeseen circumstances may require a partially built spacecraft to be placed in storage for a maximum of 3 years in a controlled environment.
- **Ground tests:** A solar array and battery may not be installed, requiring external power for testing via a ground-enabled plug. A workhorse battery may be used during testing, which may not be an exact duplicate of the flight battery in performance.
- **Prelaunch:** External or internal power is used, flight batteries may be installed, and the solar array is stowed.
- **Launch:** Battery power is used at a high discharge rate, and the system operates through the launch environment of shocks and vibration.

TABLE 5.8
Power System Design, Analyses and Review Phases

1. Requirements allocation and conceptual design phase
   - Requirements definition/allocations
   - Review of system requirements
   - Top-level design trades and conceptual design
2. Preliminary design and analysis phase
   - Component specifications
   - Preliminary design and analysis
   - Preliminary design review
3. Detail design and analysis phase
   - Detail design and analysis
   - Critical design review
4. Support phase
   - Support component and system tests
   - Support outside suppliers
   - Support satellite integration and test
   - Prepare operations manuals
   - Support launch
5. Continuing tasks
   - Cost and schedule control through the spacecraft delivery

- **Transfer orbit:** A solar array generates limited power. The battery powers the pyrobus loads only. Redundancy management is enabled.
- **Deployment:** Partial or full solar array power is available after deployment. Only the bus and the pyro loads are powered.
- **Pre-operational drift orbit:** Full power generation but still low loads.
- **Non-operational on-orbit:** Full power generation but less than full load. Supports eclipse and battery charging.
- **Normal operational orbit:** Full power generation and full load. The eclipse and battery energy balance is maintained in every orbit.
- **Station keeping:** Full power generation and full load. In addition, the battery supports arcjets during N–S station keeping.
- **Reacquisition:** Loads shed by ground commands, arrays slewed back-to-back if this mode persists for more than 30 min or so.
- **Deactivation or de-orbiting:** The power system supports this maneuver as the last function. Then the power system's role is over.

5.13 POWER SYSTEM FUNCTIONS OVER LIFE

The power system engineer must also be cognizant of the major satellite-level events from prelaunch to customer handover. A typical sequence used for an example satellite (like DMSP) follows:

- **Prelaunch:** The spacecraft is on the launch pad when the decision is made to launch or abort. The system is typically single-string, so potential single-point failures are identified. A launch decision proceeds as below.
  - The power system is on, and the satellite goes on its internal power about 10 min before liftoff, when the solar simulator is turned off.
  - Both batteries are on to supply power during the final 10 min before liftoff and during ascent. No charging can occur until the satellite is deployed and faces the sun.
  - The power converters are on and in discharge mode. Hardware detection and switches are enabled. Software-controlled redundancy is typically off.
  - The array drive electronics are on, but the array is not driven. All components drawing power directly from the battery are on, except those turned off by an internal switch.
- **Ascent mode:** The power system is on but has not changed from the prelaunch phase.
- **Pre-handover:** Two redundant cutters for each of the two bands are cut to deploy the solar array. Both bands must be cut for the deployment to occur. Two cutters for the boom hinges and dampers are activated. Redundant pin pullers activate the solar arrays cantilever angle.
- **Handover:** The spacecraft control computer initiates handover based on time as adjusted during the flight.
- **Orbit operation:** The power system maintains the energy balance in each orbit. The satellite is fully operational.

FURTHER READINGS

Beik, O. and Emadi, A., "Toward integrated digital aircraft control systems: For electrified-system optimized size, cost, and efficiency," *IEEE Electrification Magazine*, 5(4), 46–52, Dec. 2017.

Beik, O., Patel, M.R. and Talebzadeh, S., Large spacecraft electric propulsion using multiphase generator, in *2023 IEEE Aerospace Conference*, Big Sky, MT, USA, pp. 1–8, 2023.

Saude, B., LaSart, N., Blair, J. and Beik, O., "Microgrid-based wind and solar power generation on moon and mars," *IEEE Transactions on Smart Grid*, 14(2), 1329–1332, March 2023.

Part B

PV–Battery System

6 Solar Array

6.1 INTRODUCTION

The solar array is made of numerous photovoltaic (PV) cells connected in a series–parallel combination to obtain the required voltage and current. The fundamental characteristics of the PV cell—the building block of the array—are covered first in this chapter before moving on to the array's construction, performance, and design.

6.2 PHOTOVOLTAIC CELL

A PV cell converts sunlight into direct-current electricity. The PV effect was discovered in 1839 by the French physicist Antoine Henri Becquerel. It remained in the laboratory until 1954, when Bell Laboratories produced the first silicon solar cell. It powered the first Russian satellite in 1958, followed by applications in the US space program. Since then, it has been an important source of power for satellites and is now rapidly entering power grids on Earth in response to climate change initiatives around the world.

The PV effect is the electrical potential developed between two dissimilar materials when their common junction is illuminated with photons. When the junction absorbs light, the energy of the absorbed photons is transferred to the electron system of the material, resulting in the creation of charge carriers that are separated at the junction. The charge carriers create a potential gradient (voltage), are accelerated under the electric field, and circulate as electrical current if the external circuit is closed. The product of the voltage and current in the circuit is the photon power converted into electricity. The power that is not converted into electricity remains at the junction, elevates the cell temperature, and eventually dissipates in the surroundings.

The basic PV cell consists of a p–n or n–p junction of two semiconductors with a terminal for each. The physics of the PV cell is very similar to that of the classical junction diode. From the solid-state physics point of view, the cell is basically a large-area diode with the junction positioned close to the top surface. Early cells were p–n types with the p layer facing the sun. The cell design was changed to n-on-p to improve radiation resistance. The new n–p cell extended the mission's life over a decade. The series resistance is one of the limiting factors in determining the conversion efficiency of PV cells. It is influenced by the current collecting grid thickness and the semiconductor structure. The space-qualified cell efficiency is quoted at air mass zero (AM0), which represents the condition in outer space. The voltage developed and the fraction of the incident energy converted into electricity depend on the characteristics of the junction material and the wavelength of the radiation.

The basic cell construction shown in Figure 6.1 has metallic contacts provided on both sides of the junction to collect electrical current induced by the impinging photons on one side. A conducting foil or solder contact is provided all over the

DOI: 10.1201/9781003344605-8

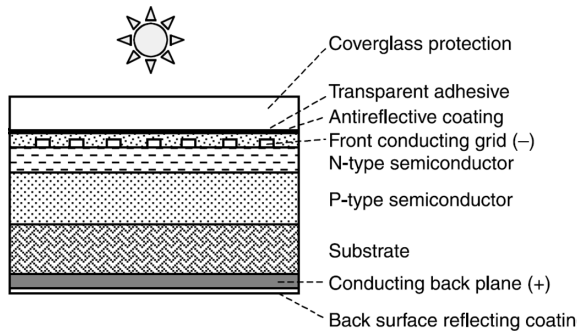

FIGURE 6.1 Basic construction of a photovoltaic cell with performance-enhancing features.

bottom dark surface and on one edge of the top illuminated surface. A thin conducting mesh on the remaining top surface collects the current while allowing the light through. The spacing of the conducting fibers in the mesh is a matter of compromise between maximizing the electrical conductance and minimizing the blockage of light. In addition to these basic features, several enhancements are also included in the construction. For example, the front face of the cell has an antireflective coating to absorb as much light as possible by minimizing the reflection. The protection against damage due to energetic particles hitting the surface is provided by the coverglass applied with a transparent adhesive.

6.3 PV TECHNOLOGIES

The most important measures of the PV cell's performance are the photoelectric energy conversion efficiency and the cost per watt capacity. Together, these two parameters indicate the economic competitiveness of PVs with alternative power generation technologies. The conversion efficiency is defined as $\eta = \dfrac{\text{electrical power output}}{\text{solar power impinging the cell}}$.

The energy conversion is different from the energy absorption. Not all the energy that is absorbed by the cell is converted into electricity. A photon of blue light having 3 eV of energy generates around 0.5 eV of electricity, and the remaining 2.5 eV is absorbed as heat. This heat must be dissipated back into the space; otherwise, it would decrease the electrical conversion efficiency. A high-emissivity coating on the back surface helps to dissipate the heat effectively, thus improving the electrical conversion efficiency. The continuing development efforts to produce more efficient, low-cost cells have resulted in various types of PV technologies available on the market today in terms of conversion efficiency and cost. Starting with the original single-crystal, single-junction silicon cell, various available cell technologies include thin-film, multijunction, semi-crystalline, poly-crystalline, amorphous, inverted metamorphous, concentrated, and others. The newest multijunction cells under concentrated sunlight yield conversion efficiency around 40% in the laboratory and 35% in production batches.

A new cell technology often used in present-day spacecraft is the triple-junction cell structure $GaInP_2$/InGaAs/Ge on germanium substrates. It yields an energy conversion efficiency approaching 30% at the beginning-of-life by cascading three junctions in series. The top junction extracts sun energy in the middle spectrum of the sunlight. The escaped energy in the left-hand spectrum of the sunlight is captured by the middle junction, and the rest of the sunlight's energy is captured by the bottom junction of the cell. Such space-qualified cells are made by companies like Spectrolab (a Boeing company) in CA and also by Emcore in NM. Such cells from both sources are used in spacecraft at present. Figure 6.2 is the catalog sheet of the

SPECTROLAB
A BOEING COMPANY

NeXt Triple Junction (XTJ)

Typical Electrical Parameters
(AM0 (135.3 mW/cm²) 28°C, Bare Cell)

Parameter	Unit	100 mm 2 per	100 mm 1 per	150 mm 2 per
Eff_{mp}	[%]	29.5%	28.9%	29.5%
V_{oc}	[V]	2.633	2.633	2.633
J_{sc}	[mA/cm²]	17.76	17.76	17.76
V_{mp}	[V]	2.348	2.300	2.323
J_{mp}	[mA/cm²]	17.02	17.02	17.02

Performance Retention Under Radiation
(1 MeV e-fluence (e-/cm²)

	1 MeV e- fluence (e-/cm²)				
Parameter	3E+13	1E+14	1E+15	3E+15	1E+16
$J_{mp}/J_{mp,o}$	1.00	1.00	0.97	0.93	0.84
$V_{mp}/V_{mp,o}$	0.96	0.95	0.89	0.84	0.77
$P_{mp}/P_{mp,o}$	0.96	0.94	0.85	0.78	0.65
Eff_{mp} %	28.3%	27.7%	25.1%	23.0%	19.2%

* per AIAA S-111-2005 Standard

	1 MeV e- fluence (e-/cm²)				
Parameter	3E+13	1E+14	1E+15	3E+15	1E+16
$J_{mp}/J_{mp,o}$	n/c	n/c	0.96	0.94	0.84
$V_{mp}/V_{mp,o}$	n/c	n/c	0.91	0.86	0.82
$P_{mp}/P_{mp,o}$	n/c	n/c	0.87	0.81	0.69
Eff_{mp}	n/c	n/c	25.7%	23.9%	20.4%

* Characterized per ECSS-E-ST-20-08C (Sec. 7.5.15) (48 hr 25ºC photon soak & 24 hr 60ºC dark anneal)

n/c: not characterized

Solar Cell Structure

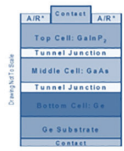

Typical IV Characteristic
AM0 (135.3 mW/cm²) 28°C, Bare Cell

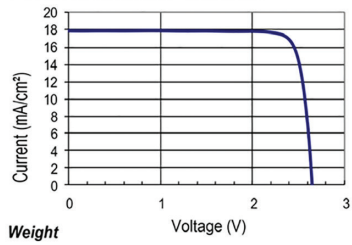

Weight

84 mg/ cm² (Bare) @ 140 µm (5.5 mil) Ge wafer thickness

Temperature Coefficients *(15°C - 75°C)*
(Fluence 1MeV Electrons/cm²)

	1 MeV e- fluence (e-/cm²)				
Parameter	BOL	1E+14	1E+15	3E+15	1E+16
DV_{oc}/DT	-6.1	-6.4	-6.7	-7.0	-7.0
DJ_{sc}/DT	10.6	8.8	9.8	10.7	10.0
DV_{mp}/DT	-6.5	-6.7	-6.9	-7.1	-6.9
DJ_{mp}/DT	6.6	7.3	13.2	13.9	14.9

* per AIAA S-111-2005 Standard

Thermal Properties

Parameters	Value
Solar Absorptance	0.90 (5 mil CMG-AR, 0.88 for bare cells)
Emittance (Normal)	0.85 (Ceria Doped Microsheet)

Intellectual Property

Space products are protected by Spectrolab's portfolio of patents > 90 U.S. patents.

Regulatory

AS9100 CERTIFIED

ISO 14001

7/16/18

Spectrolab, Inc. 12500 Gladstone Avenue, Sylmar, California 91342 USA
• Phone: 800.936.4888 • Website: www.spectrolab.com • Customer Service DLSYLCustomerService@Boeing.com

FIGURE 6.2 A vendor's catalog sheet of a 28.3% efficient NeXt Triple Junction (XTJ) photovoltaic cell.

28.3% efficient NeXt Triple Junction (XTJ) PV cell. It displays information useful to the design engineer, such as (i) typical electrical parameters like current and voltage outputs, (ii) radiation degradation factors on current and voltage at various 1 MeV equivalent fluence levels, (iii) temperature coefficients on voltage and current, (iv) the *I–V* curve, (v) thermal properties, (vi) weights, and (vii) the cell structure of the three junctions. The effects of these factors on the solar array design will be seen later in the chapter.

6.4 EQUIVALENT ELECTRICAL CIRCUIT

The steady-state equivalent electrical circuit of the cell is shown in Figure 6.3. The cell receives photon charge from the sun at a constant flow rate; hence, it acts as a constant current source shunted by a diode. The circuit parameters are as follows. The series resistance R_s represents the internal resistance to the current flow. It is primarily due to the resistivity of the material. The shunt resistance represents the leakage current across the junction. It depends on the n–p junction depth, the impurities, and the contact resistance. The value of R_{sh} is inversely related to the leakage current to ground. In an ideal PV cell, $R_s = 0$ (no series loss) and $R_{sh} = \infty$ (no leakage to ground). Since the magnitudes of the diode current and the resistances R_s and R_{sh} vary with temperature, the cell output and the conversion efficiency decrease with increasing temperature.

In the equivalent circuit, the current delivered to the external load equals the source current (photo current), I_s, proportional to the illumination, less the diode current, I_d, and the ground shunt current, I_{sh}. The open-circuit voltage, V_{oc}, of the cell is obtained when the load current is zero, i.e., when $I = 0$, and is given by:

$$V_{oc} = V + IR_s \tag{6.1}$$

The diode current is given by the classical diode current expression:

$$I_d = I_o\left[\frac{qV_{oc}}{{}_eAKT} - 1\right] \tag{6.2}$$

where

I_o = the diode saturation (dark) current
q = electron charge = 0.1592×10^{-18} coulombs
A = curve-fitting constant

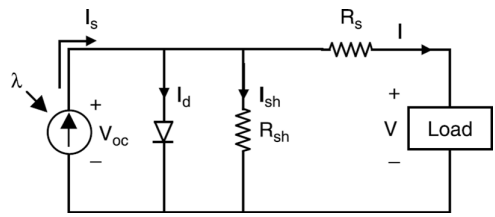

FIGURE 6.3 Equivalent electrical circuit of a photovoltaic cell.

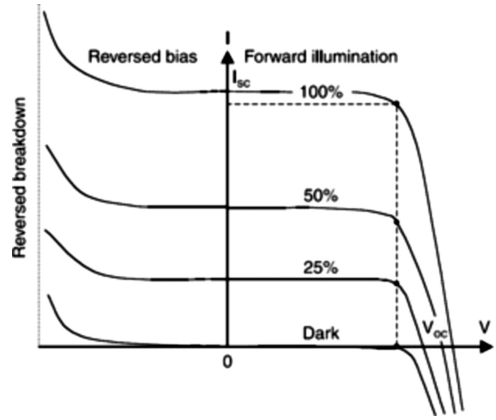

FIGURE 6.4 Terminal *I–V* characteristics under full, partial, and zero illuminations.

K = Boltzmann constant = 1.38×10^{-23} J/K
T = absolute temperature, in kelvin

The load current is therefore given by the expression:

$$I = I_s - I_0\left[\frac{qV_{oc}}{_eAKT} - 1\right] - \frac{V_{oc}}{R_{sh}} \tag{6.3}$$

The last term in Equation 6.3 is the ground leakage current. In practical cells, it can be ignored since it is negligible compared to I_s and I_d. The terminal current versus voltage (I–V) characteristics under dark, partial light, and full light are shown in Figure 6.4. The voltage developed and the fraction of incident flux converted into electrical power depend on the junction material and the wavelength of the radiation. The maximum power that can be extracted from the cell under full light is equal to the area of the dotted rectangle. The maximum power is approximately proportional to the short-circuit current. In the forward direction, the power generation is maximum at the knee point of the curve.

The diode saturation current can be determined experimentally by applying voltage (V_{oc}) to the cell in the dark and measuring the current going into the cell. This current is often called the dark current or the reverse diode saturation current. If the voltage is externally applied in the reverse direction, say during a system fault transient, the current remains flat and power is absorbed by the cell. However, beyond a certain negative voltage, the junction breaks down as in a diode, and the current rises to a high value. In the dark, the current is zero for voltage up to the breakdown voltage, which is the same as in the illuminated condition.

6.5 *I–V* AND *P–V* CHARACTERISTICS

The electrical characteristic of a PV cell in sunlight in the useful working range is represented by the *I–V* curve in the first quadrant only, as shown in Figure 6.5a. The two most important parameters widely used for describing the cell's electrical

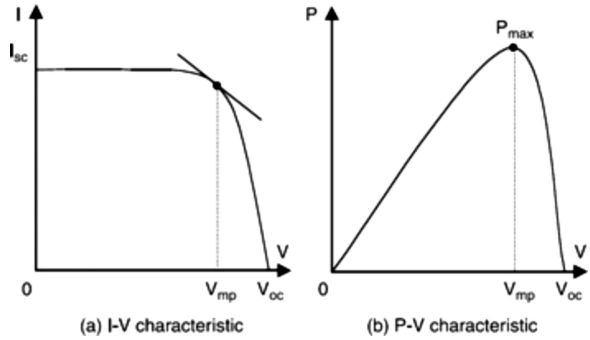

FIGURE 6.5 Cell characteristics in sunlight and the maximum power point. (a) I-V Characteristics. (b) P-V Characteristics.

performance are the open-circuit voltage, V_{oc}, and the short-circuit current, I_{sc}. The short-circuit current is measured by shorting the output terminals and measuring the terminal current under full illumination. Ignoring the small diode and the ground leakage currents under zero terminal voltage, I_{sc} is the photocurrent, I_s. The current under this condition is the maximum current the cell can deliver. The *I–V* characteristic is developed from the test data at various illuminations, temperatures, and ionized radiation doses. The bottom right of the curve at zero current is the open-circuit voltage measured with the output terminals open. The maximum photovoltage is produced at the open-circuit voltage.

By ignoring the ground leakage current, Equation 6.4 with $I=0$ gives the open-circuit voltage as

$$V_{oc} = \frac{AKT}{q} \log_n \left(\frac{I_s}{I_0} + 1 \right) \tag{6.4}$$

The constant KT/q is the absolute temperature expressed in volts (300 K = 0.026 V). In practical photocells, the photocurrent is several orders of magnitude greater than the reverse saturation current. Therefore, the open-circuit voltage is many times the KT/q value. Under constant illumination, I_s/I_o is a sufficiently strong function of the cell temperature, and the solar cell ordinarily shows a negative temperature coefficient of the open-circuit voltage.

The output power of the panel is the product of the voltage and current outputs. In Figure 6.5b, the power is plotted against the voltage. Notice that the cell produces no power at zero voltage or zero current and produces the maximum power at the voltage corresponding to the knee point of the *I–V* curve. This is why the PV power circuits are designed such that the panel operates closed to the knee point, slightly on the left-hand side. Therefore, the PV panel is modeled approximately as a constant current source in the electrical analysis of the system. On the left-hand side of the knee point, the cell works like a constant current source, generating voltage to match the load resistance. On the right-hand side, the current drops rapidly with a small

rise in voltage, and the cell works like a constant voltage source with an internal resistance.

6.6 ARRAY CONSTRUCTION

The solar array consists of numerous cells mounted on a base substrate on rigid panels or flexible cloth. The construction can take various forms, as described below.

6.6.1 Rigid Panels

This traditional construction method has been widely used in the past with crystalline silicon cells on rigid flat panels and is still used where advantageous. The cells are mounted on a rigid substrate made of an aluminum honeycomb with face sheets. Typically, the face sheets have been made from aluminum, but fiber composite sheets such as graphite, Nomex™ and Kevlar™ have also been successfully used for mass reduction. Honeycomb substrates are available in ¼, ½, ¾ and 1 inch thicknesses. Silicon adhesive is used to fix the PV cells onto the panels. Extreme care is exercised in applying the adhesive, since even a trace of silicon in the cell production facility can degrade the cell output voltage considerably.

The array is protected from the space environment primarily by a coverglass such as fused silica Microsheet™. An antireflective coating minimizes light reflection. It enhances the light absorption by the cell and produces more power. A suitable coating is also applied to the back surface for temperature control. The electrostatic discharge (ESD) concern is addressed by the Indium tin oxide (ITO) coating on the front surface. However, it reduces power generation, which must be compensated for a larger panel area or thicker coverglass.

Figure 6.6 shows a satellite with one wing of the solar array and key panel construction features. The series of strings of cells on the panels are routed such that the magnetic moment is minimized. If the propellant plume is a concern, the strings are oriented perpendicular to the plume flow such that the plume affects only one whole string versus some parts of all strings. This way, if one string were damaged due to a heavy plume, the required power would still be produced with the built-in

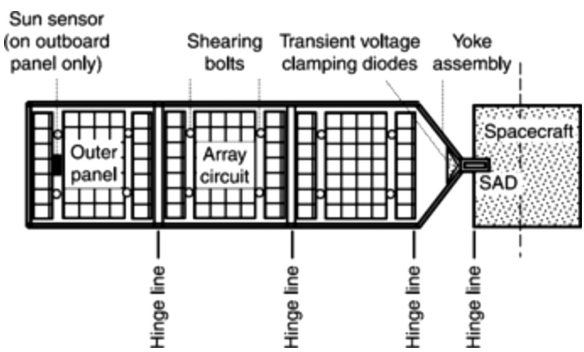

FIGURE 6.6 Satellite showing one wing of the solar array fully deployed.

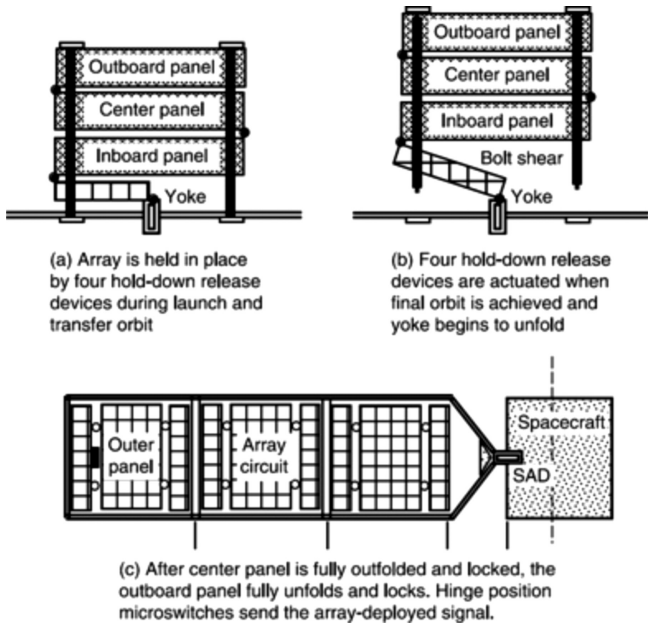

FIGURE 6.7 Solar array wing: (a) stowed, (b) being deployed, and (c) after full deployment.

redundancy in the number of string circuits. Exposing all strings to the plumes may pose a relatively higher risk.

The rigid panels are initially stowed with the spacecraft body during launch. They are deployed by cutting various spring-loaded cables and bolts with electro-explosive devices. Figure 6.7 displays the sequence of one wing being stowed, being deployed, and being fully deployed.

6.6.2 Body-Mounted Array

The body-mounted array finds applications in small satellites for science missions, such as the one shown in Figure 6.8. The cells are mounted directly on the spacecraft

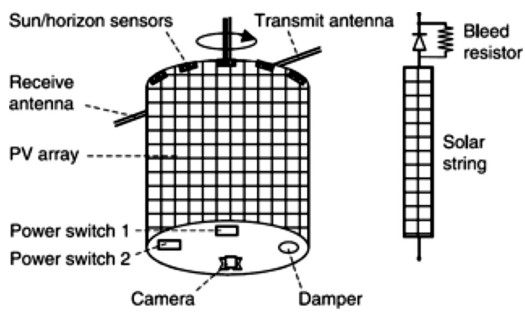

FIGURE 6.8 Body-mounted array with bleed resistors in solar strings.

body without using a honeycomb substrate. It saves substrate mass and also gimbals. The obvious disadvantage is that it needs 57% more cells for the same power. However, it is generally found advantageous in the following situations: The spacecraft distance from the sun, the sun angle, or the operating temperature vary over a wide range, flatly deployed panels interfere with an instrument's line of view. When the body-mounted array rotates, the illuminated strings are at rated voltage and the dark strings are at zero voltage. This can cause ESD discharge along the circumference of the body. The remedy is to use bleed resistance across the isolation diode, as shown in Figure 6.8. It equalizes the potential of the sunny side and the dark side through a bleeding current.

6.6.3 Three or More Wings

The three-wing array shown in Figure 6.9 may give essentially the same benefits as the body-mounted array, provided that the deployed array wings do not interfere with the instruments. The wings can be canted at different angles as required for powering the mission. This architecture is most likely to be used for small science missions on satellites with peak power tracking systems design.

6.6.4 Flexible Array

The PV arrays can be installed on flexible materials such as Kevlar or similar cloths. This will reduce the array's mass. The array is folded when stowed and deployed like an accordion panel or rolled out. Such arrays have been used on the first Hubble Space Telescope (Figure 6.10), the EOS-AM, Olympus, and the International Space Station. They are now more common in commercial satellites because of their easy installation and mass and volume reduction. They need to be designed to withstand the thermal snap when exiting the eclipse. The snap is caused by the cell side facing the sun heating up quickly, while the back side is still cold due to insignificant heat transfer from front to back. Hence, a large thermal gradient builds up across the cloth's thickness. This and the mismatch in the coefficients of thermal expansion between the cell area and the metal frame jointly cause the front to bend (buckle) since the flexible cloth cannot support bending stress.

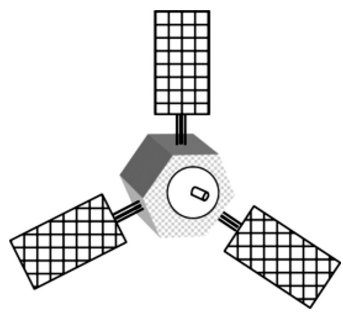

FIGURE 6.9 Three-wing solar array for small science mission satellites.

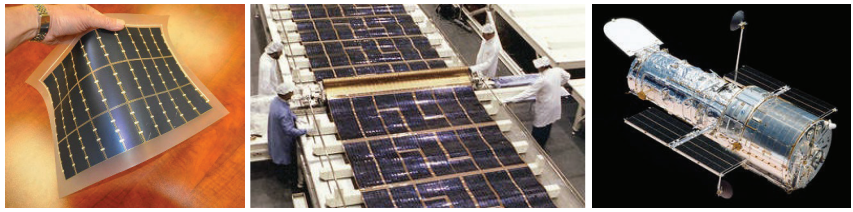

(a) Flexible solar panel (b) Hubble's original solar arrays (c) Hubble telescope.

FIGURE 6.10 Flexible photovoltaic solar panels. (a) Flexible solar panel. (b) Hubble's original solar arrays. (c) Hubble telescope. (Hubble's original solar arrays. Source: NASA.)

6.7 ARRAY PERFORMANCE

The major factors influencing the electrical performance of the solar array are the sun's intensity, sun angle, and operating temperature.

6.7.1 Sun Intensity

The *I–V* characteristic of a PV array shifts down at lower sun intensity with a small reduction in voltage, as shown in Figure 6.11. However, the photoconversion efficiency of the cell is insensitive to solar radiation in the practical working range. Figure 6.12 shows that the efficiency is practically the same at full sun (1353 W/m^2) and ½ sun and starts falling off rapidly only below ¼ sun (340 W/m^2). This means that the conversion efficiency is high. We obtain a lower power output in the penumbra only because less solar energy is impinging on the cell. However, the power extractable during penumbra cannot be utilized in practical designs because of the low voltage. Hence, it is ignored.

6.7.2 Sun Angle

The cell output current is given by

$$I_s = I_0 \cos\theta \tag{6.5}$$

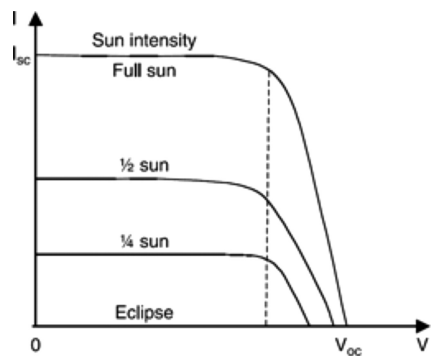

FIGURE 6.11 Current versus voltage characteristics at various illumination levels.

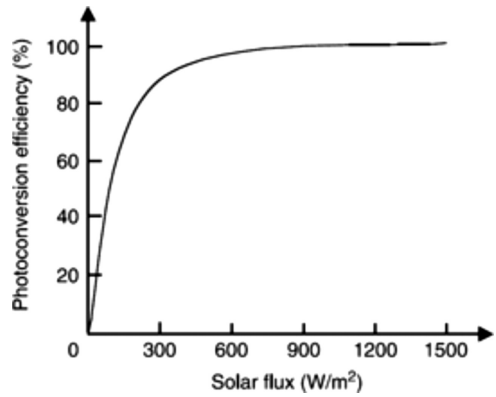

FIGURE 6.12 Photoconversion efficiency over a wide range of solar flux.

TABLE 6.1
The Kelly Cosine Values of the Photocurrent in Silicon Cells

Sun Angle (°)	Mathematical Cosine Value	Kelly Cosine Value
30	0.866	0.866
50	0.643	0.635
60	0.500	0.450
80	0.174	0.100
85	0.087	0

where I_o is the photocurrent with a normal sun ($\theta = 0$). The cosine law holds well for sun angles ranging from 0 to about 50°. Beyond 50°, the electrical output deviates significantly from the cosine value, and the cell generates no power beyond 85°, although the mathematical prediction would give 7.5% power generation. The actual power–angle curve of the PV cell is called the Kelly cosine and is given in Table 6.1. The Kelly cosine presented in the table is useful to accurately assess the power available from the sun at low angles during the transfer orbit.

6.7.3 Temperature Effect

With increasing temperature, the short-circuit current of the cell increases, whereas the open-circuit voltage decreases, as shown in Figure 6.13. Since the increase in current is much less than the decrease in voltage, the net effect is the decrease in power, which is quantitatively evaluated by examining the effects on current and voltage separately.

Assume that I_o and V_o are the short-circuit current and the open-circuit voltage at reference temperature T, and α and β are their temperature coefficients in units of A/°C and V/°C, respectively. If the operating temperature is increased by ΔT, then the new current and voltage are given by

$$I_{sc} = I_o + \alpha \Delta T, \quad \text{and} \quad V_{oc} = V_o - \beta \Delta T \tag{6.6}$$

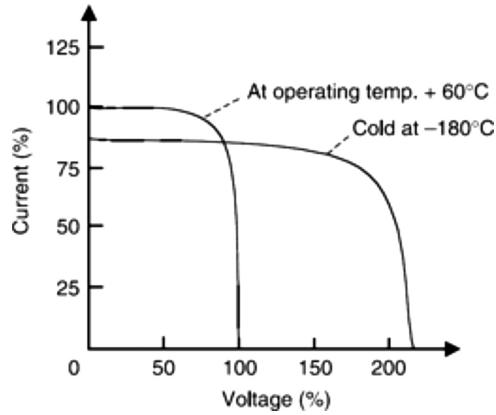

FIGURE 6.13 Temperature effect on *I–V* characteristics.

Since the operating current and voltage change approximately in the same proportion as the short-circuit current and open-circuit voltage, respectively, the new power is

$$P = VI = (I_o + \alpha\Delta T)(V_o - \beta\Delta T)$$

This can be simplified in the following expression by ignoring the small term containing the products of α and β,

$$P = V_o I_o + \alpha\Delta T V_o - \beta I_o \Delta T,$$

which reduces to

$$P = P_o - \left[(\beta I_o - \alpha V_o)\Delta T\right] \tag{6.7}$$

For a typical 2×4 cm single-crystal silicon cell, α is 250 μA/°C and β is 2.25 mV/°C. Therefore, power varies approximately as

$$P = P_o[1 - 0.005\Delta T] \tag{6.8}$$

This expression indicates that for every degree Celsius rise in the operating temperature, the silicon cell power output decreases by 0.50%.

Figure 6.14 depicts the power output versus voltage characteristics at two operating temperatures. It shows that the maximum power available at the lower temperature is higher than that at the higher temperature. Thus, a cold temperature is better for the PV cell, as it generates more power. However, the two P_{max} points are not at the same voltage. In order to extract maximum power at all temperatures, the PV system must be designed such that the array output voltage can increase to V_2 for capturing P_{max2} at lower temperatures, and decrease to V_1 for capturing P_{max1} at higher temperatures. If the array is operating at a fixed regulated voltage, the higher power

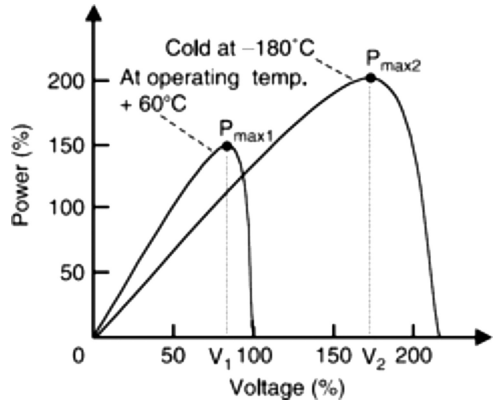

FIGURE 6.14 Temperature effects on *P–V* characteristics.

generation capability at a cold temperature cannot be utilized by the loads, and the excess power generation by the cell must be wasted in the shunt circuits.

The array undergoes a wide temperature cycle in each orbit. During sunlight, it operates around 50°C–60°C on the front face, 40°C–50°C on the back face, and with a 10°C gradient. The temperature is calculated from the thermal model using the heat received primarily from the sun. The solar array temperature is determined by the following thermal equation:

$$\begin{aligned}&\text{solar flux} + \text{Earth's albedo} + \text{Earth's thermal radiation}\\&\quad + \text{heat coming from adjacent components of the spacecraft}\\&\quad = \text{electrical power output} + \text{heat radiated back into space}\end{aligned} \tag{6.9}$$

The incidence and radiated heat from the spacecraft body vary with location in the orbit, as shown in Figure 6.15. The array temperature variations over one geosynchronous Earth orbit (GEO) and one low Earth orbit (LEO) are shown in Figure 6.16. During an eclipse in GEO, the temperature drops exponentially to as low as −175°C. The time constant depends on the mass composition of the array component and is typically in the 30–60 min range. The front-to-back face temperature gradient for

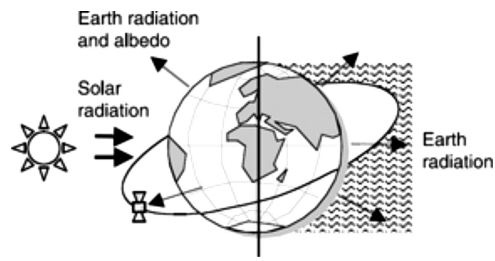

FIGURE 6.15 Heat input and output of a satellite in Earth orbit.

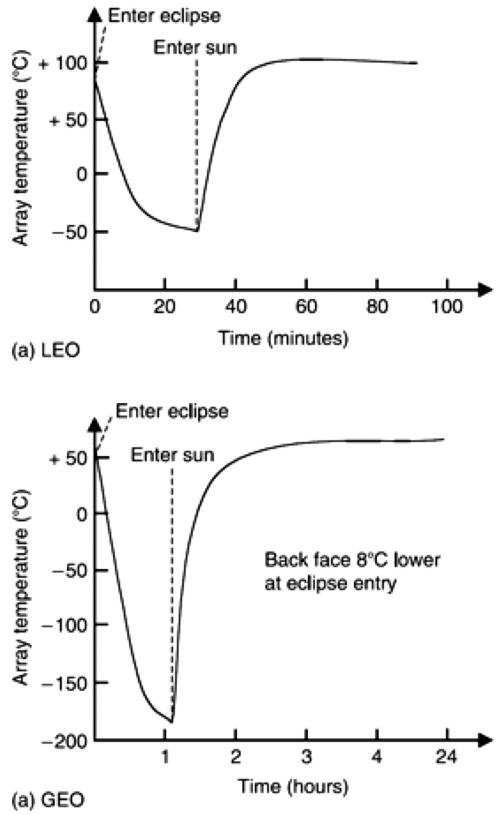

FIGURE 6.16 Solar array temperature variations over one low Earth orbit (LEO) and one geosynchronous Earth orbit (GEO). (a) LEO. (b) GEO.

rigid arrays with aluminum face sheets can be 5°C–10°C under steady sun and up to 20°C in sunlight after an eclipse. Various techniques are used to control the temperatures of spacecraft parts.

6.7.4 Sun Acquisition

The array wings after deployment must be oriented to acquire the sun's normal to the array surface. The sun sensor used for this purpose has two PV cells mounted on two 45° wedges and connected differentially in series opposition through an actuator motor, as shown in Figure 6.17. When the sun is perfectly normal, as in (i), the currents from both cells are equal to $I_o \cdot \cos 45°$. Since they are in series opposition, the net current in the motor is zero, and the array stays put. On the other hand, if the array is not normal to the sun, with an error angle δ as in (ii), the sun angles on the two cells are different, giving two different currents, namely:

$$I_1 = I_o \cos(45 + \delta), \text{ and } I_2 = I_o \cos(45 - \delta) \tag{6.10}$$

The motor current is, therefore:

$$I_m = I_1 - I_2 = I_o \cos(45+\delta) - I_o \cos(45-\delta) \tag{6.11}$$

Using the Taylor series expansion: $f(x+h) = f(x) + hf'(x) + \frac{h^2}{2!} f''(x) + \cdots$

We can express the two currents as:

$$I_1 = I_o \cos 45 - I_o \delta \sin 45,\ I_2 = I_o \cos 45 + I_o \delta \sin 45 \tag{6.12}$$

The motor current shown in Figure 6.17c is then

$$I_m = I_1 - I_2 = 2I_o \delta \sin 45° = \sqrt{2} I_o \delta \tag{6.13}$$

if δ is in radians.

The motor turns toward the sun until the current is zero, and then it remains there. At that position, the error angle, δ, is zero, i.e., the array is normal to the sun. The two current sensors shown in (iii) also work as sunlight and eclipse binary detectors. As on the International Space Station, sun sensors are generally mounted on the main solar array body itself. They may indicate that the solar array is off-pointing when, in fact, the array is shadowed from the sun, or the sun sensors themselves are shadowed, or when the solar array is feathered in order to avoid the rocket exhaust plumes during rendezvous with the space shuttle or any other vehicle.

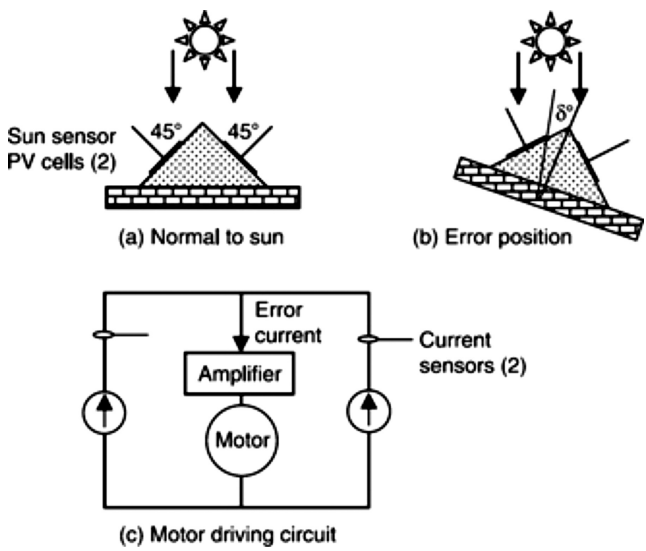

FIGURE 6.17 Sun-pointing actuator principle. (a) Normal to sun. (b) Error position. (c) Motor driving circuit.

6.7.5 Shadow Effect

The array consists of many parallel strings of series-connected cells. One such string is shown in Figure 6.18. A large array may be partially shadowed due to a structure interfering with the sun's line. If a cell in a long string becomes completely shadowed, it loses the photovoltage but still must carry the current by virtue of being in series with other fully operational cells in the string. Without internally generated voltage, it cannot produce power. Instead, it acts as a load, producing the local I^2R loss and heat. The remaining cells in the string must work at a higher voltage to make up for the loss of the shadowed cell voltage. Higher voltage in healthy cells means lower string current as per the *I–V* characteristic of the string. This is shown in the middle dotted *I–V* curve in Figure 6.18b. The current loss is not proportional to the shadowed area and may go unnoticed as a mild shadow on a small area. However, if more cells are shadowed beyond the critical limit, the *I–V* curve is reduced below the operating voltage of the string, making the string current fall to zero and losing all power from the string.

The commonly used method of eliminating the loss of a string due to the shadow effect is to subdivide the string length into several segments with bypass diodes in a cross-tied arrangement (Figure 6.19). The diode across the shadowed segment bypasses only that segment of the string. This causes a proportionate loss of the string voltage and current without losing the whole string's power. Some modern PV cells come with such internally embedded bypass diodes to eliminate the need for

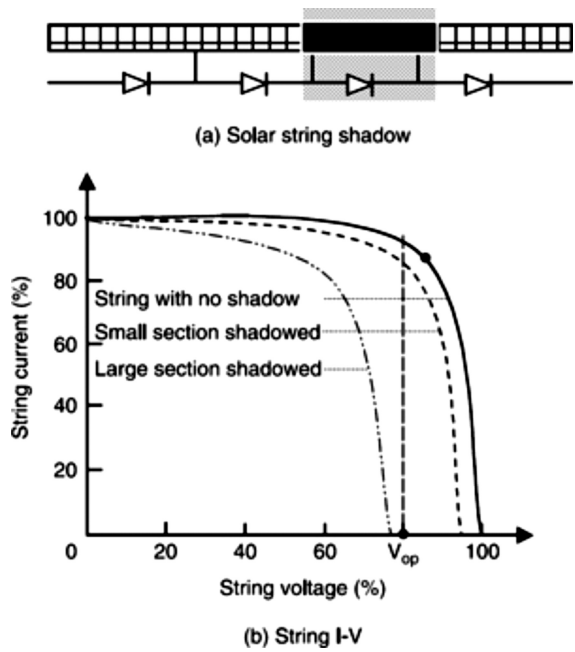

FIGURE 6.18 Shadow effect on a long photovoltaic string of a solar array. (a) Solar string shadow. (b) String I-V.

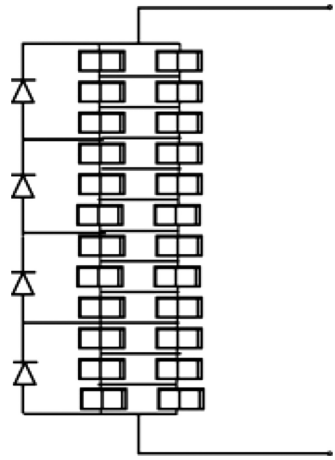

FIGURE 6.19 Bypass diodes in the photovoltaic string to minimize power loss under heavy shadow.

separate diodes on the back of the panel. Cross-strapping cells in adjacent strings, also shown in the figure, is often used to improve reliability against open cells but is not related to shadow effect mitigation.

If a part of the array is shadowed for a part of the orbit, the decrease in incident energy during the sunlight portion of the worst-case orbit may need to be accounted for in the energy balance. It is given by:

$$E_{\text{sun}} = \frac{1}{T_{\text{sun}}} \sum_i (1 - \text{shadow}_i) \cdot \cos\theta_i \cdot \Delta t \tag{6.14}$$

where T_{sun} = sunlight duration, θ_i = angle between the solar vector and the array normal at time step i, shadow_i = fraction of the solar array surface shadowed at time step i, and Δt = time step interval of the analysis.

6.8 ARRAY DESIGN

At the end of its life, the array must generate the required power equal to the sum of all loads, the power losses, and the battery charge power with some margin. The following factors directly or indirectly influence the total number of cells required in the array design:

a. Radiation and other environmental effects,
b. Protection (e.g., coverglass material),
c. Degradation factors,
d. Temperature,
e. Temperature coefficients for I_{sc} and V_{oc},
f. PV cells, manufacturing, and cost,
g. Magnetic dipole moment minimization.

6.8.1 Degradation Factors

Degradations in the solar array's performance come from the following two distinct groups of factors: (i) initial degradations at the beginning-of-life due to manufacturing imperfections and tolerances, and (ii) accumulated degradation over time up to the end-of-life due to various environmental effects.

1. Initial degradations at the beginning-of-life
   - Cell mismatch in the assembly
   - Cell-to-cell wiring loss
   - Array wiring loss over panels and boom
   - The plasma effect causes leakage current from the array to space
2. Accumulated degradation over time to end-of-life
   - Ionized particles cause damage due to the cumulative radiation dose
   - Ultraviolet radiation changes the optical properties of the cover glass and the cell
   - Thermo-elastic stress cycles cause soldered joints to crack over time
   - Micrometeoroids and debris impacts reduce the power-generating area of cells and damage conductors, particularly at the solder joints
   - Flue gases change the optical properties of coverglass and cell
   - Bypass diode failure causes a sub-string to be lost, reducing the string current

6.8.2 Radiation Damage

Different charged particles in the space environment have different masses and velocities, resulting in significantly different energy levels. Heavy particles confine damage to the vicinity of the particle track, thereby doing more damage for a given energy. Different particles having the same energy have different damaging effects on I_{sc} and V_{oc}. Therefore, their damaging effect is converted into the equivalent of 1 MeV of energy. The sum is expressed as, say, 2×10^{15} e/cm^2, where the letter e is called *electron fluence* but it really represents 1 MeV energy. Therefore, the fluence levels are different for I_{sc} and V_{oc}, and the higher of the two applies to the $P_{\max}$ point. The degradation curves are established by testing numerous cells at various fluence levels.

6.8.3 Offsetting from Sun

The full load power is often not needed for a long time, such as during on-orbit storage. We may expect that offsetting the array from the normal sun could minimize the ionized radiation damage and extend the array's life. Such expectations are based on the less than 90° angle of incidence of charge particles on the array. However, offsetting does not help in this regard because the direction of the charged particles does not matter in their degradation effect. The fluence is like a cloud of homogeneous gas or liquid in which the array is immersed, particularly in GEO and MEO. The immersion area is what really matters. In LEO, however, there are some indications that the direction may matter, but probably not much.

If the inboard panels are kept stowed for several years until they are needed later in the mission, the radiation damage on the stowed panels would be somewhat less. However, this reduction in damage is insignificant; it may be 1% for every 2 years of preservation. As mentioned earlier, the radiation particles are like a cloud of gas in which the array is immersed. Deployed or not, the charged particles enter the array and do the damage.

6.8.4 Magnetic Moment

The satellite's magnetic moment is primarily produced by the solar array current loops and the torque coils. It is a vector defined as $M = (\text{current} \times \text{area of the loop})$ A·m^2, regardless of the shape of the loop. The vector direction follows the right-hand rule. For a loop current in one plane, the moment is perpendicular to the plane. In the Earth's magnetic field, B, it produces a torque, T (in N±m), of magnitude given by the cross-product.

$$T = M \times B = M \times B \sin\theta \tag{6.15}$$

The potential energy, U (in joules), stored in the loop is given by the dot product

$$U = M \cdot B = M \times B \cos\theta \tag{6.16}$$

The moment increases with the current. Since current is proportional to the array area and the array area is proportional to power, the moment increases roughly as square of the power, i.e.,

$$M = k \cdot P^2 \tag{6.17}$$

where k is the constant of proportionality derived from test values in similarly built designs.

The torque direction is such that the coil (dipole) tends to orient itself parallel to the B field so as to minimize the potential energy, which is always in a stable position. In doing so, if the coil turns at an angular speed, ω, the power delivered by depleting the potential energy is $T \cdot \omega$. When changing the attitude (position and direction) to maintain the desired orbit, additional fuel must be spent by the attitude control system to overcome this torque. The amount of this additional fuel is proportional to the time integral of $T \cdot \omega$ over the mission life, i.e.,

$$\Delta\text{fuel} = \int_{\text{life}} T \cdot \omega \; dt \tag{6.18}$$

The magnetic moment of the solar array is minimized by laying the string circuits so as to minimize the loop area. This is done not only to minimize the fuel requirement but also to minimize its influence on payloads, particularly the instruments that are sensitive to magnetic fields.

6.9 CONCENTRATOR ARRAY

In a concentrated solar array, to improve the conversion efficiency, the sunlight is concentrated to tens or hundreds of times the normal sun's intensity by focusing on a small area using low-cost lenses. The primary advantage is that such a cell requires a small fraction of active area compared to the standard cell. This significantly reduces the PV material requirement, although the total energy collection area remains the same. Besides increasing the power and reducing the size or number of active cells, such cells have the additional advantage that the cell efficiency increases under concentrated light up to a point.

Two options for concentration cells are depicted in Figure 6.20. In the dome-shaped concentrator, the active cell lies in the center of an aluminum cup covered with a typically 15-mil transparent silicon dome. Since the dome lens produces a high level of concentration, even slight misalignments due to a small pointing error can result in a significant loss of power. The thin-film inflatable array with dome concentrator is under development for space antennas and is being considered for extending into power systems, particularly for high-power electrical propulsion.[1] The line concentrator concept, on the other hand, produces relatively less concentration but is less sensitive to pointing errors.

Concentrator solar cells can dramatically reduce the cell cost, which is 35%–45% in conventional arrays. However, two key issues seriously affect the cell design at high concentrations. One is the minimization of the series resistance, and the other is more active cooling of the array to remove the energy not converted into electricity. The mounting structure can be a flexible cloth or a rigid panel made of a honeycomb structure. The rigid panel approach takes away some of the mass benefits of the flexible blanket array but offers well-proven deployment and the ability to place PV cells on the outermost panel for the transfer of orbital power.

The primary advantage of concentrator technology is its low cost per watt, which is achieved by replacing the active solar cell area with a less expensive optical

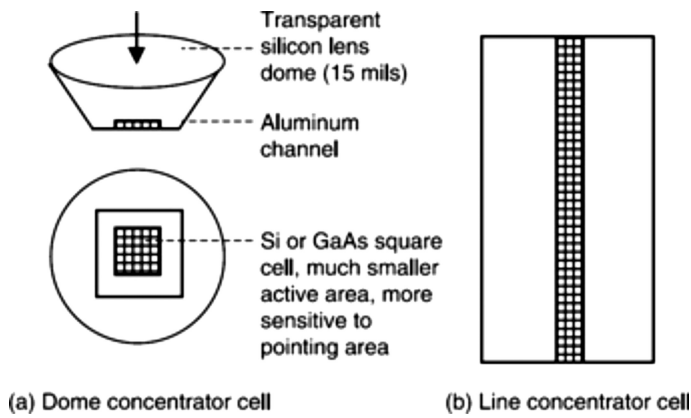

FIGURE 6.20 Solar concentrator cell construction. (a) Dome concentrator cell. (b) Line concentrator cell.

surface. A secondary advantage comes from the fact that the enclosed cell is naturally protected from radiation and space plasma. This makes it suitable for high-voltage applications.

The concentration cells have limited benefits in traditional space applications for two reasons. The reduced active area saves some PV material costs, but the pointing error may offset the benefit. Moreover, the energy collection area remains the same, hence the same substrate mass.

REFERENCE

1. Laug, K.K. and Holmes, M.R., Paraboloidal thin-film concentrators and their use for power applications, in *Proceedings of the 34th Intersociety Energy Conversion Engineering Conference*, SAE, 1999, Paper No. 2552.

FURTHER READINGS

Algora, C. and Diaz, V., Influence of series resistance on guidelines for manufacturing of concentrator p-on-n GaAs solar cells, in *Progress in PV Research and Applications*, John Wiley and Sons, 2000, Vol. 8, pp. 211–225.

Brown, M.A. and Moore, J., Solarcon concentrator solar array, in *Proceedings of the 36th Intersociety Energy Conversion Engineering Conference*, ASME, 2001, Paper No. AT-38, pp. 75–78.

Carlson, D.E., Recent advances in photovoltaics, in *Proceedings of the 30th Intersociety Energy Conversion Engineering Conference*, ASME, 1995, pp. 621–626.

Chern, P.C. and Leipold, M.H., *Stress Fiat and Proof Testing of Silicon Wafers*, Jet Propulsion Laboratory, 1987, Report No. NASA TSP-5.

Cook, G., Billman, L., and Adcock, R., *Photovoltaic Fundamental*, DOE/Solar Energy Research Institute, February 1995, Report No. DE91015001.

Delleur, A.M., Kerslake, T.W., and Scheiman, D.A., Analysis of direct solar illumination on the backside of space station cells, in *Proceedings of the 34th Intersociety Energy Conversion Engineering Conference*, ASE, 1999, Paper No. 01-2431.

Gluck, P.R. and Bahrami, K.A., A simple algorithm to compute the peak power output of GaAs/Ge solar cells on the Martian surface, in *Proceedings of the 30th Intersociety Energy Conversion Engineering Conference*, ASME, 1995, pp 321–325.

Guha, S., et al., Low cost and light weight amorphous silicon alloy solar array for space applications, in *Proceedings of the 34th Intersociety Energy Conversion Engineering Conference*, ASE, 1999, Paper No. 2553.

Jones, P.A., Murphy, D.M., and Piszczor, M., A linear refractive PV concentrator solar array flight experiment, in *Proceedings of the 30th Intersociety Energy Conversion Engineering Conference*, ASME, 1995, Vol. I, pp. 309–314.

Karam, N.H., et al., Development and characterization of high efficiency GaInP/GaAs/Ge dual and triple junction solar cells, *IEEE Transactions on Electron Devices*, 46, 2116–2125, July 1999.

Krut, D.D., et al., High efficiency space concentrator with soft angular dependence and related cell technology, in *Proceedings of the 36th Intersociety Energy Conversion Engineering Conference*, ASME, 2001, Paper No. AT-90.

O'Neill, A., et al. The stretched lens array (SLA), an ultra light concentrator for space power, in *Proceedings of the 36th Intersociety Energy Conversion Engineering Conference*, ASME, 2001, pp. 79–84.

Saude, B., LaSart, N., Blair, J., and Beik, O., "Microgrid-based wind and solar power generation on moon and mars," *IEEE Transactions on Smart Grid*, 14(2), 1329–1332, March 2023.

Schumacher, D., Beik, O., and Emadi, A., "Standalone integrated power electronics system: Applications for off-grid rural locations," *IEEE Electrification Magazine*, 6(4), 73–82, December 2018.

Stern, T.G. and Bonebright, P., Flight tests of a solar array concentrator on *Mightysat II*, in *Proceedings of the 35th Intersociety Energy Conversion Engineering Conference*, ASME, 2001, Paper AT-37, pp. 69–74.

7 Battery

7.1 INTRODUCTION

In a spacecraft, energy storage is required to meet the load power demand when the solar array cannot supply all the loads, e.g., during an eclipse, and to store the excess energy when the power generation exceeds the load demand at any time. The battery is one of the most widely used technologies available in the industry. It stores energy in electrochemical form and comes in two basic types:

- **Primary battery**, in which the battery is the main source of energy with an irreversible electrochemical reaction. It finds applications in short-duration missions and in relatively low-power spacecraft. The load power during launch and ascent when the solar array is nonoperational is met by a primary battery on board the space vehicle. One such battery is the lithium carbon monofluroid, which has a specific energy of 500–600 Wh/kg, which is significantly higher than the commonly used secondary batteries. This battery, once used up is then jettisoned in space after the ascent in order not to carry dead weight onward to save the on-board fuel.
- **Secondary battery**, in which the battery is the secondary source of energy, typically when the primary source is not available. With reversible electrochemical reactions, it finds applications in long-duration missions where another independent power source is always available for recharging the battery periodically. Most photovoltaic-based spacecraft use a secondary battery.

7.2 BATTERY CELL

The battery is made of multiple electrochemical cells assembled in a series–parallel circuit combination to obtain the required voltage and current. The cell stores electrochemical energy at a low electrical potential. Commonly used electrochemistries produce 1.6–4.0 V when fully charged. The cell capacity, denoted by the letter C, depends on the physical size. It is measured as the ampere-hour (Ah) charge the cell can deliver at room temperature until it reaches a cut-off voltage. The battery can deliver C amperes for 1 h or C/n amperes for n hours. A nominally 3.5 V cell discharged down to 2.7 V delivers practically the full capacity of the cell. The Ah capacity at 0.1 V discharge is only a few percent greater than that at 2.7 V discharge.

The battery voltage rating is stated in terms of the average voltage during discharge. The higher the battery voltage, the higher the number of cells required in series. The product of the voltage and the Ah rating determines the energy rating in watt-hours (Wh) the battery can deliver to a load in the fully charged state.

DOI: 10.1201/9781003344605-9

The battery charge and discharge rates are stated in fractions of the capacity. For example, charging a 100 Ah battery at a 10 A rate is said to be charging at a *C*/10 rate. Discharging this battery at the *C*/2 rate means drawing 50 A. At this rate, the battery will be fully discharged in 2 h. The state of charge (SOC) of the battery at any instant is defined as

$$\text{SOC} = \frac{\text{Ah capacity remaining in the battery}}{\text{rated Ah capacity}} \tag{7.1}$$

The SOC affects the cell voltage, specific gravity, and freezing point of the liquid electrolyte. The electrolyte in a fully charged battery has a high specific gravity and freezes at a much lower temperature. On the other hand, a fully discharged battery freezes at a higher temperature. This shows the importance of keeping the battery fully charged when exposed to low temperatures. The battery depth of discharge (DOD) is defined as

$$\text{DOD} = \frac{\text{Ah capacity drained}}{\text{rated Ah capacity}} \tag{7.2}$$

For the case where the battery is charged to 100% SOC on each cycle,

$$\text{DOD} = 1 - \text{SOC} \tag{7.3}$$

Major secondary batteries used in the spacecraft industry in the past have been nickel cadmium (NiCd) and nickel hydrogen (NiH_2), both now replaced by lithium-ion (Li-ion). New electrochemistries are being continuously researched for space and terrestrial applications. Lithium-polymer (Li-poly) and Nickel metal hydride (NiMH) are two such examples in the commercial world.

The selection of electrochemistry for a given application is a matter of performance and cost optimization. The following figures of merit are often used in comparing the relative performance of various electrochemistries:

- **Specific energy**, also called the gravimetric energy density, is the energy stored per unit mass, Wh/kg.
- **Energy density**, also called volumetric energy density, is the energy stored per unit volume, in Wh/liter.
- **Specific power and power density**, defined as the power the battery can deliver per kilogram of mass and liter of volume, respectively. It is sometimes important to think in terms of the power parameters as well, since the internal resistances of the battery may limit the rate at which the energy can be discharged within practical design limits.
- **Cycle life**, defined as the number of charge/discharge (C/D) cycles the battery can deliver while maintaining a minimum cut-off voltage and/or a minimum charge retention.

7.3 TYPES OF RECHARGEABLE BATTERIES

The NiCd battery has been the workhorse of the spacecraft industry since the earliest missions and may still be used in some special missions. However, since the mid-1980s, it has been replaced with the NiH_2 battery for general use in space. The NiH_2 provided deeper DOD for comparable cycle life, thus requiring lower Ah capacity, which translates into lighter weight. Today, the industry has moved toward lithium-based batteries, e.g., lithium-ion (Li-ion) for general space use for higher energy density; and lithium-polymer (LiPo) and lithium-iron-phosphate (LFP) for even higher energy density compared to Li-ion. No single electrochemistry available on the market can meet the wide range of space mission requirements. All chemistries will perhaps continue in use where they fit the best for a minimum mass and cost design. However, the unique construction and performance features of the electrochemistries commonly used in the past and at present are briefly presented hereunder.

7.3.1 Nickel Cadmium (NiCd)

NiCd is a mature electrochemistry that powered almost all satellites until the mid-1980s. It comes in a sealed, vented prismatic cell with positive and negative electrode plates made of a sintered nickel structure. The positive plate is impregnated with nickel hydroxide active material and the negative plate with cadmium hydroxide active material. The plates are die-cut with corner radii and coined edges to prevent shorting. The negative plate design includes a thin Teflon™ impregnation on the surface. This feature extends the operating life by enhancing oxygen recombination and retarding cadmium migration. The positive and negative plates are separated by nonwoven nylon or asbestos, which has been replaced with Pellon 2536™. The electrolyte is potassium hydroxide, and the casing is made of stainless steel.

The NiCd electrochemistry offers relatively lower specific energy, is temperature-sensitive, and has a relatively shorter cycle life. Its major disadvantage is the memory effect, which degrades its performance if not used fully in repeated cycles. Moreover, cadmium has been placed under environmental regulatory scrutiny. For these reasons, NiH_2 replaced NiCd for most space applications after around 1980.

7.3.2 Nickel Hydrogen (NiH_2)

The NiH_2, which typically comes in a cylindrical shape with domes on the sides, has been the most widely used cell in space, both in low Earth orbit (LEO) and geosynchronous Earth orbit (GEO) satellites, for 20–25 years, beginning about 1980. Over 100 major satellites carrying more than 10,000 NiH_2 cells have been flown successfully. They have accumulated almost one billion cell-hours of highly reliable operation. The NiH_2 battery takes the best from two electrochemistries: the nickel oxide electrode from the NiCd and the hydrogen catalyst electrode from the fuel cell. For the initial International Space Station (ISS) design in the early 1990s, NiH_2 was selected after evaluating many other options, including the regenerating fuel cell.

Compared to NiCd, the NiH_2 chemistry has many advantages, such as (i) that it can withstand some abuse in overcharge and overdischarge; (ii) superior C/D

cycle life; and (iii) a linear linear dependence of the SOC with the internal pressure that can be measured by strain gages mounted on the outside wall. Temperature-compensated strain gages are accurately matched in bridge circuits and processed by signal conditioning amplifiers. A two-stage regulator provides stable power for the circuit. Adhesive and conformal coating materials are used for mounting the gages, and the flexible circuit board is made of space-qualified, low-outgassing materials. The strain gages are calibrated individually on each cell.

On the other hand, NiH_2 has the following disadvantages: (i) low energy density in Wh/l; (ii) possible pressure vessel rupture; (iii) high self-discharge rate around 0.5%; (iv) high loss of capacity in storage; (v) cylindrical shape making handling, packaging, and heat transfer difficult; and (vi) safety concerns.

7.3.3 Nickel Metal Hydride (NiMH)

Concerns about working with cadmium in the NiCd battery and disposing of it helped spark interest in using the NiMH battery for a variety of applications, particularly in electric cars, during the 2000s. In general, NiMH electrochemistry presents few health and safety risks, primarily because the electrode materials are nontoxic. Its anode is made of a metal hydride, which eliminates the environmental concerns of cadmium. NiMH offers an improvement in specific energy over NiCd. Another performance improvement is that it has a negligible memory effect. The NiMH, however, is less capable of delivering high peak power, has a high self-discharge rate, is adversely sensitive to high temperatures, and therefore is susceptible to damage due to overcharging.

Electrochemically, the NiMH is similar to the NiH_2, except that the working hydrogen is stored as a solid metallic hydride rather than gas. Having no internal pressure to withstand, these cells are made prismatic. This significantly improves energy density and safety. With less volume to pack, the battery requires less support structure, which improves the specific energy as well. The disadvantage is that the linear pressure versus SOC relation of NiH_2 is no longer available. The NiMH is prismatic and has the same operating voltage as the NiCd. Therefore, the two are easily interchangeable. NiMH, however, produces heat during charging as opposed to the endothermic charging of NiCd.

7.3.4 Lithium-Ion

Lithium-ion (Li-ion) technology offers significantly higher specific energy and energy density than NiH_2. Li-ion batteries are widely used in electric vehicles (EVs), computers, and many other commercial applications. Its large improvement in energy density comes from lithium's low atomic weight.

Space-qualified Li-ion cells come in two variety. One is a small cylindrical cell No. 18650 from Sony Corporation and others, each 18 mm in diameter × 65 mm long, with a 1.5 Ah capacity at 3.7 V average voltage and delivering 5.5 Wh of energy when fully discharged. It is mass-produced to be cost-effective. The battery is assembled by stacking numerous cells in series–parallel circuits as needed to meet the mission requirements. Companies like ABSL Energy Systems make such cells

and also assemble them into space-qualified batteries. As an alternative to the small cylindrical cells, large prismatic cells are also available from Quallion LLC and GS Yuasa in 51 Ah, 102 Ah, and 134 Ah capacities, as shown in Figure 7.1. The current version of the International Space Station has replaced the original NiH_2 battery with a Li-ion LSE134.

Since Li-ion is nonaqueous, it is free from electrode corrosion. On the negative side, lithium is a highly reactive metal and must be stabilized by encapsulating the molecules in carbon using an expensive form of graphite. The lithium electrode reacts with the liquid electrolyte, creating a sort of passivation film. Each time the cell is discharged and then charged, the lithium is stripped away, a free metal surface is exposed to the electrolyte, and a new film is formed. The cell uses thick electrodes to compensate for this degradation. Otherwise, life would be short. The average discharge voltage of 3.7 versus 1.25 for NiCd and NiH_2 requires about one third the number of cells in series for a given battery voltage, thus reducing the assembly and test costs.

Figure 7.2 depicts a typical terminal voltage during one full discharge-charge cycle of a small cylindrical Li-ion cell (18,650 versus SOC). The shape of this curve depends on the discharge and charge rates, operating temperature, and age of the cell. The depicted data is at a moderate rate, showing average discharge voltages of 3.5 V, an end-of-discharge cut-off voltage of 2.7 V, an average charge voltage of 3.7 V, and an end-of-charge voltage of 4.2 V. Note that, at the cell terminals, the average charge voltage is higher than the average discharge voltage due to the voltage drop in the internal resistance of the cell.

Li-ion electrochemistry has a high charge efficiency. The computational efficiency is 100% all the way to 100% charging. Other desired characteristics of a

- Hermetically sealed
- Anodized aluminum case and cover
- Wound prismatic construction

Cell Specifications		LSE51	LSE102	LSE134
Chemistry		Lithium Cobalt Oxide		
Cell Capacity				
Capacity (Ah)	Nameplate	51	102	134
	BOL	57	114	148
Energy (Wh)	Nameplate	189	377	496
	BOL	211	422	548
Energy Density at BOL (Wh/L)		289	337	349
Specific Energy at BOL (Wh/kg)		139	152	155
Cell Electrical Specifications				
Nominal Voltage (V)		3.7	3.7	3.7
End of Charge (V)		4.1	4.1	4.1
End of Discharge (V)		2.75	2.75	2.75
Max. Continuous Charge Current (A)		25.5	50	67
Max. Continuous Discharge Current (A)		76.5	150	134
Max. Pulse Discharge Current (A) (5 seconds)		153	300	402
Cell Mechanical Properties				
Dimensions (mm)	Width	130	130	130
	Thickness	50	50	50
	Height *	131	216	271
	Weight (kg)	1.52	2.77	3.53
	Volume (L)	0.73	1.25	1.57
Temperature range (°C)				
	Charge	10 ~ 35	10 ~ 35	10 ~ 35
	Discharge	-10 ~ 35	-10 ~ 35	-10 ~ 35
	Storage	-10 ~ 10	-10 ~ 10	-10 ~ 10

* Excluding terminals.

FIGURE 7.1 Technical data sheet of large prismatic Li-ion cells.

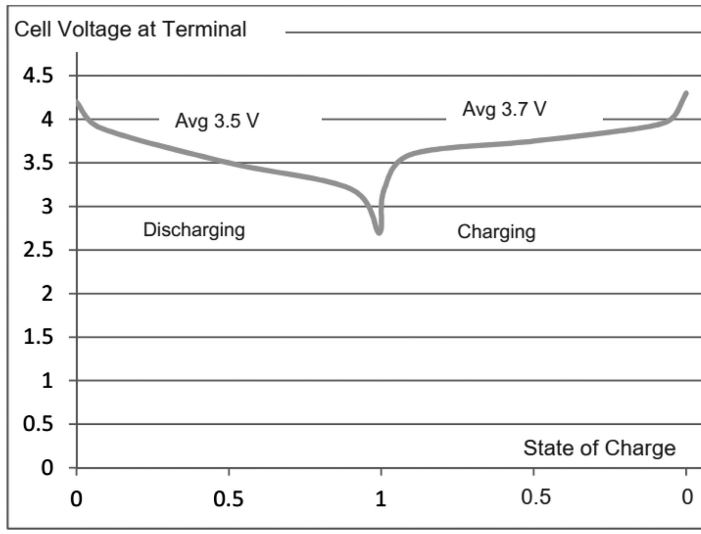

FIGURE 7.2 Typical terminal voltage at moderate discharge and charge rate in space-qualified Li-ion cylindrical and prismatic cells.

space-qualified Li-ion cell are high-rate capability and a potentially long cycle life at high DOD. Its low temperature sensitivity supports operation over a wide temperature range. It has a low internal impedance, less than 1 mΩ in a 50 Ah cell, which supports high charge and discharge rates. It can deliver high short-term peak power without having an adverse effect on life.

Since Li-ion batteries can release lithium gas and flames when overcharged, they need effective overcharge control. The maximum charge voltage and minimum discharge voltage must be maintained for successful incorporation of Li-ion cells into the space power system design. In this respect, Li-ion chemistry is very different from NiH_2 in that Li-ion does not tolerate overcharge or overdischarge. As a battery with many cells in series and parallel is cycled, it often becomes unbalanced due to small cell-to-cell differences in the rate of capacity fade, rate of impedance increase, or rate of self-discharge that are accumulated over many cycles. For charge balancing, various techniques such as switched capacitors and resistance or inductor equalization have been explored.

Li-ion has a better low-temperature performance in the −20°C to +40°C range. It can operate even at −40°C with some capacity loss. Poor cell performance at lower temperatures is attributed to the electrolyte becoming viscous or solid and poor lithium diffusivity in the electrodes. An 8-cell 25 Ah battery was space-qualified in 2001 for 2000 cycles at 100% DOD for the *Mars Lander* mission, requiring such a low temperature range. The battery was designed for 3.0 to 4.1 V operation, a 2.5 V cut-off voltage, and *C*/5 and *C*/10 charge rates. Tests reported by Bruce and Marcoux[1] at various temperatures cover the design and fabrication features of large-capacity cells up to 100 Ah. In cells for aircraft applications, the main concern is irreversible capacity loss at elevated temperatures. The loss in capacity at high temperatures

comes primarily from the positive electrode degradation. In cells for space use, however, the shelf life and cycle life are critical.

Li-ion Cell Life: As for any other electrochemistry, the cycle life of a Li-ion cell is inversely related to DOD and the operating temperature. The industry standard defines the Li-ion battery life as the number of charge-discharge cycles until its charge retention capacity reaches 80% of its original capacity when new.

The cycle life of any type of battery cell can be established by extensive testing of numerous cells under controlled conditions and then analyzing the data as follows. For example, a set of data analyzed by the authors shows the cycle life of Li-ion cells as shown in Table 7.1.

The average of the last column in Table 7.1 is 304,000. We can then deduce that the cycle life of the Lithium cells from this vendor can be expressed approximately as follows:

$$\text{Lithium ion cycle life} = \frac{304,000}{\%\ \text{DoD}} \tag{7.4}$$

This relation is valid at 20°C operating temperature and a C/3 charge-discharge rate. Similar testing and analysis can be done at other temperatures as well to establish a relationship between the cycle life and operating temperature at the applicable charge-discharge rate(s) as necessary.

Basic features of the Li-Ion cell:

Cell voltage when fully charged: 4.1–4.2 V
Cell voltage when fully discharged: 2.70–2.75 V
Average cell voltage during discharge: 3.5–3.7 V
Energy density: 300–600 Wh per liter
Specific energy: 200–300 Wh per kilogram
Specific power: 250–350 watts per kilogram
Charge (Coulombic efficiency): 95 to almost 100%
C/D ratio: 90%–95%

TABLE 7.1
Li-ion Cell Life to 80% Capacity Retention (at 20°C and C/3 Charge-Discharge Rate)

%DOD	Cycle Life	Life Cycles *X* %DOD
5	65,000	325,000
10	32,000	320,000
20	16,000	320,000
40	9000	280,000
60	5000	300,000
70	4000	280,000

C/D cycle life at 100% DOD in every cycle: 2000–3500 cycles.

$$\text{Battery cycle life at } X\% \text{ DoD} = \frac{\text{Cycle Life at 100\% DoD from vendor's data} \times 100}{X\%}$$

Over the last decade, the Li-ion battery has been, and will be for the foreseeable future, the battery of choice for most space and terrestrial energy storage applications. For changing in a significantly favorable way the everyday lives of people in every country on earth, the 2019 Nobel Prize in Chemistry was awarded to its three inventors with the citation: "Lithium-ion batteries have revolutionized our lives and are used in everything from mobile phones to laptops and electric vehicles. Through their work, this year's Chemistry Laureates have laid the foundation of a wireless, fossil fuel-free society".

7.3.5 Lithium Polymer

Li-ion solid polymer electrolyte (Li-poly or LiPo) batteries are similar to those of Li-ion, except that the electrolyte of Li-ion is replaced by a solid polymer that encapsulates the electrodes. The cell is constructed with a film of metallic lithium bonded to a thin layer of solid polymer electrolyte. The solid polymer enhances the specific energy by acting as both the electrolyte and the separator. This construction also offers an improvement in safety compared to Li-ion by reducing flammability. Moreover, the metal in solid electrolyte reacts less than it does with liquid electrolyte. There are various types of Li-polymer cells with markedly different characteristics.

On the safety side, the Li-ion system is relatively less reactive and more reliable than the present lithium metal systems and may perform better over some solid polymer electrolyte systems. However, the possibility of electrolyte spills is a disadvantage over a solid electrolyte. Some materials used in the Li-ion cells may be toxic and carcinogenic, such as lithium, nickel, and arsenic compounds, and possibly cobalt, copper, and polypropylene.

7.3.6 Lithium Iron Phosphate (LFP)

LFP batteries are widely used in the EV market and utility-scale applications as they offer improved safety, lower cost, low toxicity, and a long cycle life.

The LFP energy density is lower than that of other common lithium-ion battery types such as nickel manganese cobalt and nickel cobalt aluminum, and it also has a lower operating voltage. The lithium-titanate oxide cells are in the development stage and have not been fully commercialized as yet. Figure 7.3 compares the three lithium-based cells. The cycle life of nickel manganese cobalt cells is in the range of 700–2000 cycles, the range of LFP cells cycle life is 3000–5000 cycles, and lithium-titanate oxide cells have a cycle life exceeding 20,000 cycles. In addition to a much longer life, lithium-titanate oxide cells have better fire safety records and can support fast charging at a 10°C rate to reach near full charge in $1/10^{th}$ of an hour (e.g., 6 min). Table 7.2 compares different battery technologies.

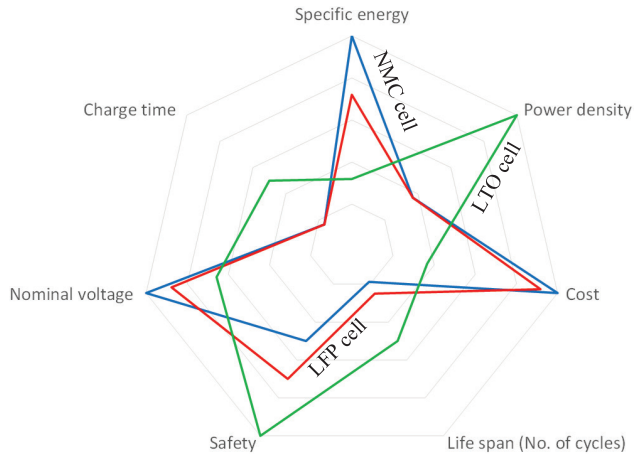

FIGURE 7.3 Li-ion battery cell comparison.

TABLE 7.2
Various Lithium-Based Battery Chemistries Compared

Chemistry >	LFP	LNMC[a]	LMO	LTO[b]
Energy density (Wh/kg)	130–160	220–250	180–200	70–100
Power density (W/kg)	220–250	220–250	220–250	1000–1200
Cycle Life at 100% DOD	3000–4000	1000–2500	2000–2500	10,000–20,000
Safety	Good	Good	Good	Better
Cost US$/kWh	About 350	About 350	About 350	About 850
Technology	Commercial	Commercial	Commercial	Development

[a] LNMC technology offers a high-voltage version suitable for use in EV.
[b] LTO can support fast charging at 10°C rate to fully charge in 1/10th hour (e.g. in 6 min).
EV, electric vehicles; LFP, lithium-iron-phosphate; LTO, lithium-titanate oxide.

7.4 ELECTRICAL CIRCUIT MODEL

The equivalent circuit model of a battery is a voltage source in series with an internal resistance, as shown in Figure 7.4, where E_i is the internal voltage and R_i is the internal resistance. Typically, E_i decreases and R_i increases linearly with the ampere-hour discharge. That is, the internal voltage is lower and the internal resistance is higher in a partially discharged battery as compared to their values—designated as E_o and R_o, respectively—in the fully charged state:

$$E_i = E_o - K_1 \cdot \text{DOD}$$
$$R_i = R_o + K_2 \cdot \text{DOD} \tag{7.5}$$

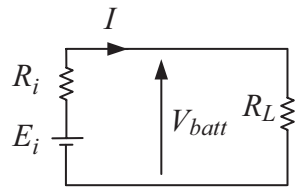

FIGURE 7.4 Equivalent electrical circuit of a battery showing internal voltage and resistance.

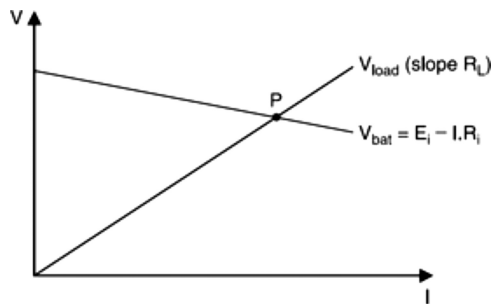

FIGURE 7.5 Battery line and load line intersecting at the operating point.

where K_1 and K_2 are constants of the electrochemistry to be found by curve fitting the test data. Under load, the terminal voltage drops with increasing load, and the operating point P is the intersection of the battery line and the load line, as shown in Figure 7.5.

7.5 PROPERTIES AND PERFORMANCE

The battery's performance depends on the electrochemistry and on many other parameters in a highly nonlinear manner. The major performance characteristics of the battery in general are discussed in this section.

7.5.1 Charge (Coulombic) Efficiency

The charge efficiency, also known as coulombic efficiency, is defined as the ratio of the ampere-hours being deposited internally between the plates over those injected from the external terminals during charging. It is different from the charge-discharge ratio and the energy efficiency defined in the sections below. The coulombic efficiency varies as a function of the SOC, charge rate, and operating temperature and is generally higher than 97%. The charge efficiency is almost 100% when the cell is empty of charge, which is the condition in which all charge received is deposited between the plates. As the SOC approaches 1, the charge efficiency tapers down to zero. The knee point where the charge efficiency starts tapering off depends on the

charge rate and temperature. For example, at a *C*/2 charge rate, the charge efficiency may be almost 100% up to about 80% SOC. At a fast charge rate, on the other hand, the charge efficiency would be lower.

7.5.2 Charge/Discharge Ratio

After discharging certain ampere-hours, the battery requires more ampere-hours of charge to restore its full SOC. The C/D ratio is defined as the ampere-hours input over the ampere-hours output for a full SOC. For example, a C/D ratio of 1.05 means the battery requires 5% more ampere-hours to restore to a fully charged state than what was discharged. This ratio increases more than linearly with increasing temperature and is higher with lower charge and discharge rates. Charging in LEO is usually at a much faster rate, which is more efficient than the slow charging rate typical in GEO. Therefore, a low C/D ratio around 1.05 may be needed in some batteries like NiCd and NiH_2 in LEO missions, while a higher ratio around 1.1 may be needed in GEO missions. A high C/D ratio causes excessive corrosion of the nickel electrodes and a large amount of oxygen, leading to heating and popping during recombination on the hydrogen electrode. On the other hand, a low C/D ratio causes reduced usable capacity, low discharge voltage, and capacity degradation. The C/D ratio for Li-ion cells is favorable; it is near 1.0 under most practical operations.

The battery performs better at slow charge and discharge rates. A fast discharge rate results in fast voltage degradation and low ampere-hour capacity for the load. For these reasons, high charge and discharge rate applications require different design considerations than low-rate applications.

7.5.3 Round-Trip Energy Efficiency

In both the charge and discharge modes, a small fraction of energy is converted into heat. An important figure of merit for a battery is its energy efficiency over a round trip of full charge and discharge cycles, which is defined as the ratio of the energy output over the energy input at the electrical terminals of the battery. In terms of the cell performance parameters,

$$\text{Round trip energy efficiency} = \frac{\text{Average discharge voltage} \times \text{Ah capacity}}{\text{Average charge voltage} \times \dfrac{C}{D}\,\text{ratio} \times \text{Ah capacity}} \tag{7.6}$$

For example, if a 50 Ah Li-ion cell under normal operating conditions has at its terminals an average discharge voltage of 3.5 V, an average charge voltage of 3.7 V, a charge-discharge ratio of 1.05, and a coulombic charge efficiency of 100%, then its output energy delivered to the load is $50 \times 3.5 = 175$ Wh, the input energy drawn from the source is $50 \times 1.05 \times 3.7 = 194$ Wh, and the round-trip energy efficiency is $175/194 = 0.90\%$ or 90%. It means that about 10% of energy is wasted internally as heat in every charge-discharge cycle.

7.5.4 Internal Impedance

The internal impedance of the cell is made up of resistance, inductance, and capacitance. The resistance comes primarily from the electrodes and electrolyte, the inductance from the leads in and out of the cell, and the capacitance from the two electrode plates. The internal power loss during discharge or charge can be seen as having an internal resistance (R_i). The value of R_i depends on the battery capacity, operating temperature, and SOC. The higher the cell capacity, the larger the electrodes and the lower the internal resistance. The R_i varies with the SOC, and it also varies with temperature. For example, a 50 Ah NiH2 cell at 100% SOC has a Ri of 10 mΩ at −20°C, which drops to 2 mΩ at +20°C.

7.5.5 Self-Discharge

The battery slowly self-discharges even with no load under open circuit. This rate is usually much less than 1% per day for most electrochemistry in normal working conditions, but it significantly increases with temperature. The battery must be continuously trickle charged to counter the self-discharge rate in order to maintain its full SOC. After the battery is fully charged, the charge efficiency drops to zero. Any additional charge will be converted into heat. If overcharged at a higher rate than the self-discharge rate for a long time, the battery would overheat, posing a potential explosion hazard.

7.5.6 Self-Heating

When the battery is initially put to charge, the internal heat generation rate is negative for a while, meaning that the electrochemical reaction during the initial charging period is endothermic (absorbing heat). The reaction changes to an exothermic one and generates heat as the battery approaches full charge. The temperature rise during this phase depends on the cooling method used to dissipate the heat by conduction, convection, and radiation.

The internal power loss (in watts) causes self-heating in the battery. It has a major impact on the battery's temperature. During charge, it is equal to the sum of the heat generated by the charging of active materials and the heat generated by the overcharge reaction.

7.6 CYCLE LIFE

The battery gradually degrades in performance over time. In a degraded state with one cell dropping below, say, 2.5 V in a Li-ion battery, the rest of the cells providing voltage above 2.5 V may make up for the failed cell, and the battery as a whole may still provide the minimum required voltage. If the battery voltage falls below its required level at full load, it can still deliver the required voltage for a short time if the load can be shed to lower the DOD.

Unlike the Li-ion battery life discussed in Section 7.3.4, the end of cell life of NiCd and NiH_2 batteries for space applications was defined as one or more cell

voltages dropping below 1.0 V at any point during the C/D cycle, usually at the end of discharge. The cell can fail either randomly or due to wear. It can fail open, short, or somewhere in between (a soft short). A short that starts soft eventually develops into a hard short. In a low-voltage battery, any attempt to charge with a shorted cell may result in physical damage to the battery and/or the charge regulator. On the other hand, a shorted cell in a high-voltage battery with numerous series-connected cells may work for a long time. However, it loses the voltage and ampere-hour capacity and, hence, would work as a load on the healthy cells. An open cell, on the other hand, disables the entire string of series-connected cells.

A spacecraft battery rarely fails randomly. Its primary failure mode is associated with electrode wear due to repeated C/D cycles. The battery life is measured as the number of times it can be discharged and recharged before the electrodes wear out. Battery life depends to a lesser degree on electrolyte concentration, electrode porosity, and charge and discharge rates. The electrolyte concentration makes a significant difference in the cycle life of the NiH_2 cell. The battery life depends strongly on the electrochemistry, the DOD, and the temperature. According to historical data on numerous satellites flown in many decades past, the cycle life at 50% DOD for NiCd was 10,000 cycles at 0°C and 3000 cycles at 30°C. And for NiH_2 at 50% DOD, it was 30,000 cycles at 0°C and 9000 cycles at 30 C. This data falls on a straight line with cycles plotted on a log scale on the y-axis versus temperature on a linear scale on the y-axis. At 25% DOD, the life will approximately double at a given temperature for both electrochemistry.

It is noteworthy that the life at a given temperature is an inverse function of the DOD. If the life is 3000 cycles at 50% DOD, then it would be about 6000 cycles at 25% DOD. This makes the product of the cycles to failure and the DOD roughly constant in the first approximation. The following is then an approximate formula for the cycle life of a battery,

$$\text{Cycle life at } X\% \text{ DoD} = \text{Life at } 100\% \text{ DoD from vendor's data} \frac{100}{X\%} \tag{7.7}$$

The product of cycle life at the actual %DOD multiplied by the actual %DOD decreases with increasing temperature but is constant at a given temperature. Such is true for most electrochemistries. This means that the total watt-hour energy the battery can deliver over its life is roughly constant in the first approximation. The battery lasts proportionately more cycles if less energy is used in each cycle. Such an observation is useful in comparing the costs of various batteries for a given application at the conceptual design stage.

The battery does not work fully until it dies. Its capacity remains fairly constant until it rapidly fades at the end.

The number of C/D cycles in a satellite equals the number of eclipses during the mission's life. It is at least an order of magnitude greater on LEO satellites than in GEO. Such a long cycle life requirement in LEO can be achieved only by limiting the battery design to a low DOD, typically 30% compared to 80% in GEO satellites. Obviously, such a design requires a proportionately larger battery. A long cycle

life at a given DOD and operating temperature reduces the battery mass in direct proportion.

Since the battery cycle life is influenced primarily by the end-of-discharge DOD and temperature, the cell life prediction model is generally developed by fitting exponential curves to the test data on cycles to failure versus DOD at temperatures the battery would be subjected to the orbit. Factors such as the charge and discharge rate and the electrolyte concentration are not included in such a model but are factored into the cell life data by actual tests or from previous experience. A reliability model then incorporates the predicted cell wear-out life and the random failure rates to estimate the mean time before battery failure by taking into account the number of cells in series, the bypass diodes, and other components in the battery as a whole.

7.7 BURST POWER CAPABILITY

In fast discharge applications, such as for meeting a pulse power demand, the battery may be required to deliver the maximum possible power for a very short time. The peak power it can deliver can be derived using the maximum power transfer theorem in electrical circuits. It states that the maximum power can be transferred from the source to the load when the internal impedance of the source equals the conjugate of the load impedance. The battery can deliver maximum power to a dc load when $R_{\text{Load}} = R_i$. This gives

$$P_{\max} = \frac{E_i^2}{4R_i} \tag{7.8}$$

Since E_i and R_i vary with the SOC, the $P_{\max}$ also varies accordingly. The internal loss is I^2R_i, which is also equal to the $P_{\max}$ delivered to the load. The power transfer efficiency while delivering theoretically possible peak power is therefore only 50%. Such poor efficiency may not matter for delivering a short-duration peak load. Both NiCd and NiH_2 batteries are capable of following a pulse discharge and charging lasting a few milliseconds. The battery voltage follows the load variations as expected even under pulse loading. The power peaks with durations shorter than a few milliseconds primarily come from the capacitance between the electrode plates.

7.8 BATTERY DESIGN

The battery design starts with selecting the electrochemistry and the number of batteries based on the mission requirements and the heritage database. The following factors have a strong influence on the chemistry selection: (i) Specific energy and energy density, (ii) Cycle life and stability of capacity and voltage, (iii) Round-trip energy efficiency, (iv) Mass and volume constrain, (v) Temperature effects on the performance, (vi) Ampere-hour capacity ratings available, (vii) Ease and speed of recharging, (viii) Self-discharge rate, and (ix) Safety issues.

Regarding the number of batteries, all GEO satellites have traditionally used two batteries, each with one half of the total ampere-hour capacity needed to meet the energy demand during the worst-case eclipse. For small LEO satellites, one battery

can be advantageous. The mass and cost of one large battery are always less than those of two small batteries of half the capacity. On the business side, the customer generally has a strong preference, sometimes for documented or undocumented reasons, which is taken into account.

Once the chemistry and the number of batteries are settled, the battery design depends on the following system parameters:

- Bus voltage and load current
- Charge and discharge rates and duration
- Operating temperature during charge and discharge
- Life in terms of charge and discharge cycles

Life consideration is the dominant design driver in setting the battery ampere-hour ratings. Even when the load may be met with a smaller capacity, the battery is oversized to meet the cycle life requirement. For example, with the same watt-hour load, the battery that must deliver twice as many C/D cycles needs approximately double the capacity.

The battery design proceeds in the following steps:

- Determine the number of series cells required to meet the voltage requirement.
- Determine the ampere-hour discharge required to meet the load's current demand.
- For the required number of C/D cycles, determine the maximum allowable DOD.
- The total ampere-hour capacity of the battery is then determined by dividing the ampere-hour discharge required by the allowable DOD.
- Determine the number of battery packs required in parallel for the total ampere-hour capacity based on packaging and other considerations.
- Determine the temperature rise and the thermal control requirement.
- Determine the required charge and discharge rate controls.

The actual ampere-hour capacity of each battery at operating temperature is given by the following expression:

$$\mathrm{Ah}_b = \frac{P_e \cdot T_e}{N_b \cdot \eta_{dis} \cdot \left\{(N_c - 1)V_{cdis} - V_d - V_{hdis}\right\} \cdot \mathrm{DOD}} \tag{7.9}$$

where

Ah_b = capacity of each battery
P_e = load power demand during the eclipse
T_e = eclipse duration, in hours
N_b = number of batteries in parallel
η_{dis} = discharge converter efficiency
N_c = number of series cells per battery
V_d = voltage drop in the bypass diode in case a cell fails

V_{cdis} = voltage per cell, averaged during discharge
V_{hdis} = voltage drop in harness from battery to PRU
DOD = maximum allowable DOD in the worst-case eclipse

Equation 7.9 allows one cell failure in each battery for a single fault-tolerant design. There is generally one bypass diode in the charge path and three diodes in the discharge path to limit the leakage current. Without such bypass diodes, if one battery in a two-battery system fails, the power available to the payload is significantly reduced, and one arcjet for in-space propulsion would not work. The satellite must carry more fuel to compensate for this. Some customers may prefer relay switches to the bypass diodes to minimize the power loss.

The battery round-trip energy efficiency under the worst-case scenario with one cell failing is determined using the following expression:

$$\eta_b = \left[\frac{(N_c - 1)V_{cdis} - V_d - V_{hdis}}{(N_c - 1)V_{cchg} + 3V_d + V_{hchg}}\right] \cdot \left[\frac{\mathrm{AH}_{dis}}{\mathrm{AH}_{chg}}\right] \tag{7.10}$$

where

N_c = number of series cell, V_d = voltage drop in one diode
V_{cdis} and V_{cchg} = cell voltages during discharge and charge, respectively
V_{hdis} and V_{hchg} = voltage drop in harness during discharge and charge
AH_{dis} and AH_{chg} = ampere-hour discharged and charged, respectively.

There is a tradeoff in selecting the cell ampere-hour rating due to granularity issue. The tradeoff is between using more small-capacity cells, which give a voltage closer to the bus voltage, versus fewer large-capacity cells, which give a voltage lower than the bus voltage. The latter option requires greater buck and boost ratios in the battery regulators but saves mass and cost. Fewer, larger cells have lower mass and volume and higher reliability. In any case, the battery voltage is regulated by the duty ratio, and the regulator mass and efficiency do not change much with the battery voltage. A general guideline is to place cells in series to make the nominal battery voltage during discharge equal to about 80% and during charge equal to about 93% of the bus voltage. Even fewer cells may yield more savings as long as the buck and boost converter designs are not adversely impacted.

Other factors also enter the battery design, such as the end-of-charge and end-of-discharge voltages. The ampere-hour rating thus determined must be adjusted upwards if the battery voltage does not meet the bus voltage requirement, cannot be fully recharged after the deepest DOD, or the nominal eclipse starts from a partially drained battery in some orbits.

All series cells must have equal ampere-hour ratings within a few percent to avoid a cell voltage reversal leading to total battery failure. For this reason, cell selection is a critical acceptance test conducted at the vendor site. The cells are discharged to 1.0 V and the ampere-hour output measured at room temperature to match the nameplate capacity. All cells within ±3%–5% capacity variations around the average are selected for assembly in the flight battery. Since the actual battery capacity is

the capacity of the weakest link, it is taken as the average cell capacity less 3%–5%. Battery cells are also selected based on the cell voltage variance. One may consider the magnetic signature method to gage the internal details. Only stabilized cells are included in the selection. The full SOC pressure in NiH_2 cells is significantly low when new but stabilizes after a number of C/D cycles.

7.9 LAUNCH AND ASCENT POWER

Generally, the battery is designed to meet the on-orbit load and energy balance. The same battery is also used for the spacecraft's power needs during launch and ascent phases. Several possibilities that may arise during this time are dealt with in the following manner:

Case A: The battery fully charged at the time of launch is sufficient for the launch/ascent energy requirements. This is usually the case on most satellites and does not require any extra steps for the power system engineer.

Case B: The battery fully charged at the time of launch is slightly short of the launch/ascent energy needs. In this case, a widely practiced solution is to pre-cool the battery with cold air or nitrogen before the launch to increase the battery capacity by several percent or more as needed.

Case C: The launch/ascent power demand exceeds the battery capacity beyond the case B remedy. Increasing the on-board battery capacity, even in such a rare case, is almost never done because it is very expensive. Instead, a primary battery with high specific energy is used to meet the shortage. This battery is jettisoned after the ascent.

7.10 CHARGE REGULATION

From a safety perspective, it is important that excessive charging of the battery be avoided at all times. Overcharging causes internal gassing in all electro-chemistries in varying degrees, which causes loss of electrolyte in the vented cell and premature aging. The charge regulator allows the maximum rate of charging until the gassing starts. Then the charge current is tapered off to a trickle charge rate so that the full charge is approached gently.

During battery charging, the energy management software monitors the SOC, the overall health, and the safe termination criteria. The operating voltage, the current, and the temperature are monitored. The charging timer is started after all initial checks are successfully completed. Charging may be suspended (but not reset) if the software detects a violation of critical safety criteria. The timer stops charging if the defect persists beyond a certain time limit.

Normal charging has the following three phases:

- Bulk (fast) charge, which deposits 80%–90% of the drained capacity
- Taper (cut-back) charge, in which the charge rate is gradually cut back to top off the remaining capacity
- Trickle (float) charge to counter the self-discharge rate after the battery is fully charged

The bulk charge and the taper charge termination criteria are pre-loaded in the battery management software to match the battery electrochemistry and the system design parameters. For example, the NiCd and NiMH batteries are generally charged at constant current until about 95% SOC in 75%–85% of the available sun time. Then onward, the charge current is tapered off—gradually or in a few steps—to the trickle rate, as shown in Figure 7.6. The decision is made to terminate the main charging and switch to trickle charging when the continuously monitored ΔV is detected as negative. On the other hand, Li-ion batteries, being sensitive to overcharging, can be charged at a constant voltage, tapering off the charge current as needed.

Both NiCd and NiH_2 batteries show voltage roll-off and sudden temperature rise, i.e., negative dV/dt and positive dT/dt, soon after the full charge (Figure 7.7). Both of these characteristics are used to detect the end of a charge. In NiCd and NiH_2, the voltage roll-off is 20–30 mV per cell. In NiMH, on the other hand, the ΔV is much smaller (3–5 mV per cell) and the temperature rises steadily to the final value, making the end-of-charge detection difficult. The rollover is attributed to the voltage decrease subsequent to the temperature increase that results from the oxygen reaction with hydrogen. In some electrochemistries, the voltage rollover is distinct; in others, it is rather flat. When the cells are overcharged at −20°C, the voltage rollover shows waviness with a smaller hump followed by a larger hump.

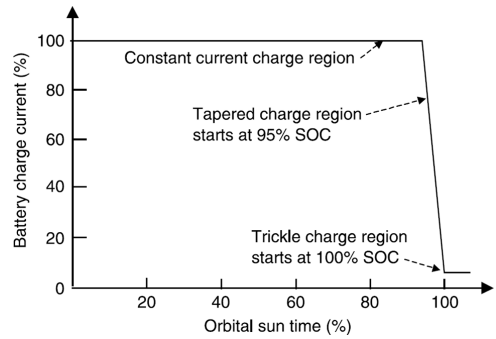

FIGURE 7.6 Battery charge profile versus orbital sun time.

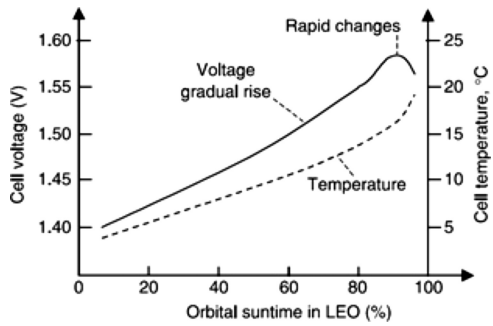

FIGURE 7.7 Battery voltage and temperature during charge, showing rapid changes at the end of charge.

The rapid reaction of oxygen with hydrogen during overcharge is an undesirable feature that causes an audible popping noise in certain cases. Popping results in the melting of the gas screen pinholes in the negative plates and heat stains in the core and the positive plate. In extreme cases, popping blows away the separator, resulting in shorts. Cells with significant positive plate swelling are prone to popping, which results in damage to the components. Swelling also causes extrusion of active material and a reduction in the gap between the two positive plates. The final result is a decrease in the discharge voltage. Positive plates that show excessive swelling absorb more electrolytes. This is accompanied by a reduced absorption of electrolyte by the separator.

The batteries are charged in one of the following three ways using the voltage-limited tapered-current method or the constant-current ampere-hour return method.

7.10.1 Multiple Charge Rates

This is the best method, in which the battery is charged gently in multiple steps. First, the battery is charged at its full charge rate until 80%–90% of its capacity is achieved. The charge current is then cut back in steps until the battery is fully charged. At this time, the charge current is further reduced to a trickle-charge rate, keeping the battery fully charged until the next load demand comes on the battery. This method therefore needs at least three charge rates in the charge regulator design.

7.10.2 Single Charge Rate

This method uses a simple, low-cost regulator that is either on or off. The regulator is designed for only one charge rate. When the battery is fully charged, as measured by its terminal voltage, the charger is turned off by a relay. When the battery voltage drops below a preset value, the charger is again connected in full force. Since the charging is not gentle in this method, a full charge is difficult to achieve and maintain. An alternate version of this charging method is multiple-pulse charging. Full current charges the battery up to the high preset voltage, just below the gassing threshold. At this time, the charger is shut off for a short time to allow the battery chemicals to mix and the voltage to fall. When the voltage falls below the low preset threshold, the charger is reconnected, again passing full current to the battery.

7.10.3 Unregulated Charging

This is the least-cost method because it uses no charge regulator. The battery is charged directly from a solar array module dedicated just to charging. The charging module is properly designed for safe operation with the given number of cells in the battery. When the battery is fully charged, the array is fully shunted to ground by a shorting switch (transistor). At this time, the battery voltage must still be slightly lower than the available solar array voltage so that the trickle charge can continue, but not much lower to avoid overcharging. The shunt transistor switch is opened when the battery voltage drops below a certain value. An isolation diode would block the battery powering the array or the shunt at night.

If one cell in one of the two batteries working in parallel fails, the two batteries will have different terminal characteristics. Charging or discharging such batteries in parallel can result in highly uneven current sharing, subsequently overheating one of the batteries. This can be avoided in two ways. One is to charge and discharge both batteries with individual current controls such that they both draw their rated share of the load. The other is to replace the failed cell immediately, which is not possible in space. In general, individual C/D control for each battery is the best strategy. It may also allow the replacement of any one battery with different electrochemistry or a different age, which would have different load-sharing characteristics. The ISS batteries are designed to be replaced several times during the life of the station.

The Li-ion battery requires additional circuitry for balancing individual cells to obtain maximum performance from the battery. The balancing method can vary from design to design. One method is to use dc-dc converters with a multitap transformer to provide energy equilibrium in each cell. Another method is to use a capacitor-switching technique called a flying capacitor, which shifts small packets of energy from higher-voltage cells to lower-voltage cells. Saft Corporation has often used a resistive dissipation method that lowers the SOC of the highest cells to match the lowest common denominator cell. Sack, Croydon, and Reynolds[2] report yet another method using segmented chargers. In this concept, the battery charger is broken up into separate cell chargers. The concept was tested on a 26 V, 45 Ah Li-ion battery under U.S. Army funding.

7.11 BATTERY MANAGEMENT

Battery management electronics include the battery monitor and controller. The main function is to monitor the battery status and optimize its performance by adjusting the charging process. Electronic circuits monitor the battery voltage, current, SOC, and temperature. If not managed properly, the battery's performance could suffer and its life could be shortened. The following are some potential performance problems:

- Low charge efficiency results in a low SOC
- Loss of capacity to hold the rated ampere-hour charge
- Premature failure leading to loss of load availability
- Excessive gassing and heating, leading to a short life
- Positive plate corrosion shortens the life
- Stratification and sulfation degrade performance

The following features incorporated into battery management can avoid the above problems:

- Temperature-compensated charging means that the charge termination occurs earlier if the battery temperature is higher than the reference temperature
- Individual charge control is required if two or more batteries are charged in parallel
- Accurate set points to start and stop the charge and discharge modes

The batteries in modern power systems are managed by dedicated computer software, which monitors and controls the following performance parameters:

- Voltage and current
- Temperature and pressure
- Ampere-hours in and out of the battery
- SOC and discharge
- Rate of charge and discharge
- Depth of discharge
- Number of charge and discharge cycles

The above parameters are determined by a number of measurements and limits, which include the following:

- Minimum charging current threshold
- Terminal voltage threshold
- Absolute temperature cut-off
- Rate of temperature change $\Delta T/\Delta t$
- Drop of the cell voltage after the peak ΔV
- Rate of voltage change ($\Delta V/\Delta t$), including the peak and the inflection
- Actual charging time

The ampere-hour integrating meter is commercially available and keeps track of the ampere-hours in and out of the battery and sends the required signals to the mode controller.

With age, NiCd and NiH_2 batteries experience declines in capacity, voltage, and end-of-charge pressure. These are accounted for by shifting the software on board. The cell voltage divergence is another concern, more so after reconditioning. One method of avoiding it is to overcharge so that all cells saturate to full voltage, provided the thermal system can handle the associated heating.

The temperature compensation of the maximum battery voltage and the SOC can improve battery management, particularly when cold. It can allow additional charging during cold periods when the battery can accept more charge. The low voltage alert is a good feature, as excessive discharging below the threshold low voltage can cause cell voltage reversal, leading to battery failure. The alert can be used to shed noncritical loads from the battery to avoid battery damage. The battery cell voltage monitor allows a comprehensive health check of the total battery. This is important just before launching, when a problem can be fixed. A 22-cell voltage monitor adds less than 200–300 g but adds much more in numerous telemetry wires.

7.12 DYNAMIC MODEL

The term impedance refers to the ratio of the cell voltage change to the corresponding change in the alternating current through the cell. It is given by

$$Z = \sqrt{R^2 + X^2} \tag{7.11}$$

where R and X are the battery resistance and reactance, respectively. The dynamic impedance characteristics discussed in this section are applicable to all electrochemistries. They apply at a given SOC, i.e., when net dc current flow or energy conversion is not involved. The internal impedance determines the battery's response to ripple, noise, and transients during charging and discharging. It varies inversely with the capacity, as large-capacity cells have a large plate area. For example, the impedance versus frequency of a 50 Ah NiH_2 cell is shown in Figure 7.8. It has a relatively constant value up to 10 Hz but rises rapidly at higher frequencies, indicating a strong inductive component. The battery values R and X are obtained by multiplying the cell values by the number of series cells in the battery. A simple dynamic model of the battery for stability analysis with the dynamic impedance $Z(s)$ in the Laplace domain is shown in Figure 7.9.

Complex battery models developed by electrochemists are not expressed in terms of electromotive force, resistance, inductance, or capacitance. Therefore, they are unsuitable for everyday use by the electrical engineer, who needs a model that represents the electrochemistry in electrical network terms. Ceraola[3] has developed a model to represent the battery's nonlinear behavior using the two electrical branches

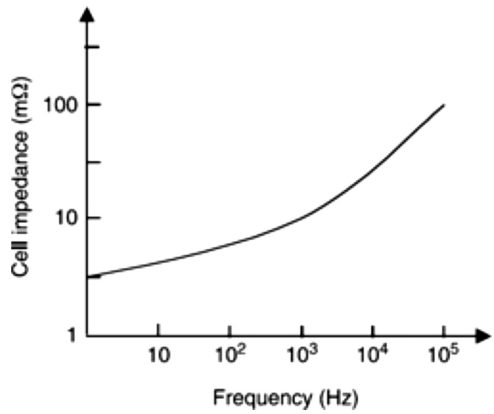

FIGURE 7.8 50 Ah NiH_2 cell impedance versus frequency.

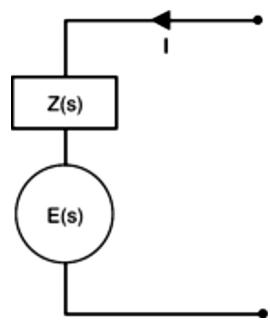

FIGURE 7.9 A simple dynamic electrical circuit model of the battery.

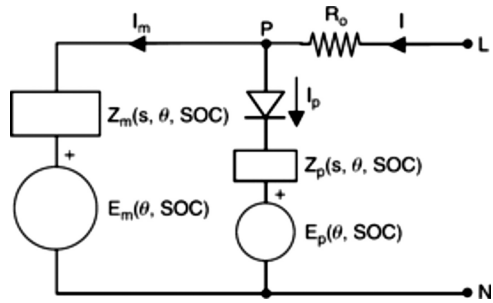

FIGURE 7.10 Dynamic circuit model of battery with main and parasitic reaction branches.

shown in Figure 7.10. The main branch is designated with the subscript m and the parasitic branch with the subscript *p*. The E_m and Z_m are the internal electromotive force and the internal impedance, respectively. Both are functions of the Laplace parameters, the electrolyte temperature, θ, and the SOC. The parasitic branch models the nonreversible reactions that draw some current but do not contribute to the main reversible reaction. The energy that is absorbed by E_p ceases to be electrical and is converted into other forms, such as gas or water electrolysis, which occurs at the end of the charge process. The power dissipated in the real parts of Z_m and Z_p is converted into heat that contributes to the self-heating of the battery. The R_o is common to both branches and represents resistance from the battery terminals to the plates.

To make such a model useful, one needs to determine the functional dependence of *E* and *Z* on *s, θ*, and SOC and the battery thermal model from which the electrolyte temperature can be determined. The dependence on *s* can be stated by expressing each *Z* in terms of the equivalent *R, L*, and *C* values. The model can be simplified for a specific operating condition, if known. For example, the parasitic branch can be ignored in the initial charging phase when the charge efficiency is near unity. At the end of a charge, however, almost all power enters the battery terminals. Since the inductance is small and can be ignored, the battery model that is valid during both the charge and discharge is shown in Figure 7.11.

The battery capacity is maximum at a certain optimum temperature and falls off on both sides of the optimum temperature. If the battery is maintained on the cooler side of the optimum temperature, the capacity at a constant discharge current and

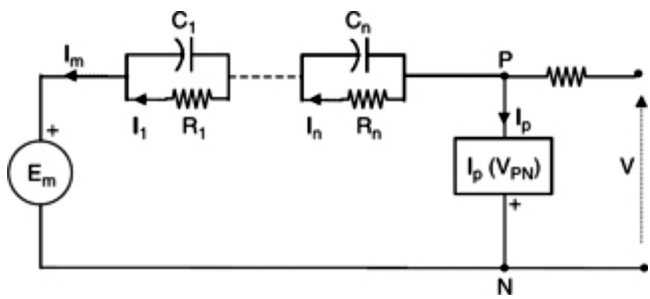

FIGURE 7.11 Dynamic circuit model of the battery during charge and discharge.

a constant electrolyte temperature is higher with a higher temperature and a lower discharge current. At a fixed discharge current, I, and temperature, θ, the capacity can be expressed as[3]

$$\mathrm{Ah}(I,\theta) = \mathrm{Ah}_o(I)\left\{1-\frac{\theta}{\theta_f}\right\}^{\alpha} \tag{7.12}$$

where Ah_o = battery capacity at 0°C at discharge current I, α = empirical constant, and $\theta > \theta_f$, the freezing temperature of the electrolyte (such as −40°C). Equation (7.12) gives the expected value of Ah = 0 at freezing temperature when the battery becomes inoperative. It is possible that $\mathrm{Ah}_o(I)$ can be expressed in terms of its value at a reference temperature I_r and empirical constants K and β as follows:

$$\mathrm{Ah}(I,\theta) = \frac{K\mathrm{Ah}_o(I_r)\left\{1-\dfrac{\theta}{\theta_f}\right\}^{\alpha}}{1+(K-1)\left\{\dfrac{I}{I_r}\right\}^{\beta}} \tag{7.13}$$

Equation (7.13) suggests that numerical values of the elements of the circuit model have to be established for each value of electrolyte temperature and SOC. In practice, they can be established only for a few discrete values of these two quantities, and the values in between can be obtained by interpolation. Determination of such parameters for the first time would require extensive analysis and testing efforts. However, having made that investment, the model for a new battery can be established by using previous data on similar batteries suitably modified for the new battery.

7.13 BATTERY CYCLE LIFE MODEL

As previously stated, the battery cycle life is related primarily to the DOD and the operating temperature. The life relationship can be expressed in terms of C/D cycles as the dependent variable, with DOD and temperature as the independent variables. In developing a statistical model for battery life, we must first select a mathematical expression that adequately defines the relationship, and then select a statistical distribution that best fits the test data. The selections can be guided by consideration of the physical behavior of the battery. For example, the number of cycles to failure decreases with increasing DOD and temperature. Various types of relationships commonly used for analyzing life test data can be considered to express such relationships. Among the alternatives, such as exponential, inverse power, and Arrhenius, more than one can give a reasonably good fit to the test data. However, the relationship that generally gives the best fit in similar life test data is the Arrhenius equation, which accounts for the chemical degradation limiting life.[4,5] That is

$$L = C_1 T^{-C_2} \cdot e^{-C_3 D} \tag{7.14}$$

where L = mean number of cycles to the first failure, T = temperature in °C, D = DOD in each cycle, and C_1, C_2, and C_3 are the relationship constants to be determined by multiple regression curve fitting techniques.

Based on the physical considerations of the wear-out mode of failure being studied, the statistical distribution selected to represent the spread of life around the mean value derived from Equation (7.14) at a given temperature and DOD should have a continuously increasing hazard function. The hazard function is a conditional failure rate, which expresses the rate of failure for the surviving population at a given number of cycles L. Also, the distribution should have good flexibility to fit the data. Two distributions that can satisfy these requirements are lognormal and Weibull. The Weibull distribution is the most commonly used for the presentation of such life test data. It is given by

$$F(L) = 1 - e^{\left(\frac{L}{\alpha}\right)^{\beta}} \tag{7.15}$$

where $F(L)$ is the fraction of the population failing by L cycles, and positive parameters α and β are scale and shape parameters, respectively. The parameter β can be assumed to be constant, while 1α is a function of temperature and DOD. The values of both α and β are derived from test data. The curve fitting can be a simple procedure using least squares regression techniques if the failure times of all samples are known. However, in typical situations, the battery test data includes samples (i) that are known to have failed during an interval rather than at a specific time, and (ii) that have not yet failed at the end of the test period. Such censored data can only be analyzed by statistical techniques developed for dealing with incomplete life test data.[6,7] They use the method of maximum likelihood, which involves selecting as an estimate for each unknown parameter the value that appears to be most probable on the basis of the given test data. The computations are based on the sample log likelihood, which is a function of the unknown model coefficients (C_1, C_2, and C_3). The estimates of the coefficients are obtained numerically by iterative methods on a computer, and the variances of these estimates are used to obtain approximate confidence intervals.

When the indicated analysis is performed on a set of test data, the expected life relationships are derived with their coefficients C_1, C_2, and C_3. Estimating the life from such considerations can be relatively less complex if the battery is used in an identical manner in each cycle over the mission's life. It becomes more complex when it is used in one way sometimes and another way at other times, with significant variation in the usage patterns. In such cases, the life may be estimated using the *Milner's cumulative damage theory*[8,9] often used in fracture mechanics and fatigue studies on metals and other materials. The theory utilizes the cycle ratio as its basic measure of damage. For the battery life with two independent variables, as shown in Figure 7.12, it can be modified as follows. If a battery temperature is T_i at DOD D_i for C_i number of cycles, and if the life relationship estimates L_i cycles as its life at T_i and D_i, then the proportional damage, PD_i, caused during that time is

$$PD_i = \left\{\frac{C_i(T_i, D_i)}{L_i(T_i, D_i)}\right\}^{\alpha} \tag{7.16}$$

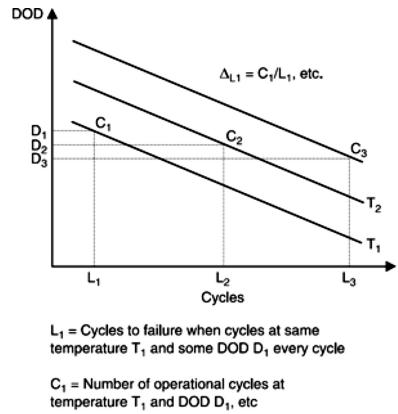

FIGURE 7.12 Life model for cycles to failure versus DOD and temperature.

where α is a positive constant to be evaluated from correlating available life data and experience. The battery can be expected to fail when the cumulative damage equals unity (i.e., when $\sum PD_i = 1.0$). The evaluation of the exponent α requires extensive data from batteries, which are much closer in scale factor to the actual battery to be modeled.

The theory keeps an incremental account of the fraction of life depleted during each segment of time, depending on the life degradation factors prevailing over that duration of use. It can be used to estimate the remaining life, i.e.,

$$\text{remaining life} = 1 - \sum PD_i \tag{7.17}$$

Milner's cumulative damage theory suggests the following for use with some judgment and experience:

- The battery life ends when the sum total of the accumulated proportional damage reaches its limiting value of 1.0.
- A short time at high wear depletes the same fraction of life as a long time at low wear.

Although the life model presented in this section could not justify direct use of life relationships in this fashion at present, it can be regarded as a potential future application. It is hoped that the theoretical considerations proposed here may serve as a guide to defining, planning and analyzing future research in this field.

7.14 ALTERNATIVE ENERGY STORAGE

Many nonlinarites in the electrochemical battery performance make the battery design a complex and tedious process. Two alternatives to batteries with many desirable performance features are:

Flywheel energy storage: The flywheel option was fully developed, with a prototype built and successfully tested by NASA Glenn Research Center to replace the ISS batteries, but it did not make the final cut.

Superconducting Coil: The superconductor energy storage technology is fully developed and used in many applications on earth, and may be suitable in space due to its naturally cool environment. Patel[10] gives further details in the first edition of this book.

REFERENCES

1. Bruce, G. and Marcoux, L., Large lithium-ion batteries for aerospace and aircraft applications, *IEEE AESS Systems Magazine*, 16(9), 24–28, 2001.
2. Sack, T.T., Croydon, T., and Reynold, R., Segmented battery charger for high density 28-V lithium ion battery, *IEEE AESS Systems Magazine*, 16(9), 15–18, 2001.
3. Ceraolo, P., Dynamic model of the electrochemical battery, in *Proceedings of the 36th Intersociety Energy Conversion Engineering Conference*, ASME, 2001, Paper No. X001.
4. Hahn, G.J. and Shapiro, S.S., *Statistical Models in Engineering*, John Wiley & Sons, New York, 1967.
5. Kendall, M.G. and Stuart, A., *Advanced Theory of Statistics*, Vol. 2, Hafner Publishing Co, New York, 1961.
6. Hahn, G.J. and Nelson, H.B., A comparison of methods for analyzing censored life data to estimate relationship between stress and product life, *IEEE Transactions on Reliability*, R-23, 2–10, April 1974.
7. Nelson, W., A survey of methods for planning and analyzing accelerated tests, *IEEE Transactions on Electrical Insulation*, El-9, 12–18, March 1974.
8. Miner, M.A., Cumulative damage in fatigue, *Journal of Applied Mechanics*, 12, A159–164, 1945.
9. Madayag, A.F., *Metal Fatigue - Theory and Design*, John Wiley and Sons, New York, 1969, pp. 170–203.
10. Patel, M.R., *Spacecraft Power Systems*, 1st Edition, Chapter 26, Superconductors in Space. CRC Press, Boca Raton, FL, 2004.

FURTHER READINGS

Britton, D.L., Progress in the development of lightweight nickel electrode for NiH_2 cell, in *Proceedings of the 34th Intersociety Energy Conversion Engineering Conference*, SAE, 1999, Paper No. 2537.

Brown, R., Nickel hydrogen life modeling, in *Proceedings of the 35th Intersociety Energy Conversion Engineering Conference*, AIAA, 2000, Paper No. 2991.

Croft, H., Staniewicz, R., Smart, M.C., and Ratnakumar, B.V., Cycling and low temperature performance operation of Li-ion cells, in *Proceedings of the 35th Intersociety Energy Conversion Engineering Conference*, AIAA, 2000, Paper No. 27-AP-B1.

Fellner, J.P. and Loeber, G.J., Li-ion performance testing and ac impedance characterization, In *Proceedings of the 34th Intersociety Energy Conversion Engineering Conference*, SAE, 1999, Paper No. 2591.

Garner, J.C., Braun, W.R., Loo, D.V., and Bowers, D., 90-Ah dependent pressure vessel NiH_2 battery, in *Proceedings of the 34th Intersociety Energy Conversion Engineering Conference*, SAE, 1999, Paper No. 2590.

Govar, C.J. and Squires, T.L, "Safety tests of lithium 9-volts batteries for navy applications, *IEEE AESS Systems Magazine*, 16(9), 34–37, 2001.

Gross, O., Fox, C., Roller, D., and Shimanek, L., Lithium-ion polymer batteries for space applications, in *Proceedings of the 36th Intersociety Energy Conversion Engineering Conference*, ASME, 2001, pp. 61–68.

Parez, M.E., et al., Energy storage for space applications, in *Proceedings of the 36th Intersociety Energy Conversion Engineering Conference*, ASME, 2001, pp. 85–89.

Patel, M.R., *Spacecraft Power Systems*, 1st Edition, Chapter 25, Flywheel Energy Storage. CRC Press, Boca Raton, FL, 2004.

Pickett, D.F., Hayden, J.W., Lucero, D., and Johnson, Z., Comparison of advanced NiCd space cell technology with other technologies in consideration for LEO and GEO orbit and planetary missions, in *Proceedings of the 35th Intersociety Energy Conversion Engineering Conference*, AIAA, 2000, Paper No. 2989.

Puglia, F., Gitzendaner, R., Ehrlich, G.M., and Marsh, C., Advancing Li-ion technology for aerospace applications, in *Proceedings of the 34th Intersociety Energy Conversion Engineering Conference*, SAE, 1999, Paper No. 2637.

Rao, G.M., Ahmad, A., and Chetty, P.K.R., Super nickel cadmium battery operation and performance on-board the Sampex spacecraft, in *Proceedings of the 30th Intersociety Energy Conversion Engineering Conference*, Vol. I, ASME, 1995, pp. 111–116.

Smith, R. and Brill, J., Updated life cycle test results for flight qualified NiH_2 cell design, In *Proceedings of the 36th Intersociety Energy Conversion Engineering Conference*, ASME, 2001, pp. 55–59.

8 Power Electronics

8.1 INTRODUCTION

Having advanced over the decades, power electronics play a vital role in spacecraft power systems to control, manage, and provide flexibility to voltages and currents in optimizing system-level power generation and utilization. This includes, but is not limited to, the bus voltage, dc–dc converters for photovoltaic solar and battery power, dc–dc converters for all loads, dc-ac inverters, and other converters. The control functions are performed by solid-state semiconductor devices used as controlled switches, which are turned on and off at high frequencies. Capacitors and inductors are used to store energy when the switch is connected to the power source. The stored energy is then discharged to continue powering the load when the switch is off. Transformers are used where needed for stepping up or down the voltage and/or for isolation.

8.2 SWITCHING DEVICES

Different solid-state devices are commercially available for use as controlled switches. However, the devices commonly used in space are metal-oxide semiconducting field effect transistor (MOSFET) and insulated gate bipolar transistor (IGBT). The device selection depends on the required voltage, current, and switching frequency. A common feature among these devices is that they are all three-terminal devices. Their generally used circuit symbols are shown in Figure 8.1. The two power terminals 1 and 0 are connected to the main power circuit. The control gate terminal G is

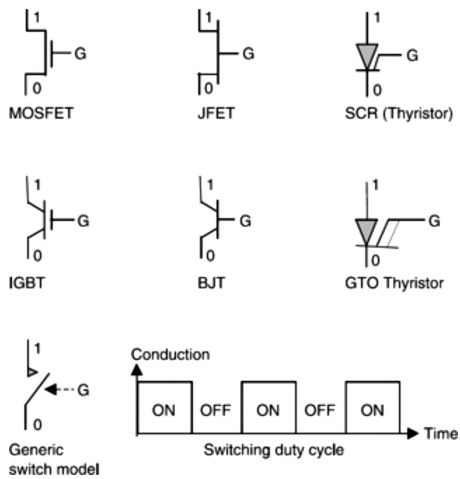

FIGURE 8.1 Semiconductor switching devices used in space.

DOI: 10.1201/9781003344605-10

connected to the auxiliary control circuit. In normal conducting operation, terminal 1 is generally at a higher voltage than terminal 0. Since the device is primarily used for switching power on and off as required, it is functionally represented by a gate-controlled switch. In the absence of the gate control signal, the device resistance between the power terminals is large—the functional equivalent of an open switch. When the control signal is applied at the gate, the device resistance approaches zero, making the device function like a closed switch.

The switch is triggered periodically on and off by a train of gate signals of suitable frequency. A sharp gate signal of rectangular, triangular, or saw-tooth wave shape without overshoot or ringing is generated by a separate triggering (firing) circuit. The gate circuit for the MOSFET is simpler than that for the bipolar transistor. Although the control circuit has a distinct identity and many different design features, it is often incorporated into the main power electronic component assembly. The transistor switch is turned on and off at a high frequency, typically 50–200 kHz and sometimes higher. The duty ratio, D, of the switch is defined as:

$$D = \frac{\text{Time on}}{\text{Period}} = \frac{T_{\text{on}}}{T} = T_{\text{on}} \cdot \text{switching frequency} \tag{8.1}$$

8.3 SHUNT REGULATOR

The power output of the solar array during sunlight normally exceeds the load plus the battery charge requirements, more so at the beginning of life. The excess power may be diverted (shunted) from feeding into the bus in order to control the bus voltage. The shunt load can be a dump resistor, which would convert the solar array power into heat. Such heat dissipation in the spacecraft body would pose a burden on the thermal system to provide adequate cooling. An alternative commonly used on spacecraft is to shunt some of the solar array strings to the ground. This forces the string to operate under a short-circuit condition, delivering I_{sc} at zero voltage. In this mode, i.e., the shunt mode, no power is delivered to the load or to the ground. The photon energy remains on the array, raising the array temperature and ultimately dissipating the excess power into space. The solar array is essentially used here as the thermal dissipator.

Another application of the shunt regulator is in a small dedicated solar array module used to directly charge the battery without a battery charge regulator. When the battery is fully charged, the solar array module is shunted to ground by shorting the switch. This way, the battery is protected from overcharging.

Figure 8.2 depicts a typical shunt regulator where a transistor is used as the switch. When excess power is available, the bus voltage rises above the rated value. This is taken as a signal to turn on the shunt switch across the required number of solar array strings. Thus, the shunt is turned on or off by a transistor controlled by the bus voltage reference. For an array with many strings in parallel, the basic configuration shown in Figure 8.2 is used for each string separately. The same gate signal is supplied to all modules simultaneously in small power applications. For shunting large power, multiple shunt circuits are switched on and off in sequence to minimize the

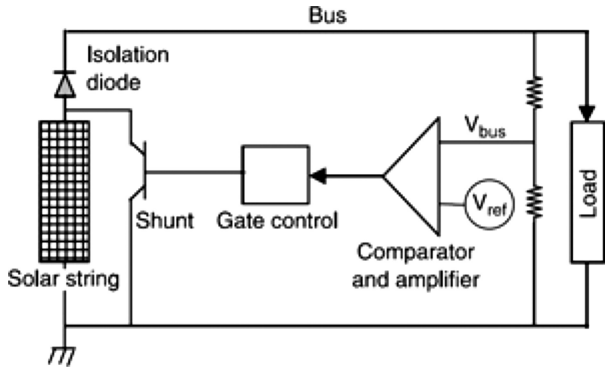

FIGURE 8.2 Full shunt regulator for bus voltage control.

switching transients and the resulting electromagnetic interference to the neighboring equipment. For fine voltage control, the last shunt to turn on is operated in pulse width modulation (PWM) mode, while all others are fully on or off. The constructional and performance features of various shunt circuits are described below.

8.3.1 Full and Partial Shunts

Figure 8.2 shows the schematic of a full shunt, where the whole string of the solar array is controlled *on, off, or in between*. Figure 8.3a shows a partial shunt, where the shunt switch controls a part of the solar string. Only the lower part of the string is shunted when required. When the shunt is on, its operation is depicted in Figure 8.3b on the *I–V* characteristic of the string. The lower section thus works like a current source, whereas the upper part works like a voltage source. The unshunted and

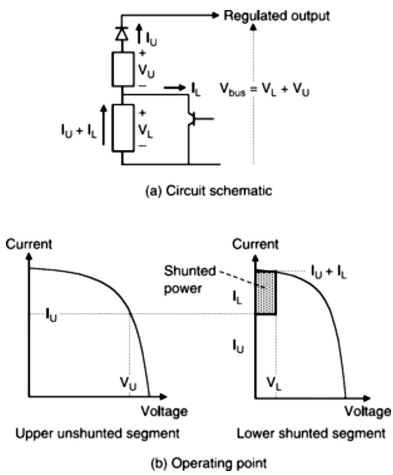

FIGURE 8.3 A partial shunt regulator with the upper segment unshunted and the lower segment shunted. (a) Circuit schematic. (b) Operating point.

shunted sections of the string are mismatched. The mismatch thus created reduces the power fed to the bus by operating away from the maximum power point, leaving some of the solar power on the array, where it appears as heat and is radiated back into space. A small percentage of power is dissipated as heat in the shunt. Since the shunting occurs only when excess power is available, the increased solar array temperature and the resulting decrease in photovoltaic conversion efficiency have no impact on the power system's performance. In the partial shunt scheme, the shunt transistor can be located on the back of the solar array, which enables easy heat dissipation into space. However, this requires more signal sliprings than power sliprings, and the shunt transistor has to withstand the wide temperature excursion cycles of the eclipse and sunlight.

The tap voltage of the lower segment, V_L = full string voltage − upper string voltage = $V_{sa} - V_U$. The value of V_L is typically 15 V in a 22 to 35 V sun-regulated bus. The shaded area in Figure 8.3b represents the shunted power. Quantitatively, it is equal to the product of the voltage and current in the lower shunted segments of the string, i.e.,

$$P_{\text{shunt}} = V_L I_L \tag{8.2}$$

Partial shunts have been used in many satellites in the past but have fallen out of favor in modern high-power satellites, which generally use full shunts. Both the full and partial shunts can be any one of the following types.

8.3.2 Linear and PWM Shunts

Figure 8.4 shows the schematic of a linear shunt. In configuration (a) without a series resistor, the gate current drives the shunt switch in the unsaturated region when the bus voltage exceeds the reference value. In this region of operation, the switch offers a variable resistance depending on the gate current. The string power is partially shunted to the ground, and the remaining power feeds the bus. If needed, an additional fixed resistance can be added, as shown in (b). A disadvantage of the linear shunt with resistor is that a part of the solar power is converted into heat in the resistor, which must be dissipated into space by the thermal system. For this reason, the resistor is seldom used in large satellites. The linear shunt without resistor physically located on the array keeps the unwanted power on the array for dissipation to outer space, thus minimizing the sliprings, thermal management, and electromagnetic interference (EMI)-related costs.

Another alternative is to use the switch-mode pulse width modulated (PWM) shunt shown in Figure 8.5. This scheme is used on most modern high-power spacecraft. Instead of operating the linear shunt in the unsaturated region, the PWM shunt is operated in the off or all the way on (saturated) state when the bus voltage exceeds the reference value. The on and off durations are repeated at high switching frequencies with a controlled duty ratio. This eliminates the power dissipation from liner shunts. The string power fed to the bus equals the whole string power times the duty ratio. The duty ratio is adjusted to keep the bus voltage in a narrow range around the reference value. A disadvantage of the PWM shunt is that it switches full current at high frequency, causing EMI on the platform. However, the PWM shunt is widely

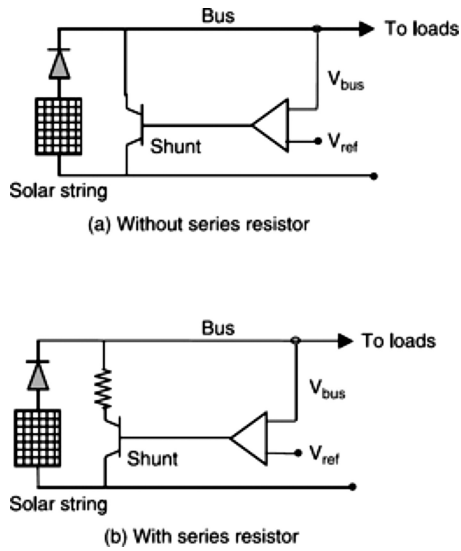

FIGURE 8.4 Linear shunt regulator. (a) Without a series resistor. (b) With a series resistor.

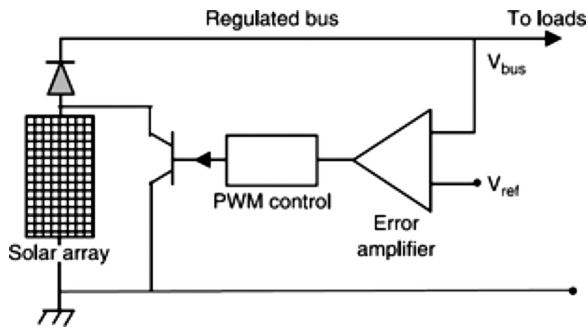

FIGURE 8.5 Pulse width modulated (PWM) shunt regulator.

used for its many benefits. On the other hand, the linear shunt is still used where EMI cannot be tolerated or where heat is needed to maintain temperature inside the spacecraft body.

8.3.3 Sequential Linear Shunt

When more than one string is required to be shunted, the one-string linear shunt shown in Figure 8.4a is used as the building block to build the array shunt circuit shown in Figure 8.6. When the solar output power exceeds requirements, the shunt drive controller first raises the gate current of shunt 1 from zero to a value that can maintain the bus voltage at the reference value. In doing so, if shunt-1 current reaches saturation level, shunt-2 is gradually turned on. If more shunting is still needed, the

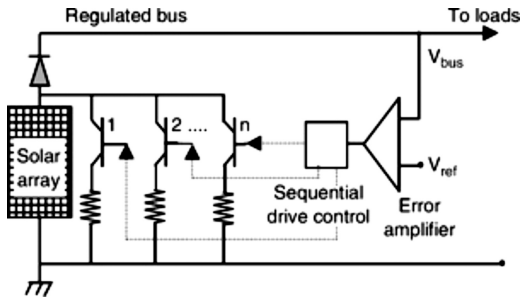

FIGURE 8.6 Sequential linear shunt regulator.

controller may reach the *n*th shunt until the bus voltage is maintained at the set level. Turning on the shunt switches is done in sequence.

8.3.4 Multistage PWM Shunt

Multiple solar strings are generally needed to shunt the excess power, particularly at the beginning of life. The shunt circuit using multiple PWM shunts is shown in Figure 8.7. The bus voltage is controlled by first placing one string in the PWM. The duty ratio controls the power shift. If more power needs to be shunted, the duty ratio of the first string is raised. After reaching the duty ratio limit of the first string, the second string is placed under the PWM, and so on. At the end, all shunts are in PWM mode, switching the power on and off simultaneously. This may create an EMI problem around the shunts. The EMI is minimized by designing the PWM control circuit to have a maximum duty ratio of 1. That way, all but one shunt are operated continuously in the saturated state, and only the last one is operated in PWM mode to shunt a fraction of power on or off at a time.

8.3.5 Polyphase PWM Shunt

In this scheme, the multistage PWM shunt schematic shown in Figure 8.7 remains the same, but the PWM modulation control is modified to operate simultaneously on as many strings as needed for the bus voltage control. The difference here is that

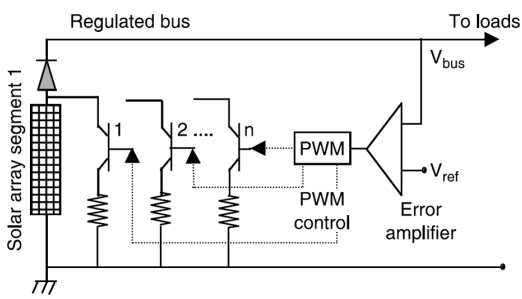

FIGURE 8.7 Multistage pulse width modulation shunt regulator.

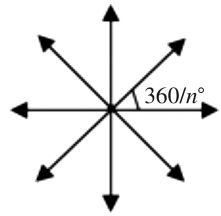

FIGURE 8.8 Polyphase pulse width modulation gate signals with 360/n° phase difference.

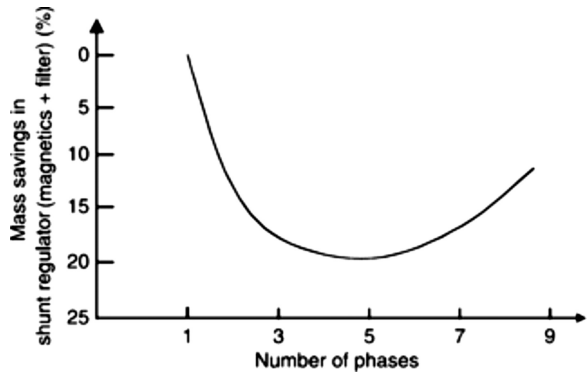

FIGURE 8.9 Shunt regulator mass versus number of phases.

the gate signals for all strings under PWM are symmetrically out of phase with each other. For example, the gate signals for an 8-string array are shown in Figure 8.8. This way, all strings are not simultaneously switched on or off, but one after another in a rotation. The major advantages of this scheme are significant reductions in ripples and EMI.

The polyphase PWM shunt regulator reduces the ripple generation, lowering the filter mass. Figure 8.9 depicts the approximate mass savings with the number of phases used. The minimum filter mass is achieved with four to six phases, depending on the power level of the bus. The savings can be up to 20% compared to the multistage PWM shunts.

8.3.6 Calibrated Step Shunt

The scheme of Figure 8.10 shows multiple shunts, each having power capability in calibrated steps such that a great many values of power can be shunted by appropriate selection of the shunts and placing them in the saturation region. It provides a good resolution on the bus voltage control, but not as fine as other schemes.

8.4 SHUNT CIRCUIT DESIGN

The following trade options exist for designing the shunt circuits:

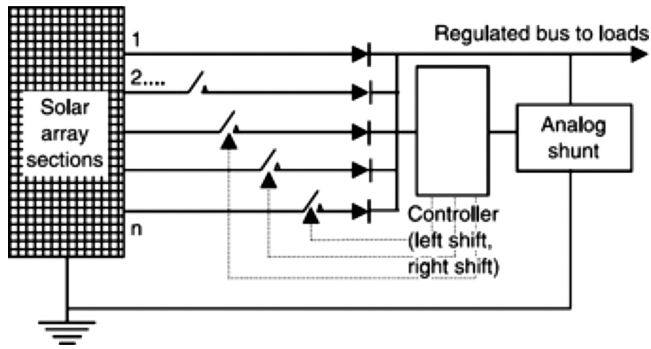

FIGURE 8.10 Calibrated step digital shunt regulator.

Full versus Partial Shunts: The full shunt (i) requires fewer slip rings and wires, loses more array power if one circuit fails, and (iii) dissipates more power loss per circuit. The partial shunt, on the other hand, requires twice as many slip rings, one set from the upper section and one set from the lower section.

Number of Shunt Circuits: Selecting too few circuits leads to (i) fewer slip rings in the solar array, but (ii) higher power per circuit, requiring more power margin to allow for one circuit failure for reliability, and (iii) higher local power dissipation, hence leading to hot spots. On the other hand, too many circuits lead to (i) smaller voltage control steps, i.e., better bus voltage resolution, and (ii) small steps requiring higher shunt control amplifier gain, which may be harder to work with due to excessive amplification of the small error signal band.

Typically, the solar array is divided into as many string circuits as required. For a 22–35 V sun-regulated bus with a full 5A shunt as an example, the maximum shunt dissipation would then be $35 \times 5 = 175$ W in the shunt just entering the linear range. This is 87.5 W per transistor, with two in parallel for redundancy. Dissipation in each shunt when saturated, on the other hand, is $(\frac{1}{2}I)^2 \times$ transistor on-resistance $= (5/2)^2 \times 0.100 = 0.75$ W in each of the two switches in parallel for each solar string, or 1.50 W total in both switches combined. Thus, the total power loss per shunt circuit in the saturated region is less than 1% of the maximum before entering saturation.

The solar array shunt control should limit the bus voltage dV/dt to less than 1% of the bus voltage per microsecond and the conduction voltage drop below 0.1% of the bus voltage per ampere of the shunt circuit current. For example, a 5 A circuit on a 100 V bus should keep the dV/dt less than 1 V/μs and the conduction drop below 0.50 V. The control signals to switch shunt circuits are derated, buffered, shielded, and double-insulated for reliability.

8.5 BUS RIPPLE FILTER DESIGN

The PWM causes ripples in the dc voltage. This ripple needs to be kept below the minimum required limit by using a bus filter capacitor shown in Figure 8.11.

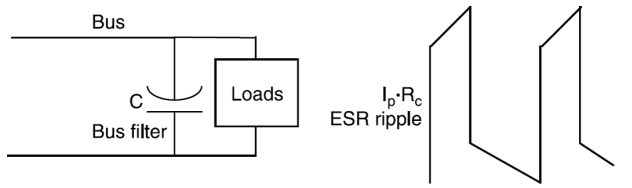

FIGURE 8.11 Bus voltage ripple at shunt switching frequency with a bus filter capacitor. (a) Bus with capacitor. (b) Switching frequency ripple.

As the capacitor charges and discharges, the equivalent series resistance of the capacitor causes a voltage drop of opposite polarity, resulting in the capacitor's voltage rising and falling. The peak-to-peak ripple voltage V_{pp} on the bus can be derived from the following expression:

$$V_{pp} = I_s R_c + D(1-D)\frac{I_s T}{C} \tag{8.3}$$

where

I_s = current switched per shunt circuit
R_c = bus capacitor equivalent series resistance
D = duty ratio of the PWM switching
T = switching period
C = bus capacitor value in farads

For a known equivalent series resistance and switching frequency, the minimum bus capacitor required to meet a given ripple specification is then found from

$$C_{\min} = \frac{D(1-D)I_s T}{V_{pp} - I_s R_c} \tag{8.4}$$

A large bus filter capacitor is desired not only to get low ripple but also to reduce the bus impedance at high frequencies. On the other hand, fast transient response requires a low value of the bus capacitor for a given loop gain crossover frequency. The engineer trades these two performance features.

The use of high frequency, i.e., low switching period, reduces the filter capacitor size as indicated by Equation 8.4. Approximate mass savings are shown in Figure 8.12 for the frequency range of 20–200 kHz.

8.6 POWER CONVERTERS

The converter basically converts one voltage level into another at the interface of two power components. The following sections describe the topology and operation of various types of power converters.

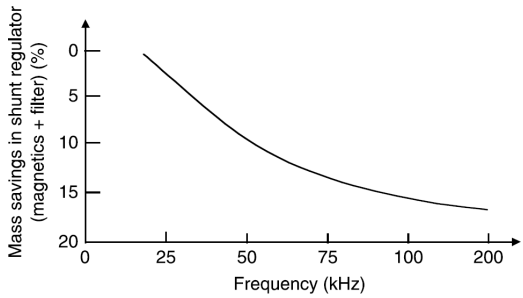

FIGURE 8.12 Shunt regulator mass versus switching frequency.

8.6.1 DC–DC Buck Converter

During sunlight, the bus voltage is maintained by the solar array output. The battery is charged only if the battery voltage is lower than the bus voltage. A dc–dc voltage converter is required to buck (step down) the bus voltage to the battery voltage during charging. Figure 8.13 is the most widely used battery charge converter circuit topology. Its operation during one on-and-off cycle of the triggering signal is shown in Figure 8.14. During this time, the switch is closed, and the circuit operates as in (i). The dc source charges the capacitor and supplies power to the load via the inductor. During the off-time, the switch is open, and the circuit operates as in (ii). The power

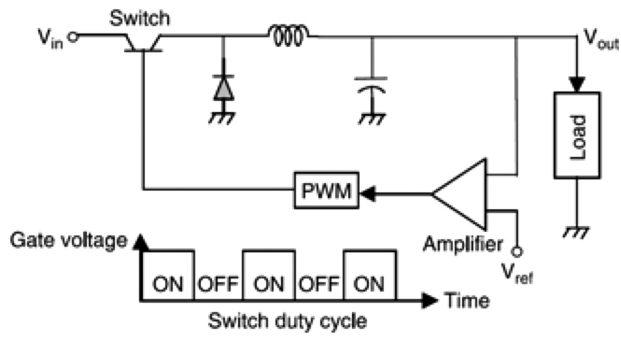

FIGURE 8.13 Battery charge (buck) converter.

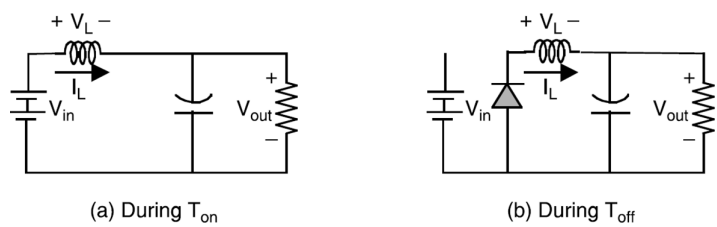

FIGURE 8.14 Buck converter operation during on and off switches. (a) During T_{on}. (b) During T_{off}.

drawn from the dc source is zero. However, full load power is supplied by the energy stored in the inductor and the capacitor, with the diode carrying the return current. Thus, the inductor and the capacitor provide short-term energy storage to ride through the off period of the switch. The load current during this period is known as the freewheeling current, and the diode is known as a freewheeling diode. The voltage and current waveforms over one complete cycle are displayed in Figure 8.15. A suitable bleeding resistor at the load terminals is sometimes incorporated into the design to keep the converter working without the load.

The analysis of the power train of the buck converter follows. The analytical principles that follow are also applicable to other dc–dc converters. The power train analysis is based on the energy balance over one switching period. Since the inductor stores energy during the on-time and discharges it during the off-time:

- Energy supplied to the load over the total period T = energy drawn from the source during the on-time, which powers the load and charges the inductor and capacitor, and
- Energy supplied to the load during off-time = energy discharged from the inductor and the capacitor during off-time.

The inductor generally uses a magnetic core with a lumped or distributed air gap. The flux density in the core has to be kept below the magnetic saturation level. For that reason, the net change in flux over one cycle of switching has to be zero. Otherwise, the core would eventually *walk away* to saturation on the high side or be depleted of energy on the low side. The magnitude of the voltage drop across the inductor is given by Faraday's law: $V_L = N\, d\varphi/dt$, where N = number of turns, φ = flux in the core, and t = time. The equation can be written as $V_L \cdot dt = N \cdot d\varphi$. As $d\varphi$ must be zero over one switching cycle, we must have

$$\int_0^T V_L \cdot dt = 0 \tag{8.5}$$

i.e., the change in the volt–second product over one cycle must be zero. Thus, in the steady state condition, the inductor volt–second balance during the on and off periods must be maintained. This, in essence, gives the energy balance.

We now apply the volt–second balance to the voltage and current waveforms shown in Figure 8.15. In terms of the inductance, the voltage drop across the inductor is $V_L = L\, dI_L/dt$. Therefore, during on-time,

$$\Delta I_L L = \left(V_{\text{in}} - V_{\text{out}}\right) T_{\text{on}} \tag{8.6}$$

and during off-time,

$$\Delta I_L L = V_{\text{out}} T_{\text{off}} \tag{8.7}$$

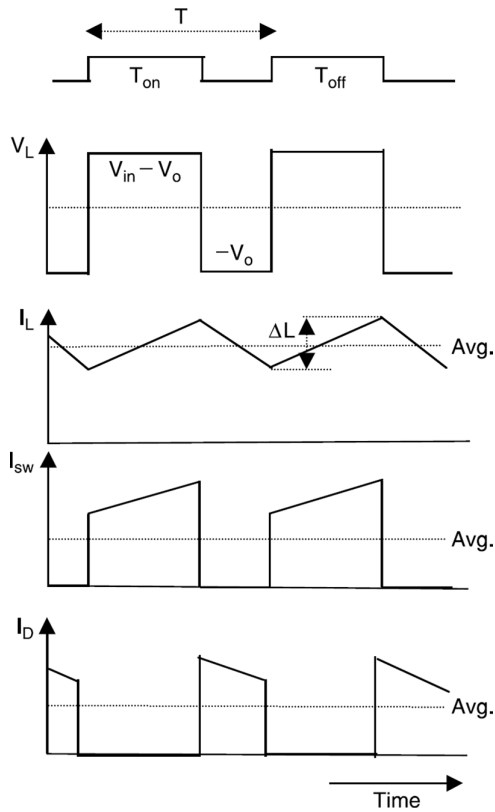

FIGURE 8.15 Current and voltage waveforms in the buck converter.

If the inductor is large enough, as is usually the case in practical designs, the change in the inductor current is small, and the peak value of the inductor current is given by

$$I_{\text{peak}} = I_o + 0.5\ \Delta I_L \tag{8.8}$$

where the load current $I_o = V_{\text{out}}/R_{\text{load}}$ = average value of the inductor current.

The algebraic manipulation of the above equations leads to

$$V_{\text{out}} = V_{\text{in}} \cdot D \tag{8.9}$$

Since the duty ratio D is always less than unity, the output voltage of the buck converter is always less than the input voltage. Thus, the buck converter can only step down the voltage, hence the name.

It is seen from Equation 8.9 that varying the duty ratio controls the output voltage. This is done in a feedback control loop with the required battery charge current as the reference. Modulating the pulse width of T_{on} controls the duty ratio. Such a converter is therefore known as a PWM converter.

The efficiency is calculated as follows: During this time, the input voltage, less the voltage drop in the transistor switch, supplies power to the circuit. The energy transfer efficiency is therefore $(V_i \times V_s)/V_i$, where V_i = input voltage and V_s = voltage drop in the switch. During the off period, the inductor voltage, less the diode drop, is the output voltage. The efficiency during this period is therefore $V_o/(V_o + V_d)$, where V_o = output voltage and V_d = voltage drop in the diode. In addition, there is some loss in the inductor, the efficiency of which we denote by η_i. The losses in the capacitor and the wire are relatively small and can be ignored for simplicity. The overall power train efficiency of the buck converter is, therefore, the product of the above three efficiencies, namely

$$\eta_c = \left(\frac{V_i - V_s}{V_i}\right)\left(\frac{V_o}{V_o + V_d}\right)\eta_i \tag{8.10}$$

With commonly used devices, the transistor switch and diode voltage drops are typically 0.6 V each. If we denote both by the device voltage drop V_d, then a sufficiently accurate simplification of the above equation is

$$\eta_c = \left(\frac{V_o}{V_o + V_d}\right)^2 \eta_i \tag{8.11}$$

The inductor efficiency can approach 0.99. The power train efficiency of 28 V output converters may be around 95%. The losses in the wires, capacitors, and magnetic core may further reduce the efficiency by a couple of percent, making it in the 92%–94% range. The converter's efficiency is a strong function of the output voltage. It decreases with decreasing output voltage, as the switch and diode voltage drops remain constant. For example, a 5 V output converter would have efficiency in the 75%–80% range.

Since the charge converter in low Earth orbit satellites handles more power and works longer hours, it must be designed for high efficiency and better cooling. The low Earth orbit charge converter design, therefore, gets more complex than its geosynchronous Earth orbit counterpart.

8.6.2 DC–DC Boost Converter

In a fully regulated bus, the bus voltage is maintained within a narrow band during the entire orbit. Since the battery voltage under discharge sags during an eclipse, a voltage converter is required to boost (step up) the battery voltage to the bus level. The boost converter topology is shown in Figure 8.16. When the transistor switch is on, the inductor is connected to the dc source. When the switch is off, the inductor current is forced to flow through the diode and the load. The output voltage of the boost converter is derived again from the volt–second balance in the inductor. With the duty ratio D of the switch, it can be shown, in a manner similar to that in the buck converter analysis, that the output voltage is given by the following expression,

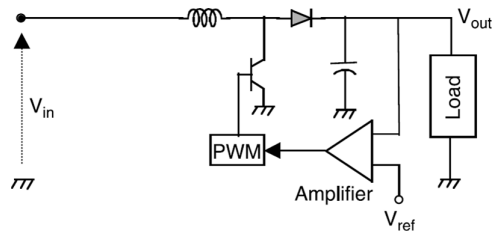

FIGURE 8.16 Battery discharge (boost) converter.

$$V_{\text{out}} = \frac{V_{\text{in}}}{1 - D} \tag{8.12}$$

Since the duty ratio is always less than unity, the output voltage of the boost converter is always greater than the input voltage. Therefore, the boost converter can only step up the voltage, hence the name. The efficiency of the boost converter can be shown to be

$$\eta_c = \left(\frac{V_i - V_d}{V_i} \right)^2 \eta_i \tag{8.13}$$

8.6.3 DC–DC Buck–Boost Converter

The cascading of the buck and boost converters as shown in Figure 8.17a results in a buck–boost converter, which can step down or step up the input voltage. A modified direct buck–boost converter that uses fewer parts is shown in Figure 8.17b. The output voltage is obtained by cascading the buck and boost converter voltage relationships. That is,

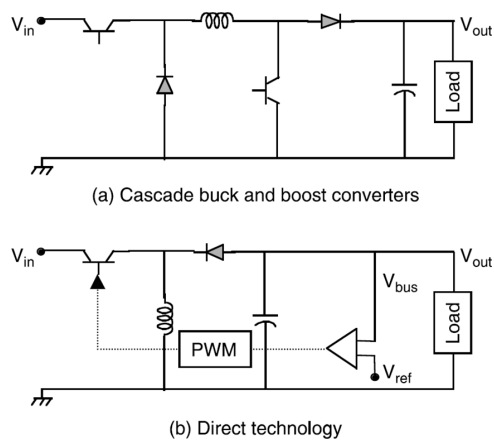

FIGURE 8.17 Two configurations of buck–boost converters. (a) Cascade buck and boost converters. (b) Direct technology.

$$V_{\text{out}} = \frac{V_{\text{in}} \cdot D}{1 - D} \tag{8.14}$$

This equation shows that the output voltage of the buck–boost converter can be higher or lower than the input voltage, depending on the duty ratio. In addition to its possible use to charge and discharge the battery with one converter, the buck–boost converter is capable of four-quadrant operation with a dc machine in variable speed applications and with flywheel energy storage. In the flywheel system, the converter would step up voltage during generating mode and step down during motoring mode.

8.6.4 Flyback Buck–Boost Converter

Figure 8.18 shows the topology of this converter, which can buck or boost the voltage depending on the turn ratio of the coupled inductor. The energy is stored on the primary side of the inductor during this time. It then becomes inductively transformed (kicked) to the secondary side when the switch is turned off and is delivered to the load via a diode. The polarity marks of the two coils are of essence in this circuit. The inductor core is generally made of potted magnetic metal powder. The energy is stored in the distributed air gap of the core. The voltage ratio and efficiency are given by

$$\frac{V_o}{V_i} = D \cdot \left(\frac{N_s}{N_p}\right) \quad \text{and} \quad \eta_c = \left(\frac{V_i - V_s}{V_i}\right) \left(\frac{V_o}{V_o + V_d}\right) \eta_i \tag{8.15}$$

where η_i = efficiency of the coupled inductors, which is typically 95%–98%.

The voltage ratio is a mere multiple of the duty ratio and the turn ratio. This gives great flexibility in the output voltage without the limitation of the duty ratio. It can buck or boost depending on the turn ratio, which can be less than or greater than one.

An advantage of the flyback converter over the classical buck and boost converter is that it electrically isolates the two sides, thus minimizing the conducted EMI and enhancing safety. Moreover, it stores the inductive energy and simultaneously operates like a classical forward buck converter with a transformer, stepping up or down the input voltage as needed.

8.6.5 Transformer-Coupled Forward Converter

The converter circuit shown in Figure 8.19 employs a transformer with a suitable turn ratio in a conventional converter such that the output voltage can be below or above the input voltage. The polarity marks are essential. The bleeding load resistor

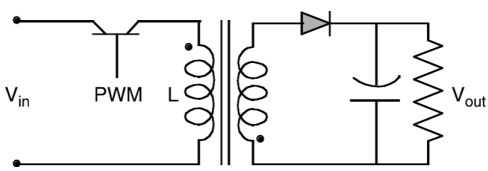

FIGURE 8.18 Flyback converter (buck or boost).

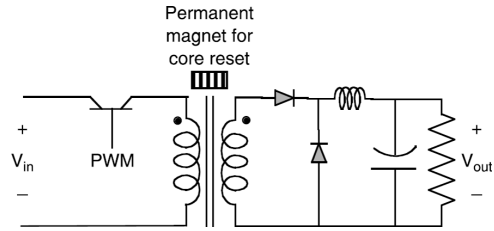

FIGURE 8.19 Transformer-coupled forward converter.

is required to keep the converter working without load. Its voltage relationship is identical to that for the flyback buck–boost converter described above. That is,

$$\frac{V_o}{V_i} = D \cdot \left(\frac{N_s}{N_p} \right) \tag{8.16}$$

and the efficiency

$$\eta_c = \left(\frac{V_i - V_s}{V_i} \right) \left(\frac{V_o}{V_o + V_d} \right) \eta_t \tag{8.17}$$

where η_t = efficiency of the transformer, which is typically 95%–98%.

8.6.6 Push–Pull Converter

This is again a buck–boost converter and is shown in Figure 8.20. The converter topology uses a center-tapped transformer, which receives square-wave excitation. It is seldom used at low power levels but finds applications in systems dealing with several tens of kilowatts and higher. It can provide the desired output voltage by setting the required transformer turn ratio. The voltage ratio and the efficiency are the same as those given by Equations 8.16 and 8.17.

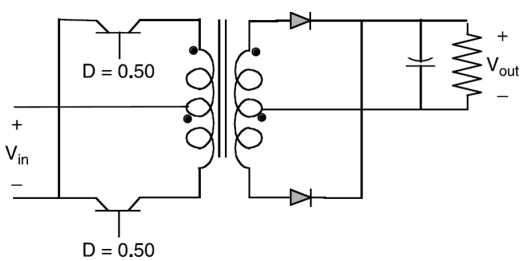

FIGURE 8.20 Push–pull converter with center-tap transformer.

8.6.7 Inductor-Coupled Buck Converter

All converters presented above need an L–C filter to control the ripple in the output voltage. The buck converter needs a heavier filter than the boost converter. Since ripples are present on both the input and output sides, it is possible to cancel them by coupling the ripple current slopes of the two sides with matched inductors[1,2] as shown in Figure 8.21. The ripple magnitudes are matched by using the required turn ratio, and the polarities are inverted by winding in magnetically opposite directions. The net ripple on the output side is zero at a certain gap, below which it changes the polarity. A gap-adjusting screw is needed to tune the gap for a precise match. The output capacitor C_o is not really needed in a perfectly coupled design, but a small value of C_o improves the performance. The coupling capacitor C is needed for performance. The total value of the two capacitors is about the same as that needed in the classical buck converter. On the output side, some ripple may be left due to the winding resistances. The input-side ripple is the same as that without the coupled inductor. The load current changes do not affect the ripple cancellation.

8.6.8 DC–DC Resonant Converter

Another type of dc–dc converter now used in many high-power applications is the zero-voltage switching converter due to its higher switching frequency, higher efficiency, smaller size, lighter weight, and better dynamic response. It is a full-bridge converter that includes inductors and capacitors as resonant elements. The switching is done when the voltage is passing through its natural zero, thus reducing the switching losses.

8.6.9 DC–AC Converters

The dc-ac converters, also called inverters, are mainly used on the load side and in the spacecraft power distribution system. From the dc end, they are connected to the dc bus, and at their output, they generate controllable ac waveforms, either 1-phase or 3-phase. There are two main types of these converters:

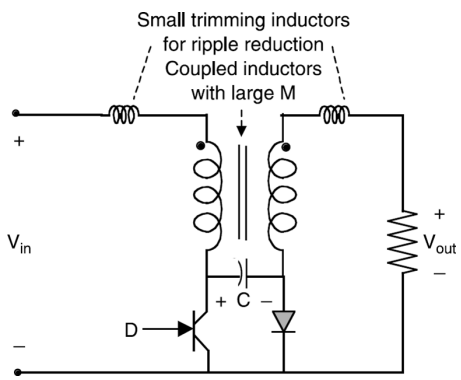

FIGURE 8.21 Inductor-coupled buck converter with integrated magnetics (Cuk converter).

- Voltage source converter (VSC), and
- Current source converter (CSC).

In the (VSC) the input is a dc voltage, either from a dc source such as a battery or a large capacitor, or a rectified voltage from an ac source. VSCs are the most common power electronics converters found in a variety of applications. Figure 8.22a shows the schematic of a VSC.

In the CSC, the input is a dc current from a large inductor. These converters are less popular, with their main applications being active power filters and applications where a long cable is used. Figure 8.22b shows a schematic of a CSC.

Unlike the VSCs, where freewheeling antiparallel diodes are used, the didoes in the CSC are in series with the active switches to make up for the lack of reverse voltage withstand capability of switches. Note that in both voltage and CSCs, the output voltage and current are sinusoidal after filtering the harmonics.

Different control schemes may be applied to power electronics converters depending on the application, cost, and other factors. A PWM may be used to control the IGBT/MOSFET switches. In the PWM approach, a dc voltage is applied to the converter input, and the local average (average per switching period) of the output voltage (1-ph, 3-ph, or multiph) is controlled by modulation of the width of the pulses

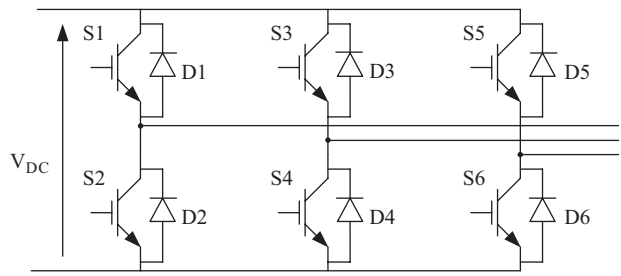

(a) Voltage source converter

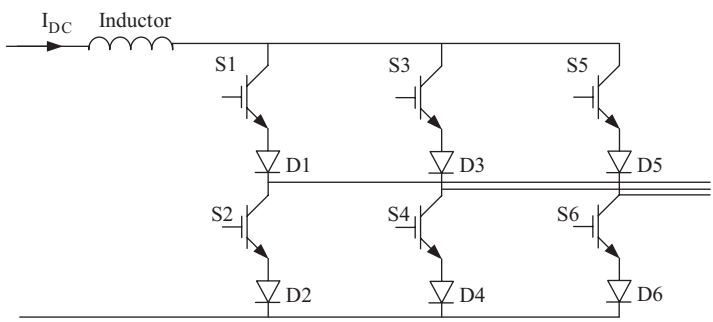

(b) Current source converter

FIGURE 8.22 Voltage source converter (VSC) and current source converter (CSC) insulated gate bipolar transistors/metal-oxide semiconducting field effect transistor-based converters. (a) VSC. (b) CSC.

applied to each IGBT/MOSFET. Different PWM techniques, such as sinusoidal PWM (SPWM) and space vector PWM (SVM), have been extensively studied.

8.6.10 DC–AC Converters SPWM Control

In SPWM, which is the most common PWM technique, the local average of the output voltage has a sinusoidal waveform (also called a fundamental component) whose magnitude, phase, and frequency are controlled by the PWM of the converter switches. The higher the switching frequency, the higher the quality of the resulting waveforms, and the smaller the filter capacitors and inductors. However, higher switching frequencies result in higher switching losses. High-switching-frequency PWM is not appropriate for high-power applications. Figure 8.23 shows the output voltage of a converter with PWM modulation. As seen, the output voltage is pulsed before filtering.

In SPWM, a sinusoidal control signal (modulating signal) is compared with a triangular carrier signal of constant amplitude and frequency to generate the switch control signals. The fundamental component of the output voltage is controlled and is proportional to the control signal. Information about the fundamental component of the output voltage is embedded (modulated) in the widths of the output voltage pulses. The demodulation takes place in the output low-pass filter, where the switching harmonics are separated from the fundamental component, or in the inductive load, where the pulsed voltage waveform is transformed to a sinusoidal current at the fundamental frequency.

An amplitude modulation index (or ratio) may be calculated as:

$$m_a = \frac{\hat{v}_{\text{control}}}{\hat{v}_{\text{tri}}} \tag{8.18}$$

where, $\hat{v}_{\text{control}}$ is the amplitude of the control signal, and $\hat{v}_{tri}$ is the amplitude of the triangular signal. A frequency modulation index is calculated as:

$$m_f = \frac{f_s}{f_1} \tag{8.19}$$

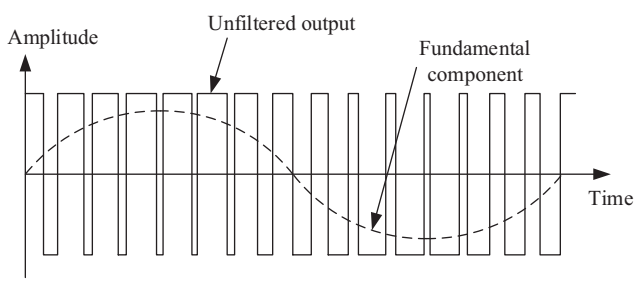

FIGURE 8.23 Converter output voltage with PWM modulation.

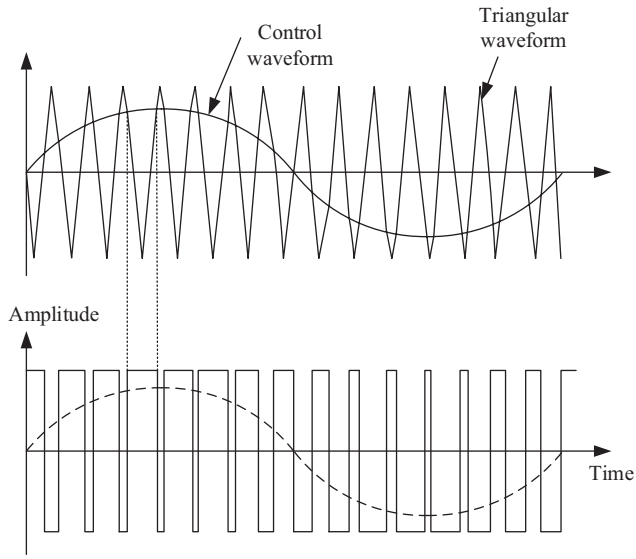

FIGURE 8.24 Generation of PWM and output voltage.

where, f_s is the frequency of the triangular signal or switching frequency, and f_1 is the frequency of the control signal and the fundamental frequency of the output voltage.

Based on the comparison of the control voltage with the triangular voltage, the switch control signals and consequently the output voltage are generated. The generation of the output voltage is independent of the load current. Figure 8.24 compares the control and triangular voltages and shows the output voltage of the converter. The comparison is performed such that, where the control voltage is larger than the triangular signal, the output pulse is at its saturated maximum; otherwise, the output voltage is at its saturated minimum. This results in a train of pulses with different widths as output voltage, as shown in Figure 8.24. The output voltage waveform shows that the local average of the output voltage is a sinusoidal waveform proportional to the control voltage. Due to the linearity of the PWM process, the ratio of the peak value of the fundamental component of the output voltage to the input dc voltage is equal to the modulation index. If the frequency modulation ratio is an odd number, the resulting output voltage waveform has half-wave symmetry and, as a result, does not contain even harmonics.

8.6.11 DC–AC Converters Square-Wave Control

In the square-wave method, the output voltage has a square waveform whose magnitude of the fundamental component is not controllable. In order to be able to control the magnitude of the fundamental component of the output voltage, the input dc voltage needs to be controlled. The inverter switch controls only the frequency and the phase angle of the output voltage. The switching frequency is minimal, i.e., each switch turns on and off once per period of the output voltage. Due to its low switching

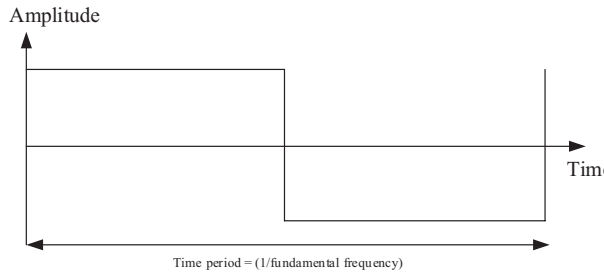

FIGURE 8.25 Output voltage in the square-wave method (over-modulation).

frequency and thus low switching losses, this scheme is appropriate for high-power applications. The square-wave control is also achieved when the amplitude modulation index in the SPWM is greater than 1, i.e. $m_a \gg 1$.

If the modulation index in the SPWM scheme is less than $1(m_a < 1)$ the peak value of the output voltage varies linearly with the modulation index. If the modulation index is greater than $1(m_a > 1)$ the linearity, the peak value of the output voltage depends on the frequency modulation index, m_f. The PWM with a $m_a > 1$ is commonly referred to as over-modulation, where the output voltage waveform of the inverter degenerates from pulse width modulated to square-wave; however, it has a higher amplitude than the PWM case. Figure 8.25 shows the overmodulated, i.e., square-wave output voltage.

8.6.12 Multilevel Converters for High Voltage

The solid-state switches, such as IGBTs and MOSFETs, that are the building blocks of power electronics converters are rated at specific voltages and currents. To use the switches in a converter beyond their current and voltage ratings, a number of switches are connected in parallel for high-current applications and in series for high-voltage applications. This results in the ac voltage being synthesized from several levels of the converter's dc input voltage, which is referred as a multilevel converter. In VSCs in multilevel topologies, capacitors on the dc link are used to create multilevel voltages. Figure 8.26 shows a schematic of a 3-level converter that uses two capacitors connected in series to achieve the required voltage levels. The midpoint of the capacitors provides a neutral point. In this scheme, commonly referred to as neutral point clamped (NPC), there are four switches connected in series with two diodes clamping the midpoint. The main challenge with these topologies is maintaining a balanced voltage between different levels. Voltage clamping and capacitor charge control are two common methods to balance the voltage between levels. Other multilevel topologies, such as flying capacitors and cascade inverters with isolated dc sources, have also been proposed.

For the three-level topology shown in Figure 8.26, each capacitor voltage under balanced conditions is half of the input dc voltage. If the upper switches S1 and S2 are turned ON, the phase-A voltage with respect to the neutral point Z is ½ Vdc, while when the two bottom switches, S3 and S4, are turned ON, the phase voltage

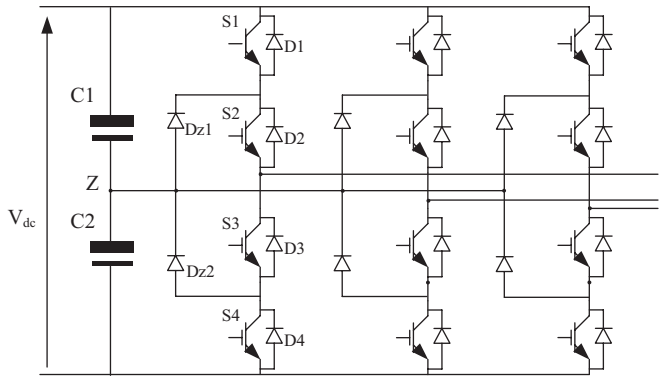

FIGURE 8.26 Three-level voltage source converters are referred to as neutral point clamped (NPC).

is −½ Vdc. If the switches S2 and S3 are ON, the phase voltage is clamped to zero, and one of the didoes is ON depending on the direction of the load current. Note that switches S1 and S3 operate in opposite ways; therefore, if one is ON, the other one must be OFF. Similarly, switches S2 and S4 operate the same way. A dead time is required between the complementary switches.

Higher-level topologies can be achieved by connecting more switches in series. Figure 8.27 depicts a diode-clamped converter. In this topology, there are six switches and four diodes per converter leg. There are three capacitors connected in series, each having a voltage of 1/3 Vdc in a balanced condition. When the three top switches S1, S2, and S3 are turned ON, the voltage across phase-A equals Vdc, while

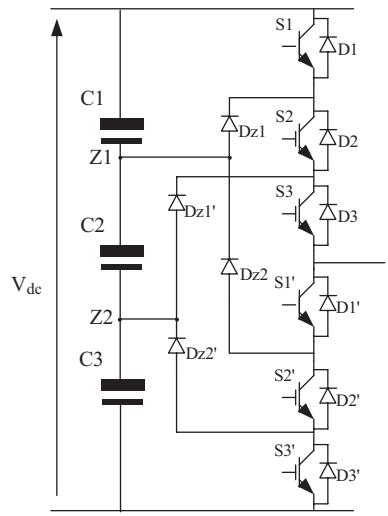

FIGURE 8.27 Four-level voltage source converters are referred to as neutral point clamped (NPC).

when the three bottom switches are ON, the voltage across the phase is zero. If the phase-A terminal is connected to either Z1 or Z2 via the conduction of three middle switches and diodes, the phase voltage is either 2/3 Vdc or 1/3 Vdc. Note that the phase voltage in the four-level converter has four levels, i.e., Vdc, 2/3 Vdc, 1/3 Vdc, and 0. The switch pairs (S1, S1'), (S2, S2'), and (S3, S3') operate complementaryly, i.e., when one is ON, the other is OFF, and vice versa.

In multilevel topologies with the same voltage ratings of the switches, the converter output voltage and hence power are proportional to the number of switches. However, as the voltage levels increase, the number of clamping diodes increases significantly. A three-level converter has six clamping diodes, while a four-level converter has eighteen. This, together with the increased number of capacitors and voltage balancing challenges, limits the application of higher voltage converters.

8.7 MAGNETICS

Inductor and transformer are two magnetic components used in spacecraft power electronics. The inductor stores energy in the form of magnetic flux passing through an air gap (distributed or in one place) in its magnetic circuit. Such stored energy is often used in L–C filters to achieve ripple-free power at the converter outputs. The transformer changes voltage level from one coil to another via mutually coupled flux in its magnetic core. The flux in the magnetic core of the inductor or transformer without any airgap does not store energy since the ideal magnetic core offers no resistance to the flux. It is like pressing an infinitely soft spring that stores no potential energy. The spring has to offer some resistance in order to store energy.

Using properly designed inductors and transformers is important, but their design is beyond the scope of the spacecraft power system engineer. Typically, these components are procured from vendors of such magnetic parts.

REFERENCES

1. Cuk, S., Switching dc-dc converter with zero input or output current ripple, in *IEEE Industry Applications Society Conference Records*, October 1978.
2. Cuk, S., Analysis of integrated magnetics to eliminate current ripples in switching converters, in *Power Conversion International Conference Proceedings*, Intertec Publishers, Oxnard, CA, April 1983.

FURTHER READINGS

Beik, O. and Al-Adsani, A.S., "Active and passive control of a dual rotor wind turbine generator for DC grids," *IEEE Access*, 9, 1987–1995, 2021.

Beik, O. and Al-Adsani, A.S., *DC Wind Generation Systems: Design, Analysis, and Multiphase Turbine Technology*. Springer, Cham, 2020.

Beik, O., Dekka, A., and Narimani, M., A new modular neutral point clamped converter with space vector modulation control, in *Proceedings of the IEEE International Conference on Industrial Technology*, 2018, pp. 591–595.

Fox, D., Testing of the engineering model of electrical power control unit for the fluids and combustion facility, in *Proceedings of the 34th Intersociety Energy Conversion Engineering Conference*, SAE, 1999, Paper No. 2435.

McLyman, W.T., *Transformer and Inductor Design Handbook*, Marcel Decker, New York, 1988.

Mohan, N., Undeland, T., and Robbins, W.P., *Power Electronics Converters, Applications and Design*, IEEE and John Wiley & Sons, New York, 1995.

Saude, B., LaSart, N., Blair, J., and Beik, O., "Microgrid-based wind and solar power generation on moon and mars," *IEEE Transactions on Smart Grid*, 14(2), 1329–1332, March 2023.

Wu, K.C., *Pulse Width Modulated dc-dc Converters - Analysis and Design*, Kluwer Academic Publishers, Norwell, MA, 1997.

Wu, K.C., *Transistor Circuits for Spacecraft Power System*, Kluwer Academic Publishers, Norwell, MA, 2002.

9 Distribution Harness and Protection

9.1 INTRODUCTION

The harness includes the insulated conductors, connectors, and shield. Its mass is determined by the detailed layout and routing of all the required wiring. For this reason, it is often considerably more than that estimated without the actual layout at the preliminary design stage. The final harness mass breakdown is typically 30% in wires connecting the power system boxes, 30% in command and telemetry wires, 10% in solar array wires, and 30% in connectors. The shield mass is included in these component wires.

9.2 AMPACITY OF WIRE

The maximum current carrying capacity (ampacity) of the wire in space is less than that on the ground due to a lack of convective cooling. This requires derating the wire ampacity for space applications from the ground-based rating. The wire size is measured in American wire gage (AWG) or British wire gage. The gage number is an inverse measure of its bare diameter and is set on a log scale:

$$\mathrm{AWG} = 20\log\left(\frac{0.325}{d}\right) \tag{9.1}$$

where d = diameter of the bare conductor in inches. Thus, for every gage up, the diameter increases by a factor of 1.1225 and the cross-sectional area by 1.26. The diameter doubles every six gages, and the area doubles every three gages. The ampacities of various gages of wire are listed in Table 9.1.

9.3 *R-L-C* PARAMETERS

The resistance (R), inductance (L), and capacitance (C) parameters of the harness are required for a detailed simulation model of the power circuit. They are determined from the expressions given below, where the values are per meter length of cable (lead and return wires together). When wires are twisted, typically at a rate of one twist every few centimeters, the actual conductor is approximately 10%–15% longer than the straight run. The resistance (in Ω/m) is given by

$$R = \frac{2\rho}{A} \tag{9.2}$$

DOI: 10.1201/9781003344605-11

TABLE 9.1
Maximum Allowable Current in Amperes for Wires and Connector Contact Pins of the Same Gage

AWG	Diameter (inches)	Single Wire in Free Air on Ground (MIL-STD-5088)	Wires in Space[a] in 70°C Ambience (MIL-STD-975 and GSFC-PPL-19)	
			Single Wire	Bundle or Cable[b]
30	0.010 0	N/a	1.3	0.7
26	0.015 9	10.5	2.5	1.4
24	0.020 1	14	3.3	2.0
20	0.032 0	24	6.5	3.7
16	0.050 8	37	13.0	6.5
12	0.080 8	68	25.0	11.5
8	0.128 5	135	44.0	23.0
4	7 × 0.0772	260	81.0	40.0
0	19 × 0.0745	460	147.0	75.0

[a] For TFE teflon insulated wires rated for 200°C. For 150°C rated insulation, use 80% of values shown. For 135°C rated insulation, use 70% of values shown. For 105°C rated insulation, use 50% of values shown.

[b] For cable bundles of 15 or more wires in 70°C ambience in hard vacuum. For smaller bundles, the allowable current may be proportionately increased as the bundle approaches a single conductor.

[c] Wires sizes 10, 14, and 18 are not used in aerospace for general wiring, and AWG 2 and 6 have no counterpart electrical connector contacts (pins).

AWG, American wire gage; TFE, MIL, STD, GSFC

where ρ = resistivity of the conductor and A = cross-sectional area of the one-way conductor(s). At 20°C, $\rho = 1.724 \times 10^{-8}$ Ω·m for copper and 2.65×10^{-8} Ω·m for aluminum, both electrolytic grades.

The resistance R_2 at temperature T_2 is derived from R_1 at temperature T_1 using the temperature coefficient of resistance α as follows:

$$R_2 = R_1\left[1 + \alpha\left(T_2 - T_1\right)\right] \tag{9.3}$$

where $\alpha = 0.00393$ 1/°C for electrolyte copper and 0.00390 1/°C for aluminum.

For a cable with two parallel round conductors of equal radii (Figure 9.1a), the cable inductance (in H/m) in free space is given by

$$L = \frac{2\mu_o}{2\pi}\left[\frac{1}{4} + \ln\left(\frac{S}{r}\right)\right] \quad \text{Or} \quad L = \left(1 + 4\ln\frac{s}{r}\right) \times 10^{-7} \tag{9.4}$$

where μ_o = permeability of free space = $4\pi \times 10^{-7}$ H/m, s = spacing between conductor centers, and r = conductor radius.

The term ¼ is due to the magnetic flux internal to the conductor. It is small and approaches zero at high frequency due to the skin effect. For twisted pairs touching

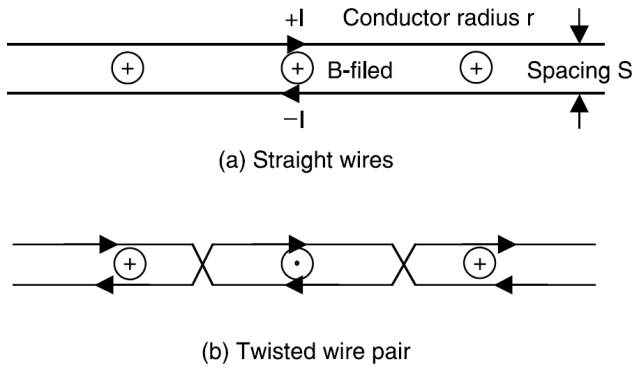

FIGURE 9.1 Parallel wires and resulting *B* field.

each other, $s = 2(r +$ wire insulation thickness). Since the insulation thickness is proportional to the wire radius for mechanical reasons, the *s/r* ratio remains approximately constant, making *L* somewhat insensitive to the wire gage. For AWG 10–30 wires, the inductance remains in the range of 0.5–0.7 μH per meter of twisted pair up to hundreds of kilohertz. Twisting does not reduce the inductance per meter but adds 10%–15% to the length. However, it produces additive and subtractive *B* fields in adjacent spans (Figure 9.1b), canceling each other's emission at a far distance. The inductance of open, untwisted wire loops at the end of an equipment box is determined from Equation 9.4. It is about 5 μH/m for practical loops and 7.5 μH/m for infinitely large loops. It is noteworthy that the single-point ground reduces the ground inductance by avoiding large ground current loops. The inductance of a ground strap is that of a single wire in free space with the ground as a return. Its values are plotted in Figure 9.2.

The battery packaging influences the harness inductance and the magnetic moment. A one-pack battery has a small harness inductance, but a two-pack battery can have a large harness inductance and a large magnetic dipole moment depending on the spacing between them. Therefore, it is important to place all packs of the battery as close as possible to minimize the interconnecting harness loop.

The capacitance (in F/m) between two parallel round conductors in the cable is given by

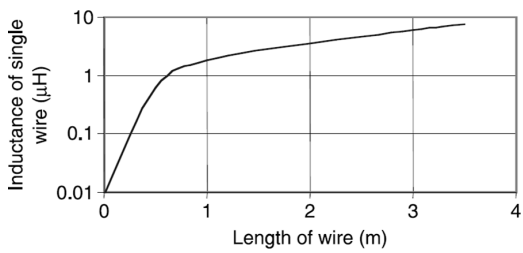

FIGURE 9.2 Inductance of a single straight wire (ground strap).

$$C = \frac{\frac{1}{2}(2\pi\varepsilon_0\varepsilon_r)}{\ln\left(\frac{s}{r}\right)}$$

or

$$C = \frac{\pi\varepsilon_0\varepsilon_r}{\ln\left[\frac{s}{2r} + \sqrt{\left(\frac{s}{2r}\right)^2 - 1}\right]} \tag{9.5}$$

where ε_o = permittivity of free space = 8.85×10^{12} F/m, and ε_r = relative permittivity of the insulation between the conductors. The first expression is for open wires at the harness ends, and the second expression is for closely spaced conductors in the cable. Unlike the resistance, the *L* and *C* parameters do not change with temperature.

Bus bars of the thin rectangular cross section shown in Figure 9.3 are often used in harness segments carrying high current. For such conductors, the *R-L-C* parameters after ignoring the end fringing are

$$R = \frac{2\rho}{ab}\ \Omega/\text{m}\quad L = \frac{\mu_o}{b}\left(d + \frac{2a}{3}\right)\ \text{H/m and}\ C = \frac{\varepsilon_0\varepsilon_r b}{d}\ \text{F/m} \tag{9.6}$$

A typical communications satellite bus designed for 10 kW, 70 V power with copper-clad aluminum bus bars, 5 cm wide × 2 mm thick, would typically have R_{dc} = 2 mΩ at 70°C, *L* = 50 nH, and *C* = 3 nF per meter of the bus length. A cable using 20 AWG round copper wires would have R_{dc} = 70 mΩ/m, *L* = 0.375 μh/m, and *C* = 0.077 nF/m.

The following approximate values can be used as a quick estimation guide for wire gages generally used in spacecraft. The AWG 10 conductor has 100 mils of diameter, 40 g of mass per meter, and 3.3 mΩ of resistance per meter at 70°C. Every three gages doubles the area, and every six gages doubles the diameter. With 2.3 A/mm^2 typical current density, the harness mass (conductor + insulation + shield, but not the connectors) is about 7 g/A one way, and the watt loss is about 2.7 × conductor mass in kg. At 100 kHz, the skin depth is 0.22 mm and R_{ac}/R_{dc} = 9. At 1 MHz, the skin depth is 70 μm and R_{ac}/R_{dc} = 27.

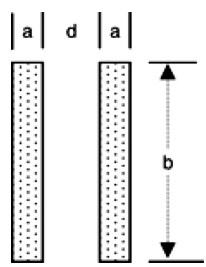

FIGURE 9.3 Rectangular bus bars for high-current harnesses.

9.4 CONDUCTOR MATERIALS

The most commonly used electrical conductor is copper because of its good performance and low cost. Annealed copper is often used for its high conductivity, but it has low tensile strength. This makes it unsuitable for use on thin wires due to the risk of breakage in handling. For this reason, wires thinner than AWG 20 are often required to use high-strength copper alloy 135, which has 40% higher tensile strength and 10% higher electrical resistance. Copper wire coated with tin, nickel, or silver is used to resist corrosion and oxidation. The suitability of various coatings is compared in Table 9.2, where tin plating is included for comparison only. Tin-plated wires are widely used on the ground but are forbidden in space due to the growth of whiskers.

Aluminum is sometimes used in power equipment where lightweight and/or low cost are desired. It is used in ground-based overhead transmission lines and pole-mounted power transformers. Aluminum has also been used in some aircraft and commercial spacecraft harnesses. The performance of aluminum is compared with that of copper in Table 9.3.

For the same power loss or voltage drop, the copper can be replaced with aluminum of a relative mass given by the product of the resistivity and the mass density ratios. An aluminum conductor, therefore, would theoretically have $(2.830/1.724) \times (2.70/8.89) = 0.50$, i.e., one-half of the copper mass. However, in practice, aluminum does not produce 50% mass savings owing to the following reasons:

TABLE 9.2
Suitability of Various Coatings on Copper Conductor

Coating on Copper	Silver	Nickel	Tin
Solderability	Good	Special process	Good
Crimp ability	Good	Special process	Good
Maximum operating temperature	200°C	260°C	150°C

TABLE 9.3
Copper and Aluminum Conductor Comparison

Characteristic	Copper	Aluminum
Resistivity Ω·m at 20°C	1.724×10^{-8}	2.830×10^{-8}
Mass density g/cm^3	8.89	2.70
Temperature coefficient of resistance α/°C	3.93×10^{-3}	3.90×10^{-3}
Melting point °C	1083	660
Flex life (relative)	1	0.5
Thermal coefficient of expansion (relative)	1	1.4
Creep rate at 65°C (relative)	1	1000

- Aluminum has a 1000 times higher creep than copper. For long-term reliability of the terminal connectors, thicker wire is required to keep the crimp joint temperature below 130°C to minimize creep. Alternatively, soldered connections are used, which are expensive and often inconvenient.
- Aluminum oxidizes instantly when exposed to oxygen. This hinders the electrical contact between the wire and the connector. Crimp terminals that produce a cold weld are often used to keep oxygen away from bare aluminum.
- The poor mechanical strength of aluminum wire often requires thicker wire for mechanical reasons alone, even where it meets the ampacity requirement.
- The insulation and the EMI shield mass increase due to the heavier gage aluminum wire required to carry the same current.

As a hybrid approach, copper-clad aluminum wires have been used in the past by some prime contractors in communications satellites with net mass savings of 10%–15%. However, aluminum or copper-clad aluminum wires are generally not allowed on NASA and defense satellites.

9.5 WIRE INSULATION AND CABLE SHIELD

The insulation is designed to withstand the rated and abnormal transient voltages. The transients can be several times the rated value. The insulation design must preclude corona and arcing at pressures below 10 torr and withstand the radiation environment and atomic oxygen. In high-radiation spacecraft, such as GPS, the system specifications require that the silicon-insulated wire not be used and the solar array wires and interconnects be welded to withstand the high radiation.

The cable shield is wrapped around the wire bundle to prevent electromagnetic interference from entering the cable or radiating out. The shield can weigh 15%–40% of the cable weight. The material options are braid versus tape and copper versus aluminum. The braid is used when extreme flexibility is required. Its mass as compared to the wire conductor is about 40% for flat cables and 20% for round cables. In tapes, 2-mil-thick copper vapor deposited on Mylar or Kapton tapes is widely used. The tape is applied to the cable with the insulation touching the cable, followed by another layer on top. The shield mass with such tapes is roughly 80% of that with the braid.

9.6 CONNECTORS

Both crimp and soldered connectors are used for connecting various wire segments. They come in Classes A and B with maximum operating temperatures of 125°C and 200°C, respectively. They are further grouped into four types, as listed in Table 9.4. Series A rectangular connectors are limited to AWG 20 pins, whereas series B round connectors come in heavy pins, some of them in assorted pins to handle different power circuits. The wires are crimped with pins using a special tool. Wires thicker than pins are not permissible but can be up to two gages thinner. In both series A and

TABLE 9.4
Connector Classification

Type	Material	Application
A	Copper alloy	General purpose
B	Ferrous alloy	Hermetically sealed
C	Matching with thermocouples	Thermocouples
D	Copper alloy	Shielding (including coaxial, twin-axial and triaxial)

B connectors, contact pins are further classified as Types A and B. The maximum voltage drop across type A and B contact pins of various gages is listed in Table 9.5.

The general military standard isolation requirement for the connector is:

- High potential withstand capability between pin-to-pin and pin-to-shell at least 4 times the operating voltage
- Insulation resistance between pin-to-pin and pin-to-shell is at least 5000 MΩ

The connector design practice as applied to the spacecraft power system generally includes the following:

- Pins in a connector and the SAD slip rings are assigned such that wires at different electrical potentials are separated and are not on adjacent pins or slip rings.
- Twisted wire pairs are terminated on adjacent pins in the connector.
- A minimum of 10% of spare pins are provided on the outer periphery of the connector.

TABLE 9.5
Permissible Contact Pin Drop in Millivolts at 200°C after Conditioning as per Military Standard MIL-C-39029

Wire Size AWG	Test Current (amp)	Type A with Silver-Plated Wires	Type A with Nickel-Plated Wires	Type B with Silver-Plated Wires	Type B with Nickel-Plated Wires
0	150	36	90	396	900
4	80	40	100	440	1000
8	46	45	113	495	1130
12	23	71	107	781	1177
16	13	84	126	924	1386
20	7.5	94	141	1034	1551
24	3	77	116	847	1276
28	1.5	92	138	1012	1518
32	0.5	74	111	814	1221

- Each connector shell is grounded to the component case with an impedance less than 2.5 mΩ.
- In defense satellites, multiple contact connectors are not used for high voltages above 300 V dc or peak-to-peak ac voltage. Separate connectors rated for the specified high voltage are used for each connection.
- Hermetically sealed boxes must use hermetically sealed connectors with connector cases welded to the boxes.

9.7 HARNESS MASS MINIMIZATION

The harness mass is not small compared to other components. It is primarily driven by the voltage drop specifications between various harness segments. For example, the round-trip voltage drop from the bus voltage control point in the power regulator unit (PRU) to any load is kept below 1%–2% of the rated bus voltage. In a 28 V bus, the round-trip drop from PRU to any load is typically kept below 250 mV for loads below 100 W, 500 mV for heavier loads, and 1 V for heater circuits drawing power only for a part of the orbit period. The voltage drop specifications, particularly in high-voltage spacecraft, do not often result in an optimized design in the following sense. If a higher voltage drop in a thinner wire can be compensated with added mass in the source that is less than the mass saved in a thinner conductor, the trade is beneficial for mass reduction at the power system level. Therefore, the harness power loss should match with the specific power of the source. For this reason, initially proposed voltage drop and derating guidelines for some spacecraft should be carefully examined before they become specifications.

The mass-optimized harness design is derived from the considerations depicted in Figure 9.4a. The power loss in the conductor is equal to the allowable voltage drop times the current. As the power loss increases, the harness mass decreases, but the mass of the power source increases to make up the loss. The total of the two masses is a minimum at a certain optimum power loss in the harness, resulting in the minimum system mass. Figure 9.4b shows the harness power loss and the source power generation in watts per kilogram versus the current density in the conductor. The harness with current density J_{opt} would result in the minimum system mass. At the optimum current density, the loss per kilogram of harness equals the power generated per kilogram of source. Analytically, the power loss per pound of copper conductor at 75°C is given by 2.54 J^2, where J = current density in kiloamperes per square inch. For optimum conductor size, it must be equal to the specific power of the source, P_{sp} W/lb. This leads to

$$J_{\text{opt}} = 627.5\sqrt{P_{sp}} \tag{9.7}$$

The optimum conductor diameter (in inches) is then given by

$$d = \sqrt{\frac{4I_{\text{rated}}m}{\pi J_{\text{opt}}}} \tag{9.8}$$

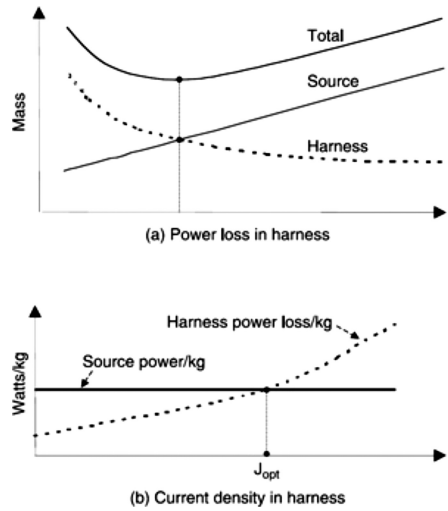

FIGURE 9.4 Harnessing mass optimization at the power system level.

where m = margin factor depending on the protection method used, typically 1.3 for fused circuits. The wire gage is then derived from Equation 11.1 and rounded up. Such consideration leads to a simple expression for V_{opt}, the optimum voltage drop (in volts) per meter run of the harness (physical distance between the source and the load). It is given by

$$V_{opt.drop} = k\sqrt{P_{sp}} \tag{9.9}$$

where P_{sp} = specific power of the source in watts/lb. The coefficient k is 0.03 for copper wires and 0.026 for aluminum wires. Harness segments having varying P_{sp} over the orbit period can be designed for optimum voltage drop using a weighted average P_{sp}.

The harness mass optimization approach leads to the following observation for the conductor sizes in view of Figure 9.5.

- The harness used with a source of high specific power, such as a triple junction solar array, may operate at a higher current density, allowing a higher voltage drop as a percentage of the bus voltage.
- A thinner wire is justified from the solar array to the PRU because the power loss in that segment of the wire is supplied by the solar array alone.
- Thicker wire is required from the PRU to loads because the power in that segment has been processed by the solar array, PRU, and battery all together during a part of the orbit. The whole system has much lower specific power compared to that of the solar array alone.
- For the same reason, the current density in the discharge path should be lower than that in the charge path. This is because the charge current comes

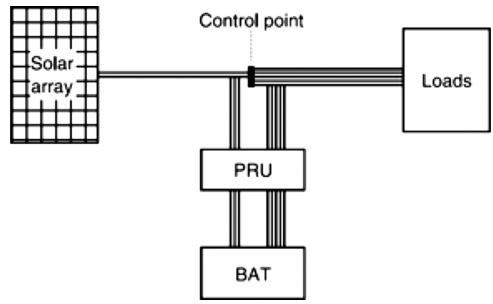

FIGURE 9.5 Progressive optimization of harness mass.

from the solar array alone, whereas the discharge current involves the whole system, comprising the solar array, charge regulator, and discharge regulator.

So, as we move closer to the loads at the end of distribution lines, the current density should be progressively lower. Each watt becomes more precious at the load point than at the generation point. In ground-based utilities, this is analogous to the cost of power to end users being more than five times the cost at a large power plant exit point. It must be noted that the above considerations lead to the minimum harness mass and not the minimum cost at the power system level. The cost of adding one pound of source is always much greater than the cost of adding one pound of harness. However, harness mass optimization may be warranted when the spacecraft mass is rigidly constrained to fit the launch vehicle or for some other reason.

9.8 HARNESS DESIGN PROCESS

The harness design is influenced by the following factors:

- The rated current and the allowable voltage drop determine the conductor gage
- The bundle size and steady-state temperature also determine the gage
- The rated voltage determines the insulation thickness, and the temperature rise determines the insulation material
- The derating requirement increases the gage thickness
- The specific power of the source is factored in to determine the optimum wire gage
- Reliability goals may require redundant wires or double-insulated wires

The harness design proceeds as follows:

1. Determine the maximum steady-state dc or ac rms current for each harness segment on the spacecraft. For each segment, size the wire to carry the required current per the applicable derating factors. The harness wires

always run in large bundles, so the derating factor for a bundle of 15 or more wires generally applies.

2. Determine the voltage drop and compare it with the requirement. If the requirement is not met with the wire selected in step 1 above, use more wires in parallel or increase the wire size until the voltage drop requirement is met.
3. If an open wire in a current path constitutes a failure, i.e., if either the voltage drop or the derating criteria are not met with one wire open and if there is no other redundant current path, then another wire should be added to guard against this mode of single-point failure.
4. Ensure that the wire(s) in a particular current path will not be damaged to the point of propagating the damage to the surrounding wires when a smart short occurs. A smart short is one that draws current insufficient to blow the fuse but in excess of the wire's derating. In such a case, determine the value of the steady-state current that can cause damage to the wire insulation and could propagate to other wires. If that current is less than the expected steady-state dc or rms fault current, then the harness must be increased in size to a point where the smart fault current cannot cause damage that could propagate through the harness.
5. The harness should be secured to withstand the mechanical repulsive forces, which can be significant during hard faults. The wires are generally tied to each other or all together in a group, often attached to structural tubes, as shown in Figure 9.6.

The mechanical repulsion force (in newtons per meter) between two parallel conductors carrying currents I_1 and I_2 in opposite directions, is given by

$$F = 80\ KI_1I_2\frac{s}{d}\times 10^{-7} \tag{9.10}$$

where K = conductor shape factor = 1.0 for round conductors.

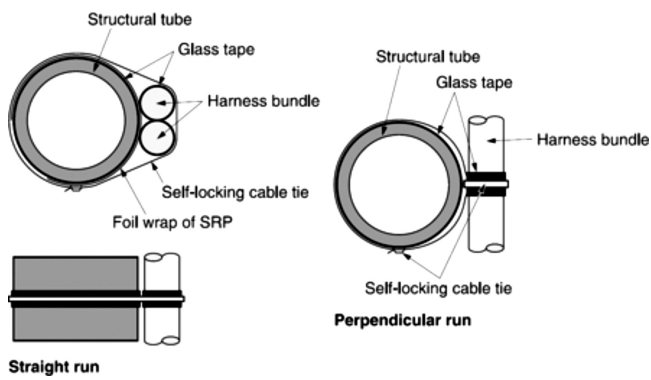

FIGURE 9.6 Placement and attachment of the harness with structural tubes.

9.9 FLEXIBLE HARNESS

The slip rings can experience cold welding on high-radiation satellites, as with a GPS. The flexible harness (coiled cable) that can accommodate the sun-tracking rotation of the solar array can eliminate the slip rings. The harness with ±90° flex has been considered for MEO satellites requiring 20,000 cycles of flexing over 15 years of mission life. Incorporating a flex harness in the design at present is within development reach. Some key features of the design are:

- The flex harness is completely enclosed inside a Faraday cage (solar array boom), hence unaffected by deployment behavior, environment shielding, EMI, etc.
- Harness flexing is required only between the SAD and the structural bulkhead.
- The harness outside the Faraday cage remains the same, so the cable interface with the bus is unaffected.

The cable needs to be ultra-flexible with very thin, hair-like strands. This may impose a manufacturing problem in crimping and ascertaining that no whiskers are left projecting out. A fully developed space-qualified flex harness could eliminate the slip rings, which weigh several kilograms per spacecraft. The harness mass, however, would remain the same. A flexible fluoropolymer insulated cable with 20-gage wires for power and 24-gage wires for signals has been built and tested in the past.

The flexible harness was used by ESA in 2002 for a Mercury mission. In this design, the solar panels rotate ±180° around one axis to keep the operating solar cell temperature below 150°C at AU < 0.375. The sun-shielded solar array drive has no slip rings but uses a flex harness sufficiently flexible for ±180° rotation.

9.10 FUSE PROTECTION

The fuses are provided to protect the power system from internal faults or faults in load circuits. The general fusion practice in the spacecraft is as follows:

- Fuses are placed near the source for protection against faults in the wires and also to reduce local fuse blow voltage spikes in adjacent loads (crosstalks). Fuses are located as close as possible to the PRU (Figure 9.7). The fuse boards are often located inside the PRU.
- All noncritical loads are individually fused to prevent a fault in any load from damaging the power system.
- In full-length redundant wires, fuses are placed in both lead wires (Figure 9.8).
- Critical loads are not fused to maximize reliability, but they use double-insulated wires. When a fuse is required in a critical load circuit, redundant fuses are used, as often required by NASA (Figure 9.9).
- Suitable load path redundancy is provided such that a single fault in a device or wiring does not permanently open or short the main bus itself or essential bus loads.

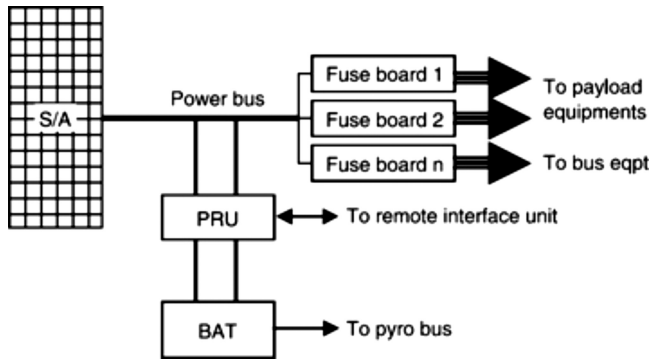

FIGURE 9.7 Fuse boards located in or near the PRU for various load groups.

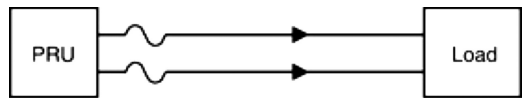

FIGURE 9.8 Full-length redundant wires with fuses in both lead wires.

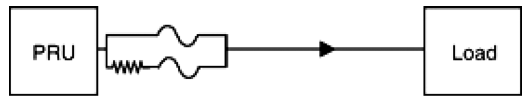

FIGURE 9.9 Redundant fuses in a single, nonredundant, double-insulated wire.

A typical construction of the fuse used for protecting semiconducting devices is shown in Figure 9.10. The fuse element may be silver, copper, or nickel, with silver being more common for long-term stability. It has a reduced section for better predictability. The body is generally filled with sand-type filler to suppress sparks when the fuse element melts and interrupts the inductive energy of the load and the wires. The fuse life is determined primarily by the metal's aging under thermoelastic cycles.

Because of the lack of a sufficient market, only a handful of commercially available fuses have been space-qualified in limited ratings. Among them are Piocofuse™ series 265 and Little™ fuses in small ratings; and Bussmann™ fuses in large ratings. They are basically commercial nonsealed fuses, except that source control drawings are added for tractability to qualify for space.

Picofuses use nickel elements in less than 1 A ratings, 50% silver and 50% copper elements in 1 to 4 A ratings, and copper elements in greater than 5 A ratings. All elemental materials have a high positive temperature coefficient of resistance. They rise in resistance with temperature, thus preventing an absolute shortage.

Nonsealed fuses, however, pose design difficulties when the bus voltage exceeds 50 V dc. This is due to arcing in partially evacuated construction. Hermetically sealed fuses address this problem. P600L™ fuses made by Mepcopal Corporation

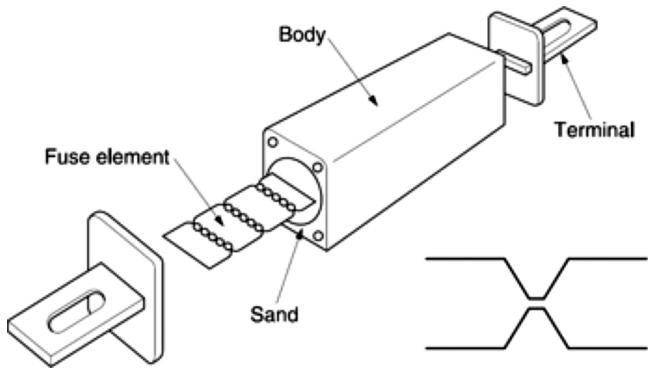

FIGURE 9.10 Typical semiconductor fuse construction.

are such space-qualified fuses. These fuses are made using thick film material. The fuse element is primarily gold, while the terminal pads are silver. These materials are deposited onto a 96% alumina substrate and coated with dielectric overglaze, which is cured at high temperatures. An arc suppressant glass of about 0.5 mm is then printed over the fuse element. When the fuse melts under a fault, the gold element melts and migrates readily into the arc suppressant glass coating, thereby effectively preventing subsequent vaporization and ionization. This suppresses arcs and restricts the circuit voltage after the fuse blows. For these reasons, Mepcopal fuses are fast and more predictable in clearing time. The hermetically sealed case contains the spark generated while blowing. In fact, they have been developed for safe operation in explosive mixtures of chemical vapors for the National Electrical Code Class 1 environment (hazardous).

The ground insulation requirements imposed on fuses vary with the voltage ratings. For example, a 100 V fuse would typically have:

- Dielectric withstand of 500 V_{rms}
- Ground leakage current is less than 1 mA
- Resistance after the fuse clears is between 1 and 10 MΩ depending on the fuse rating and the fault current it interrupts.

9.10.1 Fuse Rating

The ampere rating of the fuse is the current it would carry indefinitely on the ground. The fuse clears (melts, blows) only at higher currents, as per its own *I–t* relationship. The fuse is required to carry 110% of the rated current for at least 4 h without blowing, blow within 1 h at 135%, and blow within 2 min at 200% of the rated current. On the faster side, the fuse clearing time is in microseconds for 10 times the rated current. The general criteria for setting the current rating of the fuse are:

- The fuse carries 110% of the rated current for a long time, in hours, without exceeding 70°C above the room temperature.

- The fuse clears 135% of the rated current within a specified time in minutes, which depends on the type of fuse.
- The fuse withstands full recovery voltage, which is equal to the open circuit voltage that appears across the fuse terminals after clearing the worst fault.

The selected fuse rating is typically 1.2–1.3 times the current rating of the load circuit it protects, rounded upward to the next standard available rating. The fuse rating must be carefully selected because both conservatively sized and liberally sized fuses are bad for circuit protection. The ambient temperature has an influence on the current rating of the fuse, as shown in Figure 9.11. It is desirable to uprate or downrate the fuse accordingly.

As for the voltage rating, the fuse can be operated at any circuit voltage as long as it can blow without suffering arc damage. When the fuse blows, the sharp break in the circuit current causes the full circuit voltage to appear across the blown fuse. If the load is inductive, the transient voltage across the fuse may be substantially high due to the inductive kick. A destructive arc may be formed across the fused element and continue to grow. In the worst case, the resulting heat and pressure may cause the fuse to explode. The voltage rating of the fuse is conservatively given such that the fuse can interrupt a dead short without shattering, emitting flame, or expelling molten metal.

The equivalent circuit during fuse current buildup and interruption is shown in Figure 9.12. The total energy dissipated in the fuse body equals the energy stored in the circuit inductance plus the energy supplied by the main power source. For safety, it should not rupture the fuse body. The current buildup obeys the following equation.

$$\frac{di}{dt} = \frac{1}{L}\left[V_s - V_f - R_i\right] \tag{9.11}$$

where V_s = source voltage, V_f = fuse voltage, R = fuse resistance, and i = fuse current. The fuse clearing has two distinct phases, as shown in Figure 9.13.

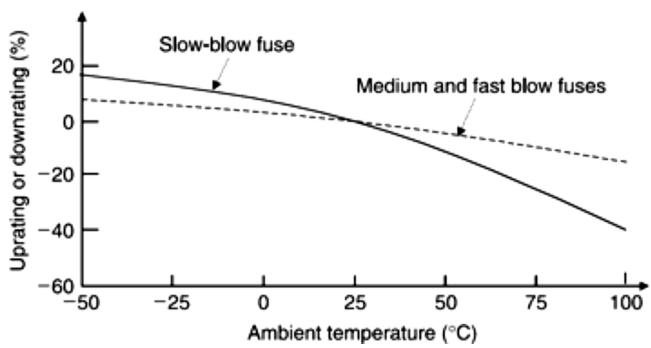

FIGURE 9.11 Effect of ambient temperature on the current carrying capacity of a fuse.

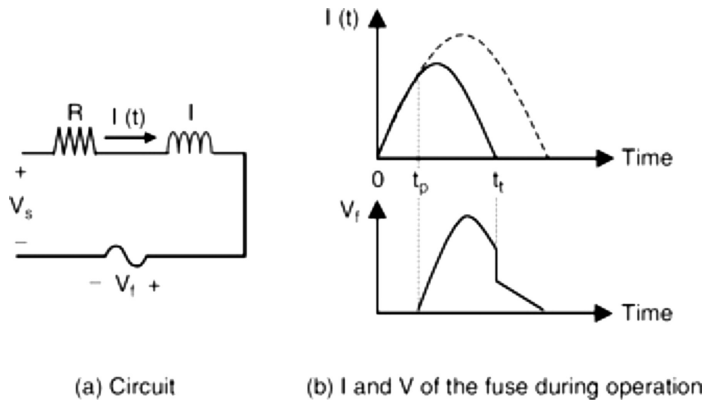

FIGURE 9.12 Equivalent circuit during fuse current buildup and interruption.

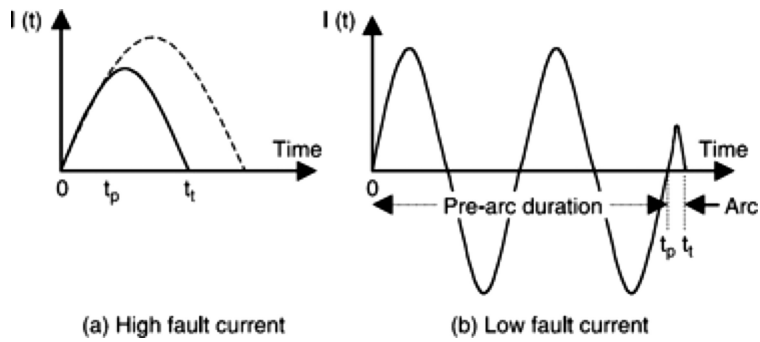

FIGURE 9.13 Fuse clearing process.

9.10.2 Types of Fuse

Although standard fuses are used in most load circuits, some loads may need relatively fast- or slow-acting fuses. Three types of fuse are available in the industry for different applications:

- Standard fuse for general use
- A time-delay (slow-blow) fuse designed to withstand the inrush current drawn by most equipment for a short time after turn-on
- A current-limiting (fast-blow) fuse, which limits the current by clearing the fault before current builds up from normal to full fault value through the inductive response of the circuit.

The typical blow time and applications are listed in Table 9.6. Figure 9.14 shows the current versus average blow characteristics of the three types. Even within a given type, significant variations exist around the average value, which must be considered in the system design to protect the circuit as required.

TABLE 9.6
Fuse Types and Their Typical Applications

Fuse Type	Typical Blow Time (seconds) at 200% of Rated Current	Typical Applications
Fast blow	<1	Transistor circuits and meter protection
Normal blow	1–10	Most standard circuits
Slow blow	>10	Circuits drawing high inrush current on switch-on, e.g., motors, transformers, heaters, capacitor charging, etc. It avoids nuisance blowing.

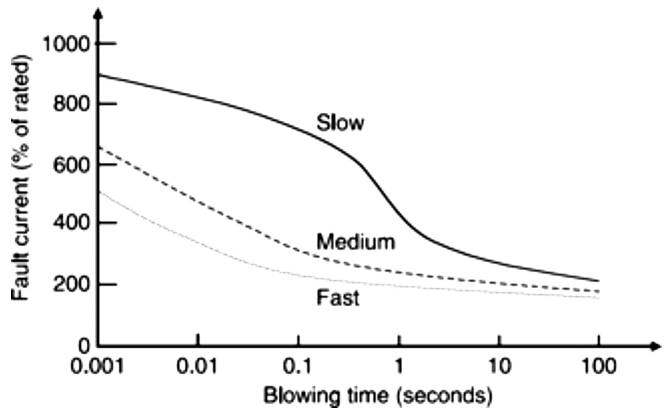

FIGURE 9.14 Current versus blow time for three types of fuses.

9.10.3 Fuse Characteristics

The fuse element generates heat at the rate of I^2R watts. Under steady-state conditions, this heat is dissipated in the surrounding environment, keeping the element's temperature and resistance stable. Under a fault, the heat generated at a very high rate raises the element to melting temperature, typically in milliseconds. Assuming adiabatic heating (negligible heat escaping the fuse body in a short time), the thermal energy balance requires I^2Rt to be equal to the heat capacity of the fuse up to the melting temperature, which is constant for a given fuse. Assuming the element resistance is constant, I^2t is also constant. The clearing time t is thus inversely proportional to I^2 in the first approximation. The fuse resistance rising with temperature alters this relationship to some extent.

The room-temperature resistance of the fuse element has significant manufacturing variations, but it primarily depends on the current rating. However, the voltage drop across the fuse at nominally rated current is kept between 100 and 200 mV by design. The manufacturing variation in clearing time is also significant.

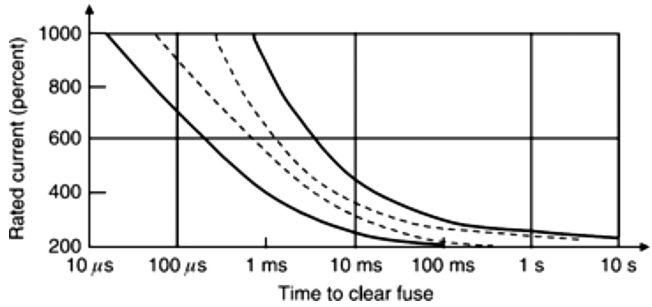

FIGURE 9.15 *I–t* characteristic band of normal-blow, hermetically sealed fuses.

For this reason, the *I–t* characteristic is generally depicted by two curves bounding the minimum and maximum times to clear the fuse at a given current (Figure 9.15). Such curves are derived by the vendor from numerous tests. Test data on recent manufacturing lots is often shown by dotted lines for guidance to the users on the latest design and manufacturing practices. Even then, the variations in clearing time are wide and must be accounted for in the power system design. Table 9.7 shows the variations in hermetically sealed fuses. Variations of 1:10 or 1:15 are common. They are even wider for traditional nonsealed fuses. The clearing time is less predictable in the normal- and slow-blow fuses because the plasma lingers for a longer duration. Plasma behavior is difficult to predict with high certainty. The fast fuse and sealed fuse, on the other hand, have a more predictable clearing time.

Many aerospace customers require transient survival analysis to demonstrate that each load's input current matches the blow curves of the fuse assigned to the load. With the actual parameters of the assigned fuse, detailed fault simulations are run on computers to verify that:

- The fuse **will** clear under the minimum fault current using the right-hand side of the *I–t* envelope in the simulation run.
- The fuse **will not** clear under maximum inrush current during start-up of motor and heater-type equipment using the left-hand side of the *I–t* envelope in the simulation run. In circuits where high start-up current lingers for a long time, posing a risk of an unwanted fuse blow, one may use a slow-blow fuse of the same rating.

9.10.4 Fuse Derating

The arcing and heat transfer in space are much different compared to those on Earth, where the fuse rating is established by tests. The space-qualified fuse is sufficiently derated from its normally rated current on Earth to obtain high reliability under the actual load current it would carry in service. The derating factor is defined as the ratio of the permissible load current to the nominal fuse rating. The purpose of derating is essentially to stay below the current when the resistance of the fuse element remains stable. Otherwise, it will experience an eventual thermal runaway leading to

TABLE 9.7
Typical Variations in Blow Time at 500% Rated Current in Hermetically Sealed Space-Qualified Fuses

Current Rating (amp)	Fuse Type	Minimum Blow Time (second)	Maximum Blow Time (second)
3	Normal blow	0.0004	0.0065
3	Slow blow	0.002	0.02
10	Normal blow	0.0004	0.0065
10	Slow blow	0.003	0.045

melting. Significant variability exists in the blow characteristic and the atmospheric pressure surrounding the fuse element in space. For this reason, nonsealed fuses for 1 A and smaller loads are typically derated to 35% and 70% for 5 A and larger loads. Since the blow characteristic of a hermetically sealed fuse is more predictable, the corresponding derating factor is 80% for fuses larger than 0.5 A rating. The largest hermetically sealed fuse available at present is 10 A. Further derating can come from higher than normal ambient temperatures. It follows the following rules:

- 0.5% derating per °C ambient above 25°C for time-delay fuses
- 0.2% derating per °C ambient above 25°C for regular fuses

Yet additional derating may be imposed based on the specific mission environment. If the total fuse derating in space is, say, 40%, then a fuse with a nominal ground rating of 10 A must be used in a 4 A load circuit in space. This, however, creates a protection problem in ground testing, where a soft fault may carry the current for a long time and burn the wires. For this reason, an additional 4 A fuse (40% of the nominal 10 A rating) is inserted in series all the way up to the launch pad. It is then removed before the launch.

Most faults in space are hard faults that clear the fuse quickly. The fuse closer to the main bus clears even quicker under fault. However, a secondary circuit fault at the end of a long line may clear slowly due to the voltage sag and the resulting low fault current.

9.10.5 Fuse Selection Criteria

The following considerations enter into the fuse selection process:

- The fuse current rating after the required derating must be equal to the nominally rated circuit current after allowing for the overload margin and the harness gage.
- The fuse voltage rating must be greater than the source voltage for ac or dc circuits.
- The maximum current interruption capability of the fuse must be greater than the maximum possible fault current at the fuse location.

- The fast fuse is not necessarily better in all applications. However, it is required to protect semiconductor devices with $I^2t_{\text{fuse}} < I^2t_{\text{semiconductor}}$. With a fast fuse, the clearing time is less than the first peak of the fault current and is more closely governed by constant I^2t because the rise to melting temperature is much closer to being adiabatic.

9.10.6 Redundant and Parallel Fuses

If a load circuit uses redundant wire pairs for reliability, then each wire pair must have a separate fuse. Even with single wires, some customers, such as NASA, require redundant fuses in most load circuits. If one fuse fails randomly under normal operation, the redundant fuse can carry a full load for the remainder of the mission. A redundant fuse in a 5A circuit cannot be achieved just by placing two 5 A fuses in parallel, which essentially derates the fuse by a further factor of one-half. Instead, an additional series resistance equal to several times the fuse resistance is inserted in series with the redundant fuse. Since the current sharing between the redundant fuse branches is inversely proportional to the branch resistance, the primary fuse normally takes about 90% of the load current.

Parallel fuses (Figure 9.16) are used to obtain a fuse assembly with a current rating in multiples of the individual fuse rating. Parallel fuses are not to be confused with redundant fuses. Parallel fuses are required to share equal current and therefore do not have additional series resistance in one branch. As a matter of fact, two parallel fuses must be matched for equal resistance at operating temperature. Parallel fusing is not feasible with nonsealed fuses due to the great variability in their resistance at the operating temperature. One of the nonsealed fuses would always be stressed beyond its derated value and blow prematurely. Two heretically sealed fuses with matching resistance, however, can be connected in parallel to share almost equal current. Even with hermetically sealed fuses, it is difficult to balance the current with more than two fuses in parallel due to a possible zipper effect. For example, consider a 20 A fuse assembly consisting of four 5 A fuses in parallel (Figure 9.16). If one 5 A fuse blows prematurely, all will blow one after another by taking progressively higher current. If the 5 A fuses are highly derated to avoid such an effect, then the protection level of the load circuit is compromised. The zipper effect, however, can be used to avoid a large fuse blow transient voltage by using a few small fuses in parallel with about 10% of the fuse resistance in series in each fuse branch. In the event of an internal equipment fault, these fuses blow in zipper sequence, reducing the fault current as they blow progressively faster in turn. The last fuse blows fast and under the smallest current, thus resulting in a less severe voltage transient.

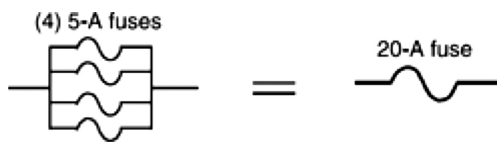

FIGURE 9.16 Parallel fuses increase the current carrying capacity of the fuse assembly.

9.10.7 Fuse Testing

Fuses are tested as follows for proper resistance after the installation but before powering the assembly. A four-arm resistance bridge and a suitable voltage source are used for these tests:

- A cold test with minimum current to assure minimum self-heating (as opposed to a hot test at full rated current).
- The maximum test current is generally 1 mA for fuses rated 1/8 A or less, 10 mA for fuses rated 1/8 to 1 A, and 100 mA for fuses rated greater than 1 A. The measurements are compared to the expected value given in the fuse specification document to verify that the fuse is within tolerance, as opposed to merely checking the circuit continuity.
- When two fuses are installed in parallel, the dc resistance of each fuse must be within 50% of the value specified for the individual fuse. The test current in this case is chosen based on the fuse assembly resistance. The design engineer must be consulted if more than two fuses are installed in parallel for a special measuring sequence or other instructions.

9.10.8 Unfused Loads

Critical loads are not fused for reliability, and some parts of the power system cannot be practically fused. For example, fuses cannot protect the main bus or the harness between the bus and the fuse board in current-limiting designs. In such circuits, all wires are double-insulated between the lead and return lines and between the lead and the structure. The double insulation is implemented by placing two physical layers of insulation between two isolated conductors. An isolated conductor layer is placed between the insulation layers of the double-insulated wire to verify the integrity of each insulation after the assembly. The insulation resistance is then measured between the intermediate conducting layer and each layer of insulation. Often, connections via a daisy chain or other method are provided to test all double-insulated points at the spacecraft level.

9.11 REMOTE POWER CONTROLLERS

Numerous solid-state remote power controllers (RPCs) are used on the ISS instead of fuses for protection against faults in various items of load equipment. The RPC has a programmable trip setting, controls the load power on and off, and provides dead-facing. When the RPC is dead-faced, it grounds both terminals to zero voltage for personnel safety. On the other hand, when the load is turned off or has tripped, the output terminals may still be alive with voltage. All three functions of the RPC are remotely programmable. The basic design features of the RPC used on the ISS are as follows:

- Solid-state switches are in series with a dead-facing relay, which is magnetically latched. The relay coil voltage can be 28 V or 120 V

- Unidirectional or bidirectional power flow
- Programmable trip setting in 256 levels (8-bit data word) with the 1553 protocol for data interface
- Various maximum current ratings are available, such as 3, 10, 25, and 50 A unidirectional and 25 and 130 A bidirectional. Several small RPCs are packaged together such that each RPC box has a mass of about 2 kg and dimensions of about 15 × 15 × 7 cm. There is only one 130 A RPC available in this size box
- Trip time of 50–100 μs with approximately constant I^2t characteristics
- Control circuit power consumption of about 5 W at ±15 V and +5 V with quiescent power less than one watt
- The on-resistance of RPC varies with rating, such that the series voltage drop at the rated current is in the 0.25–0.50 V range in each rating

9.12 EARLY FAULT DETECTION

Many faults start as soft, high-impedance arcing faults and then develop into hard faults. It is desirable to detect a high-impedance fault early, locate it, and remove it using the redundant paths. This is particularly important in high-power systems (>100 kW). Because of the high voltage, the fault current is high in such systems.

The conventional fuse and RPC protect the system from hard faults only. On the other hand, high-impedance soft faults can be detected by monitoring the system voltage. The bus voltage would have a high-frequency hash if an arc were present. A continuous frequency spectrum analysis of the bus voltage can be useful in the early detection of an arcing fault. Once detected, the fault can be located and bypassed before it develops into a hard fault.

FURTHER READINGS

Gwozdecky, K., "Wiring Harness Design Methodologies and Assembly Integration and Test for a Modular Microsatellite Platform", Thesis submitted for Master's degree in Applied Science, Institute for Aerospace Studies, University of Toronto, 2020.

Malagoli, M. and Cosquéric, L., "Space Harness Design Optimization Opportunities on ECSS Derating Rules", European Cooperation for Space Standardization, Astrium Satellite, 31 Rue des Cosmonautes, 31402 Toulouse Cedex 4, France.

NASA Technical Standards, "Installation of Harness Assemblies (Electrical Wiring) for Space Vehicles, General Specifications", Office of NASA Chief Engineer, MSFC Report No. MSFC-SPEV-494, 05/01/2009.

Patel, M.R., "High-frequency High-voltage Power Distribution System". NASA International Space Station Report No. CR-175071, 1986.

U.S. Air Force Space and Missile Systems Command Center, "Standard Technical Requirements for Wiring Harness for Space Vehicles", Report (unclassified), OMB-0704-0188, 03 June 2009, Directorate for Information Operations and Reports, 1215 Jefferson Davis Highway, Suite 1204, Arlington, VA 22202-4302.

Uppal, R., "Satellite Harness Design, Optimization and Standards" International Defense, Security and Technology (CA, USA), Trending News, Information and Analysis, 7 December 2022, Issue.

10 Ancillary Components

10.1 INTRODUCTION

In addition to major components such as photovoltaic panels, batteries, power distribution, power electronics converters, and loads, the spacecraft power system includes many ancillary components such as the solar array drive, deployment devices, deployment controller, thermal controller, relays, battery monitors, current meters, and shielding equipment, among others.

10.2 SOLAR ARRAY DRIVE

The solar array drive and array drive electronics (SAD/ADE) together provide the capability of rotating solar panels with respect to the spacecraft body. The operation of the SAD is controlled by decoded uplink commands from the on-board computer (OBC). It receives a 128 Hz timing clock and a 0.25 Hz synchronizing signal from the OBC. In the 3-axis stabilized two-wing geosynchronous satellite, one axis is always aligned with the local normal to the sun and another axis along the orbit normal. Two sets of open-loop (clock-controlled) solar array drive motors maintain the sun's orientation. A brushless dc stepper motor rotates each panel separately. The slip rings on the SAD shaft provide an interface between the rotating panel and the fixed Earth-pointing spacecraft body. One SAD controls the north panel, and the other controls the south panel. The two are interchangeable in design, where the 'forward' direction of rotation is separately selected by external means. Each SAD has only one mechanical assembly but has a redundant motor winding and redundant position telemetry potentiometer. Only one set of the windings is powered at a time. The redundant windings are fully isolated to prevent failure propagation. A reliability of 0.99 is typical for both sides combined over a 20-year mission. The mass of each SAD/ADE assembly may be about 5 kg on geosynchronous Earth orbit communications satellites.

The SAD/ADE provides telemetry defining its status and that of the solar panel. Each unit provides a potentiometer voltage signal that is directly proportional to the angular position of the panel shaft, ranging from 0 V at 0° to +5 V at 360°. The grounding scheme for ADE uses four separate grounds, one each for the power, signal, and communication circuits, and one for all equipment chassis. The ADE controls all three operating modes of the solar array, namely normal forward, slew, and reverse. The SAD is capable of rotation in the forward and reverse directions at speeds from 0 (stop) to 8 Hz as commanded by the ADE. The solar array is initially aligned with the ground. The ADE maintains the alignment in an open-loop control system. It takes the time signal from the spacecraft clock and turns panels to the sun continuously as per the clock time without further command. The SAD is fairly accurate but accumulates small errors, typically a couple of degrees per month.

DOI: 10.1201/9781003344605-12

The sun sensor detects the errors, which are corrected by periodic commands from the ground or from the spacecraft computer. On some satellites, the solar array is slewed every 6 AM until the error is zero. The spacecraft's computer commands can be overridden by the ground for maneuvering or other reasons.

The slip-ring assembly, also known as the power transfer assembly, transfers power and telemetry signals to the spacecraft body. Each power and telemetry lead wire uses a separate slip ring, but some returns may share a common ring within their derated current capability. The current collecting slip rings and carbon brushes make the rotary joint (α joint) between the sun-oriented solar panels and the Earth-oriented spacecraft body as the spacecraft revolves around the Earth. The slip-ring brushes may be traditional monofilament brushes or high-conductivity fiber brushes made with graphite or silver fibers for enhanced current collection with low power loss. For small satellites, companies like Honeybee Robotics and Moog make lightweight and compact solar array drive assemblies for positioning solar array panels.

10.3 DEPLOYMENT DEVICES

Three main methods of deploying various spacecraft components are discussed below.

10.3.1 Electro-Explosive Device

This is the traditional method of deployment, which is also known as pyrotechnique ordnance. It uses an electro-explosive device (EED), in which electrical energy is supplied to ignite the squib of explosive powder. The resulting force then deploys the component, typically under a spring-loaded force. The EED is ignited when a certain current deposits a certain amount of energy in a specified amount of time. For safety reasons, it must withstand a certain minimum amount of energy without igniting. A typical EED is rated at 1A–1W, no fire, and 4A–4W, sure fire.

The EED requires heavy shielding and great care with regard to EMI pickup. Moreover, the EED explosive is thermal and shock sensitive. Therefore, the installation of sensitive EED explosives is sometimes done at the launch pad, which costs much more than at the factory. A pyro harness is routed separately from the power and signal harnesses to minimize EMI concerns for safety. EED deployment technology, although used for several decades, has some disadvantages, such as:

- All spacecraft components must be designed to withstand severe pyroshock excitation.
- High safety-related costs in documenting, reporting alerts, and all other stringent regulations on EEDs must be complied with.
- Some manufacturers install EED squibs at the launch pad, while most install them at the factory. In the latter case, the spacecraft is transported as a class-1 explosive (sensitive to thermal and shock environments), and this adds expense.

10.3.2 Laser-Initiated Deployment

Figure 10.1 depicts the laser-initiated ordnance schematic, where the light emitted by diode D_1 is transmitted to the squib by an optical fiber. The photon energy deposited in the squib ignites the explosive. After the firing, a sense light is sent by pulsing D_2 and sensing the transmission, reflection, or refraction of the sense light. This is to confirm that the squib has been fired. This technology has been space-qualified and flown. It has the following advantages over EEDs:

- It is insensitive to EMI, RFI, ESD, EMP, and crosstalks. Hence, it eliminates accidental firing and related human safety issues. This reduces the cost not only in flight but also in the factory, in transportation, and at the launch pad.
- Insensitive to harnesses and explosive placements.
- Requires no shielding; hence, the harness mass is significantly reduced.
- Lower integration and test costs, since no EMI silence clearance is required in the factory or on the launch pad.
- Insensitive explosives allow factory installation, which costs less.
- Higher reliability.

10.3.3 Shape Memory Metal

Recently, shape memory metal deployment technology has been developed for some satellites, such as EOS-AM and PM. In the working principle, a certain metal, when heated, regains the shape it possessed before forming into a new shape. In a way, the metal 'remembers' its original shape and returns to it when heated. The heat is applied by a traditional heater, which is insensitive to EMI. The most prominent benefit of using shape memory metal deployment is the savings in safety-related costs. More recently, a new plastic with shape memory has been developed at the Massachusetts Institute of Technology. It can be shaped as a string and inserted into a body through a hollow tube. When heated, it changes into a sheet or other shape by manipulating the temperature and stress.

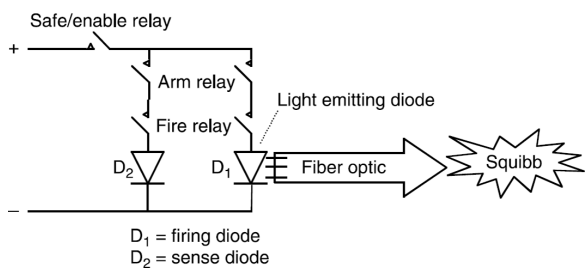

FIGURE 10.1 Laser-initiated ordnance schematic.

10.4 DEPLOYMENT CONTROLLER

The deployment controller, also called the ordnance controller, delivers a constant current to the deployment devices. In the traditional pyroelectric bridge wire, the wire resistance rises with temperature. The required voltage must therefore rise accordingly to supply the specified minimum current, typically a few amperes. If the bridge wire is supplied with a constant voltage source, it must carry the specified minimum current at the peak temperature of around 800°C. The peak current is typically several times the minimum current specified for 10–20 ms. The relay must be capable of handling the peak current a sufficient number of times without overstressing. Figure 10.2 is a typical ordnance controller circuit powered directly by the battery through the pyro enable plug. The safe and arm plugs are placed between the ordnance controller and the EED squibs. Power is supplied via a redundant path to a redundant EED, one from each battery. When the enable and arm relays are commanded on, the EED is ready for the fire command. The fire command turns on the EED cavity relay, sending a pulse of power to the EED squib, which activates the deployment mechanism that cuts a rope or a bolt.

The ordnance controller can be powered directly from the battery or from the bus via PRU (Figure 10.3). For reliability reasons, the deployment power is generally drawn directly from the battery by unfused circuits. In mid-sized communications

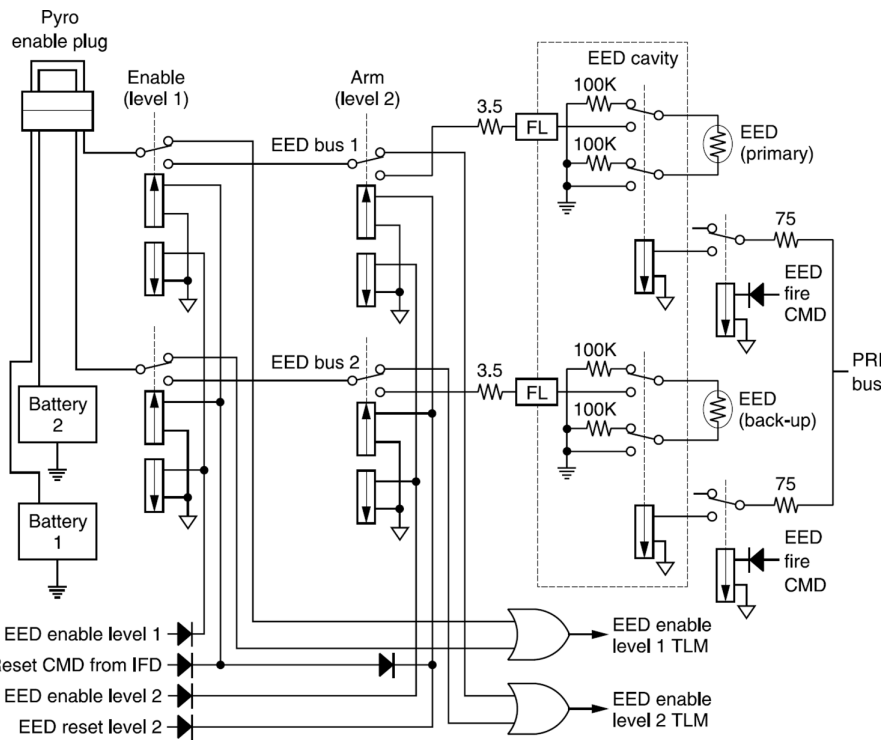

FIGURE 10.2 Ordnance controller circuit schematic.

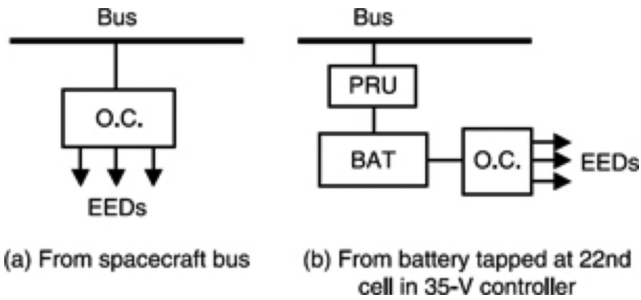

FIGURE 10.3 Ordnance controller powering options. (a) From the spacecraft bus. (b) From the battery tapped at the 22nd cell in the 35 V controller.

satellites, each battery is typically capable of supplying a peak pyro load greater than 10 A for 10 s, 25 A for 5 s, or 50 A for 5 ms with a 70%–100% state of charge. The battery bus impedance is typically greater than 100 mΩ for dc to 10 kHz. Two independent pyrobusses are tapped from the 22nd cell of each battery without cross-strapping. The voltage ranges from 22 to 35 V, and one cell failed. Each pyro bus—also known as the essential bus—powers the primary and backup pyro loads, respectively.

10.5 THERMAL CONTROLLER

Various probes are required to sense temperature at various locations of the spacecraft for use with telemetry-thermometers and temperature controllers. A probe may contain any one of the following temperature-measuring elements.

10.5.1 Thermocouple

A thermocouple utilizes the Seebeck effect, which occurs at the junction of two dissimilar metal wires. Thermally energized electrons in each metal generate a dc voltage at the hot junction, which is measured at the cold end. The magnitude of the voltage is linearly proportional to the temperature. The measurement error is minimized by keeping the cool end at a constant temperature and using a voltmeter that has high input resistance.

10.5.2 Metallic Resistance Wire

In a metallic resistance wire, the temperature change is derived from the change of wire resistance compared to the reference value R_o, using the relationship $\Delta R = \alpha R_o \Delta T$, where $\alpha =$ temperature coefficient of resistance per degree centigrade. Platinum is one element that is often used in space as it not only has high resistance but also a high temperature coefficient of resistance that is linear and stable over a wide temperature range. For platinum, $\alpha = 0.003$ per °C at 20°C.

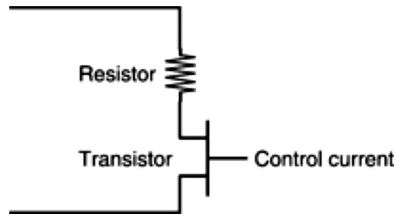

FIGURE 10.4 Proportional heat control circuit.

10.5.3 Thermistor

A thermistor is a semiconductor in which a small change in temperature causes a large change in electrical resistance. A precise measurement of the resistance gives a direct reading of the temperature at the thermistor location. This allows a simple readout instrument and the use of long leads without loss of accuracy. The temperature coefficient of resistance for the thermistor is negative and two orders of magnitude greater than that of metallic wires. The resistance of a typical thermistor at various temperatures is 75, 7, 3, and 1 kΩ at −40°C, 0°C, +20°C, and +40°C, respectively. The thermal time constant ranges from 5 to 15 s. The interchangeability tolerance is within ±0.1%.

The resistance wire and thermistor probes require applying a current and measuring the voltage across the element, from which the resistance is derived using Ohm's law. Since the thermal time constants are relatively long, the temperature is measured only periodically by passive telemetry to save energy. A constant current pulse is sent, and the voltage is measured periodically across the element. The heaters are turned on or off as needed in response to the temperature telemetry. Instead of using conventional thermostats to turn the heat completely on or off, the proportional heat control is often used. It employs a transistor in series with a fixed resistor (Figure 10.4). The control current is changed in response to the average heat required. The heat generated equals the heat required less the payload-generated heat. This avoids frequent on–off cycling with the conventional thermostat, where the heater is either on or off. The proportional heat control provides a steady current with no on–off cycles, thus eliminating the EMI. It is particularly useful with EMI-sensitive equipment, such as science instruments.

10.6 RELAYS

The electromechanical relay has physical metal contacts that open or close on command as required. It offers certain advantage over transistor switching, such as negligible power loss, and it can be used singly without an auxiliary circuit or with a very simple circuit. On the negative side, it has a limited life due to a moving contact that wears. If arcing is present under normal or abnormal operation, it results in EMI and a much shorter life.

Relays come in a holding or latching variety. Most space-qualified relays are rated for 28 V and up to 30 A dc. Larger current ratings come from Leach, and smaller

ratings from Genicom and Teledyne corporations. They are typically hermetically sealed in nitrogen at 1 atm and life-tested for tens of thousands of cycles. Typical weights of 1, 5, and 10 A dc double pole-double throw 28 V relays are 3, 15, and 45 g, respectively. All relays for space applications are derated to 50% of the ground base current rating. Contacts are designed such that the voltage drop at rated current is 0.1–0.2 V.

Relay contacts for switching high currents around 50 A are difficult to procure, heavy, and vulnerable to vibration and shock environments during the launch phase. In a relay with spare poles, two poles can be connected in parallel to double the current capacity of the relay. Multiple-pole space-qualified high-voltage relays are also difficult to procure. For this reason, many engineers find it necessary to use relays at voltages higher than rated values after derating to a lower current. Since the arcing voltage on breaking the current is equal to $L\mathrm{d}i/\mathrm{d}t$, the contact ampere rating at a higher than rated voltage decreases linearly in theory. However, manufacturers' test data suggests a square function, i.e.,

$$\frac{\text{actual current capacity}}{\text{rated current capacity}} = \left(\frac{\text{rated voltage}}{\text{actual application voltage}} \right)^2 \tag{10.1}$$

The derating data for 5, 10, and 15A latching relays is depicted in Figure 10.5. It is important to avoid arcing by absorbing and dissipating the inductive energy in the relay coil and the load circuit. Various schemes shown in Figure 10.6 for this purpose are: (i) steering and suppression (freewheeling and series) diodes, (ii) bifilar coil with one side shorted, (iii) diode and Zener, and (iv) series R–C circuit. The relay is often required to "make before break" or "not to make before break." A relay failure in maintaining this sequence can cause damage. Relay coils interfacing with the discrete command decoder are isolated from all circuitry. Connections between the command relay coil in the user equipment and any primary or secondary returns are prohibited. Steering and suppression diodes are located in the user equipment (Figure 10.7).

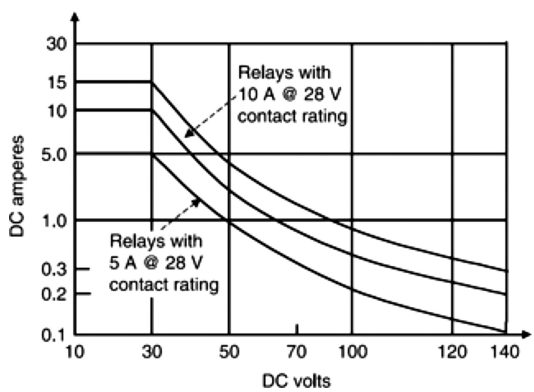

FIGURE 10.5 Typical 5, 10, and 15 A, 28 V relay derating for dc voltages above normal rating without arc suppression.

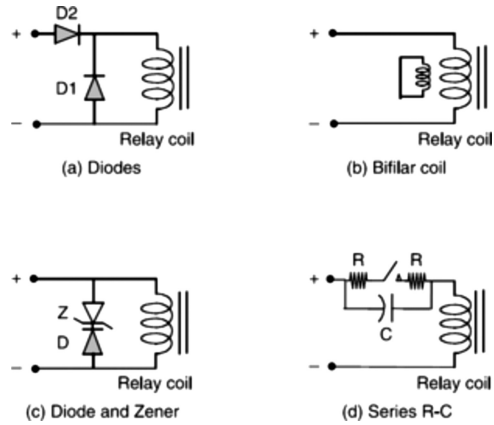

FIGURE 10.6 Relay contact protection schemes for absorbing inductive energy. (a) Diodes. (b) Bifilar coil. (c) Diode and Zener. (d) Series R-C.

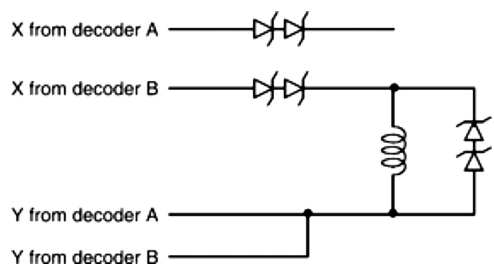

FIGURE 10.7 Typical relay load circuit.

10.7 BPM AND BCVM

In some satellites launched in the 1980s and 1990s, particularly with NiH_2 batteries, the battery pressure monitor and the battery cell voltage monitor (BCVM) were part of the PRU. Each battery pressure monitor strain gage, along with its dedicated amplifier, is adjusted for offset and gain to normalize the output. The output is adjusted at the battery vendor to meet the specified offset tolerance (in ± microvolts) at room temperature and zero pressure, as well as at room temperature and a high pressure like 1000 psig. The strain gage voltage is null at zero pressure and is typically 6 mV at high pressure. In batteries other than NiH_2, typically a couple of cells in each battery may have pressure and temperature telemetry for battery health monitoring.

10.8 BATTERY LETDOWN UNIT

The battery letdown unit is a resistor assembly used to drain the battery completely during storage on the ground, for transportation to the launch pad, or on orbit for reconditioning. For on-orbit letdown, two drain rates are used: high at the beginning

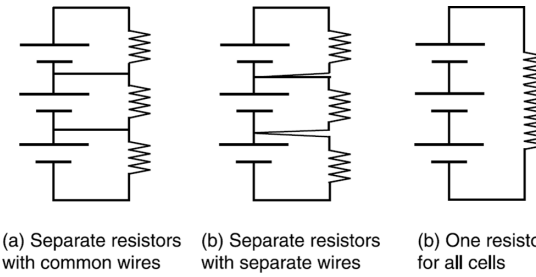

FIGURE 10.8 Battery letdown resistor network options. (a) Separate resistors with common wires. (b) Separate resistors with separate wires. (c) One resistor for all cells.

and low at the end. The drain resistance per cell is typically 1 or 0.5 Ω with a thin high-resistance harness. Three alternative design configurations of the battery letdown unit are shown in Figure 10.8. The approach (a) is often used. It works well as long as cell voltages are equal. However, cell voltages often diverge near zero at the end of draining. The unequal loop currents under this condition cause unequal voltage drops in the harness, leading to errors in the cell voltage measurements across the resistors. A measured cell voltage that is positive could in fact be negative. This problem can be remediated by:

- Software compensation for uneven voltage drops in the harness for real-time corrections.
- Dedicated resistors for each cell with their own harness are shown in Figure 10.8b. This adds some harness mass.
- A single-resistor design is shown in (c). It saves some harness mass but also loses the ability to monitor each cell's voltage and drive it to zero individually.

10.9 CURRENT METERS

Three types of current meters are used in space: the shunt, the Hall-effect transducer, and the magnetic amplifier.

Shunt: This sensor is essentially a known, precise resistance inserted in series with the load. The voltage drop measured across it is linearly proportional to the current. It has a low cost but introduces a power loss and a reliability risk of failing. Moreover, it offers no electrical isolation, which may be an issue in high-voltage buses.

Hall-effect transducer: It is an electromagnetic transducer that generates voltage when electrical current and a magnetic field are simultaneously imposed on the conducting transducer material. With reference to the flat plate transducer of Figure 10.9, a current density J applied in the x-direction and a magnetic field B applied in the z-direction result in an electric field E_H

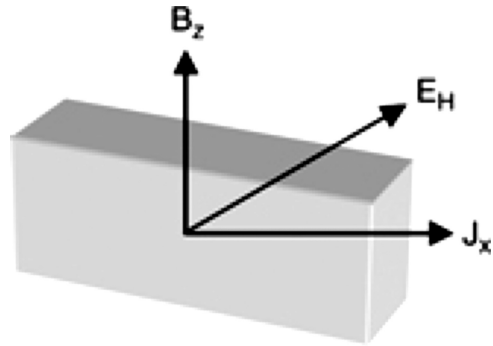

FIGURE 10.9 Hall-effect transducer as a current sensor.

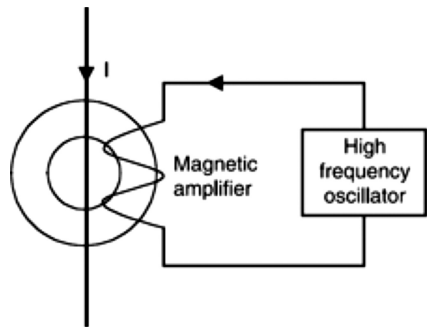

FIGURE 10.10 Magnetic amplifier current sensor.

in the y-direction with magnitude $E_H = R\ (B \times J)$, where R is known as the Hall coefficient. The voltage measured across the y-thickness is calibrated in terms of the current in the x-direction.

Magnetic amplifier: Figure 10.10 shows a schematic of the magnetic amplifier's current sensor. The current I through a magnetic core causes the core to saturate, the effect of which is measured as the increased voltage across the coil. Magnetic amplifiers are often used to measure the output current of the north and south solar array wings separately to provide a health check. In this use, the amplifier has no mission-critical failure mode. A loss of a sensor is merely that—a loss of a sensor—with no impact on the bus power. It costs more but has no power loss in the transducer itself. However, it needs an oscillator, which requires power. Having no contact with the current path, it provides electrical isolation and can be inserted as an afterthought.

10.10 CAPACITORS

Numerous capacitors are used in a typical space power system. In the bus voltage ripple filter, they store and deliver energy over one cycle. In snubber circuits, they absorb and dissipate transient voltage energy in solar circuits (PRU, LPC, etc.). The

energy storage per unit mass of the capacitor varies with its construction and voltage-withstanding capability. However, typically low-voltage (28 V) capacitors have a specific energy of 20 J/kg, medium-voltage (1 kV) capacitors have 100 J/kg, and high-voltage (20 kV) capacitors have 200 J/kg. The mass density of high-voltage capacitors is around 2 kg/l (0.07 lb/in^3). The various types of capacitors and their applications are as follows.

Tantalum capacitor: The tantalum capacitor provides relatively high-density, low-cost energy storage. The maximum voltage rating of standard production-line tantalum capacitors is 100 V with 50% military derating. Thus, a 50 V bus is the limit for 100 V capacitor applications. The tantalum capacitor is generally heavy and comes in two configurations:

- **The foil (film) type** has a high equivalent series resistance (ESR) that causes high-power loss. Naturally, this type finds applications in circuits where damping resistance is a design requirement.
- **As a solid sintered powder** bonded in one solid porous body. It has a low ESR and finds applications in ripple filters where pure energy storage is required.

Metalized polypropylene capacitor: The metalized polypropylene capacitor is available at higher voltages. A 300 V-rated capacitor of this type used on a 120 V bus provides an adequate margin after 50% derating. However, it is bulky and offers no mass advantage over the tantalum capacitor.

Ceramic capacitor: The ceramic capacitor is made of chunks of ceramics with metal foil bonded on two faces. It can be operated at very high temperatures, with the ceramic–metal bond as the only weak link. It has a low ESR and is compact, but offers no mass advantage per microfarad. Ceramic capacitors are available at high voltages. The 160- to 120 V ISS bus has used ceramic capacitors.

Film capacitor: In recent years, film capacitors have been electrostatic (nonpolarized) capacitors that have been used in a variety of applications. Film capacitors use plastic film materials as a dielectric. They have better stability and low-loss characteristics relative to other types.

10.11 FILTERS

A filter reduces the EMI entering or exiting the equipment. A low-pass filter is most commonly used to suppress conducted high-frequency interference using inductance, capacitance, or a combination of the two, as shown in Figure 10.11. The insertion loss I_L of a filter is defined as the difference between the noise voltage on load with the filter and that without the filter. It is usually expressed in decibels (dB). The capacitor is an efficient low-pass filter when connected in parallel to the high-resistance load. It has $I_L = 20 \log(\pi RC)$. The inductor is an efficient low-frequency filter when used in conjunction with a low-resistance load. It has $I_L = 20 \log (\pi L/R)$.

When L or C alone cannot provide the desired insertion loss, the L–C filter is constructed in the L, π, or T configuration shown in Figure 10.12. These filters are associated with the suppression of signals in the frequency domain, such as ripple

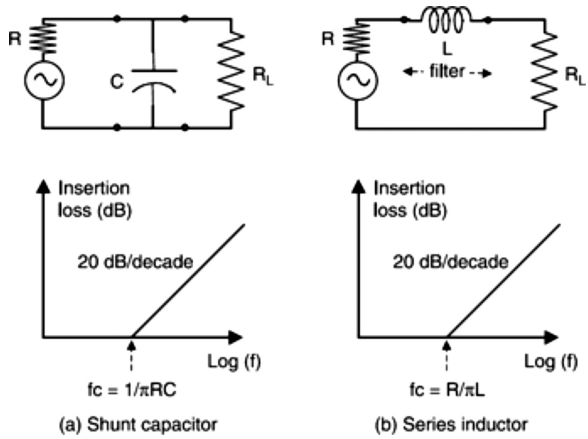

FIGURE 10.11 Single element filters. (a) Shunt capacitor. (b) Series inductor.

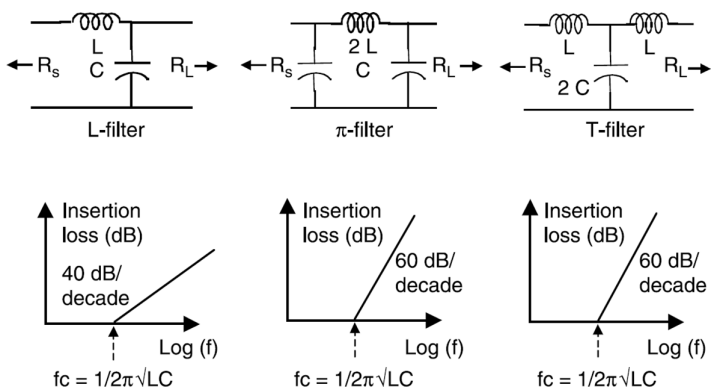

FIGURE 10.12 Basic L-C low-pass filters for power circuits.

harmonics in switch-mode power converters. They would also suppress signals in the time domain, such as transient spike voltages from ESD, EMP, and lightening-type sources. The response of such a filter is obtained by summing the pulse and frequency spectrum curves at each frequency. The π filter is commonly used at the input of a switch-mode converter to reduce the reflected ripple current. The filter is usually built into the converter. Very high-frequency noise (hash) is effectively filtered by using one or more filters in the following configurations: (i) Feed-trough capacitor, (ii) Ferrite bead around the conductor, and (iii) Ferrite bead with capacitor.

10.12 TELEMETRY AND COMMANDS

Sufficient telemetry must be provided to operate the spacecraft in a safe manner in all phases of the mission. The following is generally provided:

- The on–off status of all EPS relays and switches with positive identification
- Load currents
- Bus currents and voltages
- Array currents and voltages
- Shunt voltages and currents with shunt switch status on or off
- The open circuit voltage and short-circuit current of the solar array test coupon(s)
- Charge and discharge currents and terminal voltages of each battery
- Temperature and pressure are co-located on two or more cells in each battery
- Individual battery cell voltage, as often required by the customer.

A typical power system provides the telemetry, tracking, and command (TT&C) system with about 60 analog and 40 discrete telemetry channels. The telemetry accuracy is generally ±3% of the full-scale value of all analog signals and ±2°C of temperature. The types of telemetry used on the spacecraft are listed in Table 10.1.

The bus voltage is controlled automatically, so the telemetry is only for information. The EPS telemetry is scanned every several seconds. The battery current, pressure, and temperature are scanned less frequently depending on the nature of the load and the battery state of charge management requirement. There is no criticality in the telemetry time intervals. More frequent is better, but it must be traded with the computing requirement. Most telemetry is for information purposes, except the battery current, pressure, and temperature, in that order of criticality.

The OBC uses redundant telemetry to assure that the batteries are safe in the presence of a single EPS failure and its own failure. It is not required to continue automatic control after a failure without ground reconfiguration.

Commands are used to implement various functions and are typically of three types: (i) Digital serial, (ii) Discrete logic, and (iii) Discrete relay.

Ground commands are provided to override and inhibit autonomous functions and to manage and control the EPS. Redundant units are individually commanded. Block-switching of redundant units in response to a detected failure is prohibited.

TABLE 10.1
Types of Telemetry Used in Spacecraft

Telemetry Type	Nature	Description
Digital serial	Serial	Software driven
Digital logic	Bilevel	+5 V logic pulse or zero
Discrete relay	Bilevel	+28 V power pulse or zero
Active analog	Analog	Voltage and current sensors which are active all the time
Passive analog	Analog	Temperature sensors, normally inactive, but periodically pulsed with 1 A. The measured voltage is then converted in temperature

The electrical power system in spacecraft like GPS may have 70–80 discrete commands, 30–35 for EPS and 40–45 for pyro, and 35–40 serial telemetry points, 20–25 in EPS, 10 in SAD, and 2 in pyro. A typical 5000 W communications satellite may have 50–100 commands and a similar number of telemetry signals related to the power system monitoring functions. Most of them interface with the PRU, which controls the bus voltage.

The EPS command and telemetry interface with OBC via the TT&C system. However, the EPS is capable of remaining in safe mode in the absence of TT&C support for several minutes. It is also capable of operating indefinitely in a mode in which all commands are issued from the ground.

10.13 ELECTRONIC PACKAGING

The electronic packaging has multiple functions. It provides an internal structural support, the thermal conductivity of waste heat, and an enclosure that also provides protection against EMI and charged particle radiation. Since about 20%–30% of the electrical assembly mass is in packaging, significant mass reduction potential exists by exploring alternative packaging materials. Aluminum (0.10 lb/in^3) has been the material of choice for its high strength-to-weight ratio, good electrical and thermal conductivity, low cost, and easy fabrication. Other materials that have been used are magnesium (0.06 lb/in^3) and magnesium–lithium (0.04 lb/in^3). Although lightweight, magnesium–lithium is expensive, flammable, and a poor thermal conductor. In recent years, fiber–epoxy composites have been developed with properties tailored to meet a wide variety of requirements. Aluminum filled with graphite fibers or carbide particles may prove to offer reduced mass with acceptable thermal conductivity and stiffness. A composite fiber enclosure with a thin layer of aluminum foil for EMI shielding is about 50% lighter than an aluminum-based enclosure.

If a hermetically sealed component is specified, then the following is used in the construction:

Hermetically sealed connectors with connector cases welded to the hermetically sealed enclosure.

All circuit boards are conformally coated with an opaque polyurethane-type compound by dipping and then properly cured with no cracks in the finished card. Wide cracks due to mishandling damage or poor manufacturing are a risk. On a good circuit board, any spark due to a loose contact or arcing under a fault current would remain inside the conformal layer.

The circuit boards add significant mass to the electronic assembly. Some of the mass reduction potential may lie in using lower density Kapton (0.06 lb/in^3) versus glass (0.08 lb/in^3) and thinner and narrower copper traces (0.005 versus 0.010 inch). Circuit board fabrication is done on fiberglass board, copper plated on one side that works as the common return plane. All return leads are locally soldered to the copper back. A transformer weighing less than a pound is almost always toroidal, not potted. It is screwed to the board with a washer of the same outer diameter as the transformer and 1/8-inch-diameter machine screws with no silicon or other adhesive. A transformer weighing less than ¼ pounds, however, is glued directly on the board with a silicon adhesive tab at the bottom and also at the top. Aluminum heat sinks are bonded with the base plate to dissipate heat.

Nonmagnetic components may be potted using urethane resin filled with alumina for thermal conduction. Large magnetic components are potted using magnesia, which penetrates well. Small magnetics are merely bonded to the board with alumina-filled urethane resin.

Most electrical parts are required to be electrically isolated while maintaining good thermal contact for heat transfer. The insulators must be mechanically strong enough to withstand the short-circuit forces. The most commonly used washers as spacers are beryllia (0.10 lb/in^3) and alumina (0.14 lb/in^3), 20–40 mil thick.

Advances are continuously being made in heat sinks. A detailed look at what is currently available on the market can prove beneficial.

10.14 RADIATION SHIELD

Energetic particles passing through material lose energy through interaction with the atomic structure of the subject material. Electrons become highly scattered by the material, while protons, being heavier, penetrate deeper into the material. A particle loses all its energy after penetrating through a certain thickness of material. This thickness is known as the range, which approximately varies linearly with the energy level of the particle and inversely with the mass density of the material. For this reason, the range is commonly expressed as the product of the depth and density (g/cm^2) or in units of depth in aluminum as the basis of comparison, as shown in Figure 10.13. A practical range, $R_{p,}$ is defined as the most probable range of particles for a given incident energy.

Normal space-qualified devices are generally used in commercial space applications. These devices generally have sufficient shielding against the natural radiation of charged particles. This is because the device is in its own case, often behind a card, and also in an overall metal enclosure. A more sensitive electronic device is protected by placing it in a heavy metal enclosure, such as cast aluminum of several millimeters of thickness. Under a man-made radiation threat, such as a nuclear

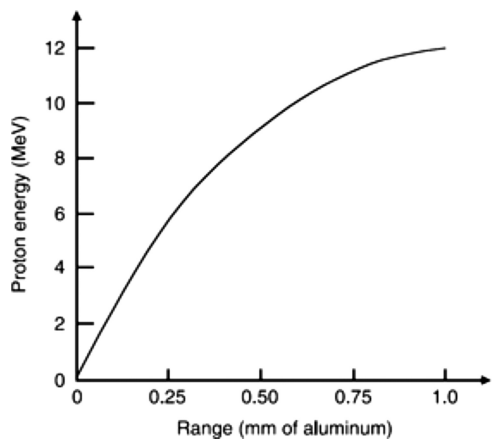

FIGURE 10.13 Range of radiation damage in aluminum.

detonation around a defense spacecraft, the device may need additional radiation hardening. Such radiation-hardened semiconductor devices are expensive.

The metal enclosure further reduces the damaging effects of the charged particles to a level that is tolerable due to the built-in radiation hardness of the electronic part inside. The selection of the enclosure metal and its thickness is a function of the estimated fluence and the tolerance dose. For example, the radiation flux entering the enclosure decreases with increasing wall thickness and mass density. Since aluminum is the most widely used enclosure material, the fluence penetration versus thickness curve is generally plotted with aluminum as the reference (Figure 10.14). The dose absorbed by an electronic part inside the enclosure therefore depends on the wall thickness. For example, the total ionization dose comprising mainly electrons and solar flare protons versus equivalent aluminum thickness in three different orbits is shown in Figure 10.15. Such curves are used to determine the required enclosure wall thickness, as described below.

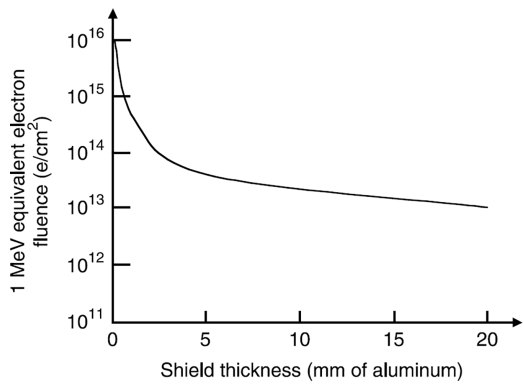

FIGURE 10.14 Radiation fluence penetration over a 10-year mission versus shield thickness.

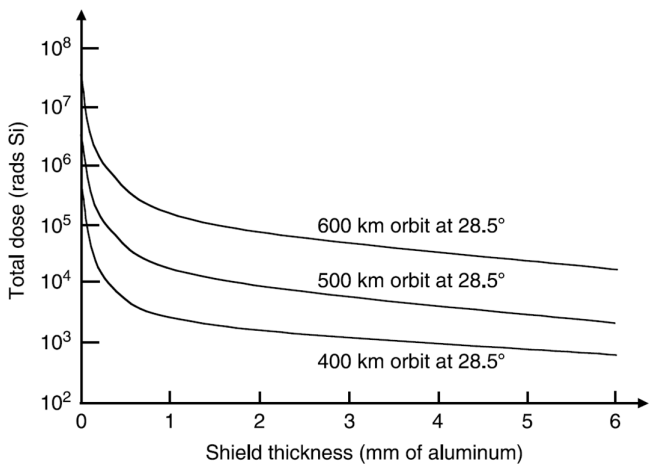

FIGURE 10.15 Total radiation dose over mission life versus shield thickness for three orbits.

10.15 EMI SHIELD

The conducting metal enclosure shields the equipment inside from radiated EMI. The metal walls provide eddy current shielding and control the near- and far-field coupling of the radiated electromagnetic fields. It attenuates the electrical and magnetic fields from leaving or entering the enclosure. The performance of the shield can be viewed in terms of the transmission line analogy, as shown in Figure 10.16.

When an electromagnetic wave traveling along a transmission path in free space with the characteristic wave impedance Z_o impinges on a metal surface (load impedance Z_L), the surface absorbs some wave power, some reflects back, and some continues beyond the shield wall thickness and reaches the victim equipment. The reflection coefficient, $\Re$, is given by

$$\Re = \frac{Z_L - Z_o}{Z_L + Z_o} \tag{10.2}$$

The higher the value of $\Re$, the more wave energy is reflected from the shield surface. For total reflection, i.e., for $\Re = -1$, Z_L must be small compared with Z_o. On the other hand, $Z_L = Z_o$ gives $\Re = 0$, there is no reflection and all the wave energy is absorbed by the shield wall thickness. This condition is known as impedance matching. The far-field transverse electromagnetic wave in free space has $Z_o = 120\pi = 377\Omega$. The electric dipoles have a dominant *e*-field and a higher Z_o. The current loops have a dominant *B*-field and lower Z_o. The load impedance of a metallic surface is given by $Z_L = (2\pi f\mu\rho)^{1/2}$ where f, μ, and ρ are the frequency, relative permeability, and resistivity of the surface material, respectively. Their values for commonly used enclosure metals are listed in Table 10.2. With these values, all metals except stainless steel have Z_L values of lower than 377 Ω. Therefore, they all provide good shielding from high impedance sources (dipole sources), but poor shielding from low impedance sources (loop currents).

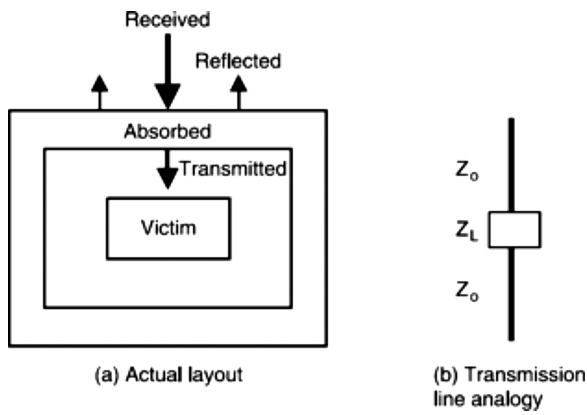

FIGURE 10.16 Reflected, absorbed, and transmitted EMI energy. (a) Actual layout. (b) Transmission line analogy.

TABLE 10.2
The Relative Permeability and Resistivity of Commonly Used Shield Metals

Material	Relative Resistivity	Relative Permeability
Copper	1	1
Aluminum	1.6	1
Mild steel	10	100–1000
Stainless steel (no-mag)	50	1

The reflection loss is defined as the ratio in dB of the wave field intensity passing through the shield to the field impinging upon it. For aluminum and steel, the two most widely used metals for enclosures, the reflection loss at various frequencies is listed in Table 10.3.

Once the outside interference enters the shield box, a part is absorbed in the metal wall as a resistive loss, and the remainder propagates further. The I^2R loss absorbed in the wall thickness depends on frequency and the skin depth of the wall and is given by

$$\delta = \left[\rho / \left(\pi f \mu\right)\right]^{0.5} \tag{10.3}$$

If the wall thickness is five times the skin depth, all the energy entering the metal wall is absorbed. For other thicknesses, the absorption loss, A (in dB), is given by

$$A = 0.134 t \left(f \mu_r / \rho_r\right)^{0.5} \tag{10.4}$$

where t = wall thickness in mm, ρ_r = resistivity relative to copper, and μ_r = permeability of the box interior relative to free space. The relation shows what is intuitively expected, namely that the greater the wall thickness, the greater the power absorption. The absorption loss values for aluminum and steel enclosures at various frequencies are given in Table 10.4.

Tables 10.3 and 10.4 show that the reflection and absorption of energy depend inversely on the resistivity. Permeability, on the other hand, has a beneficial effect on absorption but a detrimental effect on reflection. This property can be used for low-frequency magnetic shielding. The reflection and absorption losses in dB are added

TABLE 10.3
Reflection Loss in Aluminum and Steel at Various Frequencies

	E-Field Loss(dB)		B-Field Loss (dB)		Plane Wave Loss (dB)	
Frequency	Alum	Steel	Alum	Steel	Alum	Steel
60 Hz	280	240	20	0	150	115
1 kHz	240	200	30	10	140	100
150 kHz	180	130	50	20	115	80
15 MHz	115	80	75	40	95	70

TABLE 10.4
Absorption Loss in Aluminum and Steel at Various Frequencies

Frequency (Hz)	Absorption Loss in Aluminum (dB/mm)	Absorption Loss in Mild Steel (dB/mm)
60	0.8	13
1000	3.2	56
150 k	40	680
15 M	400	4240

to obtain the total loss in dB. The table values are theoretical for a perfect shield. In reality, the total dB loss is lower by a few folds due to seams and ports for connectors and displays. However, most practical boxes provide adequate shielding except for very low-frequency magnetic fields, as long as they are metallic and thick enough to support the parts inside.

The overall shielding effectiveness is often measured by testing the noise signal amplitude A with and without the shield and using the expression

$$\text{SE} = 20 \log \frac{A_{\text{with shield}}}{A_{\text{without shield}}} \tag{10.5}$$

Enclosures made of solid aluminum or aluminum-backed composite laminates provide 50–100 dB of shielding effectiveness for high-frequency noise in megahertz. The metallic backing can be less than 0.1 mm in most applications. Other conductive materials may be used, such as metal mesh and conductive fabrics. The shield does not have to be grounded for effectiveness. It is grounded for safety reasons in case of a fault in the chassis and for protection against electrostatic buildup.

If a solid plate is used to shield a component from eddy currents (Figure 10.17), not only is it required to have $t > \delta$, but also $Rt >> \delta^2$ for good low-frequency shielding against radiation from small current loops. Here t = shield thickness, ρ = resistivity of the shield material, and δ = skin depth for the signal frequency to be filtered. Only magnetic metal can provide low-frequency shielding, although it is rarely required. However, when needed, high-permeability magnetic metal tape having the required

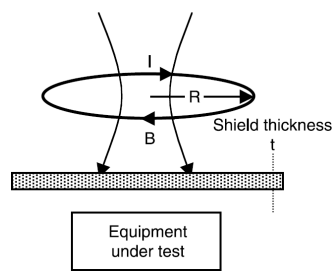

FIGURE 10.17 B-field of the current loop entering the metal shield.

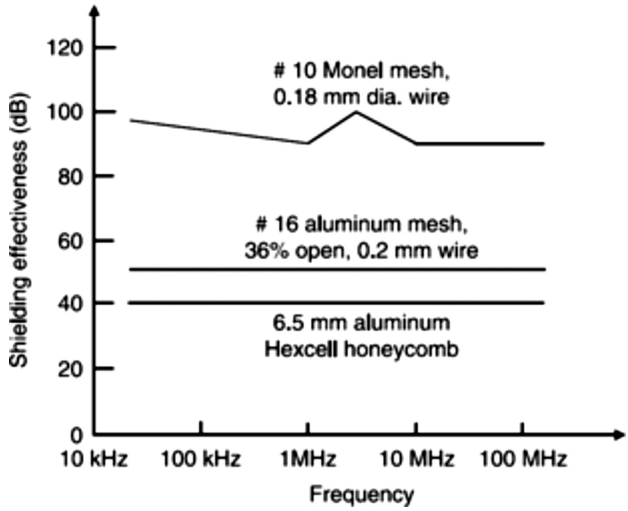

FIGURE 10.18 EMI shielding effectiveness of various materials.

saturation flux density is considered. The tape loses permeability after bending and straightening. Therefore, it often needs laser annealing after the wrapping process. The shielding effectiveness of various metal meshes and honeycombs is shown in Figure 10.18.

FURTHER READINGS

Passaretti, M. and Hayes, R., Development of solar array drive assembly for cubesat, in *Proceedings of the 40th Aerospace Mechanisms Symposium, NASA Kennedy Space Center*, May 2010.

Scheidegger, N., Ferris, M., and Phillips, N., Bi-axial solar array drive mechanism: Design, build and environmental testing, in *Proceedings of the 42th Aerospace Mechanisms Symposium, NASA Goddard Space Flight Center*, May 2014.

Part C

Power System Performance

11 Energy Balance and Power Management

11.1 INTRODUCTION

When we speak of designing the spacecraft's electrical power system, we really mean designing the electrical energy system. The satellite has a limited time in orbit to generate power, but the loads need to be powered all the time. The battery stores the required energy during sunlight and delivers it to the loads during an eclipse. The energy balance between the battery charge and discharge over one orbit period must be, on average, positive with some margin. In the simple case of constant load shown in Figure 11.1, the lightly dotted area must exceed the dark area with an acceptable margin. Otherwise, the battery would become totally depleted after some cycles. The power to and from various components must therefore be managed in order to maintain the energy balance in both the transfer orbit and the operational orbit.

On low Earth orbit (LEO) satellites, the orbit period is short, about 1.5 h. The eclipse duration, although short in clock time, is much longer as a percentage of the orbit period. Consequently, the sunlight duration as a percentage of the orbit period is much shorter, imposing a stringent demand on the power system. It must not only collect the required solar energy in a relatively short time, but also manage it efficiently over the entire orbit period. The energy balance over the orbit period is maintained by a combination of hardware and software controls, as described in this chapter. It amounts to maintaining the following integral equation:

$$\begin{aligned}
&\int_{\text{sunlight}} \left(\text{solar flux} \times \text{PV conversion efficiency}\right) \cdot dt \\
&= \int_{\text{sunlight}} \left(\text{loads} + \text{charge power} + \text{shunt power} + \text{losses}\right) \cdot dt \\
&+ \int_{\text{eclipse}} \left(\text{loads} + \text{losses}\right) \cdot dt
\end{aligned} \tag{11.1}$$

On most satellites, the energy balance is maintained autonomously on board. However, the ground control intervenes when it is necessary to (i) override the autonomous controls for any reason, (ii) trim the system to account for predicted or unpredicted degradation in performance, or (iii) recondition the battery, if required.

DOI: 10.1201/9781003344605-14

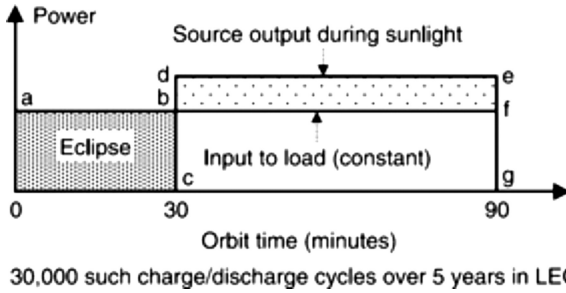

FIGURE 11.1 Energy balance over one orbit period with constant load power.

The battery telemetry options available—all with redundancy—for this purpose are:

- Two cell temperatures per battery: one at the hottest spot and one at the coldest spot
- Two cell pressure readings per battery, temperature compensated
- All cell voltages for comparative performance analysis
- Each battery's voltage and charge/discharge current

The charge rate is selected between the full charge and trickle charge rates as controlled by the power regulation unit (PRU) mode controller to maintain the bus voltage. During the transfer orbit, continuous ground control is not possible, and the on-board computer (OBC) automatically controls the battery state of charge (SOC). The OBC can adjust all charge rates from default values and can inhibit automatic functions. At launch, the battery charger's minimum rate is set at *C*/120 for charge maintenance, and the maximum rate is set at *C*/10 for sequential charging for high efficiency up to 85% SOC.

In operational orbit, normally, the batteries are charged concurrently at a *C*/20 rate when they are under the autonomous control of the OBC. The ground control has the option of charging them sequentially at *C*/10 by programming the OBC. Charging at *C*/10 is more efficient up to a certain SOC, beyond which it is switched to *C*/20.

Using the telemetry data, the OBC estimates the battery SOC using the battery cell pressure telemetry adjusted for the telemetered temperature value. Using the hysteric dead-band control, the OBC initiates charge if the cell pressure falls below the preset value selected for charge initiation, less the hysteresis level of about 2%–3%.

During charging, the OBC compares the cell pressures against the predetermined state, with 85% being a typical default value. The OBC terminates the charge when the SOC rises above a preset value and commands the chargers to one of the two trickle charge rates pre-selectable by ground command. The ground command also has the option to preset an additional amount of charge to reach *full charge* without excessive temperature and pressure rise, followed by automatic charge termination. All preset values in the battery charge and discharge management are alterable by the ground control.

11.2 ENERGY BALANCE ANALYSIS

The energy balance analysis is performed at the design stage by simulating the power flow and energy account on the computer. The program is generally structured to allow analyses of the baseline design and its derivatives, and to answer many *what if* questions in normal and abnormal operations.

The program basically determines whether the EPS is in energy balance over a desired period, e.g., over every orbit or over several orbits, for a given load profile, solar array, and battery. Such analysis is performed during all phases of the mission for a given launch date (year, month, and day). Various fault conditions, including battery cell failures (short or open) and loss of a solar array circuit, are simulated to determine energy balance under the worst-case condition(s).

Other equally important uses of the energy balance computer program are:

- Determine and/or optimize the load capability of a given EPS
- Derive the system component ratings based on the maximum power flow through each component
- Determine the power dissipation for thermal design of each component, particularly the battery, since its performance is highly temperature sensitive

11.3 COMPUTER PROGRAM STRUCTURE

The computer program is generally developed around variable parameters with no *hard-coded* numbers. Such a structure allows greater flexibility in using this tool for a wide variety of applications. Figure 11.2 depicts EPS components contributing to the energy balance program. The basic equation of currents in the energy balance analysis is:

during sunlight,

$$I_{sa} = I_{\text{load}} + I_{\text{charge}} + I_{\text{shunt}} - I_{\text{discharge}} \tag{11.2}$$

and during the eclipse,

$$I_{\text{load}} = I_{\text{discharge}} \tag{11.3}$$

The battery depth of discharge (DOD) at any time is computed, typically every second or so, as follows:

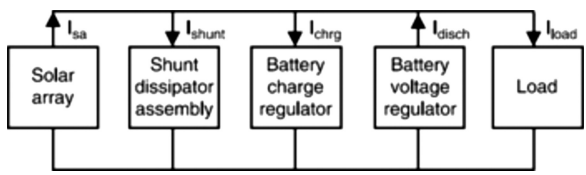

FIGURE 11.2 Power system components participating in the energy balance.

$$\mathrm{DOD}(t) = \mathrm{DOD}_{\mathrm{initial}} + \left(\mathrm{AH}_{\mathrm{delivered}}/\mathrm{AH}_{\mathrm{actual}}\right) \tag{11.4}$$

where $\mathrm{DOD}_{\mathrm{initial}}$ is the initial DOD, $\mathrm{AH}_{\mathrm{delivered}}$ is the sum of AH delivered, and $\mathrm{AH}_{\mathrm{actual}}$ is the actual AH capacity. The entire program is divided into several software modules, each representing various components. Due to the nonlinear nature of the battery cell and the solar array performance parameters, the program uses *static* lookup tables to determine the cell performance characteristics as a function of the battery current, temperature, SOC, and solar array operating voltage. Programming with a computer language instead of modeling on a spreadsheet significantly improves the capability of the program.

The major software modules of the programs can be structured as follows.

11.3.1 Battery Module

The *battery module* determines a number of battery parameters, including the SOC *(battery_soc)*, battery voltage *(battery_volt)* and battery dissipation *(battery_disp).* The ampere-hour (Ah) integration is performed to predict the battery SOC in terms of actual capacity. Ah returned to the battery and Ah removed from the battery are calculated at each program *integration step,* which is typically in seconds. The battery charge/discharge ratio is determined by the ratio of the ampere-hours put into the battery to the ampere-hours taken out of the battery. The battery voltage is determined using a lookup table, which provides the battery cell voltage as a function of the charge or discharge rate (+ for charge and − for discharge), battery temperature, and the battery SOC.

The battery dissipation is determined as a function of the difference between the cell voltage and the thermal neutral potential *(therm_neut_pot)* of the battery cell, the battery current, and the battery charge/discharge efficiency. The thermal neutral potential for the NiH_2 battery cell is 1.51 V. The battery cell efficiency during discharge can be assumed to be 100% for simplicity without much loss of accuracy. The battery efficiency during the charge portion of the orbit varies during charge as a function of the battery charge rate, SOC, and temperature. It is determined using a static lookup table and performing linear interpolation between points.

Charge cut-back and trickle charge: The battery charge current is reduced to the trickle rate linearly or in a few steps once the full charge is approached. The battery current and voltage profile over one orbit period shown in Figure 11.3 is typical for LEO satellites. A constant charge rate is maintained up to 95% SOC, typically for 50%–60% of the sunlight duration. The charge rate is then tapered off to trickle charge in the *C*/50–*C*/100 range.

Figure 11.3 is an example of the battery current analysis results on a LEO satellite. It starts at the beginning of the eclipse. During an eclipse, the discharge current rises (becomes more negative) as the battery voltage drops because of the constant power nature of the load. As the battery is placed in charge at the beginning of sunlight, the battery voltage rises under constant charge current. About halfway through the sunlight, the charge rate starts tapering and is reduced to the trickle rate at the end to maintain full voltage until the inception of the next eclipse.

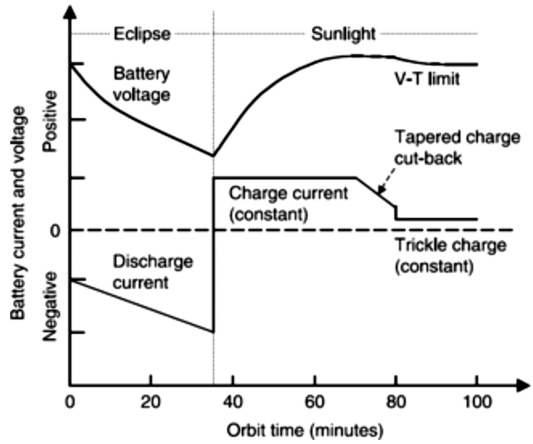

FIGURE 11.3 Battery current and voltage versus time for energy balance over one orbital period.

AH counter and sensor: The voltage of a battery may not be a reliable indicator of the SOC. The software keeps track of the ampere-hours in and out of the battery to determine the SOC and then proceed accordingly. The accumulated error can be detected by temperature and/or pressure sensors, and the ultimate safety of the battery is maintained by a suitable hardware circuit. One such self-explanatory computational flow chart often used in communication satellites is depicted in Figure 11.4 as an example.

11.3.2 Solar Array Module

The *sa_module* is programmed to incorporate the following:

- Solar cell *I–V* characteristics and array temperature
- Array configuration (number of series cells × number of parallel circuits)
- Cell and array performance degradation factors

11.3.3 Bus Module

The *bus_module* sums all currents available on the bus. They are the discharge current, charge current, solar array current, load current, and shunt current. The bus voltage is determined by using the net current as a *derivative offset* to the previous *bus_volt*. The finite difference equation used to calculate the bus voltage at the k^{th} time step in the numerical iteration process is:

$$V_{\text{bus}(k)} = V_{\text{bus}(k-1)} + \left[\left(I_{saa} + I_{\text{discharge}} - I_{\text{charge}} - I_{\text{shunt}} - I_{\text{load}}\right)_k - t \,/\, C_{\text{bus capacitors}}\right] \quad (11.5)$$

where Δt is the time interval.

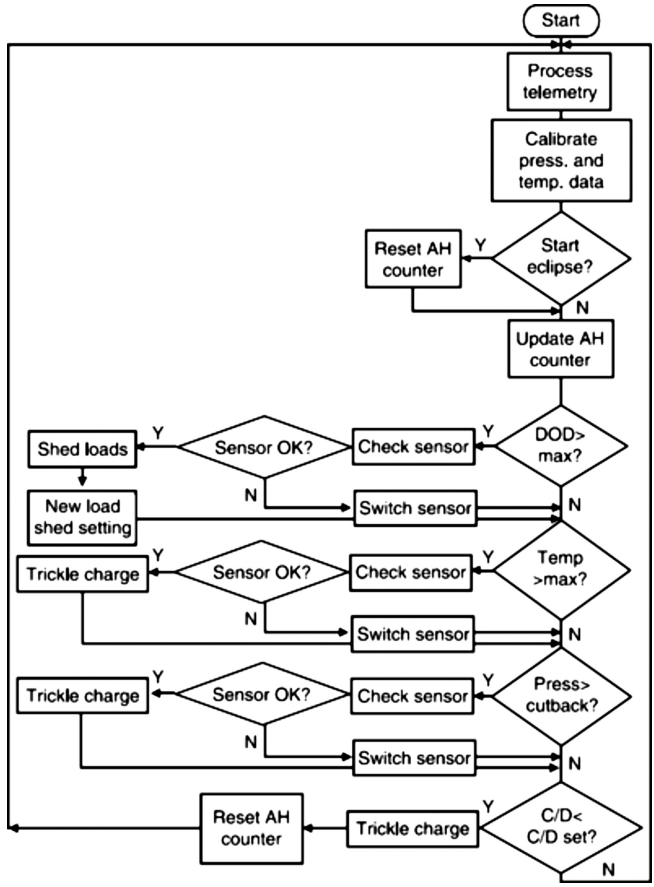

FIGURE 11.4 Logic flow chart for energy balance software.

The bus voltage regulator typically maintains the bus voltage as the source, and the load currents vary to maintain the dc equilibrium of the two currents. A bus capacitor bank is generally used to absorb the leading and trailing edge transients of fast changing loads or sources.

11.3.4 Input Variables

It is desirable to have the energy balance program flexible enough to incorporate the following system inputs in various simulation runs:

- Time-variable load plus a constant load over one or multiple orbits
- Beginning-of-life or end-of-life conditions
- Off-pointing of the solar array
- Launch and descent phases of the mission

11.3.5 Output Format

Several output files are produced on running the program, such as the battery parameters (*battery_out*), EPS performance parameters (*eps_out*), and solar array parameters (*sa_out*). The output files contain variable names and values and may be loaded into a spreadsheet program for subsequent plotting or a word-processing program for inclusion in reports.

11.3.6 Program Verification

Before using any such energy balance program, it must be calibrated and verified using a simple load profile, for which the performance can also be calculated by hand. Figure 11.5 is an example of the computed battery DODs compared with the hand-calculated values. They must compare well within the limitations of hand calculations. As seen in the figure, the assumption of constant battery charge efficiency in the hand calculation results in slightly different DOD as the battery approaches zero DOD.

11.4 ENERGY BALANCE SIMULATION RUNS

On the ***run*** command, the program initializes all input parameters, including the battery lookup tables and the solar cell lookup tables, by calling the *init_module*. In this module, the simulation start and end times and the number of orbits (single or multiple) are specified. The battery discharge/charge rate (BDR/BCR) efficiencies and the harness resistances are entered in this module. The print interval is also specified, allowing data to be printed to an ASCII file in the designated increment (say, 1 min).

The *load_module* determines the load current requirement at the bus voltage according to the load power requirement specified in the input file. The load power can be either constant or can vary as a function of time with a time increment of 0.1–1 min.

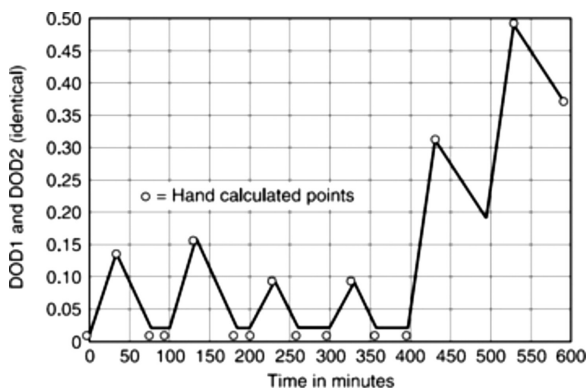

FIGURE 11.5 Calibration example for batteries depth of discharge (DOD) 1 and DOD 2. (– Computed, ooo Hand calculated.)

Static lookup data files (battery cell data and solar cell *I–V* data, for example) are located in separate files. After editing the input file(s) to reflect the case to be simulated, the energy balance program is recompiled using the new input file(s). The new executable code is then **run**. The simulation is run for the following three distinct phases of the mission.

11.4.1 On-Orbit Simulation

On-orbit power flow analyses and energy balance are carried out for the worst-case scenario at the beginning of life and also at the end of life. Since the beginning-of-life power generation is much greater than that at the end-of-life, the beginning-of-life power analysis establishes the current rating of the sliprings and the shunts, both of which always carry the greatest currents at the beginning of life. The end-of-life energy balance, on the other hand, must be verified using the worst-case orbit conditions, namely the yearly minimum solar flux, the minimum operation altitude, and the maximum eclipse time. If applicable, the solar β angle of 0° usually results in the longest eclipse time.

Besides being a design tool, the energy balance analysis is also carried out on board the spacecraft to detect and correct potential problems. This is done by performing the following forward computations.

For a given load power profile the spacecraft is about to enter, the battery DOD is projected at the end of the eclipse. If the projected DOD exceeds the maximum allowed, an alert is sent to the spacecraft computer for approaching battery-limited conditions and for possible load shedding.

For the allowable DOD and the required charge power during the next sunlight duration, the maximum allowable load is computed. If it is less than the planned load, an alert is sent to the spacecraft computer for an approaching solar array limitation condition and for possible load shedding.

11.4.2 Transfer Orbit Simulation

This phase of the mission for communication satellites begins with the separation of the spacecraft from the launch vehicle (approximately 30 min after lift-off) and ends with the spacecraft in a full 24 h orbit around the Earth. The first orbit after separation is nominally a 10.5 h elliptical orbit with perigee at the spacecraft–launch vehicle separation altitude and apogee at the geosynchronous altitude. During a transfer orbit period spanning 1–2 weeks, a series of timed apogee engine burns raises perigee to the geosynchronous height. During this period, the solar panels are stowed against the north and south equipment panels, with only the outer panel of each wing exposed. The GEO spacecraft is slowly spun around its roll or yaw axis, typically at 0.1 rpm, to maintain an acceptable component temperature. Because the solar array panels are folded against two opposite sides of the spacecraft body, which is spinning, the power output approximates a full-wave rectified sinewave. Consequently, the batteries are alternately charged and discharged at twice the spin rate (Figure 11.6). The selection of a high charge rate permits the use of all available solar array power more efficiently.

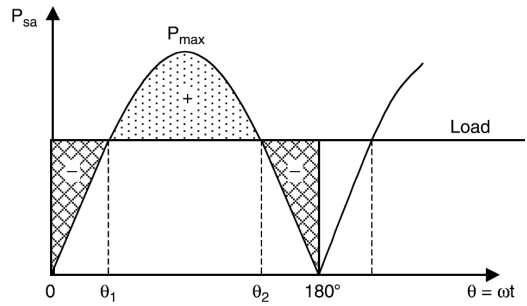

FIGURE 11.6 Transfer orbit energy balance with full-wave rectified sine wave variation in power generation.

In transfer orbit, the solar panels of a typical communication satellite may be subjected to about every conceivable sun angle between cos 30° and cos 120° during (i) Roll spin, (ii) Yaw spin, and (iii) Attitude fix during the initial Earth search. During these periods, the spacecraft may need to be maneuvered to improve the energy balance as needed.

11.4.3 Transfer Orbit Load Budget

Since only one panel is facing the sun at a time as the spacecraft spins in the transfer orbit, the power output of the array is a full wave rectified sinewave, as shown in Figure 11.6. The power generation varies with the sun angle as

$$P = P_{\max} \sin\theta \tag{11.6}$$

where

$$P_{\max} = \frac{P_{\text{bol}}}{N_p} f_{cs} \tag{11.7}$$

and θ = sun angle measured from the horizon (90° gives maximum power), N_p = number of panels on both wings, and f_{cs} is the improvement in outboard panel performance due to better cell selection (about 1.02). The sun angle is tightly constrained between 80° and 100°, except during maneuvers, when it can be between 30° and 140°.

The average power during the transfer orbit, ignoring the thermal effects, is given by

$$P_{t.o.\text{avg}} = P_{\max} \frac{2}{\pi} \tag{11.8}$$

Also denoting P_L = load power, including the orbit average losses

E_{dis} = total energy discharged during half a turn (dark-shaded area)

E_{chg} = total energy charged during the same half turn (light-shaded area)

θ_1 = crossover point between the charge and discharge modes

we have

$$\theta_1 = \sin^{-1}\left(\frac{P_L}{P_{\max}}\right) \tag{11.9}$$

$$E_{\text{dis}} = -\int_0^{\theta_1} \frac{P_L - P_{\max}\sin\theta}{\eta d}\, d\theta \tag{11.10}$$

$$E_{\text{chg}} = \int_{\theta_1}^{\theta_2} (P_{\max}\sin\theta - P_L)\,\eta_c \eta_b d\theta \tag{11.11}$$

where θ_1 is in radians, and E_{dis} and E_{chg} are in watt-hours. For the satellite to be in energy balance during the transfer orbit, E_{chg} must equal or exceed E_{dis} with a suitable margin compatible with the uncertainty at a given design stage. Such analysis determines the required peak power $P_{\max}$, the spacecraft inclination, or the maximum permissible load during the transfer orbit. It does not account for eclipses during the transfer orbit, which must be considered separately if applicable.

In situations where the load power requirement cannot be met with a uniform spin speed, pausing the spin for a while when the sun angle is favorable to allow the outer panel to collect more energy, as shown in Figure 11.7, can help the transfer orbit energy balance. The allowable dwell time in such a maneuver is determined by the allowable temperature limit on the panel or inside the body, which can become roasted under a long dwell time. Such a stop-and-go operation, however, consumes additional fuel. The mass of this fuel is charged into the power system.

11.4.4 Launch and Ascent Simulation

During the launch and ascent and until separation, the battery powers the computers, electro-explosive devices, and other essential equipment until sunlight is acquired. In an LEO mission, the battery designed for a shallow (30%–35%) DOD during normal operation orbit can be discharged to a higher (80%–90%) DOD for one time during

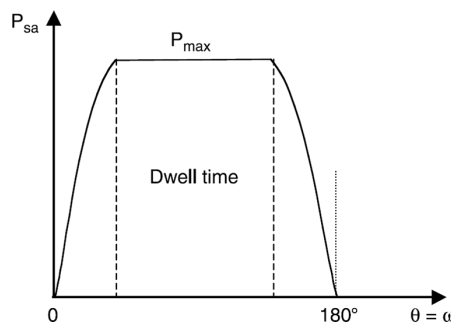

FIGURE 11.7 Dwelling at a favorable sun angle to improve energy balance during transfer orbit.

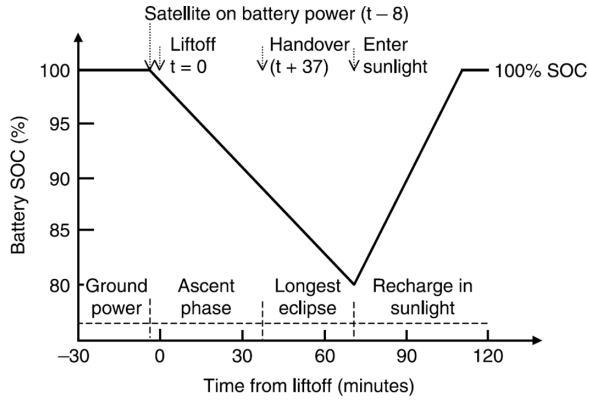

FIGURE 11.8 Energy flow and battery state of charge (SOC) during launch and ascent phases.

the launch/ascent phase. However, once the sun is acquired, the battery must be first fully charged before undertaking other maneuvers. Figure 11.8 depicts a typical battery SOC for an LEO satellite. If the battery is short of energy in this phase, two options are:

a. Cool the battery to a lower temperature by using a jet of cool air or nitrogen on the launch pad just before launch. This allows charging the battery to a higher Ah capacity. This is a widely used option.
b. If that is not enough, a small primary battery may be used to augment the main battery. The primary battery, having an order of magnitude greater specific energy, gives a mass-efficient solution. Carrying a larger main battery just for this phase is almost never done, as it adds significant mass and also costs much more.

11.5 BATTERY STATE OF HEALTH MONITORING

Since the battery is a critical component in the spacecraft power system, monitoring its state of health and remaining life is important. The data collected for on-board energy balance management can also be used for this purpose. The battery's overall state of health on board is generally monitored by the following two key indicators:

i. Cell divergences are detected using the individual cell voltage monitored by the BCVM. A trend analysis of the cell voltages is performed to detect individual cell voltage divergence. Any such divergence flags a battery weakness.
ii. Since any internal fault or abuse of the battery will build up internal gas pressure, pressure strain gages are installed to monitor the battery's overall health. Initial matching of the cells ensures that two cell pressures represent all other cells. Any unexpected pressure reading is processed as an alert flag.

The battery's state of health indirectly measures external behavior such as capacity loss. It also measures internal behavior such as severe corrosion, the remaining useful life, and the remaining useful energy. The changes in the electrode surface, diffusion layer, and electrolyte are not measurable. However, the terminal voltage and body temperature are used to indirectly determine the performance. Accurate modeling of the transport mechanism inside the cell and the electrochemical and thermal models is needed for this purpose. The cell internal impedance frequency spectrum technique developed by Kozlowski et al.[1] can retrieve useful information about the internal electrochemical conditions. The internal impedance of the cell is measured by applying a small signal excitation to the cell and measuring the response. A range of frequencies is used to account for the frequency dependence of many electrochemical impedance parameters. The impedance model of the cell between positive and negative electrodes separated by an electrolyte is shown in Figure 11.9,[2] where R and L are the wiring resistance and inductance, respectively. It represents the physical electrochemical process via electrolyte resistance, R_e, charge transfer resistance, θ, double layer capacitance, C_{dl}, and the Warburg impedance, Z_w. These parameters represent the physical electrochemical process, such as charge and mass transfer during cycling. For example, the model identifies the electrolyte resistance, R_e, versus the SOC for a NiCd battery, as shown in Figure 11.10. Such information is then used in a neural network and fuzzy logic SOC prediction model. This technique was developed at the US Naval Research Center and holds promise for monitoring the SOC, state of health, and remaining life of the spacecraft batteries.[2]

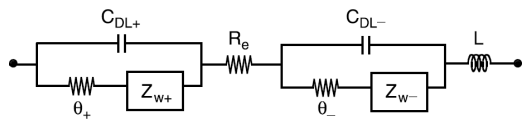

FIGURE 11.9 Circuit model for a battery with wiring resistance and inductance.

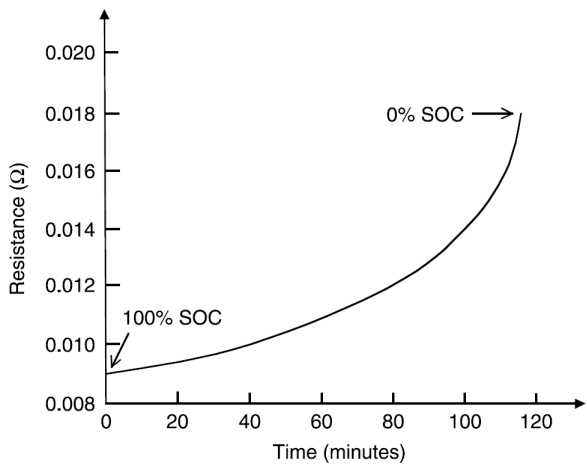

FIGURE 11.10 Electrolytic resistance of the NiCd battery from the model.

11.6 BATTERY LATCH-UP IN A SUN-REGULATED BUS

In a sun-regulated power system, the difference between the stable operation of the solar array and that of the battery often leads to an operating condition known as battery latch-up. It occurs when the satellite is coming out of an eclipse. At this time, although the solar array is capable of delivering full power, the battery continues to deliver load power instead of going into the charge mode. The bus remains latched to the battery voltage and is unable to recover to the shunt-controlled voltage even during sunlight. Subsequently, it is not possible to maintain the energy balance, either by hardware or software. This is obviously an anomaly that should be immediately corrected to prevent further discharge of the battery. The condition is typical only of the sun-regulated system. The fully regulated system is inherently free of such latch-ups.

The phenomenon is explained here with reference to Figure 11.11. The dotted parabola is the constant power load line for the spacecraft. The heavy, solid line is the *V–I* characteristic of a drained battery at the end of the eclipse. The system operates at the stable point of their interaction, A_1. The other point of their intersection, U, is unstable. The faintly dotted curve B is the *I–V* characteristic of the solar array soon after entering the sunlight. This curve keeps rising as the spacecraft moves from eclipse to penumbra to full sunlight. Until it rises to curve D, the battery continues discharging to the load at point A_1, as curve D and the load line have no point of intersection.

When the illumination rises to full sunlight curve E, there are intersection points A_2 and A_3 with the load line. But, since point A_1 is stable, it does not move to a higher voltage at point A_2. The system thus remains latched at battery voltage A_1. At this point, the current drawn from the solar array is V_1E_1 and the current drawn from the battery is E_1A_1. With curve F, the battery and the solar array match in their current capabilities. The system operates at point A_1, where it is stable because it is latched with the battery (the solar array is unstable at A_1).

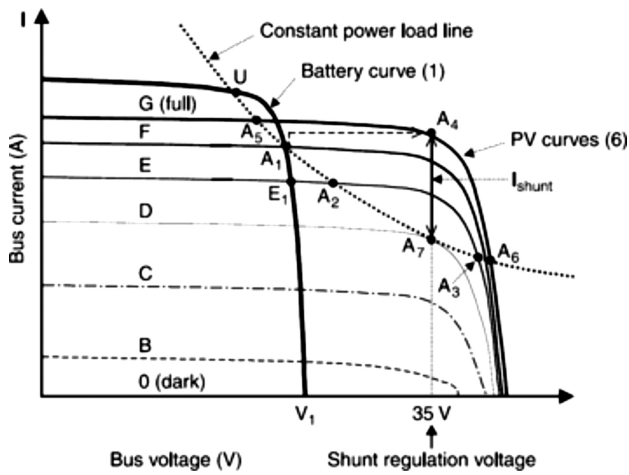

FIGURE 11.11 Battery latch-up in sunlight-regulated buses.

When the illumination rises to curve G (full sun), the operating point A_1 moves to point A_5 on curve G, but since it is unstable, it starts moving toward the stable point A_6. On the extreme right-hand side, however, the sunlight shunt regulation control set at 35 V limits it at point A_4, where $I_{shunt} = A_4A_7$. The operating point with load becomes A_4 with the shunt in control of the system now.

Thus, the battery latch-up can occur under the following two conditions at the end of eclipse:

- The battery voltage drops below a certain low point, drawing heavy current to power constant power loads, and
- The solar array's current output upon entry into the sunlight is less than the current drawn from the battery at the end of the eclipse.

The remedy for avoiding the battery latch-up is to size the solar array more than that required for meeting the end-of-life load power with sufficient margin. In Figure 11.11, the *I–V* curve of a fully illuminated solar array should be at least above curve F (point A_1) to unlatch the system from the low battery voltage during the eclipse. This generally required a 5%–10% extra power margin compared to that in the fully regulated bus. The added mass and cost of the solar array constitute a major disadvantage of the sun-regulated system. For this reason, large power systems, where this penalty can be high, find fully regulated systems advantageous. If the battery voltage is too low during the eclipse, even more solar array power is required to unlatch the system. On the other hand, if the battery voltage is too high during sunlight, the charge converter works inefficiently at a low duty ratio (close to zero). The design engineer trades these two features.

Another remedy for the battery latch-up is to add one (rarely two) cells. With a 23-cell battery instead of the traditional 22-cell battery, the higher battery voltage prevents latch-up. That extra voltage in one cell is often enough to avoid the latch-up. However, the 23-cell battery becomes fully charged at $23 \times 1.6 = 36.35$ V, which is outside the 22–35 V limits on the bus. This may be allowed in a system where the battery is charged directly from a dedicated solar array without a charge regulator. If the battery charge power is derived from a dedicated section of the solar array with a charge regulator, yet another remedy could be connecting the charging array to the bus until the latch is cleared up. After exhausting all possible remedies, if the bus is still latched to the battery, there is nothing one can do except shed some nonessential or noncritical loads temporarily. Some heaters can always be momentarily shut off. The reduced load current would then allow the voltage-regulating shunts to regain control of the bus voltage. The loads can then be brought back into service.

REFERENCES

1. Kozlowski, J.D., Crawley, T., and Byington, C.S., *Model Based Predictive Diagnostics for Primary and Secondary Batteries*, Pennsylvania State University, Applied Research Laboratory, Technical Report No. 99-076, June 1999.
2. Kozlowski, J.D., Watson, M.J., Byington, C.S., Garga, A.K., and Hay, T.A., Electrochemical cell diagnostics using on-line impedance measurements, state estimation and data fusion techniques, in *Proceedings of the 36th Intersociety Energy Conversion Engineering Conference*, ASME 2001, pp. 981–986.

FURTHER READINGS

Aghamohammadi, M.R. and Khormizi, A.B., Small signal stability constrained rescheduling using sensitivities analysis by neural network as a preventive tool, in *Proceedings of 2010 Asia-Pacific Power and Energy Engineering Conference*, Mar. 2010, pp. 1–5.

Aghamohammadi, M.R., Khormizi, A.B., and Rezaee, M., Effect of generator parameters inaccuracy on transient stability performance. in *Proceedings of the 2010 Asia-Pacific Power and Energy Engineering Conference,* Chengdu, China, 28-31 March 2010, pp. 1–5.

Singh, P., Gaddam, V., Arey, S., and Yang, Z., Battery state-of-charge meters for high performance batteries based on Fuzzy logic methodology, in *Proceedings of the 34th Intersociety Energy Conversion Engineering Conference*, SAE 1999, Paper No. 01-2467.

12 Dynamic Performance and Stability

12.1 INTRODUCTION

The dynamic performance of a power system under an internal or external transient perturbation is influenced by the dynamic bus impedance and the control loop gain. Key performance attributes emerging from the dynamic study are the bus voltage ripples, transient deviations, fault and fuse blow transients, and the control loop stability under harmonic ripple excitation. On the other hand, the static performance under a slow change or after the dynamic response has settled in time is largely influenced by the static impedance of the bus. The voltage regulation long after a load change is an example of static performance. Since the dynamic and static bus impedances are similarly defined, they are jointly covered in the following section.

12.2 BUS IMPEDANCE AND SYSTEM STIFFNESS

A complex electrical network having a number of sources and loads between any two load terminals can always be reduced to a simple equivalent source, known as the Thévenin equivalent source, consisting of one source voltage V_s with an internal series impedance Z_s (Figure 12.1). The two source parameters are determined as follows.

With the system operating at no load between load points 1 and 2 in Figure 12.1, but with all other parameters at rated values, the voltage between terminals 1 and 2 equals the source voltage V_s (since the internal voltage drop is zero). Therefore,

$$V_s = \text{open circuit voltage of the system at the load terminals} \tag{12.1}$$

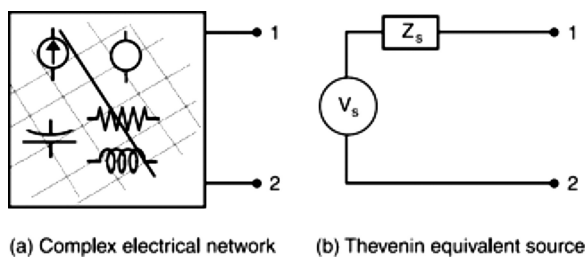

FIGURE 12.1 Complex electrical network reduced to a Thévenin equivalent source. (a) Complex electrical network. (b) Thevenin equivalent source.

DOI: 10.1201/9781003344605-15

With the load terminals 1 and 2 shorted, the internal voltage is now totally consumed in driving the current through the source impedance only. Therefore,

$$Z_s = \text{open circuit voltage/short circuit current at the load terminals} \quad (12.2)$$

The short-circuit current is determined by calculations in the actual circuit. If it is desired to determined by tests, a reduced voltage is applied to limit the current to the rated value. The full short circuit current is then calculated by scaling to the full rated voltage. Any nonlinearity, if present, must be accounted for.

The source impedance of most spacecraft bus architectures is highly nonlinear due to the use of multiple bus regulators along with dead-band regions. The dynamic performance of such systems is largely driven by the transient nature of switching from one mode to another, such as solar array shunt control or battery discharge control. Linear modeling may be acceptable for steady-state regulation and small signal load changes within the control range of each controller, but not for modeling mode change transitions, which must use transient models for the individual controls.

Two alternate ways of determining Z_s are as follows:

- Set all independent voltage and current sources in the system to zero and determine the impedance between open terminals 1 and 2.
- With the system energized and the load connected between points 1 and 2, measure the voltage drop ΔV for a slow load change ΔI. Then, Z_s is the ratio $\Delta V/\Delta I$.

The Thévenin equivalent source model derived under the steady-state static condition gives the static bus impedance Z_s. The source impedance derived under the dynamic condition—that is, for an alternating or incremental load—is the dynamic bus impedance Z_d. The Z_d varies with frequency and can be either calculated or measured with the test set-up shown in Figure 12.2. With the bus in operational mode and delivering the rated load, a small high-frequency ac current signal I_h is injected into the bus using an independent current source. The value V_h, the high-frequency voltage perturbation in the bus voltage, is measured. The dynamic bus impedance at that frequency is then

$$Z_d = \frac{V_h}{I_h} \quad (12.3)$$

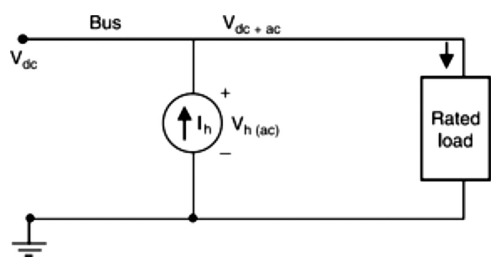

FIGURE 12.2 Dynamic bus impedance measurement by injecting ripple current I_h.

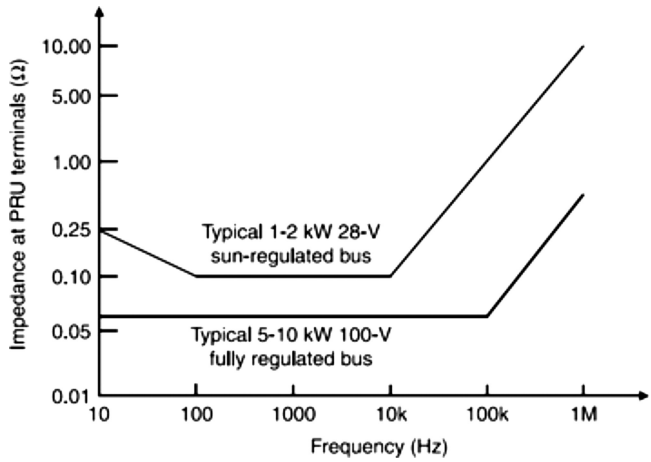

FIGURE 12.3 Main bus source impedance requirement for a typical geosynchronous Earth orbit communications satellite.

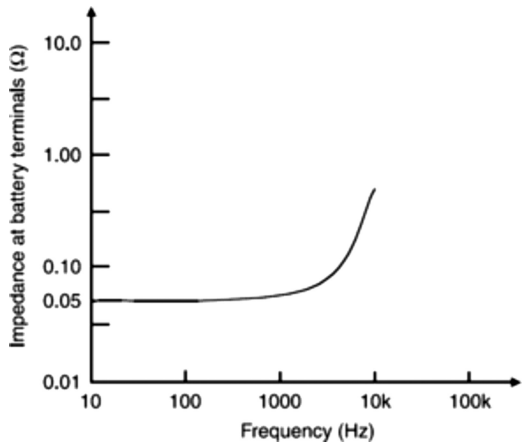

FIGURE 12.4 Pyro (battery) bus source impedance requirement for typical geosynchronous Earth orbit communications satellite.

Since Z_d has a strong influence on the system's dynamic performance, it is kept below specified limits. Figures 12.3 and 12.4 are examples of the main bus and the battery pyrobus source impedances for mid-size communication satellites.

One way of evaluating the relative fuse blow speed in a power system is to evaluate the system stiffness, which is inversely related to the static bus impedance. After the initial inductive rise of dc fault current takes place in five time constants (L/R), the steady fault current magnitude is inversely proportional to the static impedance of the source looking back from the fault location. We now define the following terms leading to system stiffness:

Rated system impedance $Z_{\text{rated}} = V_{\text{rated}}/I_{\text{rated}}$
Normalized static impedance $Z_n = Z_s/Z_{\text{rated}}$
System stiffness = fault current in multiples of the rated current

$$= 1/Z_n \tag{12.4}$$

The stiffer the system, the quicker the fuse blows. This concept is useful in a top-level comparison of two power systems of different designs.

12.3 VOLTAGE REGULATION AND TRANSIENTS

The steady-state voltage rise on removal of the full rated load current is then $\Delta V = I_{\text{rated}} Z_s$, and the static voltage regulation (as a percentage) is defined as

$$\text{voltage regulation} = \frac{\Delta V}{V_{\text{rated}}} \times 100 \tag{12.5}$$

The steady-state voltage regulation is defined as the change in the steady-state voltage after the feedback control dynamics have taken effect. It primarily depends on the control loop design rather than the dynamic bus impedance.

Under a load step change—partial or full—the voltage oscillates until the transient settles to a new steady-state value, as depicted in Figure 12.5. A good design limits and damps the oscillation in a short time to avoid the system becoming unstable. If the load current rises in step, the voltage oscillates before settling down to a lower steady-state value. The steady-state change in the bus voltage is then given by $\Delta V = \Delta I \cdot Z_s$ if there is no feedback control. The feedback voltage control loop, however, responds to bring the deviated bus voltage back to the rated value, as shown in Figure 12.6. The bus voltage is maintained within specified limits at a specified bus

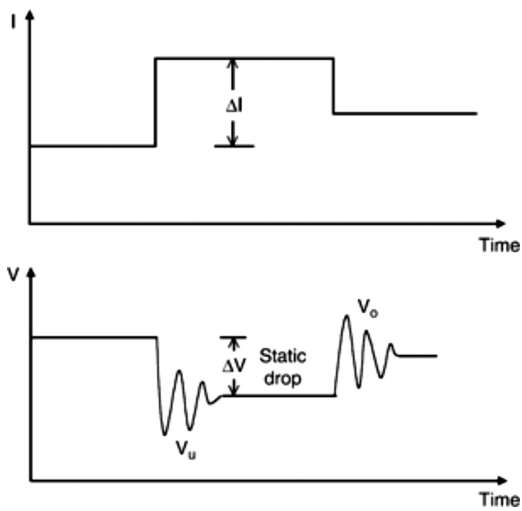

FIGURE 12.5 Transient voltage undershoot and overshoot following load step change.

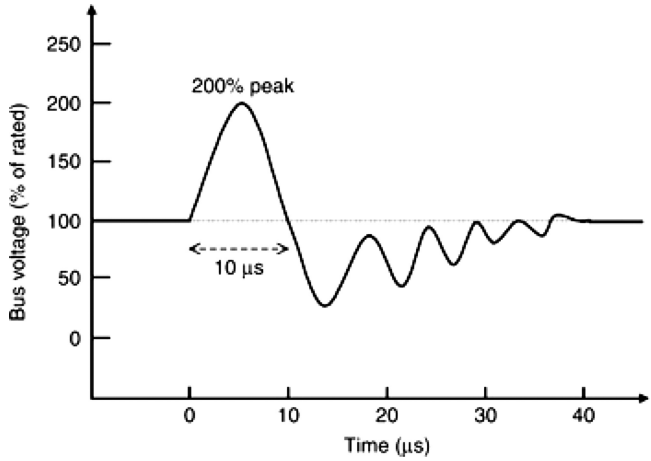

FIGURE 12.6 Main bus transient voltage limit for a typical 100 V bus.

sense point, generally the power distribution point inside the power regulator unit. In order not to flutter the system more than necessary, the control system is designed with suitable deadbands.

The bus voltage can deviate from its nominally rated value for many reasons. Computers and microelectronic circuits are more susceptible to voltage transients than rugged power equipment such as motors, transformers, and heaters. The deviation that can be tolerated depends on its magnitude and duration. Small deviations can be tolerated for longer than large deviations. The tolerance band is generally

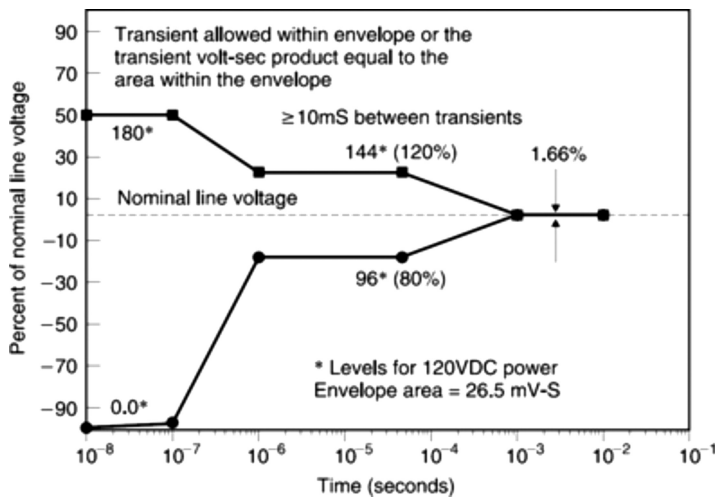

FIGURE 12.7 Bus voltage deviation limits versus duration for a typical 3 kW, 120 V low Earth orbit satellite.

defined by voltage versus time (V–t) limits. The system voltage must be maintained within the specified V–t envelope shown in Figure 12.7 as an example. The right-hand side of the band comes primarily from the steady-state performance limitations of the load equipment. The middle portion comes from voltage flicker considerations. And the left-hand side of the band comes from the electronic load susceptibility considerations, which are in the microsecond range based on the volt-second capability of the power supply magnetics and the dielectric withstand capability of the insulation.

12.4 HIGH-FREQUENCY RIPPLES

The ripple is the term used to describe peak-to-peak voltage deviation from the normal steady-state operating voltage under repetitive current pulses. The ripple is sometimes expressed in terms of the rms value, which is also defined as

$$V_{r(\text{rms})} = \frac{V_{r(p-p)}}{2\sqrt{2}} \tag{12.6}$$

The ripple is caused by switching a current on or off, such as in the pulse width modulation (PWM) operation of solar array shunts, battery power converters, and communication load modulation. Figure 12.8 illustrates the ripple voltage generation under repetitive on-off pulses of current. The PWM switching of shunt current is a major source of bus voltage ripples. The ripple frequencies are integer multiples of the switching frequency. The ripples are periodic but not sine waves, and are superimposed on the fundamental voltage, ac or dc. The ripple voltage induced on the bus due to ripple current of a certain frequency is given by

$$V_{\text{ripple}} = I_{\text{ripple}} Z_d \tag{12.7}$$

where Z_d is the dynamic bus impedance at the frequency of interest. The impedance is generally in the hundreds of milliohms, and the ripple voltage limit varies over a

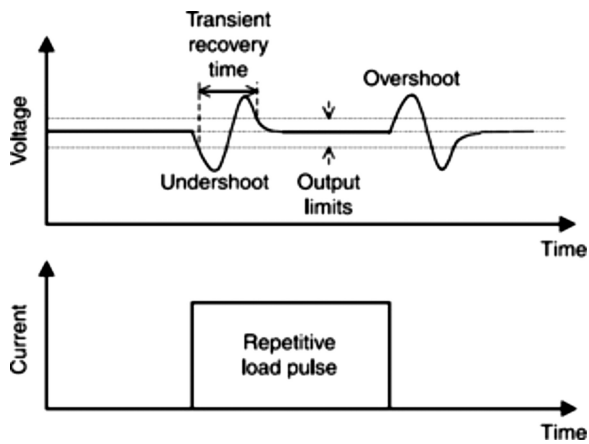

FIGURE 12.8 Bus voltage ripples under repetitive load pulses.

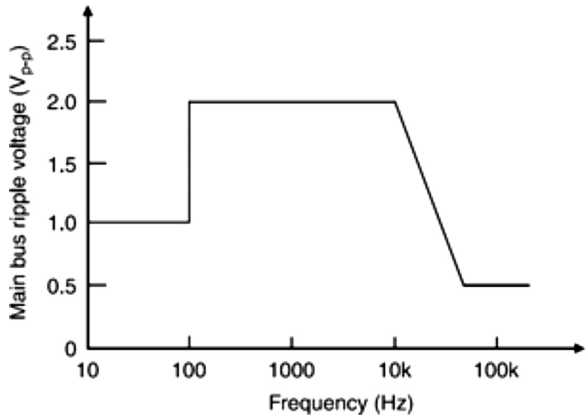

FIGURE 12.9 Bus voltage ripple limits for typical 5 to 10 kW, 100 V geosynchronous Earth orbit communications satellites.

wide range in the hundreds of millivolts. Figure 12.9 is a typical voltage ripple limit imposed on the main bus of a mid-size communications satellite.

The ripple is minimized by bus filter capacitors connected to the bus, or preferably at the component terminals causing the ripples. The ripple current is then supplied or absorbed by the capacitor rather than by the bus, thus improving the quality of power at the bus. For a 28 V sun-regulated bus for communications satellites with a 4000 W payload, a typical bus filter may be about a 4000 μF capacitor bank with an ESR less than 60 mΩ at 25°C. The filter design is made two-fault-tolerant by using a bank of many capacitors connected in parallel with internal fuse protection for each.

Equal output source impedance of the PRU in the sun and the eclipse operations can benefit the bus design for meeting the ripple limit. Otherwise, the higher of the two must meet the limit while not receiving any benefit from the lower ripple in the other mode of operation. Controlling the input ripple to the PRU is also important to avoid excessive common mode noise at the battery monitoring circuit.

Multiple ripple frequencies are often present in the system. The system's performance may suffer if ripples of numerous frequencies having about the same p–p value are present, although each individually meets the p–p ripple specification. For this reason, it is a general practice to specify not only the p–p limit at any one ripple frequency but also the total ripple distortion factor (TRDF) due to all ripples combined. The TRDF is defined in terms of the Fourier series, where a periodic voltage of any shape is decomposed into a series of sinusoidal components, i.e.,

$$V(t) = V_1 + \sum_{n=2}^{\infty} V_n \sin(n\omega t + \alpha_n) \tag{12.8}$$

The first component on the right-hand side of the above equation is called the fundamental component, whereas all other higher frequency terms ($n = 2,3\ldots \infty$) are called the harmonics. The TRDF is then defined as

$$\text{TRDF} = \frac{\sqrt{V_2^2 + V_3^2 + \cdots V_n^2}}{V_1} \tag{12.9}$$

The TRDF is useful in comparing the quality of power with respect to the ripples between two or more power systems or at various locations of the same power system. In a pure ripple-free voltage source, TRDF = 0. The greater the value of TRDF, the more distorted the bus voltage. The major operational concern arising from the ripples is the EMI. Additionally, the interaction of ripple voltage and current does not contribute to the average power. The ripple currents merely result in more I^2R loss for the same useful power delivered. Poor quality power therefore adversely affects the power system's efficiency as well.

The harmonic distortion on bus voltage caused by the nth harmonic current I_n drawn by any nonlinear load is given by $V_n = I_n Z_n$. This distortion in the bus voltage that causes the harmonic current to flow through other loads is called the victim load. A harmonic-rich bus voltage supplies distorted current to all loads, linear or nonlinear. Therefore, harmonics are generally filtered out before feeding power to the bus. A bus voltage with a TRDF less than 3%–5% is generally considered acceptable.

12.5 RIPPLE MEASUREMENT

Two simple test methods to measure ripples are shown in Figure 12.10. They consist of connecting the oscilloscope probe to the output terminal of the equipment under test either (i) directly or (ii) with a capacitor. The setup (iii) is a widely specified method for power converters. It typically uses an AWG 16 twisted pair of output wires terminated into a 50 μF capacitor and an oscilloscope with a bandwidth greater than 50 MHz.

Figure 12.11 shows another way to measure output ripple voltage using a terminated 50 Ω coaxial cable going directly to the oscilloscope. A ground plane is used

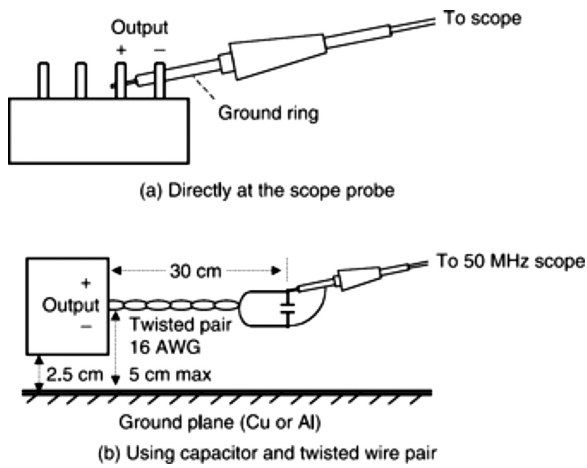

FIGURE 12.10 Ripple measurement methods. (a) Directly at the scope probe. (b) Using a capacitor and twisted wire pair.

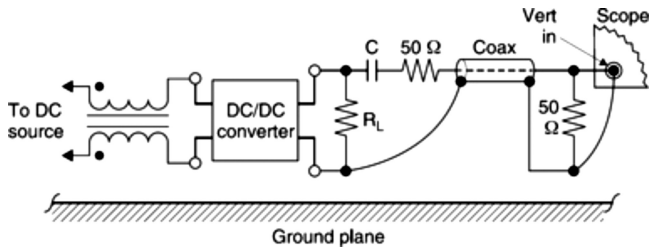

FIGURE 12.11 Ripple measurements using terminated coaxial cable.

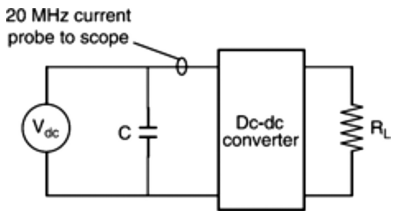

FIGURE 12.12 Reflected ripple current measurements.

between the power converter and the scope. Extraneous noise pick-up is minimized in these low-impedance shielded measurements. In addition, an input balun is used with the dc/dc converter to minimize any common mode noise pickup. Any noise pickup in this setup may be checked by connecting both input and ground leads to the same converter terminal and looking for noise on the scope. With the termination resistance matching the coaxial cable characteristic impedance, the measured ripple voltage is equal to one-half the actual value of the p–p ripple.

It is sometimes required to measure the reflected ripple current from a dc/dc converter back into the source. Such measurements are done with a circuit shown in Figure 12.12. It uses a wide-band current probe and oscilloscope, both of at least 20 MHz bandwidth to give accurate wide-band measurements. A noninductive current sampling resistor to make a voltage measurement is another method, but it takes considerably more care to get accurate results.

12.6 MINOR FUSE-BLOW CROSS-TALK

A voltage spike occurs in the system when a fuse blows. If many pieces of load equipment are connected to a common fuse board, a fuse blowing in one piece of equipment may generate a voltage spike in another. This is often known as crosstalk between equipment. Various pieces of equipments should be individually fused to minimize crosstalk between them. A full-scale circuit simulation can predict the crosstalk voltage spike. When the loads are not well defined in an early stage of the program, the energy approach presented below may give an approximate, but quick and directly usable, upper limit on the cross-talk spike. It is based on a simple circuit model of Figure 12.13 using only the cable parameters shown in (b).

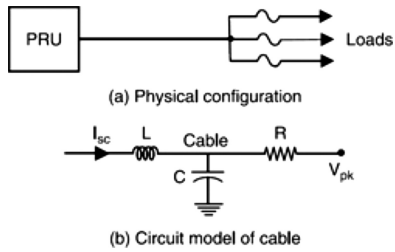

FIGURE 12.13 Cross-talk between equipment following a small fuse blow. (a) Physical configuration. (b) Circuit model of the cable.

Various wires and other resistances in series determine the steady-state fault current just before the fuse blows. With that current, the wire inductance would store energy equal to $\frac{1}{2}LI^2$. When the current is interrupted at the instant of the fuse blow, this energy is dumped on C, the capacitance of the wire, the EMI filter, or both. Thus, the cable's inductive energy gets transferred to the capacitance, and the capacitor voltage rises. Ignoring the energy loss in the transfer and the initial energy in the capacitor at rated voltage, the inductive and capacitive energies must be equal, i.e.,

$$\frac{1}{2}LI^2 = \frac{1}{2}CV^2 \tag{12.10}$$

Thus, the bus voltage at the instant of current interruption would rise to the value given by, in the first approximation,

$$\text{Voltage spike} = I\sqrt{\frac{L}{C}} \tag{12.11}$$

If the cable capacitance is insufficient to absorb the inductive energy, an external capacitance can be added so that the total capacitance keeps the voltage spike below the specified limit.

The hermetically sealed fuse blows suddenly because no plasma is generated in the sealed vacuum. Therefore, it can cause a severe voltage spike following a fuse blow and may need capacitance as estimated above at the fuse location. The regular, nonsealed fuse may require less capacitance because it blows slowly due to the lingering plasma. An alternate method of spike suppression often used is a freewheeling diode in parallel with the fuse. This technique, however, cannot be used to suppress a transient generated by a source inductance common to the affected power distribution. The most effective means of such transient control is to minimize the source inductance and use capacitive damping.

Some load faults can result in large but short-duration transient currents of hundreds of amperes. Such fault currents would result in a bus voltage transient that is severe. It may momentarily collapse the bus, as discussed in the next section.

12.7 MAJOR FUSE BLOW TRANSIENT

The bus voltage rapidly drops under faults in large equipment connected to the bus. For example, a fault in one of the arcjets with a 50 A fuse is simulated as $Load_1$ in Figure 12.14. The solar array, battery, and filter capacitors all feed current to the faults, as shown by the arrows in the figure. After the 50 A fuse blows, the available solar array power starts recharging the battery and the capacitors. The voltage takes a sharp v-turn and starts rising until it reaches the nominal bus voltage. The power system control loop then stabilizes the bus voltage within the tolerance band. The fall and rise of the bus voltage under such a major fuse blow is depicted in Figure 12.15. Thus, the entire power system is involved in clearing a large fuse. The larger the rating of the affected fuse, the deeper the voltage sag. The power system specifications generally limit such voltage sag to some minimum value set by a critical equipment requirement. For example, the central computer on a 70 V system cannot perhaps tolerate the voltage sag below 35 V for more than 5 ms. The power system design engineer must therefore run the fuse blow simulation analysis and show that such a requirement is met.

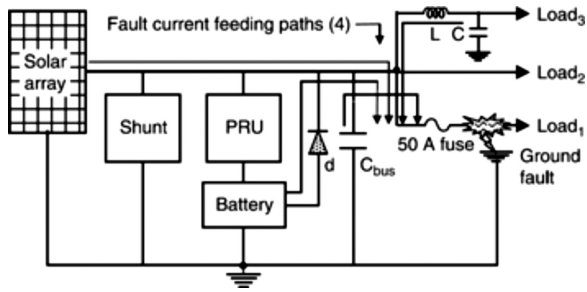

FIGURE 12.14 A circuit model for a major fuse blow transient analysis.

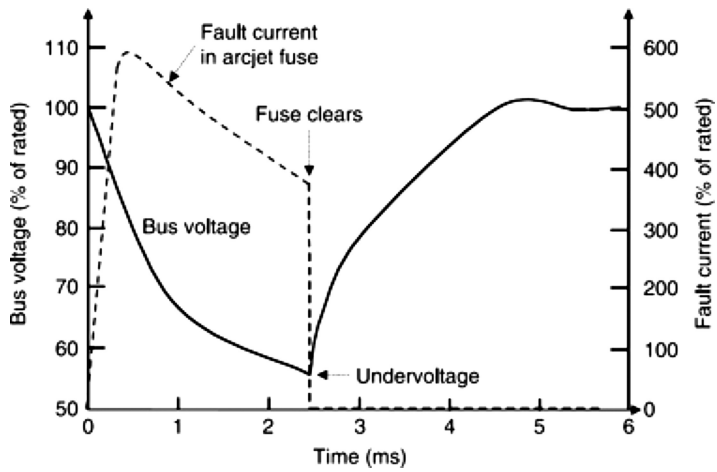

FIGURE 12.15 Bus voltage decay and recovery transients during a major fuse blow.

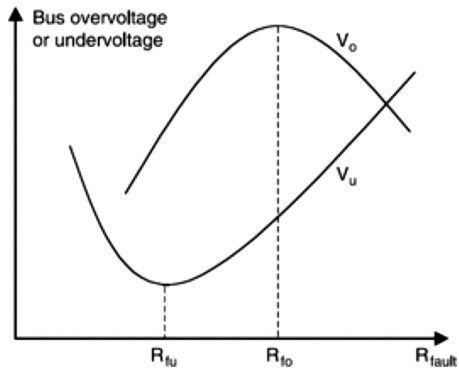

FIGURE 12.16 Bus under-voltage and over-voltage versus fault resistance during a major fuse blow transient.

Most faults are between the line and chassis, involving the ground, rather than between the line and return. The fuse-blow transient is sensitive to the ground return resistance, which may vary from fault to fault. For this reason, the fuse blow circuit simulation is carried out with various possible fault resistances. The results are parametrically plotted in Figure 12.16. Such plots can assure that under worst-case fault resistance, the bus voltage meets the requirement. In addition to the random fault resistance, there is always some minimum ground impedance depending on how the system is grounded to the structure. For example, the structure with a graphite composite face-sheet has higher ground contact resistance. The resulting spread of the current also give higher inductance. For this reason, the ground contact impedance of the graphite face-sheet used in some modern communication satellites is about three orders of magnitude higher than that of the aluminum face-sheet. This significantly changes the transient characteristics of faults involving ground. High ground impedance reduces the final fault current only slightly but greatly increases the $L\,\mathrm{d}i/\mathrm{d}t$ when the fuse blows, thus raising EMI/EMC concerns.

A typical main power bus fault response requirement is shown in Figure 12.17. In the past, fuse transients have not been a major problem, except some telemetry may give an erroneous transient reading on that instance, but recover soon. Such a glitch is generally tolerable in commercial satellites but not in military and NASA satellites because, in an extreme case, it may upset the CMOS computer or other mission-critical functions.

The EPS is generally designed to accommodate payload shedding in case the bus voltage drops to 90%–95% and is capable of powering essential spacecraft functions up to 75%–80% of the nominal bus voltage.

12.8 STABILITY AND BUS IMPEDANCE

The steady-state operating point is stable if it gets restored after an arbitrarily small momentary disturbance in the source or the load. For example, at operating point A_1 under constant power P_1 in Figure 12.18, suppose a disturbance due to any reason causes a drop of ΔV in voltage. At the new voltage, the source current is less than the load current. Consequently, the voltage decreases again, and the operating point

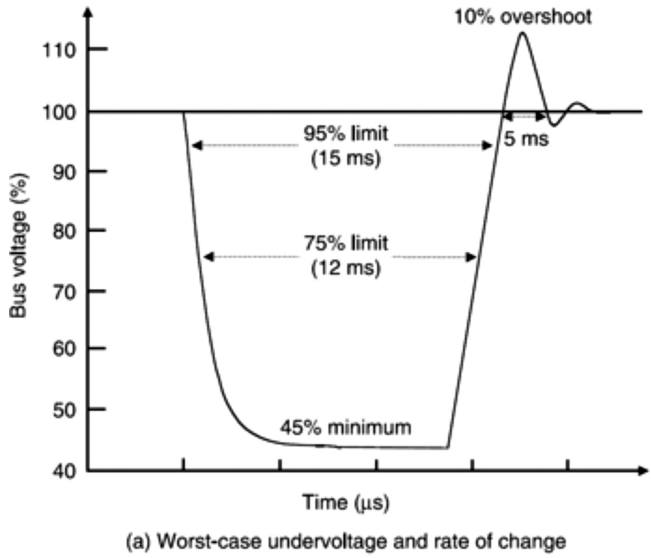

FIGURE 12.17 Main power bus fault response requirements for a typical 5 to 10 kW, 100 V geosynchronous Earth orbit communications satellite. (a) Worst-case undervoltage and rate of change. (b) Worst-case overvoltage and rate of change.

moves further away from A_1, and again further away, and again in a runaway situation. Similarly, a small increase in voltage due to a disturbance will make the system move away from point A_1 in the other direction. Thus, point A_1 is an unstable operating point where the system works like a positive feedback system.

On the other hand, at point A_2, a small change in voltage in any direction, due to any reason, produces counterchanges to bring the system back to its original operating point A_2. Thus, point A_2 is a stable operating point where the system works like a negative feedback system. Analytically, we can derive the following condition for static stability. An operating point is stable if and only if the following conditions are met at that point:

$$\left[\frac{dV}{di}\right]_{\text{source}} < \left[\frac{dV}{di}\right]_{\text{load}} \tag{12.12}$$

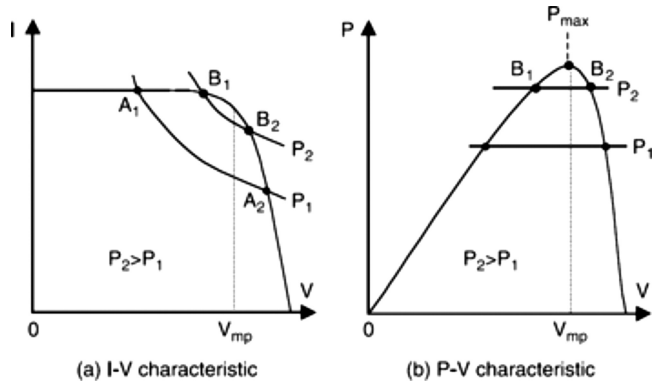

FIGURE 12.18 The stability of a solar array's operating point under a constant power load. (a) I-V characteristic. (b) P-V characteristic.

If we think in terms of the absolute values of the dynamic impedances and define Z_s as the source output impedance and Z_L as the load input impedance, then the system is stable only if

$$Z_s < Z_L \tag{12.13}$$

at all frequencies. When $Z_s > Z_L$, further analysis is needed to determine the system's stability.

The operation of a solar array under a resistive load is shown in Figure 12.19. The load line is a straight line from zero with a slope equal to the resistance value. For such a load, the above condition is always met; hence, the solar array powering a purely resistive load is always stable.

A nonlinear solar array source coupled with a nonlinear load may result in multiple equilibrium points under a given operating condition. The actual equilibrium

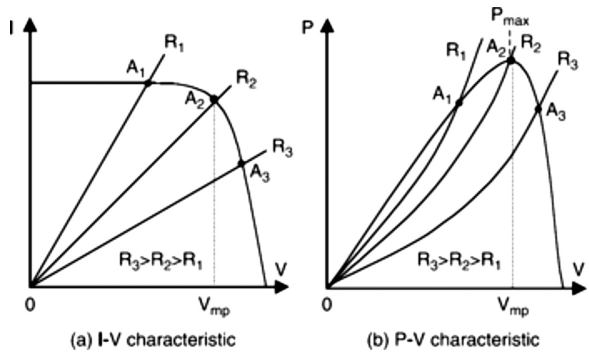

FIGURE 12.19 The stability of a solar array's operating point under a resistive load. (a) I-V characteristic. (b) P-V characteristic.

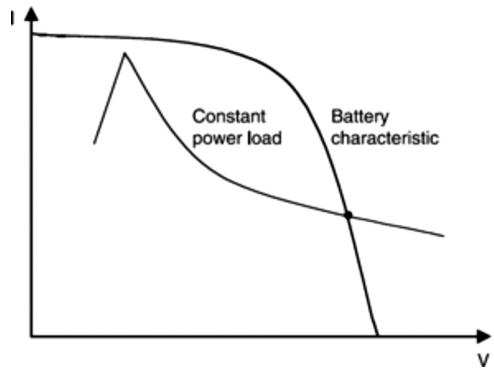

FIGURE 12.20 The stability of a battery's operating point under a constant power load.

point that the system resides at is determined by the stability of the equilibrium points and the past history of the operating point.

During an eclipse, when the battery directly supplies a constant power load, the intersection of the source line and the load line always gives a stable operating point, as shown in Figure 12.20. The unstable point in this case is outside the practical

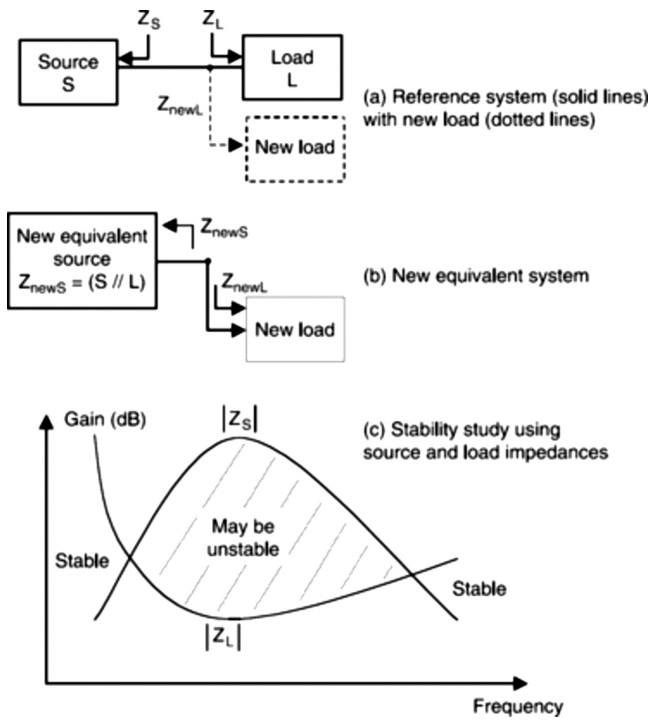

FIGURE 12.21 Thévenin equivalent source and dynamic load impedance for a stability study in a large power system.

range of the constant power load, which is tripped off before the voltage drops to the point where the battery operation may become unstable.

Figure 12.21 shows an example of the load and source impedances overlapping and the unstable operating region. The source and load impedance specifications are primarily set to ascertain the system's stability under all conditions. This task can be complex, even for a small spacecraft. It can be extremely complex for a large space platform with a variety of loads that can be connected, not all of them known in advance, such as on the ISS.[1] In those cases, the load impedance specification for every load can be established from the fundamental systematic considerations presented below. Any complex system with a number of sources and loads can be reduced to the equivalent network with the Thévenin parameters V_s and Z_s. Any additional load with impedance Z_L must be greater than this value of Z_s for stability. A critical factor in the design of a large platform such as the ISS is the stability of the system under all expected conditions of loading and transient perturbations. The ISS power systems engineers have developed a set of impedance criteria for both the source converters and the load converters to assure stability under significant variations in the load connectivity over the life of the station. When a new load is added on the large platform, the old source and load impedances combine in parallel to form the new source impedance (Figure 12.21). Thus, the new Z_s will always be less than the old Z_s. This logic may be used to set the dynamic input impedance of any load that can be connected by any user on a large ISS-type large. If the system is stable, then any additional load in parallel will keep the system stable.[2]

12.9 THE DYNAMIC STABILITY OF A CONTROL SYSTEM

A dynamic stability study determines whether the system will be stable under sustained small harmonic perturbations coming internally from the power system or from an external source via conducted EMI. Verifying the stability involves modeling the total system with all control loops. A detailed theory of the control system is outside the scope of this book, but a short review follows.

The negative feedback control system is widely used for controlling many systems, subsystems, and components, often with multiple nested loops. Figure 12.22 represents a feedback control system in terms of the transfer functions (TFs), where G is the main equipment TF and H is the TF of the feedback control loop. It can be shown that the TF of the entire system is

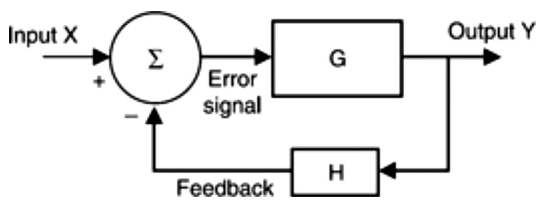

FIGURE 12.22 A classical feedback control system model.

$$\text{TF} = \frac{\text{Laplace transform of the output } y(t)}{\text{Laplace transform of the input } x(t)} = \frac{G(s)}{1 + G(s)H(s)} \tag{12.14}$$

This equation indicates that $1 + G(s)H(s) = 0$ results in an infinitely large output for an arbitrarily small input. The solutions (roots) of Equation 14.14 are called the system poles, which are in general complex, say $s = \alpha + j\beta$. We say that the output blows up, i.e., the system is unstable, if

$$G(s)H(s) = -1 \tag{12.15}$$

In other words, the open loop gain of 0 dB and the phase angle of 180° give an unstable system. Stability is often judged in two ways. In one method, the gain in dB and phase angle in degrees are plotted with respect to frequency in what are known as Bode plots, as shown in Figure 12.23. The system is generally considered stable if the gain is below zero with about a 30 dB margin and the phase angle is away from 180° with about a 30° margin. These margins vary with the spacecraft requirements and heritage data on similar buses. In one 3000 W, 120 V low Earth orbit satellite, the PRU and mode controller amplifier were required to provide a stability phase margin of at least 45° and a gain margin of at least 10 dB.

In another method for determining stability, the poles are plotted in the complex plane. The system is stable only if all poles have a negative real part, which results in damped oscillations. Or, in other words, all poles must be on the left-hand side of the complex plane (Figure 12.24). In case the system is found to be unstable, a compensating lead–lag network is introduced in series with the main equipment, as shown in Figure 12.25. The combined forward TF is then C · G, which is used in evaluating the stability of the compensated feedback system. Since the circuit parameters of the compensating network may vary with temperature and age, it is customary to check the stability under the worst compensation and load conditions, as shown in Table 12.1. The table in this example shows that the system is stable with comfortable margins under the worst conditions.

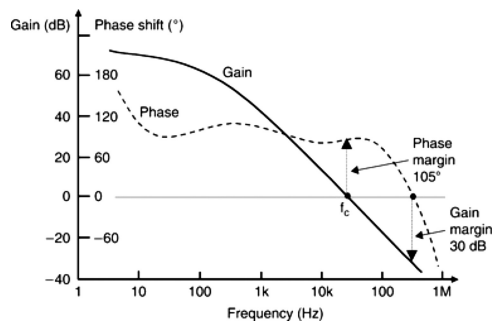

FIGURE 12.23 Dynamic stability criteria from open-loop Bode plots.

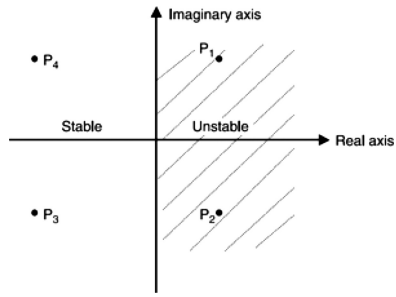

FIGURE 12.24 The dynamic stability criteria from the pole plot in the complex plane.

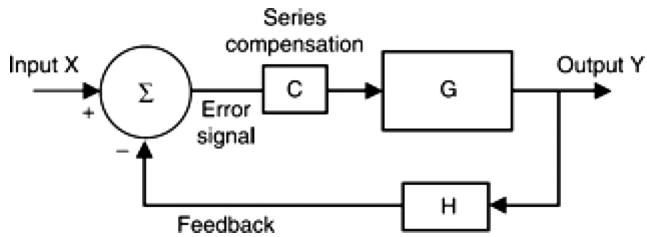

FIGURE 12.25 Series compensation (lead–lag network) added for stability.

TABLE 12.1
An Example of a Stability Study under the Worst Compensation and Load Combination for a 100 V Bus

	With Maximum Compensation Gain			With Minimum Compensation Gain		
Payload Configuration	System Band-Width (Hz)	Phase Margin	Gain Margin (dB)	System Band-Width (Hz)	Phase Margin	Gain Margin (dB)
All loads off	1700	105	40	1100	70	46
1 TWTA on	1400	104	40	1000	70	44
2 TWTAs on	1400	103	40	900	69	48
3 TWTAs on	1200	102	40	900	70	46

12.10 DYNAMIC SIMULATION MODEL

Considering the size and complexity of modern spacecraft power systems, the digital computer is the only viable tool for system modeling and simulation. Two general classes of simulation programs appear in the literature. They are: (i) generalized circuit and system simulation models or (ii) dedicated models of specific systems. The generalized computational models as a class are built using commercial programs with trade names such as PSPICE, SABER, SYSCAP, ICAP, and a number of others. All have similarities in that they offer a large library of component templates capable

of analog, analog/digital mixed signal, and mixed technology simulation (electrical, mechanical, thermal, optical, and even chemical). The templates are assigned parametric values to simulate the actual components used in the system. The simulation can be at any level: component, behavioral, functional, or control level.

12.10.1 Solar Array Model

Two approaches can be taken for modeling the solar array: micro and macro. In the micromodel, each cell is modeled by its *I–V* characteristic. The advantage of this approach is that cell-to-cell variations internal to the array can be modeled. For example, a local cell failure or shadowing can be inserted into the model. However, the number of cells needed for a full simulation on a large satellite can be prohibitive and inefficient. The macro model, on the other hand, can represent the entire array as one component with the total *I–V* characteristic of all cells combined in series–parallel connections.

The shunt control loop may show some sensitivity to the capacitance of the solar string circuits. However, in practical shunt control loop designs, the gain and phase margins in the stability analysis are found to be insensitive to the cell capacitance varying over a wide range around the nominal value. The solar cell capacitance can be calculated from the solar array impedance measurements under sweeping frequency, dc voltage, and current bias conditions. The capacitance of a 2×4 cm silicon solar cell is typically 0.25 μF when in the dark. Under illumination, it is about 0.50 μF near the short circuit current and 0.75 μF near the peak power point. A typical dynamic ac model for one 5 A, 70 V solar circuit is shown in Figure 12.26.

Lindmayer[3] gives the ac impedance (in ohms) of the solar circuit as

$$Z_{ac} = \frac{R_d}{\sqrt{(1+\omega\tau)}} \tag{12.16}$$

where $R_d = dV/dI$, the slope of the solar cell *I–V* curve, i.e., the dynamic resistance, and τ = diffusion time constant of electrons in the p-region of the cell. The Z_{ac} includes the ac resistance of the equivalent diode as well as the R_s and R_{sh} components. It varies with the dc operating point and also with the cell temperature via the τ term. The capacitance, C_s (in farads), can be analytically obtained from NASA/JPL data[4] as follows:

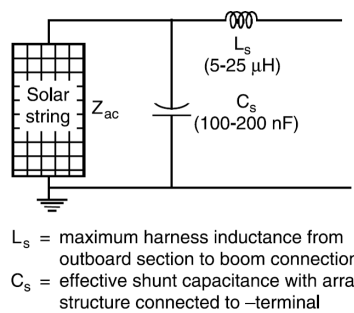

FIGURE 12.26 The solar array circuit dynamic model for system simulation.

$$C_s = A\sqrt{\frac{q\varepsilon N_a}{2(V_b - V_a)}} \tag{12.17}$$

where

A = cell area, q = electron charge, ε = permittivity of silicon, N_a = acceptor density in the p-region, V_b = barrier voltage, and V_a = applied voltage (positive in forward bias).

A typical 2 Ω·m silicon cell with $\varepsilon = 1$ pF/cm, $N_a = 1{\cdot}10^{16}\,\text{cm}^{-3}$, and $V_b = 0.8$ V at room temperature gives a value for C_s, in μF/cm^2, of

$$C_s = \frac{0.0288}{\sqrt{0.8 - V_a}} \tag{12.18}$$

The maximum and minimum values of C_s occur at open circuit and short circuit, respectively. Not much has been published on the variation in C_s with temperature, probably because the changes in dc operating voltage far outweigh the temperature effects. However, C_s increases with increasing temperature by about 0.1% per °C.

12.10.2 Other Component Models

The battery model as discussed in Chaper 7 can be simply a constant voltage source with an internal resistance or a complex nonlinear voltage source. The choice depends on the degree of precision desired from the model. For a 100 Ah NiH_2 cell, the battery's internal inductance is about 0.35 μH/cell.

The solar shunt regulators and the battery charge and discharge regulators can be modeled at their own component levels in the microsense, or at their behavioral levels in the macrosense. Both approaches are valid, although the latter is perhaps simpler and yet sufficiently accurate for a wide variety of analyses.

The communications loads (TWTA and SSPA) are constant power loads. Many bus loads such as arcjets and reaction wheels, are also constant power loads. They are cut off when the voltage drops below certain values. During on-time, the constant power load is modeled as a variable resistance of value $R = V^2/P$, where V is the actual bus voltage at any given time. If the voltage remains below the left-hand column value for a time greater than that in the right-hand column, the load is cut off. On the other hand, constant resistance loads like heaters remain connected all the time. Before trip-off, the constant power loads reflect as negative resistance on the converter, while all other loads reflect as positive resistance.

12.11 SIMULATION RUNS

The labor involved in building the dynamic model is rather extensive. Once the model has been built, independent calibration with known solutions is the next major task. It is used for the analysis only after verification has been carried out satisfactorily and reviewed by a team of independent engineers.

The operating point of the system is determined by the source (solar array or battery), the power conditioning equipment, and the load characteristics. Since the solar array output power and the load demand vary over a wide range, several modes of

operation exist, and all must be analyzed. Some uses of the dynamic simulation are: (i) Stability studies, (ii) Impedance plots versus frequency, (iii) EMI–EMC compliance verifications, (iv) Trade studies and parametric studies, (v) Failure effects and worst-case analyses, (vi) Fuse blow under-voltage and over-voltage, and (vii) Troubleshooting.

However, the dynamic simulations are performed primarily to determine that all four primary control loops are stable and have adequate gain and phase margins. In shunt mode, the regulated bus voltage control loop (shunt loop) and the battery control loop (BCR loop in charge mode) are two loops that are independently active. Also in shunt mode, the battery charge current is a constant current load, which is part of the overall solar array load. In discharge mode, bus voltage regulation (BVR) is performed by the BVR loop. For these loops, linear circuits can be modeled using PSPICE or SABER.

There are two primary areas of interest. The small signal analysis is to obtain the phase/gain characteristics of each control loop under various conditions and the output impedance characteristic. The large signal analysis is to assure that each loop meets its specified performance characteristic for the specified disturbances, i.e., the loop intra-mode large signal response. Often, inter-mode computer simulations may require combining two or more control models to simulate the inter-mode response, i.e., the transfer of control from one loop to another.

Spacecraft-level tests can detect inter-modal transient problems, which may require re-compensation of the BCR and BVR control loops. Examples of changes that can be implemented to remedy such problems are: (i) the addition of the output filter for each BVR, (ii) a mode controller error amplifier to reduce inter-modal transients, (iii) a BVR switching circuit that affects the average switch model, and (iv) BVR error amplifier.

REFERENCES

1. Wilde, R.K., Aintablian, H.O., and Gholdston, E.W., International Space Station U.S. major elements laboratory power quality test, in *Proceedings of the 34th Intersociety Energy Conversion Engineering Conference*, SAE, 1999, Paper No. 01-2434.
2. Fassburgh, H.D., Gholdston, E., and Mong, A., Development and implementation of stability requirement for the International Space Station electrical power system, in *Proceedings of the 36th Intersociety Energy Conversion Engineering Conference*, ASME, 2001, Paper No. AT-48, pp. 281–288.
3. Lindmayer, J. and Wrigley, C.Y., *Fundamentals of Semiconductor Devices*, D. Van Nostrand, New York, 1965, pp. 47–48.
4. NASA/ JPL, *Solar Cell Radiation Handbook*, 3rd edition, 1982, Report 82-69, pp. 1–19.

FURTHER READINGS

Aghamohammadi, M.R. and Khormizi, A.B., Small signal stability constrained rescheduling using sensitivities analysis by neural network as a preventive tool, in *Proceedings of the 2010 Asia-Pacific Power and Energy Engineering Conference*, Mar. 2010, pp. 1–5.

Aghamohammadi, M.R., Khormizi, A.B., and Rezaee, M., Effect of generator parameters inaccuracy on transient stability performance, in *Proceedings of the 2010 Asia-Pacific Power and Energy Engineering Conference*, Chengdu, China, 28-31 March 2010, pp. 1–5.

13 Electromagnetic Interference and Compatibility, and Electrostatic Discharge

13.1 INTRODUCTION

The electromagnetic interference (EMI) and electromagnetic compatibility (EMC) standards specify requirements for all equipment working together in a system—such as a spacecraft, ship, or plane—to meet the design performance with a suitable margin. The standard outlining such requirements is MIL-STD-461. It specifies the maximum emission limit of the potential culprit and the minimum susceptibility level of the potential victim's equipment. Many military contracts now require compliance with the latest version of MIL-STD-461. While its compliance is technically not required outside the US military, many civilian organizations also use this document, such as NASA.

In a brief history of EMI and EMC standards, the US Department of Defense issued MIL-STD-461, 462, and 463 in 1967 to incorporate EMI and compatibility at the research and development stage for defense communications technology. The standard 461 covered the electromagnetic emission limits and susceptibility (immunity) levels for the military equipment, 462 prescribed the tests and measurement methods, and 463 contained definitions and acronyms used in these documents. These standards were then accepted jointly by the US Army, Navy, and Air Force, and soon by the space industry and many other countries as well. Based on over three decades of experience working with these standards, MIL-STD-461 and 462 were combined into MIL-STD-461D in 1999, which was revised into MIL-STD-461E and then to F and G in 2015.

The EMI emitted from equipment A (culprit) can enter surrounding equipment B (victim) either by conduction via wires or by radiation in space. For a system made of equipment A and B to perform together as required, B must be compatible—able to tolerate or not be susceptible—to A's interference in order for B to perform successfully, and vice versa. Every component of the system must have an emission level below and a susceptibility level higher than the limits specified in MIL-STD-461. It is difficult to design the components to meet these requirements in a compact system, such as in the engine room of a Navy submarine.

The EMI requirements broadly fall into two general groups, the conducted EMI and the radiated EMI. In addition, some spacecraft-specific requirements may also be imposed. The spacecraft customer generally requires three documents from the

DOI: 10.1201/9781003344605-16

supplier: (i) EMI Control Plan, (ii) EMC Test Plan, and (iii) EMI Test Report documenting the test results and the steps to be taken to remedy the failures, if any.

Electrostatic charge accumulates on any probe in a space environment, regardless of whether it is inside or outside the Van Allen belts. The accumulated charge raises the electrical potential of the probe, causing a current to flow from the probe to the surrounding plasma. If the current cannot maintain a balance of charge, the probe potential will keep rising until arcing takes place. Such a problem can occur, particularly when the spacecraft leaves or enters an eclipse and the interaction with space suddenly changes. Arcing can also arise due to differential charging of insulated surfaces that are not connected together. Each isolated surface acts as an independent probe in space, which floats to a potential that results in no net current to or from the space plasma. That potential is of the order of the plasma kinetic energy. Insulating surfaces do not distribute surface charge, hence can charge up to a much higher differential potential until discharge takes place by way of arcing and/or flashover. The charging, the subsequent electrostatic discharge (ESD), and their remediation in geosynchronous Earth orbit (GEO) and in low Earth orbit (LEO) are significantly different as discussed later in this Chapter.

13.2 SOURCES OF EMI

In the commercial world, radiated EMI comes from radio and TV towers, mobile radio vans, lightening, and nearby power lines. The conducted EMI comes mainly from power cables. In space systems, the main sources of EMI are:

i. Switching large currents or voltages at high frequency, causing large dI/dt and dV/dt,
ii. Electrostatic discharge, and
iii. Nuclear detonation in the surrounding.

Conducted EMI: Active components, such as switches and diodes, are the main sources of conducted EMI in switch-mode power converters. The switching-frequency voltage ripple is primarily influenced by the dynamic impedance of the equipment. The high-frequency EMI, however, arises due to the parasitic ringing in voltage following a current switch. Therefore, refined component models are needed to predict accurate ringing frequency, amplitude overshoot, and rising or falling transients. Such models must be verified through tests. Accurate circuit models for the following high-frequency components are needed in the applicable frequency range: (i) Active components (switches, diodes, etc.), (ii) Passive components (transformers, capacitors, inductor, resistor, etc.), and (iii) Printed circuit board patterns used in the spacecraft. Accurate models of these components cannot only predict the high-frequency EMI level but also identify the cause. An optimized EMI solution can then be achieved before fabricating the hardware.

Radiated EMI: The power system harness is a major source of low-frequency electromagnetic radiation and coupling. Around a short wire (<10% of the signal wavelength), generally one type of field dominates, either the magnetic field (B-field) around high-current lines or the electric field (E-field) around high-voltage lines.

The B-field is negligible around a coaxial cable with small eccentricity and also at some distance from a twisted wire pair carrying a differential mode current. For the wires depicted in Figure 13.1, the B-field falls off as $1/r$ for a single wire, as $1/r^2$ for two parallel wires carrying equal and opposite currents, and as $1/r^3$ for a current loop, where r is the distance of the victim from the center of the EMI source. The high-frequency electromagnetic field travels at the speed of light in the medium of propagation. The field is characterized into two types, namely the far field and the near field, in terms of the wavelength λ, which is the ratio of speed of light over frequency.

13.3 MODES OF COUPLING

The electromagnetic field coupling between the two components can occur via one or more of the following parameters: (i) Stray capacitance, (ii) Mutual inductance, and (iii) Ohmic conduction. The E-field coupling for an ESD type of transient is governed by the mutual capacitance between the source and the victim. The EMI via B-field coupling is governed by the mutual inductance between the source and the culprit, which can be strong, emitting from equipment like a high-current bus, transformer, or motor.

The total inductive and capacitive couplings between two parallel unshielded wires over a ground plane are determined by the mutual inductance and capacitance, which in turn depend on the geometry of the cables and the frequency. At power frequencies up to 100 kHz, the coupling is primarily magnetic. In this frequency range, the following are some practical design guidelines for controlling the cable coupling:

- The coupling increases with the common run length and frequency and decreases with an increase in spacing.
- The noise voltage of the victim's termination load is a function of the load impedance. A capacitive filter connected from the victim line to ground can be used to decrease the load impedance at noise frequencies, provided the victim's interface can accommodate such capacitance.
- The cable shield characteristic is defined by the transfer impedance. Lower impedance results in more effective cable shielding. Good impedance values are in the milliohms per meter range.
- The twisted shielded wire pair is effective up to 2 MHz, above which the coaxial cable is required.
- High-current power lines and low-impedance loads are prime sources of low-frequency magnetic coupling. Therefore, the power line leads are always twisted with their returns.
- The effectiveness of twisting increases with the number of twists per meter and decreases with the frequency. It is effective only on balanced or single-point ground systems and up to 100 kHz. Above this frequency, capacitance from the wires to the ground causes ground current to circulate, which generates common-mode coupling. Practical twist pitch is 30–50 per meter.
- The capacitive coupling of the electric field is best avoided by shielding the culprit, victim, or both cables and grounding the shield (Figure 13.1).

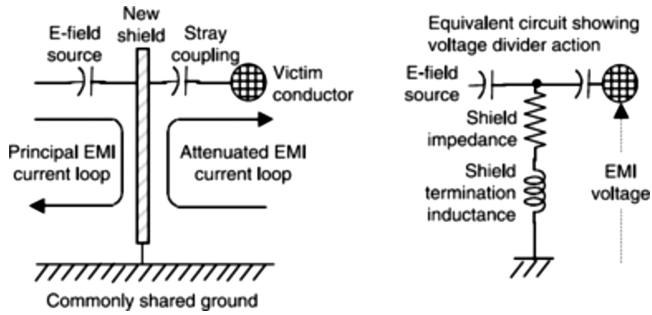

FIGURE 13.1 Shield protection from capacitive coupling. EMI, electromagnetic interference.

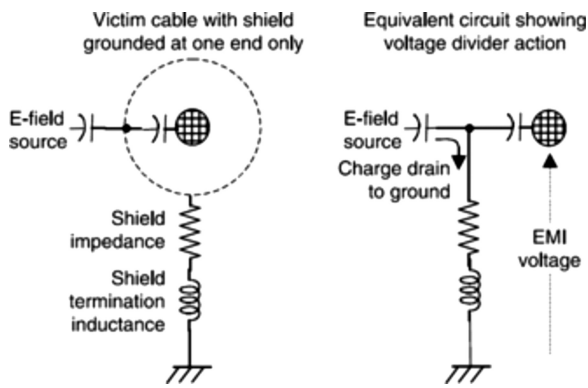

FIGURE 13.2 Victim cable with a shield grounded at one end.

- Single-point ground is used at low frequencies where the wavelength of the frequency to be suppressed is longer than 10 times the shield length. If the culprit wire is shielded, the ground point is at the exit from the culprit source. If the shield is on the victim's wire, the ground point is at the entry to the victim's electronics (Figure 13.2).
- The shield grounding at high frequencies should be at both ends of the shield. This directs the return current away from the ground and into the shield, thus decreasing the ground loop currents and common-mode radiation pickup (Figures 13.3 and 13.4).
- A single-point grounded shield does not reduce common-mode EMI (Figure 13.5).
- A 360° peripheral low-resistance bond should be used via a connector back-shell assembly to assure low-impedance shield grounding in high-quality shield cable. This bond resistance limits the shield's performance.

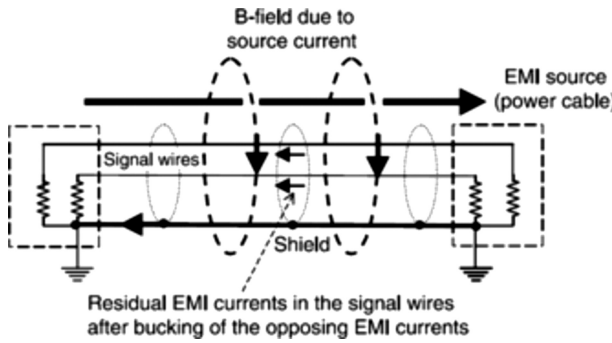

FIGURE 13.3 A shielded cable with both ends grounded. EMI, electromagnetic interference.

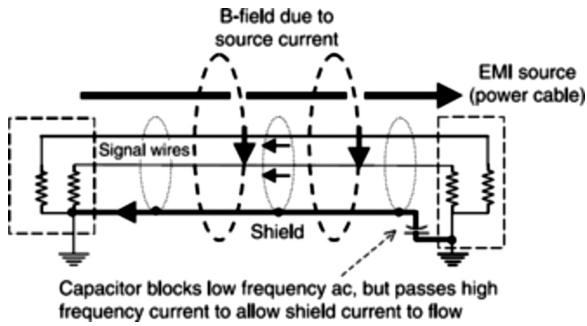

FIGURE 13.4 A cable with a shield grounded at one end for low-frequency signals and at both ends for high-frequency signals. EMI, electromagnetic interference.

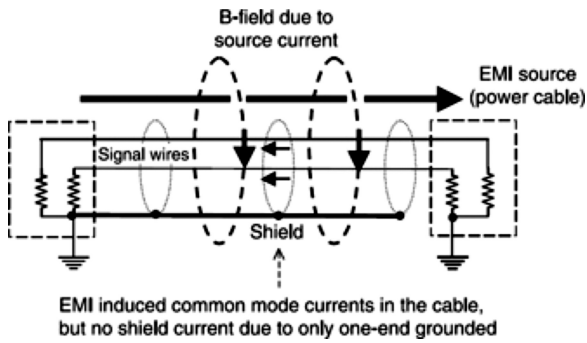

FIGURE 13.5 A shielded cable with only one end grounded. EMI, electromagnetic interference.

13.4 EMI/EMC SPECIFICATIONS

The EMI standard establishes the maximum interference an equipment or a system, such as the power system as a whole, can conduct or radiate into the load equipment. The EMC standard, on the other hand, establishes the minimum conducted and radiated interference that an item of equipment connected to the power system must withstand without being susceptible to a functional impairment. Obviously, the susceptible level must be higher than the emission level with a comfortable margin, usually tens of dB depending on the criticality of the equipment in the system. The EMI/EMC levels are specified in dB, which equals 10 $\log_{10}$ (signal power/reference power) or 20 $\log_{10}$ (signal voltage or current/reference voltage or current). Thus, 3 dB doubles the power, or 6 dB doubles the voltage or current. The EMI/EMC requirement is specified in two parts, the conducted and radiated emission levels of the culprit equipment, and the conducted and radiated susceptibility levels of the victim equipment. The general requirements for all spacecraft and launch vehicles come from MIL-STD-461. The safety margin specified between the emission levels and the susceptibility level is generally 20 dB for critical equipment and 6 dB for all others.

13.5 EMI SUPPRESSION METHODS

Various methods of controlling and/or suppressing the EMI, in the order of their importance, are listed below, and some are discussed further in the next section:

- Minimize the EMI generation in the first place by
  - Minimizing the current loop area in switching circuits
  - Minimizing the switching transients' dI/dt rate in large current loops
  - Using snubber capacitors to minimize the voltage transients' dV/dt rate
- Minimize the E-field and B-field couplings between the culprit and the victim's equipment by
  - Minimizing the inductive coupling by twisting wires or using coaxial cables
  - Minimizing the capacitive coupling by using shields, reducing the area of exposed metal, and keeping it far from the ground (since $C = A\varepsilon/d$)
- Divert the energy impinging on the victim's equipment to the ground by using
  - Proper grounding scheme
  - Faraday shield, single or double
- Protect the equipment from the coupled energy by using
  - L–C filters for conducted EMI
  - Enclosure shield for radiated EMI

13.5.1 Twisting Wires

The twisting not only reduces the spacing between conductors; it also produces self-contained B-fields of opposite polarities around the adjacent spans. Thus, it results in a much lower B-field at a far distance due to the cancellation effect. It does not,

however, reduce the local B-field close to the cable. Twisting a pair of wires is the simplest method to minimize EMI at the lowest cost. It was patented by Alexander Graham Bell in 1881 to minimize noise interference in telephones. Remarkably, we still use them in many other places because they work so well. Note that twisting two wires carrying a common-mode current cannot null the B-field. The only effective way to eliminate common-mode EMI is to block common-mode current by breaking the ground loop.

13.5.2 Grounding

Two configurations of the single-point ground used for dc or ac power systems up to 20 kHz are shown in Figure 13.6. Configuration (a) is preferred. Configuration (b) is simple but less effective for high-frequency EMI since the ground wire inductance increases the Z_{ground} between two pieces of equipment. The grounding at a single point in the system effectively minimizes the radiated EMI by avoiding ground current loops. The power return is grounded only at one point. All ground leads are directly connected to one point, which is then solidly connected to the structure. Single-point grounding reduces the ground inductance. It is used when the circuit dimensions are less than 3% of the wavelength to be suppressed.

13.5.3 Cable Shielding

Military and scientific satellites with stringent EMI requirements cannot tolerate any unshielded segment of the harness or even an open fuse board. All harness groups—power, signal, and pyro—are kept in separate bundles with separate shielding. Commercial satellites, on the other hand, may have fuse boards or some segments of the harness unshielded. All shields (power and signal) are grounded about every meter to a single-point ground. The cable shielding alternatives are braids versus tape made of copper or aluminum. The braids are used where extreme flexibility is required. In tapes, 2-mil-thick copper vapor deposited on Mylar or Kapton insulating tape is widely used. The shield mass as compared to the wire conductor is about 40% for flat cables and 20% for round cables.

13.5.4 Bonding

Fabricating a shielding enclosure made of metal and connecting it together and then to the ground is known as bonding. The connecting wires are bonded together by various processes. The bond is schematically shown on the circuit diagrams by a

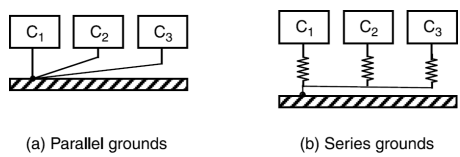

FIGURE 13.6 Single-point grounding schemes. (a) Parallel grounds. (b) Series grounds.

heavy dot before the conducting part meets the ground symbol. The solid bond generally requires conductors with an impedance less than a few milliohms. Movable parts may be bonded using a strap with resistance less than a few milliohms and inductance less than a few tens of nanohertz. The mechanical and electrochemical stability of the bond are required. Welding is recommended for magnetic enclosures, while brazing and soldering are recommended for conductive enclosures. The corrosion in bonding two dissimilar metals, such as a copper strap to a steel box using steel fasteners, is controlled by selecting two materials in contact with about equal galvanic potentials. This requires the electric potential differences between them to be near zero. Otherwise, the condensed humidity between the two components acts as an electrolyte, creating a voltaic cell. Copper, silver, platinum, and gold are cathodic, having positive galvanic potential, while many other commonly used metals are anodic, having negative galvanic potential.

13.6 COMMON-MODE EMI

Even a small common-mode current can cause trouble. We recall that the induced voltage is given by $e = -L\, dI/dt$. A typical value of the wire inductance L is about 80 nH/m. If the rise time of say 100 mA is 1 ns (ESD type discharge), it induces a voltage equal to $80 \times 100/(1 \times 10^{-9}) = 80$ V/m length of the cable. This can upset many sensitive electronic and control circuits.

13.7 BROADBAND EMI

EMI is classified as narrow-band or broadband, depending on the signal's spectral distribution relative to the resolution bandwidth of the receiver used for the measurement. It is essential to know which type of signal is being measured to avoid erroneous test results and the wrong interpretation of data. In this context, knowledge of the instrument's impulse bandwidth is necessary to correctly determine the absolute amplitude of an emission. Determination of the receiver's impulse bandwidth can be done with a series of measurements, but not simply by multiplying its 3 dB or 6 dB bandwidth with a constant factor. Only accurate knowledge of this parameter allows a meaningful comparison of the measured emission levels to a limit line and verification of a product's compliance with an EMI standard.

13.8 ELECTROMAGNETIC PULSE/NUCLEAR THREAT

The electromagnetic pulse (EMP) is a man-made threat that arises from a nuclear detonation around the spacecraft. It can destroy satellites in low and mid-Earth orbits. A nuclear burst can upset electronic systems hundreds of miles away. Therefore, it is usually included in the defense spacecraft power system requirements. The nuclear threat requirement is generally included on defense satellites in any orbit.

The EMP is basically the burst of electron flow resulting from the gamma radiation. It is an intense time-varying electromagnetic field with a very short pulse in the nanosecond to microsecond range. The radiation and propagation of electromagnetic waves in space obey Maxwell's equations. The wave carries little energy to the

equipment at a distance but is deposited in a fraction of a microsecond, making the rate of energy deposition (power) extremely high.

13.9 ESD IN SPACECRAFT IN GEO AND LEO

One of the concerns in the GEO's high-energy plasma environment is the differential charging of different parts of the spacecraft, leading to high electric fields and subsequent arc discharges between components. The ambient thermal plasma current densities are insufficient to discharge spacecraft surfaces rapidly. However, the electron charge accumulated on insulating surfaces increases the electric field across adjacent conductors above the breakdown level, leading to arcing. The resultant arcing currents traveling through conductors can upset electronic components and induce spurious signals. A common design solution for GEO is to coat all outside surfaces of the spacecraft with conducting materials. This prevents differential charging by distributing the charge over all surfaces and equalizing their potentials. Coating materials having a surface resistivity less than 5 kΩ/square are considered adequate to eliminate differential charging.

In LEO, because of the high thermal plasma current density, surfaces do not ordinarily collect much differential charge. The major concern in LEO is the absolute charging of spacecraft surfaces with respect to the surrounding plasma. Normally, the collected plasma current bleeds off the absolute potential rapidly. However, some spacecraft impose differential charging on themselves by using distributed high voltages. If conductors at different voltages are not exposed to space plasma, all spacecraft surfaces float within a few volts of the surrounding plasma potential. However, if conductors of similar area at different voltages are exposed to space plasma, a rule of thumb is that the most negative surfaces float negative in the plasma for about 90% of the total voltage difference between the surfaces. This is true, for instance, of solar arrays, where interconnects between solar cells or cell edges are exposed to the plasma, yet the operation of the array depends on the voltage distribution. Spacecraft designs not using solar arrays also place different surfaces at different potentials. High-voltage spacecraft in LEO environments have experienced significant interactions with their environment.

The LEO has a low-energy plasma environment ($E \sim 0.1$ eV) but a high electric field generated in the conductor moving in the Earth's magnetic field ($V \times B \sim 0.3$ V/m). This can add up over a long conductor and may cause arcing. The remedy is not to expose the bare parts of large conductors but to apply an insulating coating to all large conductors in LEO. In GEO, on the other hand, conductive coating and grounding the structural parts together at one point equalize the potential of the parts and eliminate the ESD.

13.10 DIELECTRIC BREAKDOWN

The ESD from one surface to another involves dielectric breakdown of the insulation in one of three mechanisms: (i) Strike through a gap, (ii) Puncture through solid insulation, or (i) Creepage around solid insulation. It is not like lightening, as no discharge can ionize the vacuum. However, the rise time is much faster than

lightening, in the order of a nanosecond versus about 50 microseconds in lightening. There is also an indirect way for ESD to interact between parts. The ESD current flowing through the enclosure couples energy into the wires, which is then conducted to the circuit boards inside. Large *dE*/*dt* and *dB*/*dt* associated with the ESD-induced transients cause electromagnetic radiation, which in turn propagates to the inside circuits. This must be analyzed along with the withstand level for every component with ample margin in order to avoid circuit board damage in the event of an ESD failure during tests or in operation. A safety factor of 10 is typically used for ESD protection.

Ground tests for the International Space Station found that dielectric coatings often break down at 100 V in LEO plasma. Rated dielectric strengths and the strengths measured in LEO were not consistently reached before breakdowns occurred in simulated space plasma. It is suspected that this is due to the porosity of the coatings, which allows plasma ions to reach much closer to the underlying conductor than the nominal dielectric coating thickness. Even coatings with rated dielectric strengths of much more than 100 V seemed porous enough to the plasma ions to have real dielectric strengths of less than 100 V. Thus, for surfaces that must be exposed to high negative potentials, it is important that dielectric coatings be used. Or, its outer surfaces are strong enough to stand off the full system voltage in plasma.

13.11 EFFECTS OF ESD

The ESD failure can affect the spacecraft equipment in the following ways: (i) Human safety, (ii) Operational disturbance, and (iii) Component damage.

The operational disturbances and component failures can be as follows:

- Noise in radio communication and flicker in video display
- Switching of logic gates
- Component failure by overvoltage on semiconductor junction insulation
- Ignite spacecraft electro-explosive devices (critical failure)
- Ignite fire in hazardous areas (Class 1, explosive fuel vapors)

13.12 ESD MITIGATION

The primary options for arc discharge mitigation on the spacecraft are:

- Controlling the spacecraft's floating potential in order to eliminate the initiating arcs
- Limiting the bus voltage and/or string current that could feed an arc to levels below the threshold for sustained arcs
- Use of a proper grounding and bonding scheme

The above options can be implemented as follows:

- Increase the conducting area on the spacecraft, thus lowering the floating potential.

- Use a plasma contactor, thus lowering the spacecraft's potential (as done on the ISS).
- Lay out the solar array strings to reduce the potential difference between the adjacent cells below 60 V.
- Use grout between cells to insulate the gaps between them.
- Limit the string current below 1 A and use diode isolation.

In circuits using transformers, one of the windings and the chassis are always grounded to the spacecraft structure ground. The core, on the other hand, is kept floating with respect to the chassis by maintaining some gap between the chassis and the core. It is possible that the charge from the spacecraft can enter the core by flashover from the chassis, but it cannot enter the winding unless the major winding insulation punctures. The floating core design is required by military standards, but the issue is debatable as to its superiority over the grounded core.

The ESD effects are analyzed and controlled in the following steps:

- Examine every surface of the spacecraft. If the electrical resistivity of any surface is greater than 10 kΩ/square, apply conductive coating (indium–tin–oxide) if practical on that surface.
- Apply a grounded shield to all cables outside a Faraday cage.
- Determine the expected ESD-induced transient voltage and the withstand level for every component. If the analysis shows a safety factor of less than 10, ESD testing is performed to establish survivability. If the component does not survive with an acceptable margin, additional shielding and/or filters are added to the design.

13.13 ESD CONTROL IN A SOLAR ARRAY

The entire array (the cells, coverglass, and substrate) is designed to perform at full specification under the effects of electrostatic charging. In GEO, this often requires an indium–tin–oxide coating, which reduces the solar array power output by a few percent. For example, a 700 Angstrom (0.07 μm) coating reduces the cell power output by approximately 4%.

Regarding the grounding and conductivity of the array, the following are noteworthy:

- The back of the array is grounded to the aluminum honeycomb core of the panels in at least three places on each panel. The honeycomb from each panel is then connected to a ground lead from the boom.
- The panel end and the SAD end of the boom are both electrically tied together and connected to the spacecraft structure via a set of two 20-kΩ bleed resistors, as shown in Figure 13.7.
    - If a conducting tape is used on the boom, it is grounded by overwrapping the boom with the bus wire, which is grounded to the array structure in the same way as the boom.

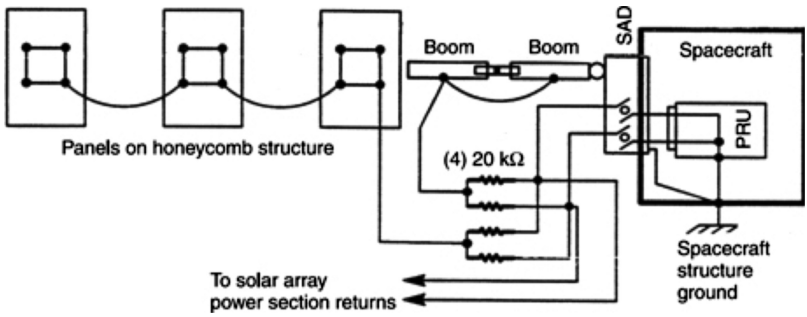

FIGURE 13.7 A solar array grounding scheme for electrostatic discharge protection. SAD,

- In an early design stage, the best option is an array layout to eliminate closely spaced cells with large voltage gradients.

As a protection against ESD, the following design and/or construction features are generally implemented on the solar array:

- The back surfaces of the panels are coated to have an electrical resistivity of less than 100 MΩ/square.
- The booms have conducting outer surfaces. The use of nonconducting tapes or paints over the conducting boom surfaces is minimized. The conducting tapes used on the boom are grounded.
- Blankets and loose surfaces are grounded to the array structure by means of the appropriate number of bonding straps.
- Snubber capacitors are used in the SAD before the slip rings and/or in the PRU.

13.14 PART SENSITIVITY

The ESD results in high potential (up to 20 kV) of short duration (100–1000 ns). Energy levels depend on the surface areas involved. The current injected into the spacecraft depends on the local structure configuration and impedance of the propagation paths. The surge impedance of the biaxial and twin-axial cables is 50–60 Ω. For twisted shielded wire pairs, it is about 60 Ω for AWG 20 wires and about 120 Ω for AWG 30 wires.

Although the energy level in the ESD is small, typically in the range of several millijoules, the energy required to damage sensitive components such as CMOS, FET, and pin diodes is even smaller (microjoules to millijoules). Robust components such as magnets and vacuum tubes can withstand much higher energy levels. Online components are more vulnerable than offline components.

The ESD sensitivity is generally measured in terms of the voltage the part rises to under the charge. MIL-HDBK-263 lists ESD sensitive parts in terms of the ESD voltage ranges. The list is in three classes, class I parts sensitive to less than 1000 V, Class II sensitive to 1000–4000 V, and class III sensitive to 4000–15,000 V.

ESD specifications require testing up to 15,000 V using an ESD simulator, which basically consists of charging a capacitor from a dc source via high resistance (slow charge) and then discharging it to the equipment under test via low resistance (fast discharge).

The EMI/EDMC and ESD are covered by Patel[1,2] in further detail in two dedicated chippers.

REFERENCES

1. Patel, M.R., *Spacecraft Power Systems*, 1st Edition, Chapter 15, Electromagnetic Interference and Compatibility, CRC Press, Boca Raton, FL, 2004.
2. Patel, M.R., *Spacecraft Power Systems*, 1st Edition, Chapter 16, Electrostatic Discharge, CRC Press, Boca Raton, FL, 2004.

FURTHER READINGS

Bruce, R.A. and Ramahi, O.M., *EMI/EMC Computational Modeling Handbook*, Springer International Series in Engineering and Computer Science 630, 2nd Edition, Springer, Berlin, 2001.

Ferguson, D.C., Interactions between spacecraft and their environment, in *Proceedings of the Intersociety Energy Conversion Engineering Conference*, 1992, Paper No. 0092-X.

Part D

Special Power Systems

14 Interplanetary and Deep Space Missions

14.1 INTRODUCTION

Since the interplanetary and deep space environments are significantly different, the spacecraft power systems for such missions differ from those used in Earth orbits. The mission environment depends on the spacecraft's distance from the sun (Figure 14.1, Table 14.1). The planets of the sun are divided into two groups: the inner planets (Mercury, Venus, Earth, and Mars) and the outer planets (Jupiter, Saturn, Uranus, and Neptune). The inner planets are small and composed primarily of rock and iron. The outer planets are much larger and consist of hydrogen, helium, and ice. The inner planetary missions are characterized by higher solar flux and elevated spacecraft temperatures. Mercury's orbital temperature can reach 300°C. Venus has a CO_2 atmosphere 90 times denser than on Earth, causing the greenhouse effect and the resulting temperature up to 477°C on the surface. Protecting the spacecraft from heat is a major design concern. On the other hand, missions to the outer planets, comets, asteroids, and deep space are characterized by lower solar flux and cooler spacecraft temperatures. The temperature in Saturn's orbit can be as low as −250°C. Pluto is even farther from the sun and so cold that methane freezes on its surface. Generating electrical power and protecting the spacecraft from extreme cold are major concerns on such missions.

If one could look at our solar system from far above the Earth's North Pole, the planets revolve around the sun in a counterclockwise direction. All planets except Venus and Uranus rotate on their axes also in this same direction. The solar system is remarkably flat—only Mercury and Pluto have inclined orbits. The moons of various planets mimic the behaviors of their planets and move in a counterclockwise direction, with a few exceptions. Some remarkable patterns also exist. For example, Mercury rotates on its axis three times for every two revolutions around the sun, and

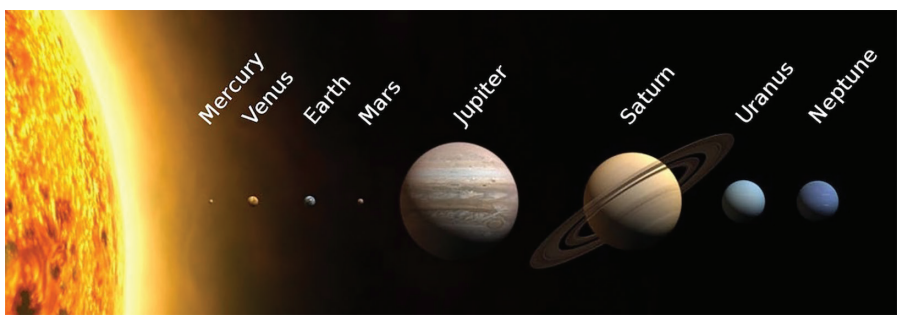

FIGURE 14.1 The planets in our solar system with their distance from the sun.

DOI: 10.1201/9781003344605-18

TABLE 14.1
The Solar Flux and PV Power Generation in the Orbits of the Various Planets in our Solar System

Planet	Distance from the Sun (AU)	Solar Flux Relative to Earth Orbits	PV Power Generation Accounting for Temperature Difference	Diameter (km)
Sun	-	-	-	1,391,400
Mercury	0.39	10.40–4.52	Severe loss of voltage	4,879
Venus	0.72	1.93	1.63	12,104
Earth	1.0	1.0	1.0	12,756
Mars	1.52	0.36	0.59	6,792
Jupiter	5.20	0.037	0.084	142,984
Saturn	9.54	0.0098	0.031	120,536
Uranus	19.20	-	-	51,118
Neptune	30.06	-	-	49,528

Uranus and Neptune are deficient in hydrogen. The asteroids are small rocky bodies that move in orbits primarily between Mars and Jupiter. Numbering in thousands, they range in size from 1000 km in diameter to microscopic grains. Comets circle the sun in two main groups. The Kuiper belt is a ring of debris that orbits the sun beyond Neptune. Many comets with periods less than 500 years come from the Kuiper belt. For missions away from the Earth, either closer to the sun or farther away from the sun, the solar array, battery, and power electronics designs differ significantly because the extreme temperature on either side, high or low, has a large impact on their performance. The solar flux at any distance in deep space is given by

$$I = \frac{I_{\text{Earth}}}{R^2} \tag{14.1}$$

where I_{Earth} = solar flux in the Earth's orbit (1358 W/m^2) and R = distance from the sun in astronomical units (AU). This equation assumes the sun to be a point source and may give some error at distances less than a few sun radii. The solar array power output varies linearly with the incident solar flux. Therefore, as the spacecraft moves away from the sun, the power decreases inversely with the distance squared. In the PV power system, the array temperature also decreases in the same ratio, which results in a higher PV conversion efficiency. The combined effect of the flux and the temperature changes is such that the photovoltaic power generation varies not inversely with the distance squared but to a lesser exponent in R^{α}, where α is approximately 1.5. Thus, the power generation is less than two times with two times the solar flux and more than one-half with one-half the solar flux.

Table 14.1 lists the planets in our solar system with their distances from the sun, in AU, and approximate power generation rates in their orbits, considering both the solar flux and the temperature variations. The data transfer rate to Earth from outer space depends on both the distance and the power available, as depicted in Figure 14.2.

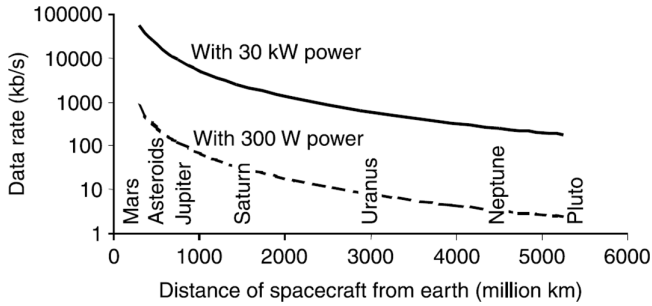

FIGURE 14.2 The data transfer rate from outer space at two power levels.

14.2 TEMPERATURE IN DEEP SPACE

The Stefan–Boltzmann law determines the temperature of an object that receives and radiates heat. With the spacecraft surface radiating to absolute zero in deep space, the surface temperature is determined by

$$T = \left[\left(\frac{I}{\sigma}\right)\left(\frac{\alpha}{\varepsilon}\right)\right]^{\frac{1}{4}} \tag{14.2}$$

where T = absolute temperature in K, I = solar flux in W/m^2, σ = Stefan–Boltzmann constant (5.67×10^{-8} W/m^2 K^4), α = absorptivity, and ε = emissivity of the surface. For a solar panel with one side absorbing and two sides radiating, the above equation becomes

$$T = \left[\left(\frac{I}{\sigma}\right)\left(\frac{\alpha}{2\varepsilon}\right)\right]^{\frac{1}{4}} \tag{14.3}$$

The α/ε ratio of various surfaces varies from 0 to 1 (Table 14.2). It is near zero for shiny mirror-type surfaces, near 1 for flat black surfaces, and 2–8 for highly absorbing surfaces. Typical solar cells have this ratio near 0.8.

As an example of using the above equation, we determine below the solar array temperature in the Earth's orbit during sunlight after ignoring the Earth's albedo and infrared radiation on the spacecraft. The array with α/ε ratio of 0.8 would give rise to

$$T = \left[\left(\frac{1357}{5.67 \times 10^{-8}}\right)\left(\frac{0.8}{2}\right)\right]^{\frac{1}{4}} = 313\text{K or } 40°\text{C} \tag{14.4}$$

And the array with an α/ε ratio of 0.6 would give rise to

$$T = \left[\left(\frac{1357}{5.67 \times 10^{-8}}\right)\left(\frac{0.6}{2}\right)\right]^{\frac{1}{4}} = 291\text{K or } 18°\text{C} \tag{14.5}$$

TABLE 14.2
Absorptivity and Emissivity of Various Surfaces

Type of Surface	Absorptivity, α	Emissivity, ε	Ratio α/ε[a]
Solar reflector (mirror)	Low	High	<0.1
Solar reflector	Low	High	0.1–0.2
Flat black reflector	Low	Low	1
Flat black absorber	High	High	1
Solar absorber	High	Low	2–8

[a] A typical PV array has this ratio around 0.8.

On the other hand, a spacecraft in deep space at a distance of 2 AU from the sun receives solar flux equal to 1/4th that on Earth. Its solar array with an α/ε ratio of 0.8 would give rise to a temperature of

$$T = \left[\left(\frac{1357/4}{5.67\times10^{-8}}\right)\left(\frac{0.8}{2}\right)\right]^{\frac{1}{4}} = 221\text{K or} - 52°\text{C} \tag{14.6}$$

As for power generation, missions beyond Mars cannot effectively generate PV power because of decreasing solar intensity. Moreover, the greatly varying sun angle, illumination intensity, and temperature on such missions cause wide variations in *I–V* response.

14.3 LUNAR MISSION

The moon is not a planet; however, it is Earth's closest neighbor of significant size. *Apollo-11* was the first manned mission by the U.S. that landed on the moon in 1969. In recent years, there have been renewed efforts in lunar missions. In particular, for a microgrid power system to be setup on the Moon and a base to be built that houses humans. Technologies developed on Earth will be tested on the Moon, which will act as a base for missions to Mars and other planets. The following are the environmental features that impact the power system design for lunar missions.

- The moon, being the Earth's natural satellite, is approximately at the same distance from the sun as the Earth. The solar flux in the moon's orbit is therefore essentially the same as that in the Earth's orbit.
- There is no atmosphere around the moon. The pressure ranges from 10^{-8} to 10^{-2} torr. This is essentially a vacuum, which can support a high-voltage power system. However, outgassing from the surrounding equipment can alter the local pressure. This should be accounted for in the high-voltage breakdown considerations.
- There is no space plasma. Plasma means ionized gas, and if there is no gas in the atmosphere, there cannot be any plasma.

- The temperature on the lunar surface ranges between −175°C during the night and +75°C during the day, about the same as that in the Earth's orbit.
- The gravity is about 1/6th of that on the Earth's surface.
- The moon has a negligible magnetic field. This means that the sun's charged particles can reach the moon's surface unimpeded without being deflected or trapped in belts. The solar array degradation rate due to charged particles would therefore be higher than on Earth.
- The meteoroid impact rate is higher on the moon, giving a higher rate of mechanical damage to the solar array.

14.4 NEAR-SUN MISSION

For missions near the sun, the solar intensity increases to 100 suns at 0.1 AU (about 21 sun radii, 1 sun radius equals 0.00476 AU) and to 2500 suns at 0.02 AU (about 4 sun radii). The PV power system design for near-sun missions between Mercury and the sun needs special considerations due to its high temperature. The PV cell loses power generation capability at such temperatures due to a loss in the open circuit voltage. Various options to limit the temperature below 1000°C include array tilting, adding mirrors on the surface to decrease absorptivity and increase emissivity, partially silvered cover glass, and various louvers and shades to control the solar flux. Moreover, a PV cell with a high band gap is needed. Figure 14.3 from a paper by Brandhorst and Chen[1] shows effective power output as a function of AU distance and band gap of various PV cells operating below 1000°C. At distances greater than 0.5 AU, the bandage has no significant effect on power generation. At a distance of less than 0.5 AU, the higher band gap PV cell generates more power up to 0.1 AU. If the PV cell is closer than 0.1 AU, it becomes useless. The curves assume that the cell temperature is limited to 1000°C in all cases.

It is apparent from Figure 14.3 that the PV power system has limitations in approaching the sun at a close distance. An alternative approach may be to use thermo-photovoltaic direct energy conversion. There are several advantages, including easy coupling to a thermal source operating above 2000 K. The feasibility of such an approach has been demonstrated under department of energy (DoE) funding but has not been fully developed. Another alternative is to use the thermoelectric converter with the sun as the heat source. Such a system is feasible for solar probes requiring instrument power under a few hundred watts. The solar probe launched by NASA/JPL in 2003 to study coronal heating and solar winds had three different power systems: (i) a low-temperature solar array for $AU > 0.5$, (ii) a high-temperature solar array operating at or below 400°C between 0.5 and 0.1 AU, and (iii) a thermoelectric converter for $AU < 0.1$ when the solar array is retracted inside the umbra of the sunshield. Near the Earth, the low-temperature solar array generates 2700 W of power. Since this is far more than needed, most of it is shifted into the power system. Between 0.5 and 0.1 AU, the power is provided by the high-temperature solar array, which is retracted inside the umbra of the sunshield at 0.1 AU when the array temperature exceeds 400°C. Inside 0.1 AU up to 4 sun radii, 200 W of power is generated by using infrared heat from the primary sunshield on the TE converters.

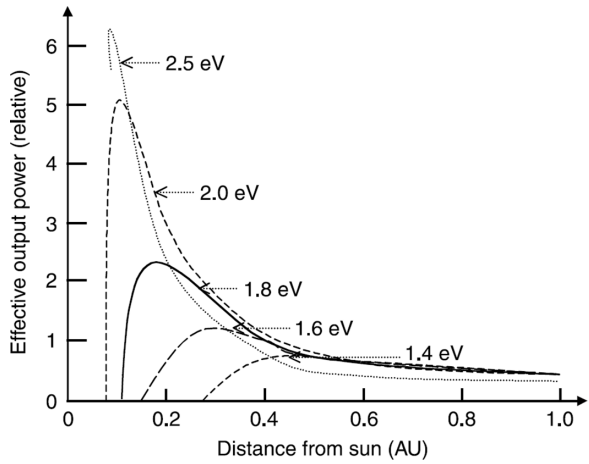

FIGURE 14.3 Distance from the sun versus power output of PV cells with various band gaps operating under 1000°C.

14.5 MARS MISSION

The Mars environment has the following features:

- The distance from the sun is 1.66 AU, with the average solar flux at 36% of that in the Earth's orbit.
- The typical operating temperature for large-area solar arrays ranges between −100°C and 0°C. The low temperature affects material properties and PV cell performance.
- The surface gravity is about 40% of that on Earth.
- The atmosphere consists of 95% CO_2, 3% nitrogen, and 2% all other gases.
- The atmospheric pressure is low, on the order of 10 torr. This happens to be the worst possible value on the Paschen voltage breakdown curve for CO_2. At 10 torr, the breakdown voltage between bare conductors in CO_2 is 50 V. Therefore, the power system design with exposed conductors must be limited to 35 V to leave some design margin. Higher voltages must be encapsulated or shielded in an enclosure with a suitable pressurized gas, which can conveniently be CO_2.
- The dry, low-pressure atmosphere is conducive to electrostatic charging. The spacecraft's surfaces are likely to collect a large amount of triboelectric charge via moving surfaces and wind-born dust particles.
- The temperature ranges between −100°C and −30°C, somewhat cooler than in the Earth's orbit.
- The great dust storms on the Mars surface cover an area greater than 1 million km^2 with durations over 100 days and a peak opacity exceeding 6. The dust is about 60% SiO_2. Such storms occur with a yearly probability of 30%–80%. The atmospheric dust scatters and absorbs solar wavelength

radiation to affect its magnitude, angular distribution, and the solar radiation spectrum.

- Local dust storms covering less than 1 million km^2 occur with a probability of 5% in the equatorial regions. They have only a minor impact due to their limited size, short duration of a few days, and opacity of around 1. Frequent dust storms occur with gusts of 30–75 miles per hour.
- The dust haze, ground fog, CO_2, and water ice clouds obscure the sunlight. The dust particles that precipitated and collected on surfaces following the dust storm activity reduced the transmission of light and decreased the surface emissivity. This raises the array temperature. The PV cell current loss of 0.28% per Martian day due to dust precipitation was measured over a short period of time in 1997 during the *Pathfinder* mission. The dust collection problem makes the solar array effective only for 3–6 months on Mars.
- The wind speed in the upper atmosphere can exceed 100 m/s. However, near the surface boundary layer, the dust wind speed can range from 3 m/s at the surface to about 50 m/s at a 5 m elevation.
- With an atmospheric pressure of only 6 torr, the PV array's aerodynamic loading is modest in high wind, about twice the body force.

Mars has a negligible global magnetic field—about 3×10^{-5} times that of Earth. However, NASA's Mars global survey data suggest that the planet has pockets of magnetic areas that can be 10–20 times stronger than the Earth's magnetic field.

The electrical power system design issues in low Mars orbit are somewhat similar to those in LEO, including AO degradation and arcing to plasma. On the surface of Mars and the moon, Paschen breakdown of atmospheric gases in a low-pressure neutral environment and chemical and electrical interactions with dust may also be two design concerns.[2,3] The Mars environment is thick. It provides effective shielding from meteors and proton/electron radiation. Therefore, the PV array design can ignore radiation degradation and meteoroid damage. The design must, however, consider the radiation protection of human crews and sensitive electronics.

NASA is studying a novel wind power system using the sandstorms on Mars. Wind turbines designed to provide general electricity at Earth's South Pole and in remote regions of Alaska, where there are about 6 months of darkness each year, may someday lead to similar wind machines for Mars bases. One reason to propose wind power on Mars is that wind turbines could generate electricity during the month-long Martian global dust storms that can make days on the red planet as dark as night. Wind power and solar power may complement each other on Mars. When a large dust storm blocks the sunlight, a wind turbine can generate electricity.

14.6 MISSIONS TO JUPITER AND SATURN

Jupiter is the largest planet with an immense magnetosphere. Its hydrogen and helium atmosphere contains pastel-colored clouds. Saturn is similar to Jupiter in many ways. The sun is not bright enough near Jupiter and Saturn, making the PV power system

ineffective. The electrical power is therefore generated using the radioisotope thermoelectric generator (RTG), which is covered in the next chapter. A few missions to Jupiter and Saturn are described below.

NASA's *Galileo* spacecraft to Jupiter at a distance of 5.2 AU from the sun was a mission in two parts: the orbiter and the probe. The probe was designed to enter the Jupiter's environment. After delivering the probe, the orbiter was routed to Jupiter's moon Ganymede. The probe recorded a temperature of −171°C above the clouds, 305°C near the surface, and a wind speed of 400 miles per hour. The probe was destroyed due to high atmospheric pressure. In 2003, the orbiter concluded its 14-year exploration of Jupiter and its moons. This 3000-pound spacecraft traveling at 108,000 miles per hour ran out of the on-board fuel used to steer it during its 35 orbits of Jupiter. *Galileo* was then purposely plunged into its own atmosphere to avoid crashing and contaminating Europa, one of Jupiter's watery moons. The radiation hardening of the power system components is more important in Jupiter's orbit than in the orbits of other planets. This is because Jupiter has a strong magnetic field and strong Van Allen-type radiation belts. Spacecraft encountering the powerful radiation belts of Jupiter have undergone single-event upsets. This becomes a significant design issue for Jupiter missions. The *Pioneer-10* spacecraft was built by TRW Corporation and launched in 1972 to probe the environment of Jupiter. It was designed for a 3-year life but kept ticking for more than 30 years. It passed Pluto's orbit in 1983. In 1997, it was some six billion miles away from Earth, much beyond Pluto, cruising at 27,700 miles per hour to become the farthest man-made object in deep space. It used RTGs with plutonium-238 and produced more than two-thirds of its 1972 power in 1997. Citing diminishing returns, NASA halted all regular communications with *Pioneer-10* in 1997. The last regular signal received from it was 1×10^{-21} W and took 9 h to reach Earth. In 2002, scientists at NASA's Jet Propulsion Laboratory sent a signal more than 12 billion kilometers away in an attempt to contact the spacecraft. After 22 h, they detected Pioneer's response on a 70 m dish antenna in Madrid, Spain. Even without communication to and from Earth, it will continue its journey in deep space. It carries pictures of terrestrial men and women and our address, i.e., the location of the Earth in our solar system. It cannot reach Proxima Centauri, the nearest star next to our sun, as it would take 100,000 years at the current speed. *Voyager-1* is another spacecraft, launched in 1977, that passed by Jupiter and Saturn. In 2004, it left our solar system and entered interstellar space, when it was more than three times as far as Pluto from the Earth. However, it is still working after more than a quarter century since its launch. If it continues at its present speed of over one million miles a day, it could take 40,000 years before reaching our nearest star, Proxima Centauri. The *Cassini* spacecraft was launched in 1997 on a 7-year mission to Saturn. It was designed to send back data after entering the orbit of Saturn in late 2004 and making 60 orbits in various orientations around the planet over a 4-year period. The mission was a joint undertaking of NASA, the European Space Agency, and the Italian Space Agency. It carried RTG with 30 kg of plutonium on board. Because there was such a large amount of the potentially deadly radioactive element, antinuclear groups opposed its launch. Public concerns have negatively affected the future of nuclear power in space, although the Russians have built and

flown many small nuclear reactor–thermoelectric converter power systems similar to the U.S.-built SNAP-10.

14.7 DEEP SPACE MISSIONS

The power system for a deep space mission typically includes RTGs, power electronics, and a small battery located inside the spacecraft body. The RTG heat may be sufficient to protect the power system from low temperatures. If not, additional isotope heat is needed to keep the electronics at the required temperature. For example, an unheated interplanetary spacecraft launched to explore the rings of Saturn would experience an average temperature of about −190°C, the liquid nitrogen (LN) temperature. For this reason, low-temperature power electronic circuits have the potential to find applications in deep space missions and also in cryogenic instrumentation for superconducting energy storage. Such circuits designed and operated at low temperatures may result in a more efficient system layout than room-temperature circuits. The advantages include reducing or eliminating the thermal shutters and the need for isotope heat, which can cause overheating during launch. Understanding the performance of power electronics at extreme low temperatures is needed for this purpose. The following is known about the operation of power electronic components near LN temperatures.

The performance of certain semiconductor devices improves with decreasing temperature, down to LN temperature. At low temperatures, the majority of carrier devices demonstrate reduced leakage current and reduced latch-up susceptibility. In addition, these devices show higher operating speeds resulting from increased carrier mobility and saturation velocity. An example is the power MOSFET, which has lower conduction loss at a low temperature due to the reduction in drain-to-source resistance $R_{ds(on)}$ resulting from increased carrier mobility. NASA has tested other components such as resistors, capacitors, and magnetics that are needed for various power converters at LN operating temperatures. Many of them have been found suitable for operating on unheated interplanetary spacecraft.[4]

The battery can be a roadblock at very low temperatures. The Li-ion battery offers a somewhat favorable combination of energy and power density. However, its temperature performance below −40°C is poor. Tests[5] have shown the following about the Li-ion cells:

- Between room temperature and −20°C, variations in electrolyte resistance and the anode-to-electrolyte resistance are negligible, but the cathode electrolyte interface resistance increases substantially.
- The cell voltage and Ah capacity fall to approximately one-half at −40°C (Figure 14.4). As a result, practically no energy was delivered at −40°C. This is due to a substantial increase in the total internal resistance.

Poor cell performance at low temperatures can be attributed to the electrolyte becoming viscous or solid at low temperatures.[6] It is also attributed to the poor lithium diffusivity in the electrolyte. Work is under way to improve the low-temperature performance of the Li-ion cell.

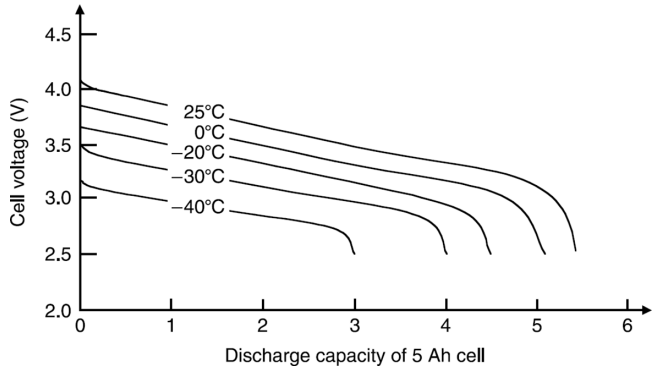

FIGURE 14.4 The capacity of a 5 Ah Li-ion cell at low temperatures in interplanetary missions.

REFERENCES

1. Brandhorst, Jr., H.W. and Chen, Z., PV approaches for near-sun missions, in *Proceedings of the 34th Intersociety Energy Conversion Engineering Conference*, SAE, 1999, Paper No. 2631.
2. Kerslake, T.W. and Kohout, L.L., Solar electric power system analysis for Mars surface missions, in *Proceedings of the 34th Intersociety Energy Conversion Engineering Conference*, SAE, 1999, Paper No. 01-2482.
3. Kilecki, J.C. and Hilalrd, G.B., *Proceedings of the Electrical and Chemical Interactions at Mars Workshop*, NASA Report CP-10093, 1992.
4. Elbuluk, M.E., et al., Low temperature performance evaluation of battery management technologies, in *Proceedings of the 34th Intersociety Energy Conversion Engineering Conference*, SAE, 1999, Paper No. 01-2543.
5. Nagasubramanian, G., Low temperature electrical performance characteristic of Li-Ion cells, in *Proceedings of the 34th Intersociety Energy Conversion Engineering Conference*, SAE, 1999, Paper No. 01-2462.
6. Smart, M.C., Huang, C.K., Ratnakumar, B.V., Surampudi, S., and Sakamoto, J.S., Factors affecting Li-Ion cell performance, in *Proceedings of the 37th Power Sources Conference*, 1996, Paper No. 239.

FURTHER READINGS

Choi, M.K., Power and thermal systems with thermoelectric generators at 930°C for solar probe inside 0.1 AU, in *Proceedings of the 36th Intersociety Energy Conversion Engineering Conference*, ASME, 2001, Vol. II, pp. 1161–1163.

Haines, J.E., Inner planets sample return missions, the challenge for power systems, in *Proceedings of the 34th Intersociety Energy Conversion Engineering Conference*, SAE, 1999, Paper No. 2483.

Jenkins, J.E. and Dakermanji, G., Near Earth asteroid rendezvous-Shoemaker spacecraft power system flight performance, in *Proceedings of the 36th Intersociety Energy Conversion Engineering Conference*, ASME, 2001, Volume I, pp. 251–256.

15 Radioisotope Thermoelectric Generator

15.1 INTRODUCTION

For environments where the sun's reach is limited, such as outer planetary missions, the use of PV is ineffective due to insufficient solar flux. For such missions, other sources of energy, such as batteries or a source capable of long-term power generation, are required. The battery, if not rechargeable, has a limited life span, and hence it is only applicable for low-power and short-to-medium duration missions. For high-power, long-duration missions, an on-board nuclear energy source or a radioactive isotope is often used to generate electrical power. The radioisotope heat is directed at a TE junction, which generates electrical potential just as in a thermocouple.

The radioisotope thermoelectric generator (RTG) has been fully developed and used for decades at power levels ranging from a few watts to a few hundred watts. Such a power source has the advantage of supplying power for a long time—decades—thereby eliminating the need for a battery. However, a battery may be used as backup for some parts of the mission.

An obvious disadvantage of such systems is the heavy radiation shielding required around electronic components. Also, the nuclear fuels that are safe and easy to handle with little shielding, such as curium-244 and plutonium, are expensive. Inexpensive and easily available fuel, such as strontium-90, is unsafe to work with.

High-energy particles emitted from the radioactive isotope material are the primary sources of energy, which heat the absorbing material. The mass of the isotope decays exponentially at a rate characterized by its half-life, $T_{½}$. The thermal radiation decreases proportionally with the remaining mass. Therefore, the thermal power $P(t)$ radiated at any time also decays exponentially from its initial value P_o, as given by

$$P(t) = P_o \exp\left(-0.7t / T_{\frac{1}{2}}\right) \tag{15.1}$$

Table 15.1 compares the isotope fuels presently used in RTGs with their half-lives and specific power achievable. The advantages of an RTG are:

- It provides power for a long period of time, independent of the spacecraft's environment, orientation, and distance from the sun.
- It is suitable for missions far away from the sun, too close to the sun, or lunar missions with long eclipse periods.

DOI: 10.1201/9781003344605-19

TABLE 15.1
Characteristics of Three Alternative Isotopes for RTGs

Isotope	Half-Life (years)	Thermal Power Radiated per gram of Isotope (W/g)	Radiation Level (Curies/W)
Curium-242	0.45	~100	27
Strontium-90	28	~0.25	153
Plutonium-238	86	~0.55	30

- The power output is not affected by radiation damage in the Van Allen belts or by man-made nuclear threats.

The RTG consists of numerous thermoelectric converter (TEC) cells connected in a series–parallel combination to obtain the required voltage and current. Each TEC converts the isotope's thermal energy into electrical energy. The power conversion efficiency, η, of the TEC is defined as

$$\eta = \frac{\text{electrical power output}}{\text{thermal power depletion}} \tag{15.2}$$

The efficiency depends on the material properties and the hot and cold junction temperatures, T_h and T_c, respectively, in °K. The theoretical limit on this efficiency is the Carnot efficiency, which is

$$\eta_{\max} = \frac{T_h - T_c}{T_h} \tag{15.3}$$

Practical designs yield about half the theoretical maximum efficiency due to thermal design limitations and numerous interconnects. The most widely used material, plutonium-238 with Si–Ge TE cells, gives about 7% conversion efficiency. Removing the remaining 93% of the system's energy as waste heat poses a significant design challenge. The specific electrical power output of RTGs is typically low. Based on the total power system assembly mass, it was 2 W/kg in the *SNAP-19* spacecraft and 5 W/kg in the *Galileo* spacecraft.

15.2 THERMOELECTRIC FUNDAMENTALS

The working principle of the TEC is based on the Seebeck effect, which generates electrical potential when two dissimilar materials are maintained at different temperatures. It involves electron or hole transfer between the two dissimilar materials under thermal energy. The two materials can be conductors or semiconductors. The TEC for space power applications uses semiconducting materials, one p-type and the other n-type, as shown in Figure 15.1. If two such dissimilar materials are held at a temperature difference $\Delta T = T_h - T_c$, an electric potential difference V_{12} is produced at their junction. It is given by

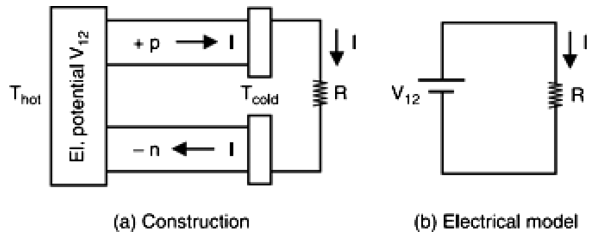

FIGURE 15.1 Single-stage unicouple thermoelectric converter. (a) Construction. (b) Electrical model.

$$V_{12} = \alpha_{12}\Delta T \tag{15.4}$$

where α_{12} is known as the Seebeck coefficient of the couple, generally expressed in μV/°C. The α_{12} is often called the TE power, although it is not really a power. It is a characteristic constant that depends on the material's properties. The coefficient α_{12} is considered positive if the Seebeck voltage polarity produces current in the p-type material from high temperature to low temperature. The current under this voltage then delivers electrical power to the external load connected in the loop.

Each arm of the two materials has electrical resistivity ρ and thermal conductivity k. The parameters ρ, k, and α all vary with the operating temperature. Since ρ and k cause a loss of power and reduce the conversion efficiency, the figure of merit, Z, for each material in the couple is defined as

$$Z = \frac{\alpha_{12}^2}{\rho k} \tag{15.5}$$

Another figure of merit for each material is the power output per unit mass. It is defined as

$$Z' = \frac{\alpha_{12}^2}{\rho} \tag{15.6}$$

The figure of merit of both materials together in the couple is defined as

$$Z_{12} = \frac{\alpha_{12}^2}{\left(\sqrt{\rho_1 k_1} + \sqrt{\rho_2 k_2}\right)^2} \tag{15.7}$$

where ρ and k are the electrical resistivity and thermal conductivity of the two materials 1 and 2, respectively.

For a junction of two metallic arms, such as in thermocouples used to measure temperature, the Seebeck coefficient is low, around 50 μV/°C. Both ρ and k are large, resulting in poor efficiency around 0.1%, which is unsuitable for power generation. Some semiconductors have a high Seebeck coefficient in the 300–500 μV/°C range. Their conductivity is relatively low, resulting in a relatively high conversion efficiency in the range of 5%–7%.

The fraction of heat removed from the junction and delivered to the load in the form of electrical power is

$$P_e = \left(1 - \frac{T_c}{T_h}\right)\left\{\frac{\sqrt{1+Z\bar{T}}-1}{\sqrt{1+Z\bar{T}}+\frac{T_c}{T_h}}\right\} \tag{15.8}$$

where

$$\bar{T} = \sqrt{T_h + T_c} \tag{15.9}$$

Low-grade commercial TECs have potential terrestrial applications such as recovering waste heat from various industrial processes and vehicle exhaust to decrease fuel consumption. Typical space-qualified RTGs use high-grade SiGe TECs with plutonium-238 as the heat source. The SiGe material is doped with phosphorus for the n-leg and with boron for the p-leg. For widely used SiGe couples, Z_{12} is around 0.001 with ±30% variation depending on the material grade and quality of the manufacture. Various TEC configurations used in the RTG designs for space applications are described below.

15.2.1 Single-Stage Unicouple

This is the most basic and elementary construction of the TEC converter that is shown in Figure 15.1. One end of the p and the n arms are kept in a common reservoir at a hot temperature, T_h. The other end of the arms is kept at a cold temperature, T_c. The dc voltage is generated between the p and n terminals at the cold end, which is proportional to the temperature difference $\Delta T = T_h - T_c$. A load with resistance R would draw electrical current I and power I^2R. Any form of heat can be converted into electricity. The conversion efficiency obtained with the state-of-the-art materials is about 7%–10%.

If the cold temperature reservoir is a liquid metal bath, as is typical, the p and n terminals must be kept in two different reservoirs that are electrically isolated in order to withstand the generated voltage. Otherwise, the resulting electrical short would prevent power transfer to the load.

This configuration derives its name because there is only one TE couple, which sees ΔT in one stage only. The heat energy at T_c is discharged from the TEC system as waste heat. The efficiency is therefore relatively lower than in the other configurations described hereafter.

15.2.2 Single-Stage Multicouple

Two or more p–n couples are stacked together in the single-stage multicouple TEC assembly. Figure 15.2 shows one such assembly with two couples, which are thermally in parallel and see the same temperature difference $\Delta T = (T_h - T_c)$ in one stage only. Electrically, however, they are in series. The total voltage output of the

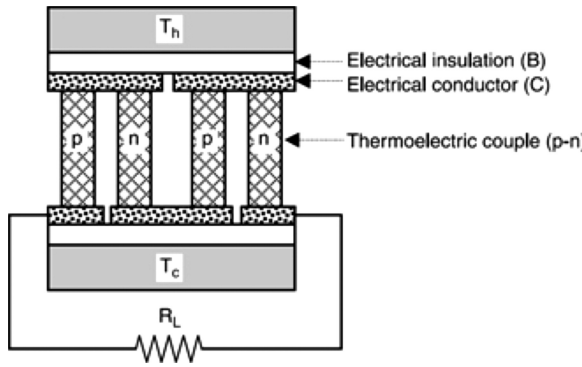

FIGURE 15.2 A single-stage multicouple thermoelectric converter.

assembly is therefore twice that of one element. Material B in the figure is an electrical insulation with high thermal conductivity, so that the copper straps C are at the same temperature as the adjacent heat reservoir.

This configuration gives twice the voltage with twice the TE material. Therefore, the specific power per kilogram of the active material remains the same. However, the specific power of the system is higher due to the overhead mass being less than double.

15.2.3 Multistage, Multicouple

In this configuration, the heat is extracted in two stages, as depicted in Figure 15.3. The temperature drops from T_h to T_m in the first stage, having two couples, and from T_m to T_c in the second stage, also having two couples. The material B (unshaded) is an electrical insulation of high thermal conductivity to minimize the temperature drop across it. The copper strap C (checkered) is a material with high thermal and electrical conductivities. It conducts the electrical current and distributes the heat uniformly across the device so that all couples in the same stage see the same temperature difference.

15.2.4 RTG Assembly

The Seebeck voltage per junction is around 300–500 μV/°C. Numerous junctions are connected in series to obtain the desired voltage, and numerous strings of series junctions are connected in parallel to obtain the desired current. The series–parallel combination is a matter of design that results in the maximum power transfer to the load. The RTG is basically an assembly of all TECs, which is typically a cylindrical canister as shown in Figure 15.4. Once activated (ignited), the isotope heat generation cannot be turned off. The refractory metal insulation shield and the graphite isotope capsule could be damaged if they were subjected to atmospheric oxygen while operating at high temperatures and could experience sublimation damage even before the mission starts. For this reason, the RTG is filled with pressurized xenon gas until

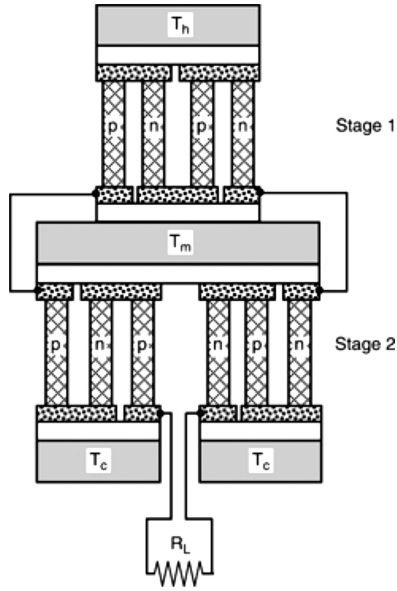

FIGURE 15.3 A multistage, multicouple thermoelectric converter.

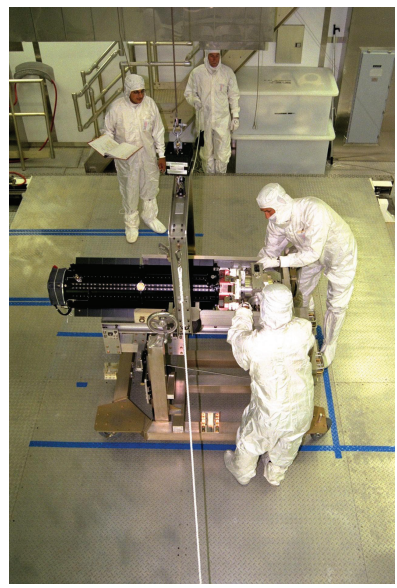

FIGURE 15.4 Radioisotope thermoelectric generator being installed for the Cassini spacecraft. (NASA.)

after launch. The very low thermal conductivity of xenon makes it possible to store and launch the RTG hot and generate the needed pre-launch and launch power. Once in space, the xenon is vented.

15.3 ELECTRICAL MODEL OF THE RTG

The electrical equivalent circuit of an RTG is shown in Figure 15.5. The total voltage generated due to the Seebeck effect works as an internal voltage source. With an open circuit (zero load current), the external terminal voltage V is the same as that generated internally. We designate this voltage as the open-circuit voltage (V_{oc}). When electrical current is drawn by load resistance R_L, there is an internal voltage drop. This is represented by an internal resistance, R_i, which is approximately constant at a given temperature. The external terminal voltage V therefore decreases linearly with increasing load current, i.e.,

$$V = V_{oc} - IR_i \tag{15.10}$$

With the external terminals shorted, the maximum current flows to the load. We designate this current as I_{sc}. The above equation gives

$$I_{sc} = V_{oc}/R_i \tag{15.11}$$

Equation 20.10 can be rearranged using Equation 15.11 as

$$I = I_{sc} - \gamma V \tag{15.12}$$

where $\gamma = I_{sc}/V_{oc}$, a characteristic admittance of the RTG power source.

Equation 15.12 sets the I–V characteristic of the RTG. It is a falling straight line from I_{sc} at zero voltage to zero current at V_{oc}, as shown in Figure 15.5. On the other hand, the voltage, V, required to circulate current I through the load increases with the current in a straight line. This line, known as the load line, has a slope of R_L. An RTG with the source line shown by a solid line and the load line shown by a dotted

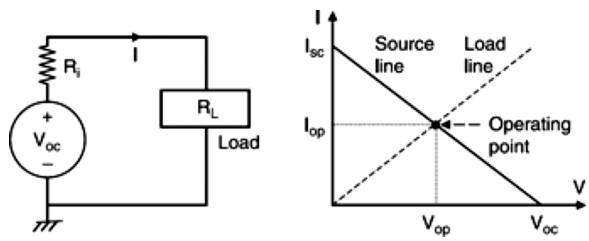

FIGURE 15.5 Electrical equivalent circuit model and operating characteristics of thermoelectric converter.

line operates at the point of their intersection. At that operating point, the electrical power transferred to the load is

$$P = V_{op} I_{op} \tag{15.13}$$

15.4 MAXIMUM POWER TRANSFER

The power, P, transferred from TEC to the load at any operating point P in Figure 15.5 is

$$P = VI = V\left(I_{sc} - \gamma V\right) = VI_{sc} - \gamma V^2 \tag{15.14}$$

The power system design for extracting the maximum power from RTG to the load must operate at a voltage such that, at the operating voltage,

$$dP/dV = I_{sc} - 2\gamma V = 0 \tag{15.15}$$

Equation 15.15 gives the corresponding operating voltage $V_m = I_{sc}/(2\gamma)$, which is also $½V_{oc}$, and the current at that voltage is $½I_{sc}$.

The maximum possible power transfer, therefore, is

$$P_{\max} = \tfrac{1}{2} V_{oc} \times \tfrac{1}{2} I_{oc} = \tfrac{1}{4} V_{oc} I_{sc} \tag{15.16}$$

It occurs when the RTG is operated at a voltage that is one-half of the open-circuit voltage. This point is shown as $P_{\max}$ in the power versus voltage plot shown in Figure 15.6. The power at zero voltage is obviously zero. It is also zero at V_{oc} since the current is zero there. In between, the power rises with the operating voltage, reaches the maximum value $P_{\max,}$ and then falls to 0 at V_{oc}. The RTG conversion efficiency is at its maximum at the maximum power transfer point. The *I–V, P–V* and η–*V* curves with the operating voltage as an independent variable are shown in Figure 15.7.

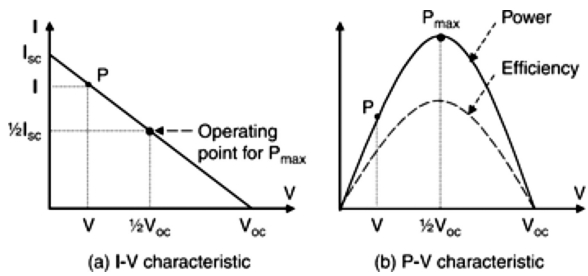

FIGURE 15.6 A thermoelectric converter operation for maximum power transfer to the load. (a) I-V characteristic. (b) P-V characteristic.

15.5 THE EFFECT OF TEMPERATURE AND AGING

The characteristics displayed in Figure 15.7 are for a given ΔT across the TE junctions. The *I–V* line of the RTG shifts upward for a higher ΔT, and downward for a lower ΔT, as shown in Figure 15.8. The amount of shift is a characteristic of the couple's material.

Aging has little effect on the RTG output because the basic heat source has a half-life of decades. For this reason, the power generation degrades little, as shown in Table 15.2. Most power degradation is due to the slow precipitation of the phosphorus doping in the n-type leg of the thermocouple. The *I–V* and *P–V* curves shift uniformly with time and temperature, such that the maximum power point remains at the same voltage (Figure 15.9). This is a happy coincidence for the design engineer. The conversion efficiency is a function of the contact resistance and the hot and cold side temperatures, as shown in Figures 15.10 and 15.11, respectively.

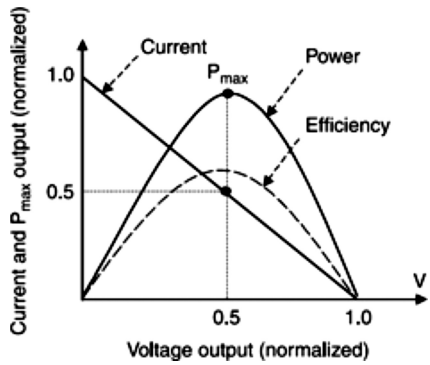

FIGURE 15.7 Thermoelectric converter current, power, and efficiency versus operating voltage.

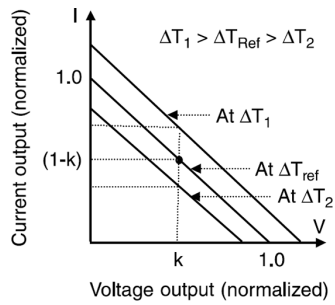

FIGURE 15.8 Thermoelectric converter current versus voltage at different temperature gradients.

TABLE 15.2
Measured Power Levels of the RTG in *Voyager II* versus Time

Date	Voyager II Power Output (W)	Percent of Initial Power Generation
August 1977 (launch date)	478	100
December 1980	436	91
December 1985	398	83
December 1990	370	77
December 1995	344	72
December 1998 (21 years)	327	68% (after 21 years)

Data from Mondt, J.F., *Proceedings of the 36th IECEC*, ASME, 2001, Vol. I, pp. 133–139.
RTG, radioisotope thermoelectric generator.

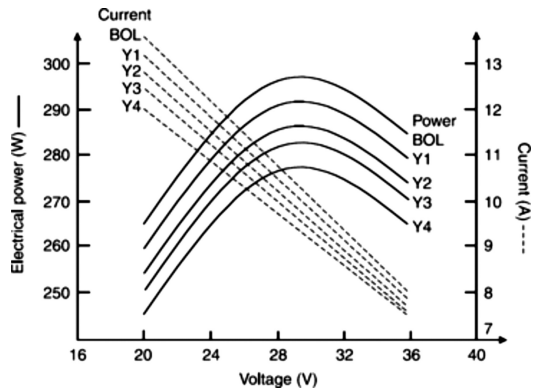

FIGURE 15.9 *I–V–P* characteristics of radioisotope thermoelectric generator s with age. BOL, beginning-of-life.

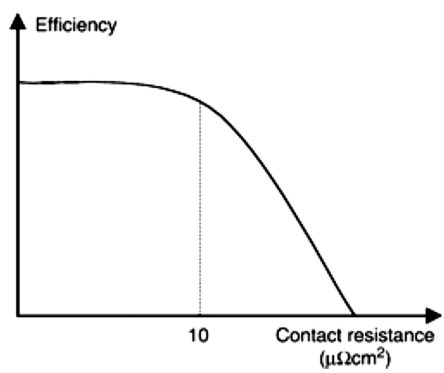

FIGURE 15.10 Thermoelectric converter conversion efficiency versus contact resistance.

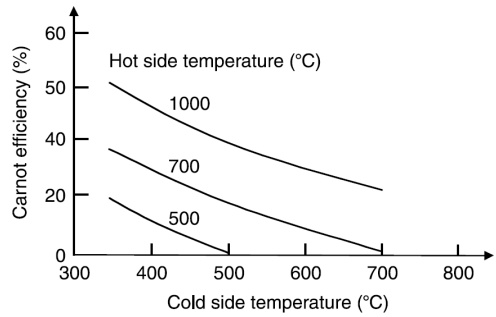

FIGURE 15.11 Thermoelectric converter conversion efficiency versus temperature.

TABLE 15.3
Performance Characteristic of the Standard RTG in Use

- Mission life 5 years (minimum)
- BOL power 285 W
- EOL power 255 W (notice the negligible decay over mission life)
- Suitable for space shuttle launch
- RTG module 42 cm diameter × 114 cm long
- Total mass 55 kg
- TE 572 SiGe unicouple in 16 circumferential rows
- Operating voltage 28–30 V
- Operating temperature gradient $\Delta T = 707$ K
- Operating temperature: 1273 K hot junction, 566 K cold junction

BOL, beginning-of-life; EOL, RTG, radioisotope thermoelectric generator; TE

15.6 FLIGHT HISTORY OF RTGs

RTG technology has been developed and flown on many interplanetary and deep space missions for a couple of decades. RTGs have been used in the *Pioneer, Explorer, Voyager, Galileo, Ulysses*, and *Cassini* missions, as described in Chapter 14. These missions have used essentially a standard RTG assembly designed to meet the mission requirements listed in Table 15.3. A number of such assemblies are used as needed for a particular mission.

15.7 SEGMENTED TECs

In a unicouple TEC, the same heat and the same current are seen by each segment in each leg. High conversion efficiency can be obtained by operating the TEC material over a wide temperature range and using different materials in each temperature range where they possess optimum performance. This can be accomplished in two ways:

- Multistage TEC, where each stage is electrically isolated but thermally in contact with each other, operates over a fixed temperature difference.

- Segmented TEC, where each of the p and n legs is made of multiple segments of different materials placed in series. Such a TEC is estimated to have a conversion efficiency of around 15% versus 7% using the state-of-the-art BiTe, FeSi, PbTe, and SiGe alloys. In the segmented TEC concept, the length and cross section of each segment are adjusted in accordance with its thermal and electrical conductivity to achieve the desired temperature difference across each material and the maximum efficiency of the couple. The overall operating temperature drops from 1275°C to 300°C in typical segmented TEC designs.

15.8 ADVANCED RTGs

The DoE has issued a directive to develop and maintain the nuclear space power program to support defense and deep space missions. The program has funded research and development for the Advanced Radioisotope Power System (ARPS), with a goal to triple the conversion efficiency of the present TECs. A key thrust is on using advanced SiGe cells with improved thermal conductivity and contact resistance of less than 10 $\mu\Omega/cm^2$. The program included building an engineering model with 100 W output and a flight qualified unit. Table 15.4 summarizes the ARPS's goals.[1]

Three technologies under evaluation to achieve these goals are: (i) segmented alkali metal thermal to electric converter (AMTEC) with 15% efficiency and 7–9 W/kg specific power, (ii) Stirling engine with 25% efficiency and 6–7.5 W/kg, and (iii) thermo-photovoltaics (TPVs). In each case, the heat comes from the natural radioactive decay of nonweapons-grade plutonium-238 pellets, clad in protective layers of graphite and iridium.

In the AMTEC, the isotope heat vaporizes sodium that flows through a β-alumina electrolyte tube to produce electricity. β-Alumina is an alkali metal that conducts ceramic—a solid electrolyte that conducts sodium ions. An electrochemical potential is generated when sodium is present at two differential pressures separated by an electrolyte. The free electrons are captured by the electrodes, which are used to power the load and then get recombined with the sodium ions. The temperature in the vapor circulation drops. The conversion efficiency is a function of the differential temperature.

TABLE 15.4
Goals of Advance RTG Research Programs

Performance Parameter	Preset State-of-the-Art RTG Capabilities	Goals of the Advanced Radioisotope Power System
System efficiency	6.5%	13%–25%
Specific power	5 W/kg	9–10 W/kg
Life	>20 years	Based on needs of mission
TEC junction	SiGe	Improved SiGe
Operating temperature	1275°C to 575°C	1000°C to 700°C
Isotope	Pu-238	Pu-238

RTG, radioisotope thermoelectric generator; TEC, thermoelectric converter.

The electrical characteristics of the AMTEC module are similar to those of the conventional TEC. The terminal voltage drops linearly with increasing current. The power output peaks at a certain voltage, approximately one-half of the open-circuit voltage. As in traditional TEC, the open-circuit voltage and the maximum power in AMTEC are higher at higher-temperature gradients.

15.9 THERMOELECTRIC COOLER

The TEC junction can also be used to cool a small device locally by replacing the load with a battery and sending the current backward into the TEC. This is actually the TEC working in reverse mode. The junction works in reverse by taking the electrical energy and converting it into a temperature drop. Such a reverse operation is called the Peltier effect. Peltier heat absorption is given by

$$Q_p = \pi_{12}\, J_{12} \tag{15.17}$$

where

Q_p = rate of Peltier heat absorption per unit area of the junction,

π_{12} = Peltier coefficient of the couple, J_{12} = current density taken as positive for current flowing from material 1 to material 2 at the junction.

Assuming that the cold junction is perfectly insulated thermally, it produces a temperature drop

$$\Delta T_{\max} = \tfrac{1}{2} Z T_c^2 \tag{15.18}$$

The cooling effect can also be created by using the TEC as a heat sink in the forward mode for cooling a delicate small device. In this mode, the heat near a device is converted into electrical energy, conducted by wires, and dissipated into a load away from the device to be cooled.

REFERENCE

1. Mondt, J.F., Advanced radioisotope power system technology development for NASA mission 2011 and beyond, in *Proceedings of the 36th Intersociety Energy Conversion Engineering Conference*, ASME, 2001, Vol. I, pp. 133–139.

FURTHER READINGS

Choi, M.K., Power and thermal systems with thermoelectric generators at 930°C for solar probe inside 0.1 AU, in *Proceedings of the 36th Intersociety Energy Conversion Engineering Conference*, ASME, 2001, Vol. II, pp. 1161–1163.

Woerner, D.F., Next-Generation Radioisotope Thermoelectric Generator Study, NASA Final Report No. JPL D-99657, Jet Propulsion Laboratory, California Institute of Technology, Pasadena, CA, June 2017.

16 High-Power, High-Voltage Systems

16.1 INTRODUCTION

For decades, the spacecraft's power levels stayed under several hundred watts, with a low-voltage power system at 28 V dc. However, the power levels for science, military, and commercial spacecraft have been rising steadily, approximately doubling every 7 years. As the power level increases, the voltage level needs to increase due to obvious benefits such as efficiency and mass. For example, the mass savings in just the distribution cables at various power and voltage levels are shown in Table 16.1.

Some geosynchronous Earth orbit (GEO) communications satellites use power in the 7–15 kW range at 70–100 V. The ISS uses 120 kW of average power at 120 V bus voltage, while the voltage of the PVs in the ISS on the U.S. side is 160 V. Some strategic Defense Initiative (SDI) weapons platforms may require steady power of several megawatts and burst power of hundreds of megawatts at voltages approaching 100 kV. The spacecraft that are being considered for crewed applications, such as travel to Mars, are expected to have high voltages, such as a 1000 V dc bus with a few MW power levels. Figure 16.1 shows the power level of different spacecraft in different decades.

Power systems up to 100 kW have been designed at voltages up to 200 V. Distribution systems above 200 V are considered high voltage (HV) in space due to the various environmental conditions the spacecraft must undergo during launch and operation. The space plasma, the wide variations in operating pressure and temperature, the outgassing of the materials, the corona, and atomic oxygen are the key design issues.

TABLE 16.1
Power Distribution Cable Mass with Copper Conductors versus Power and Voltage Levels

Voltage Level (V)	20 kW over 10 m Distance (kg)	100 kW over 30 m Distance (kg)	Example of Use
28	155	7000	Heritage voltage level
70	20	900	GEO satellites
120	7	290	ISS and EOS
200	3	140	SP-100

GEO, geosynchronous Earth orbit.

DOI: 10.1201/9781003344605-20

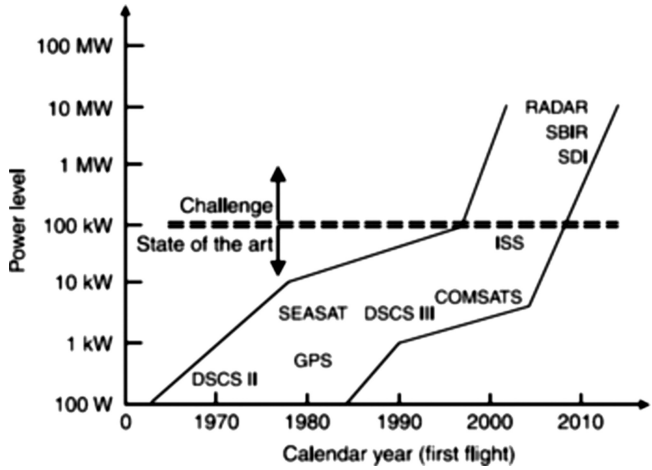

FIGURE 16.1 Spacecraft electrical power requirement growth trend.

16.2 HIGH-VOLTAGE PV ARRAY

For spacecraft over 25 kW, a HV power bus is required for mass and efficiency optimization. In solar PV systems, this can be achieved by:

i. Connecting array sections in series to create the desired high voltage output, or
ii. Stepping up the source voltage using power electronics converters. For instance, in the case of PV panels with 160 V output in the ISS, a dc–dc converter stage can be used to step this voltage up to desired levels for a HV bus.

An array voltage of 1000 V has been considered for high-power solar arrays with long cables. If the system were to operate at a nominal voltage of 1000 V, a 100 kW array would require a current of 100 A, thus limiting I^2R loss in the conductor. In addition, the resulting low magnetic field interacting with the Earth's would keep the drag and the re-boost fuel cost under control.

The solar dynamic power system is an alternative candidate for high power, an example of which is shown in Figure 16.2.[1] In such a system, the energy can be stored as thermal energy in the form of latent heat in a phase change material, thus eliminating the battery, which is generally heavier than the solar array in low Earth orbit (LEO) satellites. The heat is then used to spin a turbine, which in turn rotates an electric generator. However, the gyroscopic effect of large rotating machines on spacecraft needs to be taken into account in the spacecraft's dynamics.

16.3 NUCLEAR REACTOR TEC SYSTEM

For high-power space defense, DoE and DoD have funded nuclear reactors with TEC for a 100 kW_e prototype in the past, such as the SP-100 power system. It used TEC modules of multicouple SiGe/GaP thermoelectric cells with a conversion efficiency

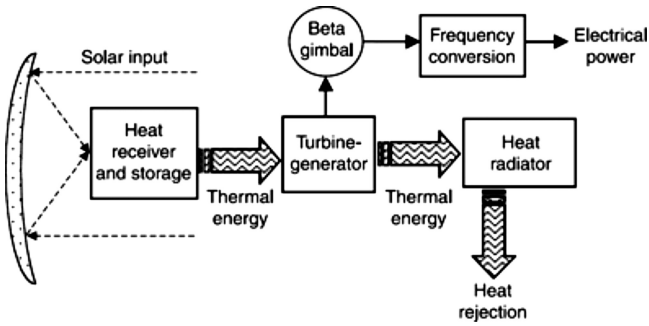

FIGURE 16.2 Solar dynamic power system schematic.

of about 7%. However, the working heat losses reduced the overall system efficiency to 5%. A 100 kW_e electrical output system, therefore, requires the reactor thermal power of 100 kWe/0.05 = 2000 kW_t. The remaining 95%, or 1900 kW_t of the reactor heat must be radiated back to space in order to control the spacecraft temperature within the material's working limits. The radiator design, therefore, becomes the principal design driver.

The SP-100 used a fast-spectrum liquid lithium-cooled reactor and SiGe/GaP TEC with $Z = 0.0007$ for the state-of-the-art design and 0.0014 for the future advanced TEC design. In the baseline concept, the nuclear reactor boils the liquid metal. The hot liquid is circulated on the platform by a liquid lithium pump loop, transferred through an intermediate heat exchanger, and delivered to an array of heat pipes mounted to the 12-sided conical main body. The TEC panels receive heat radiantly from the heat pipe array. Thus, the heat is transferred from the reactor core to the TEC modules, each of which generates 4.6 kW_e at 100 V. The panels are deployed for effective radiation of waste heat into outer space. The lithium coolant is pumped by an electromagnetic pump driven by a dedicated TEC module, which is powered by the temperature drop between the working fluid and the pump radiators to assure pumping as long as the reactor is at a certain temperature.

The safe voltage to avoid electrical breakdown in then-planned SP-100 mission orbits is around 150 V. Twelve TEC modules connected in parallel produced 50 kW_e at 100 V. Two such groups are connected in series, with the midpoint electrically grounded to the spacecraft structure. The load voltage between two outer conductors is therefore 200 V (Figure 16.3), which is about the optimum from an electrical efficiency point of view. Any point in such ±100 V system effectively has only 100 V from the structure ground at midpoint while giving the load voltage of 200 V, keeping the load current and ohmic loss low. The SP-100 power system uses a regulated voltage bus with a shunt dissipator, which absorbs and dissipates the excess power into space after meeting the load requirement. The shunts are made of traditional high-temperature tungsten filament resistance wires. They are turned on automatically in response to the bus voltage error signal. The TEC panels are diode-isolated and are combined in a single 200 V dc bus at the power module, which is located far from the reactor on the opposite end of a long extension boom. Such physical

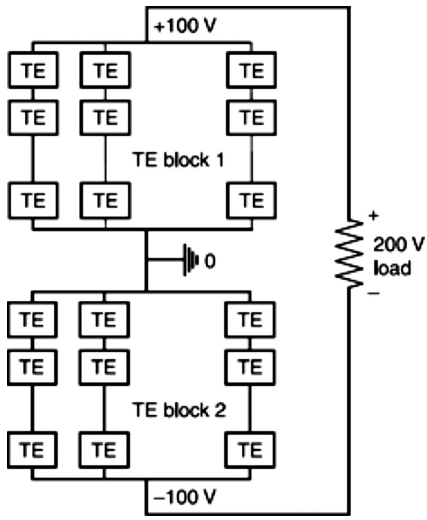

FIGURE 16.3 SP-100 thermoelectric converter assembly for a 200V system between ±100 V lines.

isolation helps reduce the shielding required from nuclear radiation. A 300 W, 28 V auxiliary power supply from a dedicated TEC is provided for startup, maintenance, and the shunt-down period. Under certain mission constraints, solar or battery-only options may also be considered for this purpose.

16.4 HIGH-VOLTAGE DESIGN ISSUES

The design issues that are common to all power systems using high voltage are discussed in this section.

16.4.1 Paschen Breakdown Voltage

The breakdown voltage between two bare conductors in a given gas depends on the p–d product, where p is the gas pressure and d is the separation distance. It is shown in Figure 16.4, known as the Paschen curve. The spacecraft passes through a wide pressure variation, ranging from the atmospheric pressure on Earth before launch to 1×10^{-10} torr in high orbits. During this transition, it always passes through the minimum breakdown voltage point on the Paschen curve. The power distribution system normally has numerous bare spots on conductors and terminals. They would spark somewhere sometime during the spacecraft's journey from the Earth to a high orbit, regardless of the distance between them. Outgassing can make pressure prediction difficult. For this reason, a HV system can be turned on only after reaching orbit (0.1 Pa vacuum). Alternatively, the equipment must be filled with an insulating gas (such as nitrogen) under some pressure or completely encapsulated with a solid, void-free insulation.

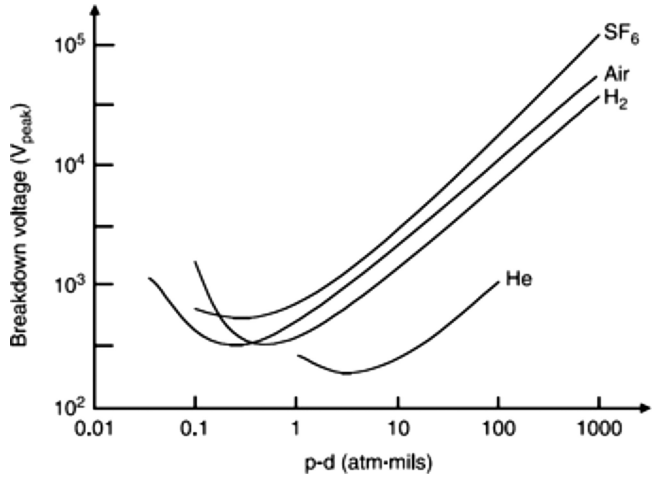

FIGURE 16.4 Pressure-spacing product versus breakdown voltage in various gases (Paschen curves).

Preliminary data have shown that material outgassing causes the local pressure around the HV component to increase to the point that it is no longer a good vacuum. This, in turn, results in a lower corona (spark) inception voltage. The approach to increasing the corona voltage, therefore, is to select the material with a low outgassing rate in the first place.

16.4.2 Dielectric Stress Concentration

If a HV rectangular conductor is placed in an enclosure filled with gas, the dielectric stress at the ends is not uniform but is concentrated near the conductor edges. If the conductor radius is r and the end distance is e (Figure 16.5), the maximum dielectric stress is almost[2]

$$E_{\max} = \frac{V}{e}\left(1 + 0.25\frac{e}{r}\right) \tag{16.1}$$

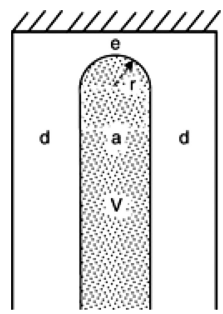

FIGURE 16.5 Voltage stress concentration at a flat conductor edge with a radius.

For E_{max} to be equal to V/d, i.e., the same as the uniform stress in the flat part with ends fully radiused, i.e., $r = a/2$, the end distance is derived by equating

$$E_{max} = \frac{V}{e}\left(1 + 0.25\frac{2e}{a}\right) = \frac{V}{d}$$

which gives

$$e = \frac{a\ d}{a - 0.5\ d} \tag{16.2}$$

For example, with $a = 3$mm and $d = 1$mm, e must be 1.2mm, i.e., 20% more than d, the insulation thickness. For a smaller radius, say $r = a/4$, $e = ad/(a \times d) = 1.5$, i.e., 50% more insulation is required at the ends.

The stress concentration at sharp corners and their effects on corona voltage and dielectric breakdown in atmospheric conditions on the ground are well studied and reported in the literature. Such is not the case in the space environment. A thorough, systematic study of this aspect of the insulation design is required. Until then, the available data must be used with interpolations and extrapolations using wide margins to minimize the associated design risks.

16.4.3 Corona Degradation

The insulation design should be such that corona (partial discharges, sparking) should not start. If started at some higher transient voltage, it must extinguish during the downslope of the transient at some voltage higher than the steady-state operating voltage. Corona has two degrading effects on the insulation's performance. It chemically erodes the material, thus shortening its life, and it produces radio-frequency EMI that may interfere with the surrounding equipment. Both of these effects are undesirable and should be avoided.

The corona voltage is a function of the type of material and its thickness used in the design. For a 1000 V electrical component, corona tests on Earth on polypropylene insulation gave the test results reported in Table 16.2. These results must be modified to account for the Paschen minimum and plasma effects, depending on the orbit in which the spacecraft is designed to operate or pass through.

TABLE 16.2
Corona Test Results on Polypropylene Insulation

Thickness (mils)	Inception(V_{rms})	Extinction (V_{rms})
5	880	835
10	1570	1420

M.R. Patel, NASA Report No. CR-175071, 1986.

A critical quantity needed for evaluating solid insulation subject to corona is E_i, which is the partial discharge inception voltage stress. This can be obtained directly by measurements, from extrapolation of the breakdown voltage–time curve, and from careful analysis of the voltage stress at the conductor edge or in a void if necessary geometric parameters are known. Large voids must be avoided in solid insulation. The dielectric stress is εE in a laminar void and $3\varepsilon E/(1+2\varepsilon)$ in a spherical void, which is much smaller than the insulation thickness. Here, ε is the relative permittivity, and E is the uniform stress in the solid insulation. Partial discharge occurs in a void when the product of the pressure in the gas and the void thickness (electrode separation) exceeds the breakdown voltage according to the characteristic Paschen curve. It can be aggravated by dielectric stress concentration around sharp corners. A good HV conductor design avoids sharp corners to keep the dielectric stress concentration low and the corona inception voltage high.

The following analysis establishes the largest permissible void size in spaceworthy HV insulation. The laminar void is assumed since it produces more stress concentration than the spherical void. If a laminar void of any size d_o exists in a solid insulation between two conductors for any reason, the breakdown voltage across such a void will depend on the gas pressure in the void. Since this pressure may vary over a wide range in and around the spacecraft at different times of the mission, the minimum Paschen breakdown voltage must be used in the calculations, which is about 297 V_{peak} or 210 V_{rms} between copper electrodes. There are now two dielectrics in series, a gap of laminar thickness d_o and the solid insulation of thickness d. If the dielectric stresses are E_o and E in the gap and the solid, respectively, the voltage across the conductors would be $V = E_o d_o + Ed$. Polypropylene insulation with a relative dielectric constant of 2.25 would take 1/2.25 times the gap stress, i.e., $E = E_o/2.25$. With $d = 20$ mils as an example, the above voltage then becomes

$$V = E_o d_o + \left(\frac{E_o}{2.25}\right) \times 20 = E_o d_o + 8.89 E_o = E_o d_o \left(1 + \frac{8.89}{d_o}\right) \tag{16.3}$$

where d_o is in mils. The product $E_o d_o$ is the voltage across the gap, which has a minimum Paschen value of 210 V_{rms}. The corona would start at this voltage across the gap. The corona inception voltage of a cable with polypropylene insulation is then

$$V_i = 210\left(1 + \frac{8.89}{d_o}\right) \tag{16.4}$$

Equation 16.4 is plotted in Figure 16.6, which shows that it takes about a 2-mil (50 μm) delamination gap for the corona to start at 1200 V_{rms}. This condition would not normally lead to an immediate failure, but eventually would do so under gradual corona degradation. Should the gap completely fail, the dielectric stress in the solid insulation would be 1200/20 = 60 V/mil, which is two orders of magnitude lower than the solid insulation's short-term breakdown strength.

As seen in Figure 16.6, the corona inception voltage decreases with increasing gap size and asymptotically approaches the minimum Paschen value of 210 V_{rms}. This is because the Paschen minimum is a constant value, although it occurs at different

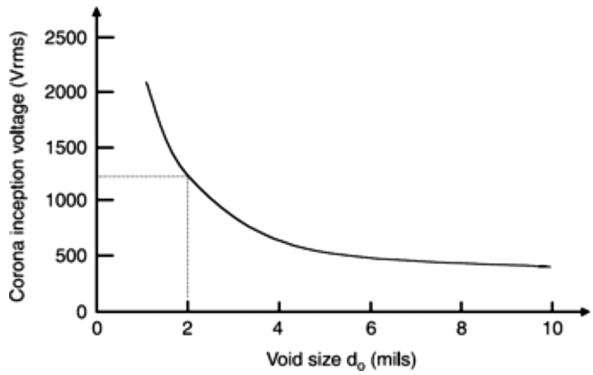

FIGURE 16.6 Corona inception voltage versus laminar void size in a flat conductor cable.

pressures for different gap sizes. As the gap increases, the corona inception voltage across the gap remains constant at 210 V, while the voltage contribution of the decreasing dielectric stress in the solid insulation decreases. This voltage is based on the worst possible combination of the gap pressure and the gap size (i.e., the minimum Paschen value). It is likely that there is always some pressure in the void due to continuous outgassing of the insulation, giving a higher corona inception voltage. The location of the void along the cable length, therefore, matters. If the void is at midpoint of the cable, outgassing may take a long time due to the high resistance offered to the gas flow in a long, narrow duct. For increased reliability, it may be desirable to bleed some gas (such as nitrogen) along the length of HV cable insulation. This would assure the desired gas pressure to maintain the required dielectric strength of the cable.

There is an increasing push for mass reduction to reduce launch costs. For this reason, many HV components do operate with some corona, which must be controlled in manned spacecraft to protect the astronauts from corona charging currents. The high value of mass minimization justifies a sacrifice in the equipment's life, provided reliability and safety are not sacrificed. A life of 5–15 years has been typical for space components, but reliability must be high since these components must operate without servicing.

16.4.4 Atomic Oxygen

The interaction of atomic oxygen with the insulation surface is of particular concern in LEO. This interaction is a reaction and/or removal of mass from the surface during the mission's life. The amount of interaction depends on the total integrated dose of atomic oxygen impingement, which is a strong function of the orbital altitude. Figure 16.7 shows such an interaction in a typical polymer. The insulation design should allow such a loss of material over the mission's life in space.

Table 16.3 shows how various insulating materials degrade under radiation and atomic oxygen. It shows that Teflon® is bad under either effect. An estimated radiation dose on the ISS over 5 years is about 100 krads, so silicon rubber may be used

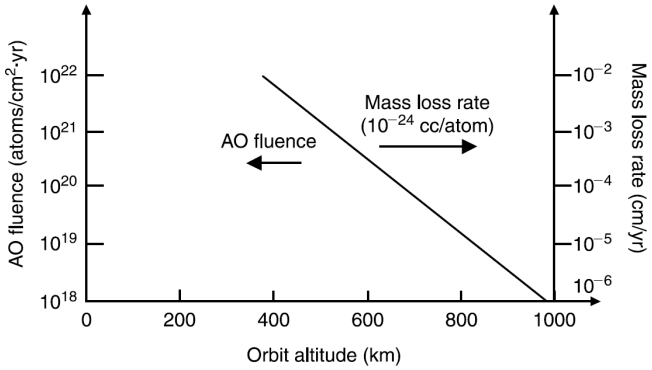

FIGURE 16.7 Mass loss due to atomic oxygen versus orbital altitude.

TABLE 16.3
Depletion Rate of Electrical Insulation in Space Environment

Insulation	Radiation Dose Before Adverse Effect is Noticed (Mrads)	Reactivity, 1×10^{-24} cm³/Atomic Oxygen Atom	Depletion Rate in 3×10^{21} Atoms/cm²·year Orbit, mil/year
Teflon	0.1	0.03	0.036
Silicon rubber	1	0.05–0.2	0.06–0.24
Kapton	100	3	3.6
Epoxies	1000	2.5	3.0

in the design, provided that the degradation under atomic oxygen is acceptable. The atomic oxygen fluence rate on polar orbits at 400 km altitude is about 3×10^{21} atoms/cm²·year, which is less than that on the ISS.

16.4.5 Plasma and Charged Particles

The plasma in the mission orbit exerts the greatest influence on the voltage that two bare conductors can withstand in space. The plasma density in electrons/cm³ versus orbital altitude is depicted in Figure 16.8. It peaks in LEO and is negligible in GEO and beyond. The plasma acts as a shunt resistance across the power components, such as the solar array, causing power loss due to the resulting leakage current between bare conductors. This loss becomes noticeable above 160 V.

A voltage much higher than 160 V leads to voltage breakdown. The breakdown voltage versus plasma density is shown in Figure 16.9. Combining Figures 16.8 and 16.9 leads to the arcing voltage between bare conductors versus orbit altitude, as plotted in Figure 16.10. The arcing voltage determines the maximum solar array output voltage and the minimum distance between printed circuit board traces to withstand the voltage over the design life of the mission. For this reason, NASA limited the ISS solar array output voltage to 160 V, with a 120 V distribution voltage and step-down converters where required for existing 28 V hardware.

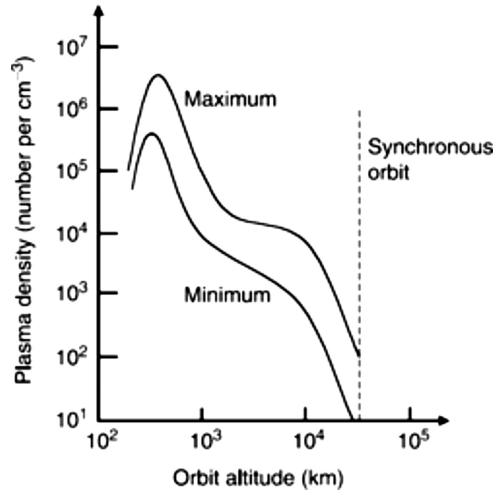

FIGURE 16.8 Plasma density versus altitude in an equatorial orbit.

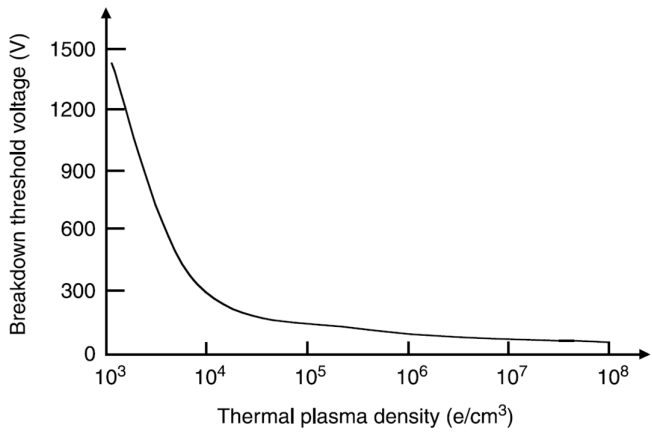

FIGURE 16.9 Breakdown voltage threshold versus plasma density between bare conductors.

In plasma-free orbits such as GEO, the conductor in a near-perfect vacuum can withstand kilovolts or even higher voltages. However, the Paschen minimum breakdown voltage limits its operation to GEO and not during launch or transfer orbit. The outgassing of the material inside the spacecraft body and the flue plumes outside create an uncontrolled gas pressure around the conductors. Moreover, the spacecraft interior during launch undergoes a decreasing air pressure as it attains orbit, and it may take a long time after the launch to achieve a good vacuum. It is probable that at some instant the p–d product may achieve a value corresponding to the minimum breakdown voltage. Under such a condition, the bare conductor would cause arcing and a short circuit. For this reason, the system designed to operate at higher than 160 V in GEO can be turned on only after achieving GEO orbit.

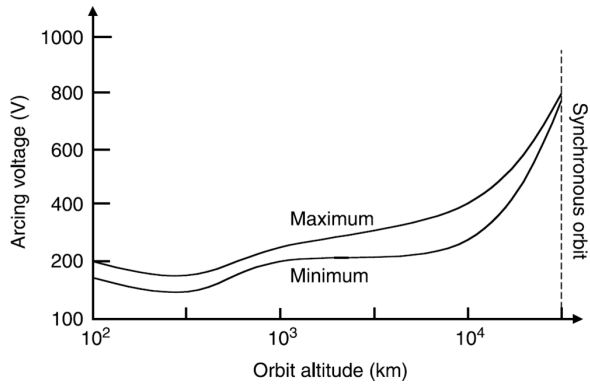

FIGURE 16.10 Arcing threshold voltage between bare conductors versus altitude.

As seen in Figure 16.10, the 300 km high orbit is the worst, with an arcing onset voltage of only 160 V. If the spacecraft must go through this orbit, the power distribution voltage must be below 160 V. If a solar array assembled by standard construction techniques—with coverglass not completely shielding the metallic interconnects—is operated at a voltage higher than 160 V in LEO, the bare interconnects can act as plasma probes and attract or repel charged particles. The generated voltages will be equal to the space plasma potential at some location on the array. Since electrons are more mobile than ions, the array will float at voltages that are mostly negative with respect to space plasma potential. Cell interconnects at voltages above this space plasma potential will collect electrons; those at voltages below this will collect ions. The voltage distribution in interconnects relative to the space plasma potential must be such that these electron and ion currents are equal (i.e., the net current collected is zero). This flow of particles can be considered a current loop through space that is in parallel with the operational system, and hence, a power loss. In addition, the coverglass used on the solar cells must also have a zero net current collection. This interaction with space plasma forces the coverglass to a small negative potential and can produce large voltage gradients in the gap region between solar cells. This can subsequently give rise to arcing conditions or transient breakdowns in space.

The severity of such plasma interactions depends on the array's operating voltage and the charged-particle environment. The operating voltage is determined from power system trades, but it will probably be less than 1000 V. At the projected operating voltage, only the low-energy or thermal plasma environment should be of concern since the array voltage is too low to influence the higher-energy environmental particles. This plasma environment has particles with temperatures of about 1 eV and densities that vary from a maximum of about $3 \times 10^6 \text{cm}^{-3}$ at 300 km to between 1 and 10cm^{-3} at geosynchronous altitudes. Hence, plasma interactions should be more severe at lower altitudes than at synchronous altitudes.

A 100 kW space-worthy system operating at 500 V dc was designed by NASA. It was made of ten arrays in parallel, each with a 10 kW capacity. It was found that, under normal quiescent conditions, the power drain due to the electron coupling current would be negligible. However, the arcing in the negative voltage regions could

seriously disrupt system operations either by introducing a ripple on the output or by terminating operations, depending on the severity and location of the breakdowns. The orbital oscillations range through ram, wake, and eclipse conditions. The shuttle experiments that indicated that large space structures could create their own plasma environment tend to make plasma interactions even more critical.

Over the past decade, the advantages and disadvantages of large space power system operations at high voltages have been argued and discussed. There are obvious advantages to using high voltages in space. Possible hazards to such operations with standard array technology have been addressed. These interactions are not insurmountable but can be overcome given an adequate understanding of the phenomena. What is needed is a systematic investigation to determine why discharges occur and how to prevent them. This would require test programs involving large arrays with self-generated voltages and flight experiments to prove that all of the interactions can be minimized.

Tests in ground simulation facilities in which small solar array segments were biased to positive and negative voltages in a plasma environment have shown that interactions can be detrimental. When positive voltages are applied, electron currents can be collected that become proportional to the panel area at voltages greater than 100 V. Arcing or breakdown can occur under negative bias voltages. This arcing threshold depends on the plasma density and can be as low as −300 V in a simulated 300 km orbit plasma environment, as shown in Figure 16.11a and b.

Relatively few tests have been conducted in which an array capable of generating high voltages under solar simulation conditions was operated in a plasma environment. PIX-I and PIX-II space experiments conducted by NASA have shown that a 9-block array would float electrically such that one block would have an average positive voltage that would be 10% of the overall voltage, with the other eight blocks progressively more negative. This test indicated that array behavior could be approximated by considering the interaction with separate blocks at an average voltage.

As for the effects of radiation, Bouquet and Winslow[3] present their study results on the lowest doses at which radiation effects on material properties are noticeable.

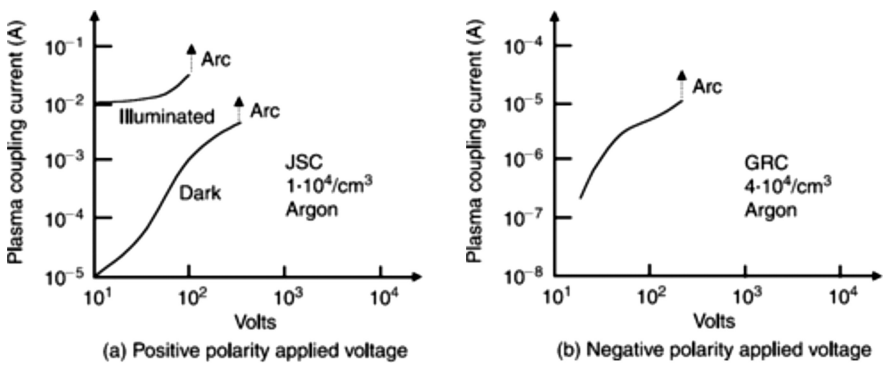

FIGURE 16.11 Plasma coupling current versus applied voltage. (a) Positive polarity applied voltage. (b) Negative polarity applied voltage.

The report compiles data on the effects of radiation on the physical properties of polymers and synthetic organic materials. The emphasis is on materials of interest to nuclear equipment and nuclear reactor designers. The data cover five categories of polymeric materials: insulators, elastomeric seals and gaskets, lubricants, adhesives, and coatings. More than 250 materials are represented. The document reflects a continuation of the work in progress. It gives available data on physical, electrical, and optical properties for each material in terms of the lowest reported threshold dose. It indicates the radiation level at which radiation effects become apparent and the dose for a 25% change in the specified property. The literature source for the data is also indicated. Both the threshold and the 25% change dose vary widely within each of the five categories of polymers. Most polymeric materials have thresholds above 10^5 rads. Some materials—fluorocarbons, nylons, epoxy resins, polyethylene oxides, and polyalphamethyl chloroacrylates—have thresholds below 10^5 rads. The threshold data are useful for setting a lower limit at which changes can be expected. They may also be used as a guide for deciding when the expected radiation is low enough to be disregarded for a given polymer. The 25% change in dose is a valuable radiation statistic because changes are real at this dose level and are neither artifacts of the experiments nor results of sample variations.

16.4.6 Temperature Extremes

The spacecraft component temperature can swing over a wide range during sunlight and eclipse durations. Such temperature extremes must be considered in the insulation selection. The components exposed to space temperature (−200°C) without survival heat may experience damage. For example, most polymer insulation may shatter (crack) at temperatures below −75°C. After such an exposure, corona may start in the cracked insulation, thus shortening the component's life when supporting high voltage.

16.4.7 Design Guidelines

The corona, outgassing, plasma, in-space propulsion exhaust, permeation from pressurized chambers, bubbles in liquid dielectrics in zero gravity, etc. make HV space insulation a different science than on Earth. More experiments are needed to understand these factors.

Two types of insulation breakdown dominate in vacuum or low-pressure gaps between bare conductors. Breakdown in small gaps is dominated by the electrode surface, whereas in large gaps it is dominated by particle contamination in the gap volume. The surface breakdown generally occurs at lower stress levels than the volume breakdown. The pressure around outgassing surfaces can be orders of magnitude higher than the ambient pressure and can be a function of external stimuli, such as temperature and incident charged particles.

If the spacecraft must operate or pass through the worst orbit in an electrically ON state, the spacecraft power distribution voltage must be lower than the breakdown voltage in plasma and the Paschen minimum voltage. For voltages higher than that, several possible design approaches can be considered:

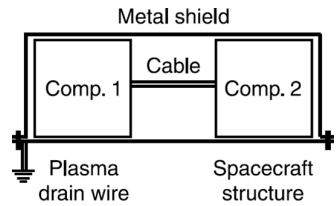

FIGURE 16.12 Space plasma shield configuration.

- Avoid the effect of plasma by placing the HV component in a metal enclosure. The enclosure drains the plasma to the spacecraft ground, thus keeping it from reaching the electronic component (Figure 16.12).
- Avoid the worst pressure for the Paschen minimum by venting a gas (nitrogen) around the bare electrodes until the spacecraft reaches a safe orbit.
- Encapsulate the HV component in solid insulation. The material selected for encapsulation must have low outgassing properties, and the manufacturing process must be void-free to minimize corona.
- Place the HV component in liquid or gaseous insulation. The high fluid leakage rate in a hard vacuum must be accounted for in spacecraft designs.
- Turn ON the electrical system only after reaching the altitude where the arcing onset voltage is higher than the distribution voltage. Until then, the electrical power requirement (for survival heat, navigation, or controls) must be met by batteries operating at low voltage.

16.5 HIGH-VOLTAGE DC AND AC SYSTEMS

HV dc systems have found increasing applications, particularly in high-power systems in electric propulsion systems. The electric vehicles adopted a voltage of 350 V, 750 V, and up to 1000 V. Electric vertical takeoff and landing aircraft, which have recently gained renewed attention, use voltages around 850 V primarily from a battery system for their propulsion. For space applications with increasing power levels, the dc bus voltage will continue to increase. Major factors that influence the HV design in space include, but are not limited to:

- The availability of commercial space-qualified parts, such as semiconductors and power electronics switches (MOSFETs, IGBTs, etc.), capacitors, and other components rated at high voltage.
- Electrostatic discharge occurs even under vacuum conditions in space.

The EMI considerations in HV dc systems are similar to those in the low-voltage dc systems. dc systems are also expected to have low levels of radiated Band E-fields. Power conditioners operating at high switching frequencies would result in minimal EMI filters. Shielding techniques are similar to those used in low-voltage systems. Solid-state switches have reduced the rate of rise and fall times in current and thereby reduced system transients.

The principal safety hazards in an electrical system are fire, shock, and audible noise. Direct-current systems are typically immune from audible noise. Fire hazards are common to all distribution systems, regardless of the voltage level. Ground faults in HV dc are cleared by RPC and RBI to protect personnel and reduce fire hazards. HV dc components developed for aircraft applications are suitable for further development for space applications. The extensive space experience in 28–160 V dc heritage allows the development of similar designs for HV dc systems. A number of HV dc components have been developed for use with HV solar arrays and battery assemblies.

The 28 V dc system used in early aircraft, both military and commercial, contributed to the selection of 28 V dc for the first spacecraft. The 28 V dc remained in use until the 1980s. Modern aircraft power systems, however, have changed to a 400 Hz, 3-phase, 200 Y/115 V variable speed constant frequency system and are again in transition to a few hundred volts dc. The now-retired space shuttle fleet generated dc power using fuel cells, but converted and distributed the power at 120 V, 400 Hz, 3-phase. The spacecraft secondary power distribution can be 208 V, 3-phase Y, such that 120 V is available for single-phase utilization. The primary voltage can be any, such as 440 V, 3-phase Y or Δ. The Japanese and European space industries preferred 120 V dc for secondary distribution on the space station even when NASA strongly preferred a 3-phase, 208 V Y/120 V, 20 kHz system in an early phase of the ISS design. The simplicity, low parts count, and previous space qualification history of dc systems offer advantages over ac systems for high reliability in space environments. The power system in the hundreds of kilowatts to megawatt rating is likely to have numerous items of equipment working at different voltages, much lower than the generation and transmission voltages. The distribution system for such a high-power platform has to be efficient, lightweight, and flexible to accommodate a variety of electrical sources and loads. It would require voltage converters to step down the generation voltage to suit the equipment to be powered at various locations.

16.6 VERY HIGH-VOLTAGE SYSTEM

Voltages ranging from 200 V to 100 kV may be needed for future high-power civil and military space missions. The state of space power technologies is changing, and HV systems need to evolve rapidly. Therefore, space-qualified HV power components will assume an increasingly greater role in the coming decades. Key design considerations for such components and systems are presented below.

The plasma arcing inception voltage in a space environment varies from 200 V in LEO to 1000 V in GEO. It is therefore obvious that HV equipment rated in kilovolts cannot have bare conductors exposed to space plasma. This requires positive insulation systems for the equipment consisting of one or more of the following design features:

- Insulating gas, typically at high pressure
- Insulating liquid
- Perfect plasma-free vacuum with minimum outgassing materials used in the construction

- Encapsulation with solid insulation, typically an epoxy-resin compound
- The incoming and outgoing insulated cables cannot be terminated at bare, exposed terminals. The insulated cable must enter a sealed casing containing the insulating medium.

The gas insulation, being mass-effective, is likely to find applications in very HV spacecraft. A 3-phase gas-insulated transmission line concept is shown in Figure 16.13, and Table 16.4 lists the relative dielectric strengths of commonly used insulating gases at atmospheric pressure. This strength increases with increasing pressure. Notice that Freon™, which is commonly used in 2-phase cooling systems, has the best electrical strength, followed by SF_6, which is inert, nonflammable, nontoxic, and odorless. Hydrogen is the least preferred electrical insulation, in addition to being a safety hazard. The liquid insulation, being 3 to 4 orders of magnitude denser than gases, possesses much higher dielectric strength and heat removal capacity. Moreover, like gas but unlike solid insulation, liquid tends to be self-healing should a discharge occur in it. The commonly used liquid insulations and their dielectric breakdown stresses are listed in Table 16.5. The design stress margin depends on the dielectric stress concentration factors and other uncertainties in the design calculations.

The two major factors that cause the insulation to degrade are the operating temperature and the corona discharge. Temperature degradation is well understood. The insulation life reduces by one-half for every 7°C–10°C rise in the

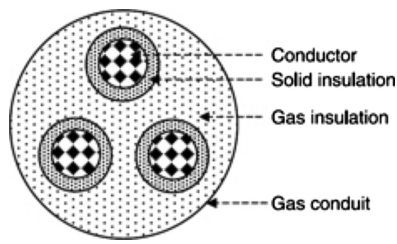

FIGURE 16.13 Gas-insulated 3-phase transmission line for very high voltage.

TABLE 16.4
The Relative Breakdown Strength of Commonly used Insulating Gases at Atmospheric Pressure

Gas	Relative Strength
Air	1
Nitrogen	1.05
CO_2	0.95
SF_6	2.5
C_5F_8 (Freon)	5.5
Hydrogen	0.6

TABLE 16.5
The Breakdown Strength of Commonly Used Insulating Liquids

Liquid	Design Stress (kV/mm)
Petroleum oil	2–6
Chlorinated hydrocarbons	4–12
Silicone oils	4–12
Synthetic hydrocarbons	10–25

operating temperature. As for the corona, it degrades different materials at different rates. The material that has high dielectric withstand capability when new generally degrades faster under corona. The material selection must therefore match the mission duration. Yet another degradation factor, applicable only to solid-encapsulated components, is thermal cycling. The differential coefficient of thermal expansion between the conductor and the polymer encapsulant induces thermo-elastic stress cycles. These may lead to internal cracks in the solid insulation, thus degrading the dielectric properties of the insulation system.

As the power transmission distance increases, the voltage drop and power loss can be kept reasonable only by using high voltage. For this reason, several kilometer-long lines would require several kilovolts if the drop were to be kept below 5%. At that voltage and distance, using SF_6 to reduce the line mass by as much as 50% may be considered. As an example, some kind of high dielectric strength gas insulation may be necessary for connecting the SP-100 power source with a space station by a several kilometers long tether cable operating at very high voltage. For such a system, it is envisioned that the SP-100 power output may be stepped up to about 10 kV and transmitted to a space station, where it would be stepped down to the user's level. The electrical and mechanical performance and mass characteristics of such a transmission line are compared using both SF_6 and vacuum. A 5 km long transmission line's mass can be significantly reduced by about half by substituting pressurized SF_6 gas for vacuum insulation. The improvements basically result from the higher dielectric field strength that can be allowed in SF_6. The insulating distance between the several kilovolt line conductors and the grounded outer tube substantially decreases with SF_6, thus decreasing the outer tube diameter and the support mass by a significant amount. There is an added mass of the pressurized SF_6 gas management system (reservoir, pumping, and pressure monitoring systems) in a sealed line construction. However, this added mass would be small compared to the mass of several kilometers long line. On the other hand, the insulation mass reduction potential in the 50 m long SP-100 boom cable is much smaller than the added mass that may be required for the gas management system. For comparison purposes, the mass of a 100 kW, 10 kV, 5 km line is estimated to be 1600 kg with SF_6 gas insulation versus 3200 kg with vacuum insulation, a net reduction of 1600 kg. The 200 V boom cable in the SP-100 concept would weigh 7200 kg for a 100 kW, 5 km line.

16.7 REPETITIVE PULSE POWER

Pulsed power is defined as a very high power for a very short time (a burst power) for specialized applications. In defense weapons, pulsed lasers and electromagnetic guns for missile launches are such applications. Others include medical, particle accelerator, and some strategic defense projects, such as simulation of the electromagnetic pulse that result from nuclear explosions. The concept of pulsed power is not new. It was used in radar systems in World War II, and its new applications are expanding. Pulsed-power sources are fully integrated systems rather than single-power supplies. In such systems, a HV constant current source (rather than a constant voltage source) is used to charge a bank of capacitors. The steady power supply is not directly connected to the load; its sole use is to slowly charge the capacitor bank. A switch is added to control the discharge of the capacitor, and a resistor limits the current. Fuses protect the equipment under adverse conditions.

HV power supplies can deliver around 10 kJ of energy per second, with voltage ratings up to 50,000 V. Since capacitor charging varies from zero to peak voltage, the energy measured is the average delivered to the load. Though both linear and switching supplies are used in pulsed-power systems, the trend is toward switch-mode technology. Most units are designed to fit on standard 19-inch racks. The switching frequency is limited to 50 kHz since the component cost for HV applications rises with the frequency.

In pulsed-power applications, the capacitor capability is measured in terms of the specific energy. A good capacitor needs a high capacitance, low-temperature coefficient, and a relatively low inductance. The capacitor dielectric has to withstand very high voltage and current, offer temperature stability, and have a fast-discharge frequency. Pulse requirements vary with the application. Electromagnetic guns (also known as rail guns) need a 5–40 kV pulse for a few milliseconds. Electromagnetic pulse simulation needs multimegawatt pulses of a few nanoseconds duration.

The trend in repetitive pulse-power system design is toward higher energies, larger average power levels, and faster pulse repetition rates. This trend results in requirements for components with higher reliability, lower losses, and longer life times. Emphasis is placed on those components and materials requiring significant development efforts. Switches are by far the weakest active components in pulse-power systems, and capacitors are perhaps one of the weakest energy storage elements in high-power pulsed systems, especially when operated at high repetition frequencies for extended periods of time. Improved insulation in systems and components is essential to increasing energy density and reliability. The pulse transformer and inductor designs require special cooling and thermal time-constant considerations.

The development of long-life, fast-discharge components is essential to many future high-energy applications. Many of these systems are needed where compactness, light mass, high reliability, and low loss are prime requirements. Capacitors and switches presently available cannot meet this combination of projected requirements in high-repetition-rate power systems. At present, the energy density of capacitors operated at continuous high pulse rates is typically a factor of three to ten less than that of those used in single-pulse systems. The basic characteristics and problems associated with spark gaps and thyratron switches used in pulsed-power systems

need to be addressed. Gas dynamic spark gaps in the thyratron switches often require more power to furnish compressed insulating gas than the average power they can pass. The corona characteristics of liquid and solid insulation limit the permissible dielectric stresses in the materials and, consequently, the energy density of the system. This brief discussion points to the major areas of development necessary for pulsed-power components.

Capacitors are the basic electrostatic energy storage elements in pulsed-power systems. The rationale for evaluating capacitor technology is to determine and understand the failure mechanisms and then work with manufacturers to develop improved performance units. Recent programs have sought to determine the capacitor's weak points, the characteristic failure mechanisms, and the required dielectric characteristics compatible with high *dI/dt* discharge capacitors operating at 1 kHz pulse rate frequency and 100 ns discharge time. The performance evaluation of low-inductance types of capacitors in the 100 ns, 1 kA, 1 kHz regime has led to the following conclusions:

- Partial discharge (corona) is the main cause of failure in the pulse-power capacitors andis detectable during energy discharge.
- A high-quality, high-frequency diagnostic system is essential to observe transients within capacitors during discharge. The high-frequency, HV probes developed for the system are required as diagnostic tools.
- Preliminary tests indicate that Teflon–silicone oil and mica-paper capacitors have a longer life in the regime tested than the polypropylene-silicone oil units, but with a lower energy density. The latter is attributed to the impregnation characteristics of Teflon units and the fabrication methods of mica units and may not represent intrinsic limitations.
- The major components of such power systems are the HV capacitor, the thyratron switch, and the air-core transformer. The following are the rough guidelines for selecting the energy storage technologies for a pulse-power system: (i) capacitor for a high pulse rate in kilohertz, (ii) battery for a few hertz pulse rate, and (iii) flywheel or superconducting coil for a still lower pulse rate.

16.8 MULTIMEGAWATT BURST POWER

The power requirements for some strategic defense spacecraft range from tens to hundreds of megawatts of burst power. Directed energy weapons, typically placed in LEO, are examples. Such a power system is required to deliver high power for a short period of time, after which it must recharge. Important considerations in selecting the system architecture and subsequent design details include the following:

- Primary energy source, energy conversion, and energy storage to meet the peak power requirement and rapid startup
- Power conditioning and distribution
- Thermal management during engagements
- Optimum voltage selection for mass minimization

- Low vibration and low torque on the weapon platform
- Long standby with low quiescent power requirements
- Low mass, low cost, and high reliability

A future reusable directed energy weapon in LEO is predicted to occasionally require power over 10 MW for several minutes. For such a short duration and occasional, very high burst power, large-scale energy storage in a flywheel or superconducting coil may be considered. However, the fuel cell may be an ideal candidate. For the Air Force Research Laboratory, Allen[4] evaluated 10–300 MW burst power system design. He considered several top-level options—chemical-dynamic, nuclear-dynamic, chemical-fuel cell, battery, and flywheel, which could be recharged using a solar array.

The study concluded that a system using a regenerative solid oxide fuel cell (SOFC) with hydrogen and oxygen reactants could deliver the required power with the lowest power system mass and is the best approach with available technologies. The PEM fuel cell system results in higher mass, primarily from the extra cooling fluid and the associated storage tank, which was significantly higher than the mass of the high-temperature radiator used with the SOFC. The fuel cell is the lowest mass system primarily because it produces power only when needed and at 270 V dc, which does not require additional power conversion or conditioning. The flywheel generally results in a heavier power system that is not used continuously. The cooling of the power system and the weapon components in the study was achieved by a circulating ammonia loop.

The 10 MW SOFC system features are summarized in Table 16.6, and the study results are summarized in Figure 16.14 for 5 min of the weapon run time.

The solar array-SOFC system mass breakdown in percentage of the total power system mass was reported as follows: 60% in the fuel cell stack, 10 in fuel and steam tanks, 8 in reactants, 6 in radiators and plumbing, 14 in the solar array, and 2% in all other components.

TABLE 16.6
Ten Megawatt Solid Oxide Fuel Cell Burst Mode Power Systems Features

Burst Power	**10 MWe, Scalable to 300 Mwe**
Burst mode duration	100–1000 s
Test duration	60–240 s/year
Mission life	10–15 years
Fuel cell efficiency	70%
Operating temperature	1250°C
Working pressure	135 atmosphere
Oxygen consumption rate	1.75 kg per MW·s Hydrogen consumption rate 0.015 kg per MW·s
Effluents	Negligible

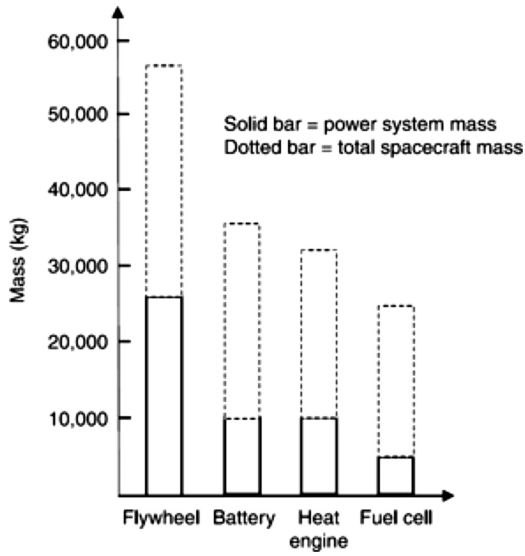

FIGURE 16.14 10 MW_e power system mass with alternate design concepts.

Recharging the fuel cell requires electrolyzing the by-product water back into hydrogen and oxygen. The SOFC can electrolyze water using the recharging process. The electrolyzer is generally a separate unit from the stack, and the two cannot operate simultaneously. Recharging the fuel cell in 1 day in Allen's study required a 213 m^2 solar array generating 70 kW. Extending the recharge time to 5 days cuts the array to 55 m^2 generating 18 kW of power (Figure 16.15). However, this may conflict with some mission scenarios due to condensed periods of conflict.

Dynamic systems may be needed for sustained high power in the tens of MW. For example, one SDI concept around 1990 required 300 MW of power for 15 min before

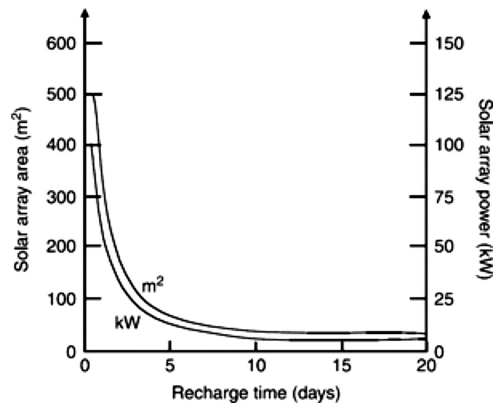

FIGURE 16.15 Solar array versus recharge time after 5 min of weapons run with a 10 MW_e load.

charging up the energy storage elements with 10 MW of steady power. Such high-power missions are expected to consider nuclear reactors as the primary energy source and rotating electrical machines for the energy conversion. In a baseline concept, the reactor heats a fluid, typically a liquid metal such as mercury or sodium potassium. The vapor then drives a turbine generator using the Brayton or Rankine cycle. The space nuclear system is similar to a ground-based nuclear power station. The major difference in space is that the waste heat must be rejected only by radiation back to space. Both systems use the nuclear fission of a heavy metal atom, which releases a large amount of energy, primarily in the kinetic energy of the fission fragmentation. A total of 200 MeV of thermal energy is released per fission. The conversion between million electron volts and watts gives 3.1×10^{10} fissions per second needed to release 1 thermal watt. This energy is used to generate steam and drive a turbine generator to convert it to electrical power. In a large-scale power system in the megawatt range, the overall thermal-to-electrical conversion efficiency is 40%–50%.

The nuclear reaction must be contained in a well-shielded enclosure. In principle, the chain reaction of the fission, once started, continues as long as the critical mass is maintained, and the energy can be released at any desired rate. However, in practice, the release rate is limited by temperature problems, so a given reactor has a maximum achievable release rate.

When using the synchronous generator, the steady-state torque on the platform is a non-pulsating constant torque (of dc nature) and does not affect the platform's pointing accuracy. However, the transient torque during a fault (e.g., a short circuit on the output terminals of the generator) is of a pulsating nature and constitutes a major dynamic disturbance on the platform. Such a torque is the product of the alternating short-circuit current and the constant magnetic flux in the air gap, which becomes frozen on the instant of a short circuit, in accordance with the constant flux-linkage theorem. Spacecraft momentum and vibration issues are important integration considerations in any system using large rotating machines. However, as cited above, rotating machines produce large dynamic torque on the platform, particularly during faults, which may hinder the pointing accuracy of the spacecraft. The disturbing torque is minimized by using such machines in one or more pairs of counter-rotating machines to cancel each other's torsion effects. There always remains a net torque on the platform, as two machines in a pair cannot be located exactly in the same place. However, the momentum cancellation of 0.999999 by using counter-rotating machines is required to minimize the spacecraft's uncontrolled spin and/or tumble. In a multimegawatt power system, a mismatch of even less than 0.01% could gyrate the spacecraft out of control, and a mismatch in the order of 0.001% could introduce significant pointing errors.

A major design challenge in the multimegawatt weapons spacecraft is the thermal management to remove heat from the electrical power source and then remove it from the spacecraft while maintaining a narrow thermal gradient between the components. A 100 MW system with 35 to 40% thermal-to-electrical conversion efficiency engaged for 10 min needs 36 GJ of heat to be dissipated eventually into space. The heat may be removed from the spacecraft as it is generated or stored on the spacecraft for gradual removal. The thermal system options are direct radiation, liquid heat capacity storage, and latent heat phase change storage with spray

cooling. The former would have the greatest mass, whereas the latter would result in the least mass system. However, a major concern with spray cooling is the large pressure differential required to pump the liquid and vapor. A second concern is the momentum of the fluid caused by the high mass flow rate. A thermal system split into at least two counter-directional fluid loops can reduce the net momentum to a tolerable level.

Many aspects of multimegawatt power system design have to be considered in conjunction with the requirements of an actual space mission. In order to take advantage of the dynamic power system's characteristics, the system must be thoroughly integrated into the spacecraft. The synchronous generator is a more likely candidate for such high-power missions due to its high air-gap torque characteristic. Among such machines, superconducting or hyperconducting generators could be advantageous for their low mass, low volume, and high efficiency. Superconducting machines use a superconducting dc field coil on the rotor, which completely loses its electrical resistance below a critical temperature, T_{cr}. The ac stator winding in this machine still uses conventional conductors. The hyperconducting machine, on the other hand, uses a high-purity aluminum conductor in both the rotor and the stator at liquid nitrogen temperature. It exhibits extremely low electrical resistance, but not precisely zero as in the superconducting machine. Both the superconducting and the hyperconducting generators are likely candidates for high-power space missions.[5] Some design data are available in published literature on a 270 MW superconducting generator development program for power grids funded by the Electric Power Research Institute.[6] In space, the platform's dynamic control and the pointing system must account for the net effect of all the rotating machines (generators, turbines, and pumps) on the platform, which depends on their exact placement. The net effect of all such machines is platform-specific and varies from one platform to another.

16.9 HIGH-TEMPERATURE COMPONENTS

High-temperature components are required in high-power solar dynamic, SP-100, pulse-power, and electromagnetic pumps for liquid metal. For energy storage at high temperatures, a sodium–nickel chloride secondary battery may be used up to 275°C, sodium sulfur up to 350°C, and Li-ion sulfide up to 450°C. A very large sodium sulfur battery with cylindrical cells with a total capacity of 48 MWh has been built in Japan for terrestrial use.

Premium-grade silicone rubber or polyamide fibers such as Nomex and Kevlar are widely used at insulation for service temperatures up to 250°C and voltages of 10 kV ac or 25 kV dc.

HV, high-temperature wires rated up to 600 V and 450°C are commercially available for use in furnace ignition leads, thermocouples, aircraft, and missiles. They are generally made from nickel-clad copper wire insulated with glass-reinforced mica tape or coated with a glass–ceramic compound. Tungsten or nichrome wires with 3M Nextel™ ceramic fiber or Rockbestos Phosroc™ insulation can operate up to 1200°C continuously and 1400°C in the short term. Such wires have also been considered for use in submarine-proof areas. Their radiation resistance has been tested up to 10^7 rads.

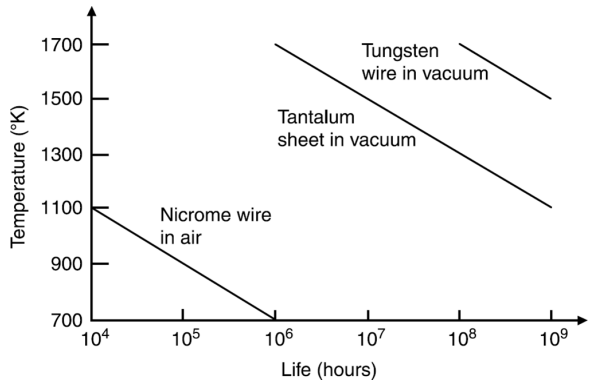

FIGURE 16.16 High-temperature heater element life characteristics.

The life of high-temperature conductors commonly used in heating elements is shown in Figure 16.16. On the insulation side, it is always important to choose a dielectric with thermal stability. One high-temperature wire candidate is cuprous oxide thin-film insulation on a copper substrate. It is available from Permalustetr, Inc., in rectangular wires and thin strips. The insulation is impervious to nuclear radiation, gamma rays, corrosion, corona, high vacuum, and cryogenic temperatures. It can operate at 1000°C without additional corrosion or oxidation of the copper. The insulation film thickness is 3–4 μm for 100 V insulation. It is highly flexible, does not outgas or craze, and allows other overcoatings. It is ceramic in nature. It is not a deposition, only a conversion coating. It would allow compact coils in inductors and transformers.

Nickel connectors are good up to 650°C. The bare connectors may be coated with some sort of insulation, such as ceramic sprays, potting compound, and ceramic fiber tapes.

The following is a brief summary of NASA/Westinghouse Lima research on the development and evaluation of magnetic and electrical materials capable of operating in the temperature range of 800°F–1600°F. Advanced space power systems are the eventual application of such materials.

High-temperature magnetic materials with satisfactory strength are needed for use in the solid rotors of electrical generators. Screening tests have been conducted on martensitic alloys using additions of tantalum plus tungsten and tantalum plus silicon to a base composition of iron with 15% nickel and 25% cobalt. They indicate that these alloys show promise for meeting the desired creep stress exceeding 60,000 psi at 0.4% creep strain and magnetic saturation exceeding 13 kilogauss at 1100°F. In the 1200°F–1600°F range where dispersion strengthening is applied to cobalt and cobalt–iron base alloys, results show the saturation magnetization goal of 12 kilogauss can be met by 27 cobalt–iron base alloys containing as much as 20 volume percent dispersoid. No problem appears to exist in meeting the goal of a coercive force of less than 25 oersteds at 1200°F–1600°F in either 27 cobalt–iron base or cobalt base compositions. Creep tests on Nivco alloy at 1100°F were conducted at pressures in the $3–5 \times 10^{-9}$ torr range at 1100°F. Design analysis suggests creep strains in

excess of 1% should be run above 1050°F. This would provide more reliable design data for rotors in inductor alternators even though the design is based on only a total creep strain of 0.4%, because this represents the integrated value of a wide range of incremental creep strains.

The tests also determined the feasibility of high-temperature capacitors using high-quality dielectric materials. Comparison of electrical data on boron nitride (Boralloy), polycrystalline alumina (Lucalox), polycrystalline beryllia, and single-crystal alumina (Linde sapphire) showed that pyrolytic boron nitride has significantly lower ac power loss, higher dc resistance, and exhibits less change in capacitance with temperature than any other material investigated in the temperature range from room temperature to 1100°F. In addition, the dc breakdown strength of pyrolytic boron nitride is 7000 v/mil at 1100°F, which is several times greater than that obtained with sapphire or beryllium.

Alkali-metal compatible ceramic-to-metal seals and combinations of materials designed into generator stators with a bore seal, a transformer, and a solenoid were investigated for compatibility under electrical and magnetic stresses at elevated temperatures and under high vacuum. Ceramic outgassing studies indicated that the firing cycle applied to a ceramic using a nitrogen–hydrogen atmosphere followed by the vacuum treatment, which they undergo during brazing, is sufficient for minimizing oxygen bearing outgassing products. These would add only a few parts of oxygen to the alkali-metal charge in a typical advanced electric power system. The stator, transformer, and solenoid to provide data on the stability of materials applied to typical electrical designs were installed in the thermal vacuum chamber, and stability testing was done at a 1100°F hot spot temperature. The chamber pressures were approximately 4×10^{-7} torr at the beginning of the 5000 h tests and were decreasing. The minimum cold chamber pressure obtained after system bake-out was 1×10^{-10} torr.

Magnetics for use at temperatures up to 600°C and voltages up to 600 V dc may consider nickel-clad copper coated with ceramic insulation or electrochemically formed aluminum oxide film. Such a coating is primarily a refractory-glass compound that can withstand flexibility and braiding requirements consistent with normal coil winding operations.

To protect the surface from oxidation films and to enhance the mechanical strength of copper at high temperatures, nickel cladding is required. The word *cladding*, as used by the copper wire industry, actually means electroplating 27% of pure nickel by mass (or area, as both nickel and copper have about the same mass density). The cladding reduces the effective conductivity of the composite wire to about 75% of the core copper because of the lower conductivity of nickel. With a core copper conductivity of 85%, the composite wire would then have a conductivity of $0.85 \times 0.75 = 0.64$ times that of pure copper at room temperature. At higher temperatures, this value may be different. In a magnetic environment, nickel is slightly ferromagnetic at room temperature but loses its magnetism at about 700°F (370°C).

The SP-100 boom cable design requires electrical conductors and insulating materials that can continuously operate in a 570°C environment. If we add approximately 30°C for the internal temperature gradient, we need conductors and insulating materials that can withstand about 600°C of continuous temperature at the reactor end. The cable temperature at 30 m away from the reactor would be around 100°C–200°C

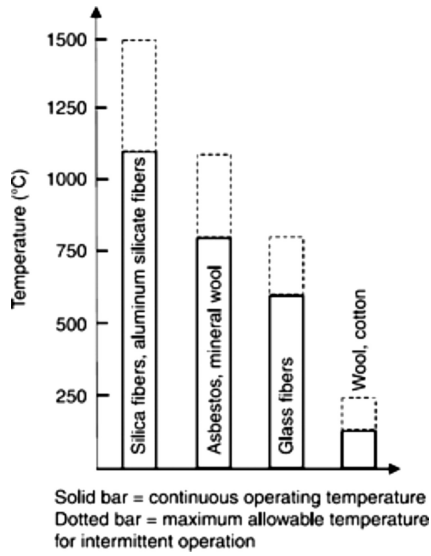

FIGURE 16.17 High-temperature insulating material operating characteristics.

depending on the wire gage used, i.e., on the internal power loss in the wire. The conductor grade, which has a high electrical conductivity (close to copper) and at the same time retains the necessary mechanical strength at 600°C, is suitable for the SP-100 boom cable application. This precipitation-hardenable alloy has high mechanical strength, resistance to softening at elevated temperatures, a high flex life, and freedom from embrittlement. The boom cable is required to be flexible for ease of deployment. Such flexibility is achieved by making the cable from numerous thin strands (10–20 mils in diameter). However, the thinner the strands, the quicker they melt, should the temperature approach the melting point even for a brief period (such as under a laser beam attack). The threats and the resulting overtemperatures determine the final conductor strand size. In the absence of a specific threat, adopting the industry and military standards appears reasonable, which call for 133 strands of 11 mil diameter in AWG No. 8 wire and 133 strands of 14 mil diameter in No. 6 wire. From the high-temperature insulation candidates shown in Figure 16.17, glass ceramic or asbestos fibers are potential candidates, although Nextel of 3M or Phosroc would surpass the requirement.

REFERENCES

1. Binz, E. and Hartung, J., Solar dynamic power for a space station, in *Proceedings of the 21st Intersociety Energy Conversion Engineering Conference*, pp. 2072–2076.
2. Patel, M.R., *High Frequency Power Distribution System*, NASA Report No. CR-175071, 1986.
3. Bouquet, F.L. and Winslow, J.W., *Radiation Data Definitions and Compilation for Equipment Qualification Data Bank*, NASA Tech Briefs, January 1987.

4. Allen, D.M., Multi megawatt space powers technology program, in *Proceedings of the 36th Intersociety Energy Conversion Engineering Conference*, ASME, 2001, Vol. I, pp. 243–249.
5. Gamota, G., One two three - zero resistance in defense applications, *IEEE Transactions on Magnetics*, MAG-17, 19–30, January 1981.
6. Patel, M.R., Nathenson, R.D., and Ahmed, M.E., Designing pancake coils of large 300 MW superconducting generator for electromagnetic and thermal loads, *IEEE Transactions on Power Apparatus*, PAS-102, 2710–2716, August 1983.

FURTHER READINGS

Barthelemy, R.R., Messie, L.D., and Borger, W., Military space power system technology for the 21st century, in *Proceedings of the Intersociety Energy Conversion Engineering Conference*, 1986, Vol. Ill, pp. 1401–1410.

Beik, O., Patel, M.R. and Talebzadeh, S., Large spacecraft electric propulsion using multiphase generator, in *2023 IEEE Aerospace Conference*, Big Sky, MT, USA, pp. 1–8, 2023.

Brandhorst, H.W. and Best, S.R., Effects of hypervelocity impacts on solar cell modules at high voltage, in *Proceedings of the 36th Intersociety Energy Conversion Engineering Conference*, ASME, 2001, Vol. I, pp. 353–358.

Gallagher, T.J., and Pearmain, A.J., *High Voltage Measurement, Testing and Design*, John Wiley and Sons, New York, 1984.

Lai, S.T., *Spacecraft Charging*, American Institute of Aeronautics and Astronautics, Reston, 2011.

Merryman, S.A., Bandy, A.J., and Gordon, L.B., The breakdown characteristics of an outgassing dominated vacuum region, in *Proceedings of the Intersociety Energy Conversion Engineering Conference*, 1987, Vol. Ill, pp. 763–765.

MIL-STD-1399, *Submarines 155 Vdc power distribution (100 kW range), interface standards for shipboard systems*.

Patel, M.R., Dynamics of high power rotating machines on space platforms, in *Proceedings of the 25th Intersociety Energy Conversion Engineering Conference*, AIAA, 1990, Paper No. 990-X.

Patel, M.R., *Spacecraft Power Systems*, 1st Edition, Chapter 22 High-power High-Voltage Systems, CRC Press, Boca Raton, FL, 2004.

SAE STD-1031, Aircraft 270 V dc power distribution bus, electrical power, HV dc, aircraft, characteristics and utilization of.

17 In-Space Electric Propulsion

17.1 INTRODUCTION

The interest in electric propulsion (EP) systems in aerospace, such as subsonic aircraft and in-space transport of spacecraft, has significantly increased in recent years. The technologies for ground applications, i.e., electric vehicles, are evolving into aerospace applications with recent advancements toward hybrid/electric aircraft and electric vertical takeoff and landing aircraft for cargo or air taxi applications.

For in-space applications, such as orbiting satellites, the propulsion system provides the power for the spacecraft to maintain its orbit and to power ancillary services such as payload, controls, and communications. Sputnik-I was the first man-made satellite that was placed the low earth orbit (LEO) by Russia, while Intelsat-1 was the first US satellite, and Appollo-11 was the first manned spacecraft to land on the moon. Most of the satellites in outer space are in LEO, with an altitude not more than one-third of the Earth's radius. However, the Apollo program's lunar missions from 1968 to 1972 sent mankind beyond LEO. Since then, the space programs have undergone significant growth, with many small and large spacecraft launched into the space. The primary propulsion systems for these spacecraft were nonelectric, with the first EP used for the Russian Zond-2 and US SERT spacecraft in 1964. This chapter discusses EP systems for in-space spacecraft applications.

17.2 IN-SPACE PROPULSION

Spacecraft are not self-driven; they need initial propulsion to be launched into space. Launch vehicles or Carrier Rockets using chemical fuel have been used for this task to carry their attached payloads (Spacecraft and Satellites) from Earth to space. After the payload is launched, it is separated from the launch vehicle. Once the spacecraft is in orbit, a propulsion system is required, which is hereafter referred to as 'in-space' propulsion, to change its trajectory or travel in space.

In communication satellites in geosynchronous Earth orbit, the satellite must maintain the assigned orbit altitude and inclination to keep locked-in with a fixed ground station in all seasons of the Earth. But the orbit slowly degrades due to various drags in space. The in-space propulsion system maintains the satellite in the desired orbit and controls its attitude toward the Earth. In-space propulsion is also needed for orbit transfer and to de-orbit the satellite for disposal at the end of a mission. The propulsion thrust of such satellites has traditionally been produced by chemical fuel carried on board. In geosynchronous satellites, over 90% of the on-board fuel is used for N–S station keeping and the rest for E–W station keeping, attitude control, and orbit transfer. Chemical propulsion typically uses the catalytic monopropellant

DOI: 10.1201/9781003344605-21

hydrazine (N_2H_4) fuel. No oxidizer is needed. Heat or a catalyst decomposes the fuel, and the chemical reaction produces heat and thrust from the exhaust gas. Some satellites use fuel and oxidizer in separate tanks to achieve higher thrust levels. Such bipropellant fuel systems generally use hydrazine and nitrogen tetroxide (N_2O_4). This yields a specific impulse (defined in Section 17.3) around 300 s.

On-board energy sources other than chemical fuel may be used in spacecraft for in-space propulsion, such as solar photovoltaic (PV), RTG, and heat-source-based systems. Some of these sources have been discussed in previous chapters. To select and design such an on-board energy source, criteria such as mission type and duration, low mass, low life-cycle cost, controllability, security, and accessibility of energy, among others, are considered.

Earth-orbiting spacecraft need less energy than the ones planned to escape Earth's gravity. Therefore, they can use a PV battery system as a source of power. An array of PV cells charges the battery during the sunlight, and the load will be powered by batteries during the eclipse. The basic task of PV is to convert the photon energy of sunlight into direct current (dc) power. Although PV energy is a readily available and reliable source in Earth's orbit, it is not scalable for travel deeper into space, where the sun's irradiation is weak. In such spacecraft, RTGs can provide energy for long-duration space missions in relatively low-power applications of several hundreds of watts, regardless of the spacecraft's distance from the sun, spacecraft orientation, or where the eclipse period is much longer than usual, such as in lunar missions. The RTG includes numerous thermoelectric converter cells in series-parallel combination to generate the desired voltage and current. Every thermoelectric converter cell converts the isotope thermal energy into dc electrical energy for the spacecraft. Batteries, either as the primary source of energy or complementary with solar PV or RTG, may also be necessary, with rechargeable batteries being more common in satellites.

Generally, spacecraft with power levels below 10 kW, solar PV, batteries, fuel cells, and RTGs have been used as viable energy sources. For larger spacecraft, such as one that meets the requirements of NASA's Human Mars Exploration program, megawatt-scale propulsion power is required. Figure 17.1 shows a paradigm of spacecraft propulsion power comparing different sources of energy based on mission duration and required power.

Chemical-based propulsion can be scaled for MW-scale spacecraft propulsion in missions with relatively short durations. The PV solar sources may be used for long-duration missions with mid-range power levels. However, the solar PV systems are limited to power levels below 200 kW or perhaps 300 kW. They are not readily scalable and are impractical where the sun's reach is limited. For example, the solar irradiance on Mars is about 590 W/m^2 and much less for farther distances, compared to 1358 W/m^2 in Earth orbits. For missions longer than a few weeks and with a MW power requirement, such as missions to Mars, heat-source-based propulsion is being considered as a viable option.

Figure 17.2 shows a simple schematic of a head-source base EP. The energy produced by the heat source is converted to high-voltage dc for an electric thruster. The conversion from heat to dc power is in three steps: (i) heat to steam, (ii) a steam turbine coupled to an electrical machine to generate ac power, and (iii) power electronics

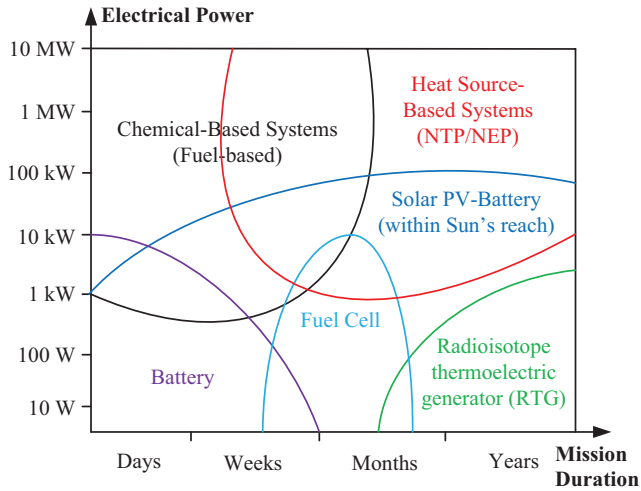

FIGURE 17.1 A viable source of spacecraft electrical power depends on the power level and the mission duration.

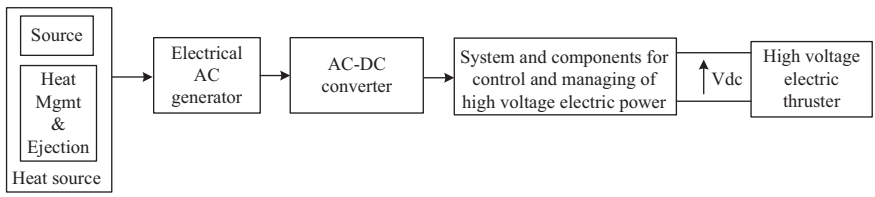

FIGURE 17.2 A simple schematic of heat-based EP.

to convert ac into dc power. EP technologies, i.e., thrusters, require a high-voltage dc power source to generate arcs and plasma that is electrically conductive. The power system control circuit must provide protection against damage to either the thruster or power system components in the event of inevitable arcing between high-voltage elements. The most frequent place for an arc to occur is in the thruster. The high-voltage power source is designed in two ways to provide protection against such arcing. One way is to incorporate an over-current sensing circuit, which turns off the high voltage in the event of an arcing fault. Alternatively, the source can be designed with a high output impedance so that an arc merely results in a deep voltage sag.

One of the special features of EP is that it reaches high propellant exhaust speeds since a vast amount of energy stored could be transferred to the propellant. Although EP produces a low thrust level compared to chemical propulsion, it yields a high specific impulse (going faster with less fuel). This is one of the main advantages of EP compared to chemical propulsion. Other advantages include flexibility and a long operating duration. These have raised interest in EP for space missions to the moon and Mars.

The EP uses about 1/10th of the propellant compared to the conventional chemical propulsion systems commonly used to propel spacecraft into orbit. The EP delivers

propulsion capable of boosting robotic and crewed missions well beyond LEO, sending spacecraft to distant destinations, sending cargo to and from points of interest, and establishing the groundwork for future missions or resupplying those already underway.

17.3 SPECIFIC IMPULSE

The function of the propulsion system is to apply impulse to change the velocity of the spacecraft. When the mass is ejected through nozzles, the reaction propels the spacecraft in the opposite direction. Since the ejected mass must be carried on board at the time of launch, the impulse produced per kilogram of the ejected mass is taken as a figure of merit for the propulsion system. The impulse is defined as the time integral of force. A constant mass flow rate of dm/dt exhausting at an effective velocity V_e through a nozzle creates a steady force $F = (dm/dt)\ V_e$. Such a force applied for Δt seconds results in an impulse $I = F \cdot \Delta t$. The impulse created per kilogram of propellant, called the specific impulse, is then given by

$$I_{sp} = I/\Delta m = F/(dm/dt) \tag{17.1}$$

The specific impulse is also known as the propellant efficiency or the thrust-to-mass flow rate. Its unit is second. The total impulse a fuel of mass Δm can create is then $I_{sp} \cdot \Delta m$. This figure of merit, traditionally used for comparing chemical propulsion systems, is less meaningful for comparing EP systems. It is therefore modified to be the impulse created per kilogram of total additional mass that must be carried on-board for EP. The additional mass is mostly in the power system and, to a lesser extent, in the propellant. Most of the added mass is in the solar array, and some is in the power conditioning equipment. A modified figure of merit for EP is developed below using the following notations:

P_e = additional power needed for EP, watts
M_p = mass to generate additional power for propulsion, kg
P_{sp} = specific power of the power source = P_e/M_p, watts per kg
M_e = mass of the expellant needed on board, kg
M_{sc} = spacecraft mass without additional masses, kg
M_t = total spacecraft mass = $M_{sc} + M_p + M_e$, kg
V_e = expellant exhaust velocity, m/s
T_b = propulsion burn time, seconds

Assuming that the expellant mass flow rate is constant during the propulsion burn time, it is M_e/T_b. We also assume a constant expellant velocity during the burn. Then, energy conservation requires the balance of power, i.e.,

$$P_e = \tfrac{1}{2}(M_e/T_b)V_e^2 \tag{17.2}$$

which, by using classical rocket equations, leads to the following two expressions:

Expellant mass:

$$M_e = \frac{M_t - M_{sc}}{1 + \left(\dfrac{V_e^2}{2T_b P_{sp}} \right)} \tag{17.3}$$

Power system mass:

$$M_p = \frac{M_t - M_{sc}}{1 + \left(\dfrac{2T_b P_{sp}}{V_e^2} \right)} \tag{17.4}$$

Both M_e and M_p rise and then fall with changing parameters. An optimization study is therefore needed to minimize M_e for a given mass ratio of M_{sc}/M_t. The study would also show the power-related mass M_p is lower at higher exhaust velocity up to a certain point, beyond which M_p rises.

For EP, one figure of merit is the impulse per kilogram of total additional mass ($M_e + M_p$), and another is the thrust-to-power ratio (TPR) given by

$$\text{TPR} = \frac{\dfrac{dM_e}{dt} \cdot V_e}{P_e} \tag{17.5}$$

With the specific power achievable with the present power system technologies, a long burn time and low exhaust velocity are inherent characteristics of electric propulsion. Significant power improvements of several folds are needed to make EP viable for lift-off from a planetary surface or orbit raising. However, EP for on-orbit maneuvering and interplanetary missions is practical and is being used at present.

In designing any type of EP, the exhaust velocity must be selected to minimize the total mass added to the power system and the propellant. That would maximize the available payload mass in a given spacecraft with a given launch vehicle capacity. This trade is depicted in Figure 17.3.

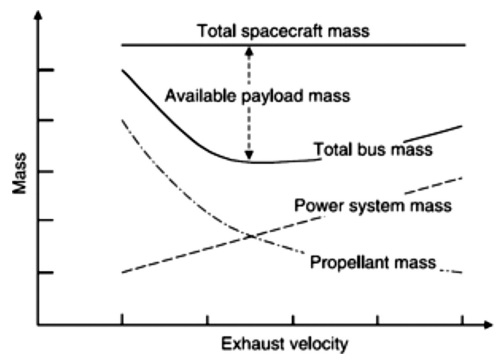

FIGURE 17.3 Payload maximization with electric propulsion.

17.4 TYPES OF EP BASED ON THRUST

17.4.1 Electrothermal Hydrazine Thruster (EHT)

The EHT, also known as Resistojet, is the simplest of all in concept and is depicted in Figure 17.4. A propellant is heated by a tungsten heating element. The energy (enthalpy) of the propellant gas is increased by heating, which is then converted into kinetic energy. The accelerated gas is directed through nozzles and propels the spacecraft. The exhaust velocity is a function of temperature and is generally kept below 10 km/s due to material life considerations. The achievable thrust level is a fraction of a Newton. The propulsion efficiency is around 75%. The propellant can be hydrogen, nitrogen, or ammonia. Hydrogen, which has high specific heat and thermal conductivity, works better than nitrogen or ammonia. However, it is corrosive and requires cryogenic temperatures for storage. Ammonia, on the other hand, is easy to store without refrigeration but is also corrosive, limiting the life of both the heater and the nozzle.

17.4.2 Hydrazine Arcjet (HAJ)

In principle, the HAJ, is similar to the EHT, except that the propellant is heated by its own ohmic heating by passing through arcing electrodes instead of using a separate heating element. Thus, the propellant is directly heated. It uses battery power during noneclipse seasons. The specific impulse is high, in excess of 1500 s, but the excessive electrode wear is life-limiting. A typical geosynchronous Earth orbit communications satellite carries four arcjet thrusters for N–S station keeping maneuvers. Two arcjets are fired at a time for N–S station keeping, one from each battery, 2 weeks before or after an eclipse season. The arcjets are always fired during

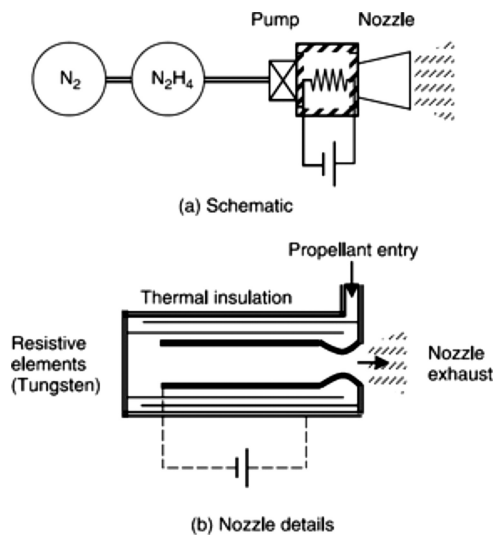

FIGURE 17.4 Electrothermal hydrazine thruster. (a) Schematic. (b) Nozzle details.

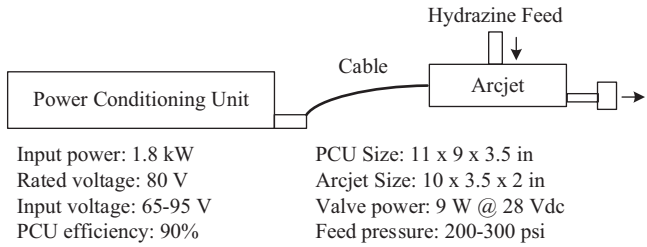

FIGURE 17.5 Hydrazine arcjet thruster typical envelope and electrical performance.

sunlight, nominally at 1200 and 2400 h with respect to local midnight. Each HAJ consumes 1–2 kW of power, depending on the spacecraft's size. The arcjet power circuits are always fused. Since this is usually the heaviest single load on the spacecraft, the arcjet fuse-blow voltage transient is generally the most severe on the bus. The computer simulation of this transient is therefore required for all new designs. The HAJ thruster's typical envelope and electrical performance are shown in Figure 17.5.

17.4.3 Ion Thruster

In the ion propulsion system (IPS), charged particles are accelerated in an electrostatic field. The thrusters are classified according to how charged ions are created from the neutral propellant. In a simple method, the vapor of a material having low ionization potential is ionized by passing through a heated porous tungsten plate. Cesium is often used as vapor material. High heat loss due to thermal radiation in the process limits the overall efficiency.

The schematic of the ion thruster in the *Deepspace-1* spacecraft is depicted in Figure 17.6. In this scheme, electrons emitted from a thermionic cathode pass through concentric cylindrical anodes. An externally applied weak magnetic field sets the electrons in spiral motion. The collision between these accelerated electrons and the propellant ionizes the propellant. An inert gas, such as argon or xenon, is used as the propellant. Thrust levels more than 1 N are possible in large units.

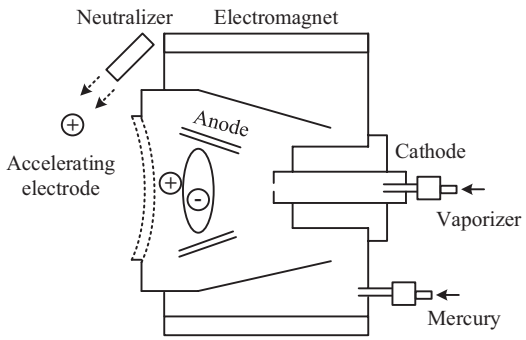

FIGURE 17.6 Ion thruster used in a *Deepspace-1* spacecraft.

Good mass savings are achieved using such propulsion for the N–S station keeping in geosynchronous satellites. A typical chemical thruster emits particles at 3 km/s. A typical ion thruster emits ions at 30 km/s and needs only 10% propellant. The ion propulsion thus saves launch costs significantly.

In the working principle, a strong electrostatic field is created between two plates held at a high voltage, generally several kilovolts. A charged particle injected into the E-field is accelerated along the electric field lines with a force equal to qE, where q is the particle charge and E is the electric field intensity. Under this force, negatively charged particles move along the rising field, while positively charged particles move along the falling field. If the expellant mass M_e having a total charge of Q is exhausted at velocity V_e through the electric potential difference of U volts (not to be confused with velocity V), the energy balance (in joules) gives

$$\tfrac{1}{2} M_e V_e^2 = QU \tag{17.6}$$

The propulsion power (in watts) required to create the propulsion thrust F then follows the balance of power, i.e.,

$$P_e = \tfrac{1}{2} F V_e \tag{17.7}$$

The above two equations lead to the propulsion thrust-to-electric power ratio.

$$\frac{F}{P_e} = \sqrt{\frac{2M_e}{QU}} \tag{17.8}$$

The thrust-to-power ratio, a figure of merit, is maximized by using a propellant with a large mass-to-charge ratio (M_e/Q). Argon, xenon, and cesium fall into this category.

The gridded (conventional) ion thruster has a high exhaust velocity. The preferred version in this family is the xenon ion propulsion system (XIPS), developed and tested at NASA/JPL. The unique feature of the gridded ion thruster is the separation of the ionization process from the accelerated beam by a series of electrostatic grids. Neutral xenon is fed into the ionization chamber, where a low-voltage discharge is struck. A high ionization efficiency is achieved by hindering the electrons from reaching the anode with a peripheral magnetic field. Ions are extracted from the plasma, accelerated, and focused into tight beamlets by the grid system. The negative accelerating grid prevents the transmission of electrons in either direction. Electron-rich plasma is emitted from the neutralizer downstream of the grids, thus neutralizing the space charge of the ion beam.

The gridded xenon ion thruster differs significantly from the Hall thruster discussed later. XIPS has by far the highest exhaust velocity of all the EP devices, but it also has a low thrust per unit power and a longer trip time. The ion flow through the grid is limited by space-charge buildup, and the thrust density is low. On the positive side, the exhaust beam is very well focused. A larger model of XIPS is being used in a four-thruster system designed to do both N–S station keeping and a significant amount of orbit raising on large commercial satellites. Boeing's BSS-702 and BSS-601HP buses are such examples. The mass savings could be up to three times as

great as those associated with NSSK alone. For low- and mid-Earth orbits, the entire orbit-raising and de-orbit functions could be performed by an IPS.

NASA's *Deepspace-1* interplanetary probe uses a gridded ion propulsion system using PV power. It produces thrust with a specific impulse (propellant efficiency) about ten times greater than a typical chemical propulsion system used during interplanetary missions. It uses a hollow cathode to produce electrons that ionize xenon gas through collisions, yielding positively charged atoms of xenon. The xenon ions are then electrostatically accelerated by a potential of more than 1000 V and emitted from a 30 cm thruster nozzle through an electrically charged grid. The power available to the IPS during the *Deepspace-1* mission came from solar arrays. The ion propulsion degrades the solar array in one way. It generates ions that are discharged into space at high velocity. A large number of low-energy electrons are also emitted to prevent the satellite from building up a negative ion, slowing down the charge. A few nonionized atoms drift out of the thruster and get ionized in collision with ions in the high-velocity stream, forming plasma. Through the drifted plasma, the low-energy electrons can flow as leakage current, draining power from the solar array.

Past, Present, and Future Ion Propulsion: NASA Glenn Research Center has been developing IPSs since the late 1950s. The first ion-base propulsion was the Space Electric Rocket Test 1 that flew in 1964. From 1998 to 2001, the NASA Solar Technology Application Readiness IPS enabled the *Deep Space 1* mission, the first spacecraft propelled primarily by ion propulsion.

The ion thrusters are currently being used in geosynchronous Earth orbit communication satellites. Three NASA Solar Technology Application Readiness ion thrusters based on the technology developed by NASA Glen Research Centre enabled the Dawn spacecraft (launched in 2007) to travel deep into the solar system.

Compared to other propulsion types, the EP enables the spacecraft to extend the operational life of satellites and reduce launch and operation costs. NASA currently leads two ion thruster developments: (i) NASA Evolutionary Xenon Thruster (NEXT) and (ii) Annular Engine.

NEXT is a high-power IPS that operates at three times the NASA Solar Technology Application Readiness power level and was developed to reduce the mission cost and travel time. It was tested for the equivalent of almost 6 years on Earth without failure. This demonstrated the operability of thrusters for a range of missions. The NEXT technology continues its development for higher power and thrust-to-power ratios so that it can be used for a broad range of commercial, scientific, and defense applications. Figure 17.7 shows NEXT in a spacecraft and identifies its main components. The process starts by releasing a neutral atom, followed by an electron release. The electron and neutral atom collide in the presence of a magnetic field in the chamber, and ionization takes place. The positive ion that is released as a result of the collision is accelerated through the electrodes, and the electron is released from the neutralizer to complete the process. This process is repeated in the NEXT that provides the thrust for moving the spacecraft.

The Annular Engine, also developed by NASA Glen Research Centre, is targeted to exceed the performance of the ion and other EP thrusters by yielding a total annular beam area of two times that of NEXT. The goals of new thrusters are

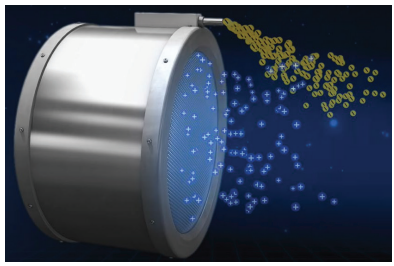

(a) Ion thruster.

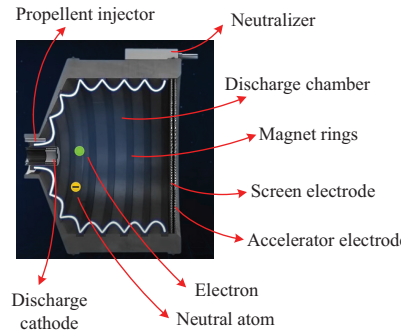

(b) Ion thruster main components.

FIGURE 17.7 NASA's nuclear electric xenon ion thruster. (a) Ion thruster. (b) Ion thruster main components. (NASA.)

to reduce system cost and complexity and enhance performance (higher thrust-to-power capability).

17.4.4 Stationary Plasma/Hall-Effect Thruster

The stationary plasma thruster (SPT), also known as the Hall-effect thruster, falls into the mid-range of the exhaust velocity spectrum. Plasma (an ionized gas that is electrically conductive) is made by stripping atoms of their electrons, confining the resulting products, and preventing them from recombining. Usually, this means heating an appropriate gas mixture to a temperature at which collisions break up the atoms and then keeping the resulting product in equilibrium for as long as needed. Forcing a large electric current through a gas mixture can create plasma. The SPT was originally developed in the former Soviet Union but has recently been improved and tested extensively by a Russian, French, and American consortium. The SPT is essentially an electrostatic ion thruster without grids. An axial electrostatic field and a radial magnetic field are established in the annular flow chamber. An equilibrium discharge is set up when electron-rich plasma is fed from the cathode while neutral xenon atoms are emitted through the anode. Some of the electrons are trapped in the crossed electrostatic–magnetic field and form a virtual negative electrode, which accelerates the ions. They ionize the xenon propellant by electron impact in the discharge region and also neutralize the space charge of the accelerated ion beam. The magnetic field produces a small azimuthal torque on the ions, which does not change the thrust.

SPTs with improved performance are in various stages of development in the 3–5 kW power range. A high-power model SPT-100 has been used for N–S and E–W station keeping operations on many satellites by Russia and is being used by Astrium, the French–German–British satellite builder, on *Inmarsat* and *Intelsat* communications satellites. It gives off about 16 km/s and generates about 80 mN of thrust using 1.5 kW of input power. This is a good combination of a thrust-to-power ratio of about 50 mN/kW and a fairly high specific impulse. Its main advantage over the gridded

ion thruster is the high thrust density, which is possible with gridless acceleration. The thrust output to power input ratio for the SPT is in the 50–70 mN/kW range. Its drawback is a wide beam angle due to not having focusing grids. This may interfere with nearby spacecraft components. However, various other alternatives for narrowing the exhaust plume are being developed.

A 12.5 kW Hall thruster that uses magnetic shielding was tested in 2015 and demonstrated continuous operations for years, which is important for deep space exploration. Since then, it has been used in space where applicable.

17.4.5 Magneto-Hydrodynamic/Electro-Hydrodynamic

The magneto-hydrodynamic (MHD) propulsion—also known as the electro-hydrodynamic —uses plasma. Neutral plasma is accelerated under both the ohmic heating and the electrodynamic force generated by the interaction of the electric field $\boldsymbol{E}$ and the magnetic field $\boldsymbol{B}$. The thrust that propels the spacecraft in MHD comes from the Lorentz force $F = \sigma \boldsymbol{E} \times \boldsymbol{B}$, where $\sigma =$ electric conductivity of the plasma. The force is perpendicular to both the $\boldsymbol{E}$ and $\boldsymbol{B}$ fields. The accelerating force is imparted to neutral particles in the gas by collision with ions, thus providing a direct and efficient increase in the propellant velocity that propels the vehicle. The electric conductivity of the plasma-mixed exhaust is an important performance factor. It varies directly with the temperature and inversely with the pressure. Its value of 0.10 Ωm is considered adequate for acceptable performance in the MHD accelerator. Since the self-induced magnetic field accelerates ions, the thrust is proportional to the current squared. The overall efficiency ranges from 10% in the kilowatt range to 40% in the megawatt range. A pulse mode of operation is essential for high-power ion thruster. Significant development in this area has been under way in Japan. A thrust power of a few newtons with a specific impulse of 2000 s is achievable. Cathode erosion is a major life-limiting factor.

A constant E-field applied to plasma is not of interest here, as it adjusts itself by developing a thin sheet of space charge, which shields the main body of plasma from the E-field (as in a conductor body). On the other hand, a constant B-field causes a Lorentz force on the charged particle in plasma. The force is given by $F = Q(\boldsymbol{E} + V \times \boldsymbol{B})$, which is always perpendicular to the velocity, V, of the particle. It causes the charged particle to gyrate about the field lines without altering the internal space-charge neutrality of the plasma. This force provides acceleration, keeping the kinetic energy constant, as the Lorentz force can do no work.

In MHD propulsion, a trace of conducting fluid such as potassium or cesium is added to the chemical rocket engine exhaust to ionize it. The thermal plasma in the exhaust is propelled by a strong magnetic field created by superconducting electromagnets. MHD accelerators have been built in the USA and Russia, although not much work is currently under way.

17.4.6 Pulsed Plasma Thruster

The pulsed plasma thruster was successfully tested for the first time on NASA's *Earth Observing Spacecraft* managed by Goddard Space Flight Center. Millisecond pulses

of electricity fired across solid bars of Teflon turn portions of the Teflon into an electrically charged gas that is forced out of the nozzle to generate thrust. Tests showed that the system was about three times more efficient than conventional chemical thrusters. This first test also eased concerns that the system would produce electromagnetic interference that could affect other systems on the spacecraft.

17.5 PERFORMANCE COMPARISON

EHT and HAJ are both electrothermal hydrazine-based thrusters in which a monopropellant is fed through a conventional thrust chamber and nozzle, usually via a preliminary catalytic decomposition chamber. The increase in exhaust velocity is derived from the electrical power added to the thrust chamber. The propellant exhaust velocity of these two devices is relatively low.

In EHT, the electric power is added using a resistance element, which is the hottest component in the system. The maximum power that can be added to the propellant is restricted by the melting point of the resistance element. This, in turn, limits the rise in exhaust velocity to 2–3 km/s, which is competitive with storable bipropellants giving 3 km/s. The EHT has been used for NSSK on many satellites and to raise small satellites from the parking orbit to the final orbit.

In HAJ, the electric power is added directly to the propellant in the form of a coaxial arc. The temperature in the arc region is several tens of thousands of kelvin, but most of the propellant near the walls is much cooler. The HAJ has been used for NSSK on many large commercial satellites since the early 1990s. It produces an average exhaust velocity of 5–6 km/s, about twice that of storable bipropellant, and a thrust of about 200 mN using an input power of just under 2 kW. Its thrust-to-power ratio of about 100 enables relatively fast maneuvers. However, its low exhaust velocity limits the mass benefit relative to chemical propulsion. HAJ lends itself well to spacecraft that already use hydrazine as a chemical propellant. HAJ used for NSSK in many large commercial communication satellites gives an I_{sp} of about 500 s, compared to 200 s in traditional monopropellant thrusters and 300 s in bipropellant and EHT thrusters. This reduces the propellant mass required for stationkeeping.

A gridless electrostatic ion thruster, such as the Russian SPT, has been used on short-duration missions with a specific impulse approaching 2000 s. The gridded ion thruster can achieve a specific impulse in the 3000–4000 s range.

The specific impulses of major types of propulsion systems are compared in Table 17.1, and the power-to-thrust ratio versus exhaust velocity is plotted in Figure 17.8. As for the voltage requirement, the HAJ generally works at present bus voltages, the SPT thruster works around 300 V, and the IPS works at voltages exceeding 1000 V.

The HAJ, SPT, and XIPS each have their own inherent advantages and disadvantages. The development continues in order to incorporate these systems in full orbital raising. When achieved, it would significantly change the design of Earth-orbiting satellites.

TABLE 17.1
Specific Impulse of Various Propulsion Systems

Propulsion Class	Specific Impulse
Chemical (liquid and solid)	200–400 s
Electrothermal hydrazine thruster (EHT)	300–400 s
Hydrazine arcjet thruster (HAJ)	500–1500 s
Pulsed plasma thruster (PPT)	1000–4000 s
Ion propulsion system (IPS)	2000–8000 s

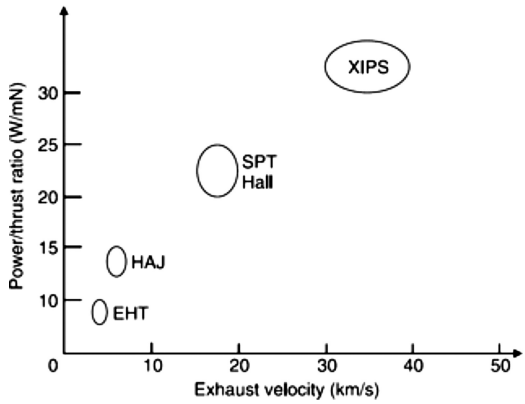

FIGURE 17.8 Power-to-thrust ratio versus exhaust velocity.

17.6 EP BASED ON SOLAR PV

The thrusters in the EP system usually require high electric voltage and power in the MW range in high-power missions. One approach to supplying this is to use solar PV panels. Figure 17.9 shows a spacecraft that uses NEXT ion thruster and PV solar as the energy source. Solar electric propulsion is applicable to a wide range of NASA missions, such as human Mars exploration and robotic exploration of the outer planets. For human Mars exploration, Kerslake and Gefert[1] have developed a 1 MW class conceptual design using various PV technologies (Figure 17.10). The time required to travel to Mars, as estimated by a NASA GRC using a xenon Hall thruster, is about 230 days.[2] The Kerslake study summarized in Table 17.2 shows that using the present $CuInS_2$ thin-film PV technology, it is feasible to design a 1 MW power system with a mass under 10 metric tons and a deployed solar array of 5800 m^2. The EPS in this study consists of a 500 V dc distribution system with 16 channels feeding eight 100 kW_e thrusters. Since thrusters do not operate during eclipses, the battery requirement is modest—about 13 kWh for housekeeping and payloads. The 500 V dc permits *direct-drive* thrusters' operation, which greatly reduces the mass of both

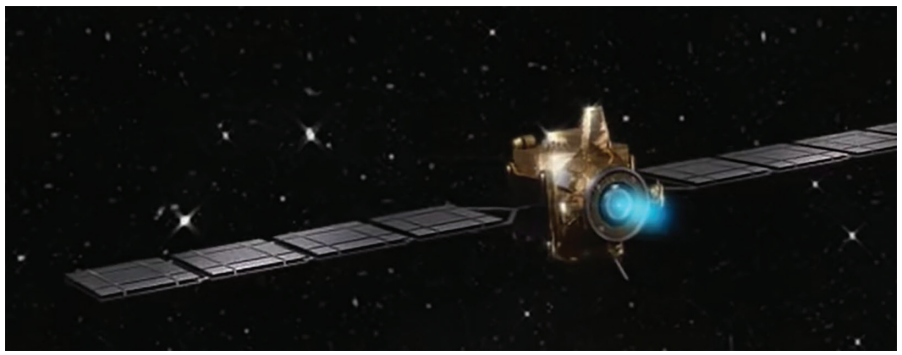

FIGURE 17.9 Spacecraft with solar electric propulsion. (NASA)

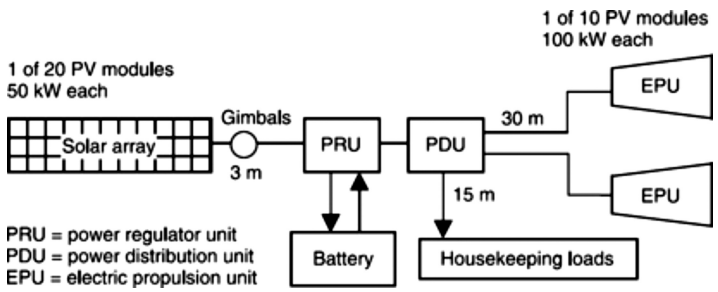

FIGURE 17.10 Power system block diagram for 1 MW class electric propulsion.

TABLE 17.2
One-Megawatt Class Solar Electric Propulsion System for Mars Exploration

Parameter	ISS cr-Si	Linear Concen.	a-SiGe Thin Film	$CuInS_2$ Thin Film
BOL power	1270 kW	950 kW	1150 kW	1050 kW
EPS Mass	46 MT	21 MT	12 MT	10 MT
PV array	14,000 m^2	3500 m^2	9000 m^2	5800 m^2
Cells/string	1450	270	340	880
Strings	990	910	9500	2370
Fluence MeV/cm^2				
for current	1.0×10^{16}	2.2×10^{14}	5.9×10^{14}	5.9×10^{14}
for voltage	2.6×10^{16}	3.7×10^{14}	1.3×10^{15}	1.3×10^{14}
Maximum leakage	260 A	1 A	0	0

MT, metric ton (1000 kg).

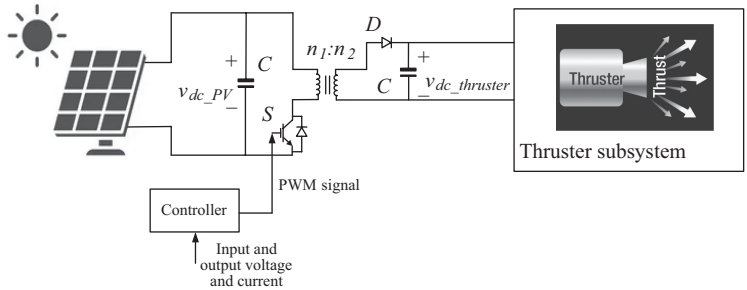

FIGURE 17.11 Solar powered based EP with propulsion power conditioning circuit and controls.

the harness and the power-processing unit, thus increasing the system efficiency. Copper wires with Teflon insulation are used. NASA data on the space plasma effect at ±500 V dc operating voltage were used to estimate the parasitic leakage current.

The solar PV array for the solar electric propulsion project needs to be able to provide power at a high voltage. The PV panels will need to be flexible, radiation-resistant, and stowed into a small, lightweight, and cost-effective envelope. To achieve the high voltages required for the thruster, the output of the PV panels needs to be stepped up with an isolated dc–dc converter with a high step-up ratio, as shown in Figure 17.11. The transformer provides galvanic isolation and the required high step-up ratio. A controller input is the solar PV voltage, and the output voltage has a control scheme that regulates the output voltage for maximum power point tracking operation. The capacitors are used as filters to reduce the voltage ripple and smooth out the average output voltage. The thruster subsystem has several components, including a propellant management system (PMS) that controls the propellant flow from the respective tank to the thruster. An alternative approach shown in Figure 17.11 uses a high-voltage solar PV array. However, this would make the PV panel large, heavier, and more difficult to assemble compared to using a dc–dc converter.

17.7 EP BASED ON NUCLEAR POWER

Most traditional spacecraft rely on chemical rockets to reach an orbit and on solar panels to generate power for on-board equipment. But solar panels have limited capabilities, especially when the spacecraft is far from the sun. The usual approach for spacecraft has been to accelerate for 5–10 min and then stop and coast along. That is an ineffective way of exploring deep space. Although some probes have left our solar system, it takes a very long time to get there. For making space travel faster, different propulsion technologies, such as nuclear-powered systems, are required.

Nuclear energy is one of the most power-dense energy sources known to humans to date. Nuclear propulsion offers a viable technological option for extending the reach of exploration missions beyond Mars, where solar panels can no longer provide sufficient energy and chemical propulsion would require a high mass of propellant that would not be feasible.

NASA is considering two types of nuclear propulsion systems for MW-scale space applications: (i) nuclear thermal propulsion (NTP) and (ii) nuclear electric propulsion (NEP).

17.7.1 Nuclear Thermal Propulsion

NTP is not a new concept. Compared to chemical propulsion, they provide higher thrust with more efficiency and significantly reduced travel time while allowing a greater payload. This enables deep space missions, reduces the travel time to Mars, and limits the flight crew's exposure to cosmic radiation. NTPs can also allow broader launch windows that are not dependent on orbital alignments and allow astronauts to abort missions and return to Earth if necessary.

NTP is not designed to produce thrust to launch the spacecraft off the Earth. Rather, NTP is used for in-space propulsion. Therefore, the spacecraft will be launched into space by chemical rockets before the NTP system is turned on. NTP works by passing a liquid propellant, such as hydrogen, through a reactor core. Uranium atoms split apart inside the core and released heat through fission. This process heats up the propellant and converts it to a gas, which expands through a nozzle to provide thrust and propel a spacecraft. Figure 17.12 shows an NTP system.

The NTP system is more energy dense and twice as efficient as chemical rockets when measured by specific impulses in units of seconds. The specific impulse is the amount of thrust created by a specific amount of propellant. The specific impulse of a chemical rocket that combusts liquid hydrogen and liquid oxygen is about 450 s, whereas the propellant efficiency of nuclear-powered rockets is around 900 s.

NTP uses lighter gases that are easier to accelerate. A chemical rocket, when it is burned, produces water vapor, a much heavier byproduct than the hydrogen that is used in an NTP system. This leads to greater efficiency and allows the rocket to travel farther on less fuel.

17.7.2 Nuclear Electric Propulsion

In NEP, the heat generated from the reactor is used to create electrical power in a power conversion unit that will provide the voltage and current for an electric

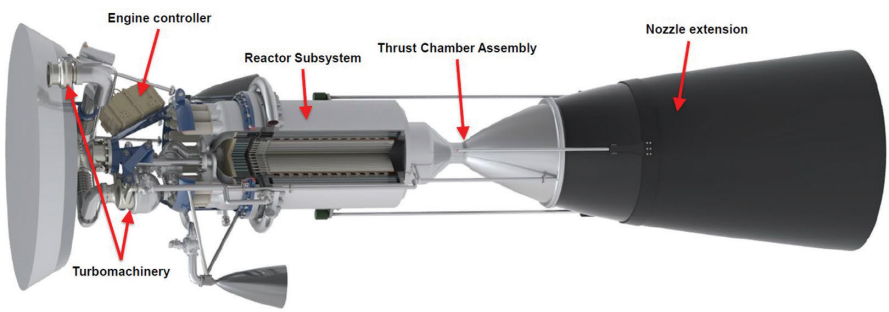

FIGURE 17.12 Schematic of a nuclear thermal propulsion. (NASA)

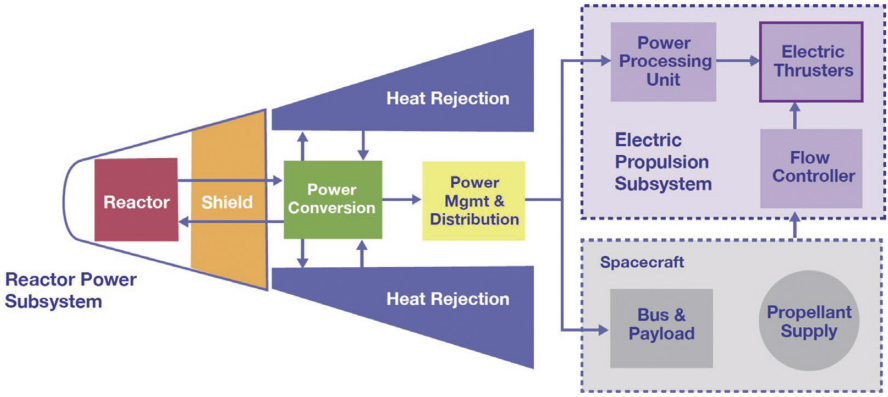

FIGURE 17.13 Schematic of a nuclear electric propulsion.

thruster. Figure 17.13 shows a schematic of a NEP system, which includes the following main components:

- A reactor unit and shield
- A power conversion unit (converting heat to electrical power)
- Heat rejection system that can safely reject and dispose of the heat
- Power management and distribution unit
- EP subsystem that includes an electric thruster and a power-processing unit that controls the power to the thruster.

In Figure 17.13, the spacecraft bus payload and electrical thruster are both fed from the electrical power generated from the EP system. In the event that the EP fails, the payload and electrical loads are shut down until the fault is diagnosed and removed. In the meantime, it is necessary to maintain the safe and continued operation of minimally critical components such as communication devices, monitoring, and control systems, and also provide a safe 'landing' scenario. To do this, backup batteries and a PV solar array may be used, as shown in Figure 17.14. The design shown therein has the following features:

- The output of the power conversion unit in NEP is connected to a common dc bus via a dc–dc converter. The converter controls a fixed dc bus voltage and accounts for any voltage fluctuations at the output of the power conversion unit. It also steps up the voltage as necessary.
- The PV solar array and the battery pack are connected to the common dc bus via their individual dc–dc converters. The main dc bus in this scheme is a high-voltage bus. The solar array is likely rated at low voltages due to mass and practicality considerations. Therefore, the dc–dc converter for the PV solar panel steps up its voltage while extracting the maximum power from the sun using maximum power point tracking. The battery is likely rated for low voltages for the same reason. Therefore, the dc–dc converter for the

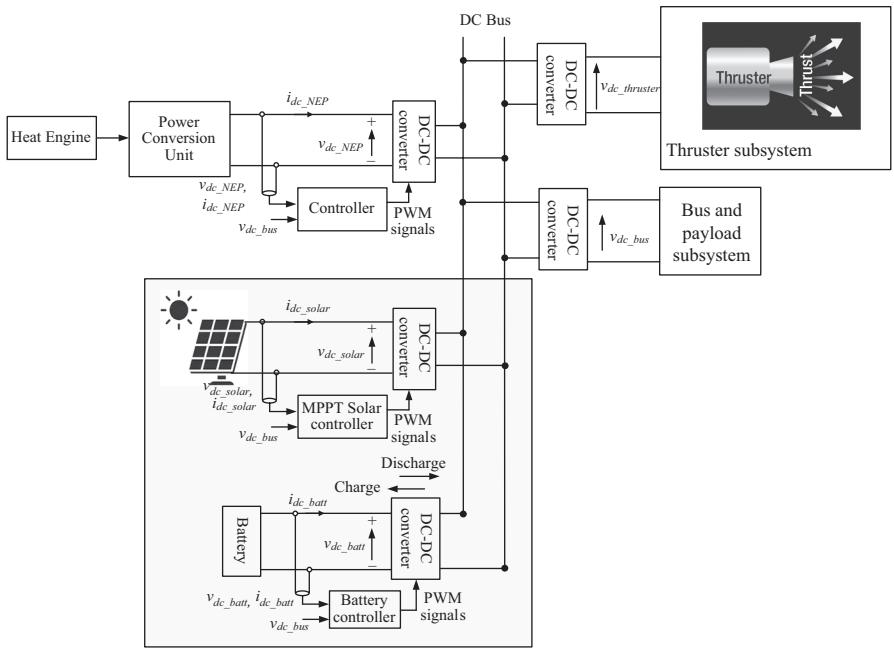

FIGURE 17.14 Nuclear electric propulsion with solar PV and a battery as backup.

battery steps up the voltage before connection to the dc bus. It also controls the charge/discharge of the battery based on the power demand of the load and the status of the solar array and NEP.

- The voltage for the thruster and the spacecraft payload is taken from the dc bus using separate dc–dc converters. Having separate converters enhances the reliability of the system. Hence, if there is a fault in the payload, the propulsion system and the thruster are protected. Additionally, it is common to use a low-voltage dc (<200 V) for the payload to stay consistent with the existing components developed for space applications. The dc–dc converter for the payload therefore steps the bus voltage down to the required voltage for the payload. The electric thruster for MW-scale spacecraft uses high-voltage dc (e.g., 20 kV). Therefore, the dc–dc converter for the thruster steps-up the dc bus voltage to match the thruster input voltage.
- The payload will likely have several dc–dc, dc–ac and other power electronics converters depending on the electrical loads of the payload, the type of mission, and other requirements. These converters will all feed from the low-voltage dc that is provided from the dc–dc converter for the load.
- For isolation purposes and to achieve high step-up/step-down voltage ratios, the dc–dc converters can use a topology with a medium-to-high frequency transformer. These topologies were introduced in the chapter on power electronics systems.

The power conversion unit in the NEP is one of the key elements. The greater the efficiency and power density of the power conversion unit, the higher the thrust that can be generated at a given mass. The power conversion unit may be:

- A static unit such as a thermoelectric generator (TEG), or
- A dynamic unit such as rotating electric machines and related power electronics.

A TEG is a solid-state device with no moving parts that converts heat from temperature differences into electrical output. However, TEG's output voltage is low-voltage dc at low current. To generate a high voltage at high power suitable for MW-scale spacecraft, a large number of TEGs need to be placed in series and parallel. With numerous interconnects, the system becomes bulky with typically low efficiency, posing a design challenge for MW-scale applications.

Figure 17.15 shows a concept probe using NEP and advanced TEG as the propulsion systems. This concept probe, referred to as the Swarm-Probe Enabling advanced TEG Reactor, or SPEAR, is a nuclear electric propulsion spacecraft that uses a lightweight reactor moderator and advanced TEGs to reduce overall core mass. This may subsequently require a reduction in operating temperatures and reduce the total power levels achievable by the core. However, the reduced mass will require reduced power for propulsion, resulting in a small, inexpensive nuclear electric spacecraft.

The TEG output voltage and current need to be controlled to extract the maximum available power from the TEG. An isolated dc–dc converter is used to control the power and voltage using a closed-loop control scheme using the PWM technique. Figure 17.14 is an example of such a scheme. A dynamic power conversion unit uses a rotating electric machine. In this case, the heat generated from the reactor is used to spin a turbine, which in turn rotates an electric generator. This is schematically

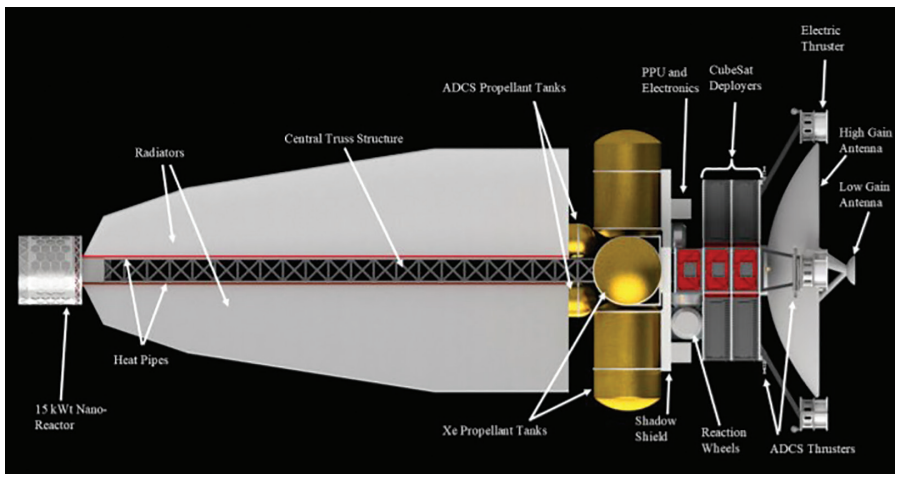

FIGURE 17.15 A concept nuclear electric propulsion using advanced thermoelectric generator. (NASA)

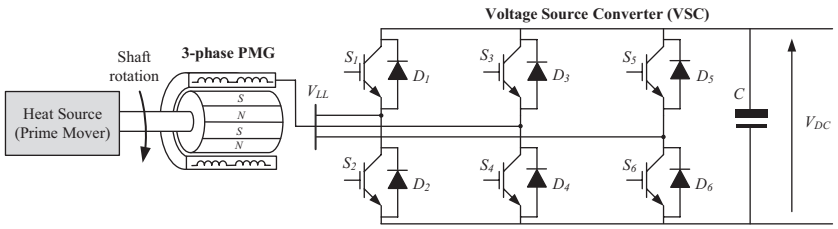

FIGURE 17.16 A nuclear electric propulsion using permanent magnet generator.

shown in Figure 17.16. In this NEP scheme, the heat source is a turbine, which is the prime mover that turns an electrical generator. The generator may be a 3-phase wound-field synchronous generator or a 3-phase permanent magnet generator.

In both synchronous generator and PWM, the stator has one set of 3-phase windings for output. In the case of synchronous generator, the rotor has a dc winding where a dc current is injected using brushes, slip rings, or a brushless exciter. For the PWM, the rotor has permanent magnets to produce the magnetic field. Compared to other machines, PMW has a higher efficiency and a lower specific volume. The 3-phase output of the generator in Figure 17.16 is rectified using an active power electronics converter, referred to as a voltage source converter. The voltage source converter output dc voltage is then connected to the dc bus of the spacecraft, providing power for the propulsion and payload.

Conventionally, large rotating machines have not been used on spacecraft because they can pose pointing accuracy issues. The steady-state torque on the spacecraft platform with a large generator does not affect the pointing accuracy. However, the transient torque during a fault (e.g., short circuit on the output terminals of the generator) is of a pulsating nature and constitutes a dynamic disturbance on the platform. Such a torque is the product of the alternating short-circuit current and the magnetic flux in the air gap. The spacecraft's momentum and vibrations are also important integration issues in any system using large rotating machines. One approach to minimizing the torque disturbance is by using such machines in pairs of counter-rotating units to cancel each other's torsion effects. However, there always remains a net torque on the platform, as two counter-rotating machines in a pair cannot be located exactly at the same place. However, in modern NEP systems, the platform's dynamic control and the pointing system will account for the net effect of all the rotating machines (generators, turbines, and pumps) on the platform, which depends on their exact placement. The net effect of all such machines is platform-specific and will vary from one platform to another.

Figure 17.17 shows a generator with a dual rotor concept for NEP that allows for dynamic control of the generator using a secondary rotor. This scheme has the following features:

- This NEP has two main components, a high-voltage, 9-phase rotating electric generator and a stationary, integrated 9-leg passive rectifier. The 9-phase generator converts mechanical power on its shaft to high-voltage alternating current (ac) at its output. The multiphase winding for the generator results

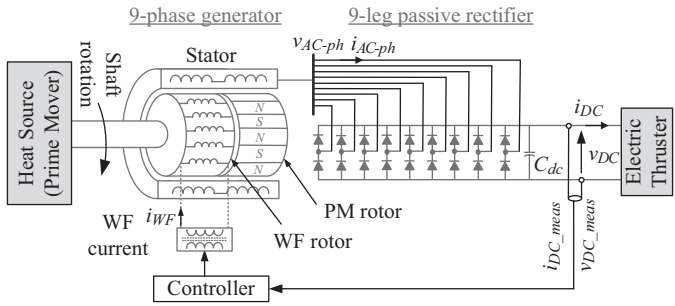

FIGURE 17.17 A nuclear electric propulsion with dual rotor generator and passive rectifier.

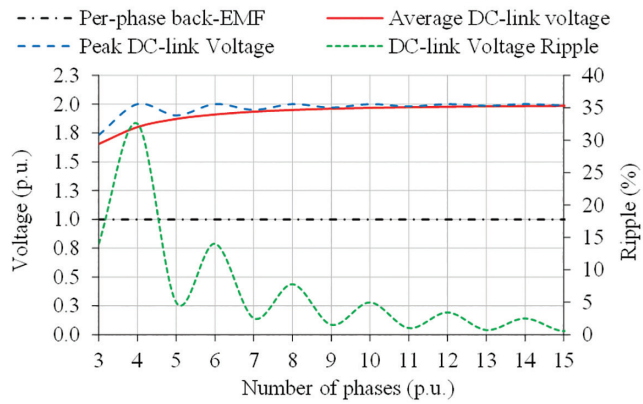

FIGURE 17.18 Relation between dc voltage and number of phases.

in enhanced power density, efficiency, reliability (inverse measure of failure rates for the components), fault tolerance (operability during faults), and security of power conversion (accessibility and availability of output power per lifetime of EP). Additionally, the multiphase winding results in higher rectified average dc voltage and lower dc ripple compared to conventional 3-phase generators. Figure 17.18 depicts the relationship between the number of phases of a generator and its rectified dc voltage. Compared to a conventional 3-phase generator, the 9-phase winding results in a 19% higher average dc voltage while resulting in a 12% lower dc voltage ripple. Note that beyond 15-phase, the average dc-link voltage does not increase; therefore, designs with greater than 15-phase are not worth considering. The phase numbers that are multiples of 2 (4-, 6-, 8-, 10-, 12-, and 14-phase) result in higher ripple and lower average dc-link voltage compared to their next consecutive odd phase number; therefore, even numbers of phases are not useful.

The generator has two rotors: (i) a PM rotor and (ii) a wound-field (WF) rotor. Both rotors are coupled on the same shaft, rotate at the same speed, and share the same

9-phase stator. The PM rotor has a fixed magnetic flux, which induces a fixed stator voltage at each rotor speed. The WF with controllable rotor current has a variable flux. Therefore, the WF-induced voltage is controlled by a current injected into the WF rotor (i_{WF}). The generator's output voltage is a vector sum of induced voltages due to PM and WF rotors; therefore, it is controlled by the WF current (i_{WF}) over a desired prescribed region. The output of the passive rectifier (v_{DC} and i_{DC}) is linearly related to the generator's output; therefore, a closed-loop feedback control system is designed to control the WF current and hence the voltage/current at the output of the rectifier.

- This NEP can be suitable for MW-scale propulsion (1–5 MW), a power level estimated for a large spacecraft for a human Mars exploration mission. The generator is a direct-drive machine that eliminates the gearbox.
- The proposed 9-phase generator and rectifier topology eliminates the need for active power electronics converters for control as the dual rotor topology enables full control using the WF current. Figure 17.19 shows the failure rate of components in power electronics converters, compiled from a report by the Department of Defense (DoD) and an industrial survey. Solid-state switches and their gate drivers contribute to 51% of converter failures. These are replaced with passive diodes in the proposed scheme; therefore, the reliability of the system is significantly enhanced.
- The 9-phase design improves power density and/or efficiency, reliability, and fault tolerance, therefore increasing the accessibility of energy over the lifetime of the NEP system. Fault tolerance is an inherent benefit of 9-phase systems, as each phase carries a smaller portion (one-third) of the current compared to a 3-phase system. The 9-phase winding results in a higher per-phase voltage for the generator (because of an improved winding factor), therefore further reducing the per-phase current and improving power density and/or efficiency. Moreover, a higher per-phase voltage results in an increased average dc voltage of 19% and reduces dc ripple by 12%, reducing

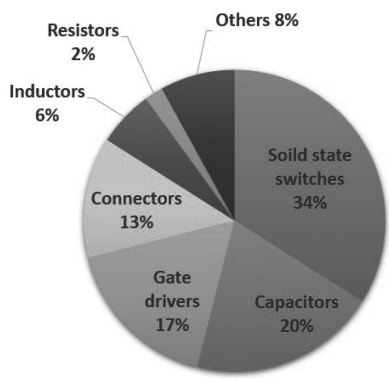

FIGURE 17.19 Failure rates of electrical components in power electronics converters.

the capacitive filtering requirements. This will result in enhanced reliability of the system, as capacitors typically contribute to 20% of power electronics failures.

- The representative mission for this NEP is the 'Opposition Class: Short-Stay Mission' for the human exploration of Mars, with an expected launch date of 2037. The design path for this mission is shown in Figure 17.20. The mission at present is planned to start in August 2037 and last around 650 days. The scheduled arrival on Mars is April 2028, and the crew will stay on Mars for 30 days. The outbound flight to Mars takes 217 days, and the return flight to Earth takes 403 days. The mission has separate cargo and crewed vehicles with assembly orbits in LEO or cislunar space. The study shows that for this mission, only a heat source-based propulsion with a high-voltage output and a minimum of 1 MW power is applicable. Therefore, this NEP scheme may be a viable option to explore for this mission. Figure 17.21 shows the top-level architecture of the proposed concept in a spacecraft. Through a common bus, the NEP provides power to an electric thruster as well as the payload and communications. Backup batteries and PV solar are used for control and communication systems during emergencies.

All space systems must safely survive the worst possible scenario—a rocket blowing up on the pad. To aid safety, the nuclear hardware on board the spacecraft would be launched in a *cold*, nonoperating state. The reactor would be switched on when the vehicle reaches 2500 km from Earth, a distance in accordance with NASA's orbital debris guidelines for preventing hazardous materials from ending up in orbits near the Earth.

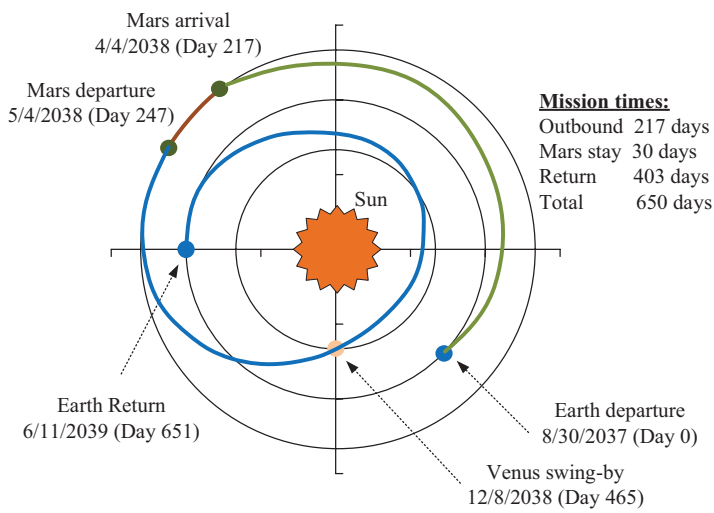

FIGURE 17.20 Opposition Class: Short-Stay Mission on Mars.

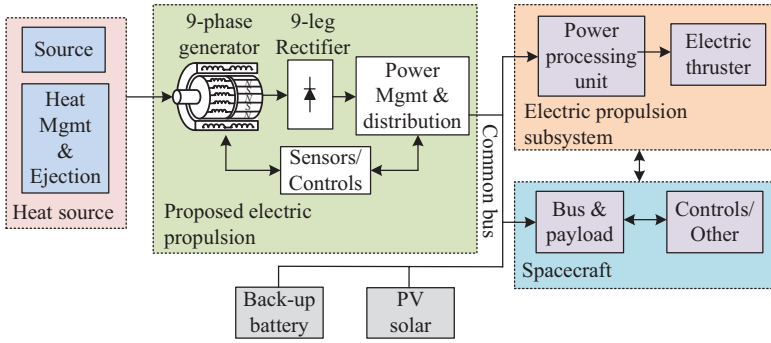

FIGURE 17.21 Top-level architecture of the nuclear electric propulsion concept with dual rotor generators in spacecraft.

17.8 MICROWAVE BEAM PROPULSION

Electric power is traditionally generated on board the spacecraft. An alternative approach is to generate a large amount of power on another satellite and transmit it by microwave beam eliminating the mass of the power generation system on the user spacecraft.

A study by Lindberry and Chapman focused on using an MHD accelerator powered by a microwave beam to augment the specific thrust of a chemical rocket engine from 450 s to 2500–4000 s with a corresponding thrust of about 300–400 N and an acceleration of 0.002–0.02 m/s^2. No other all-electric or all-chemical propulsion can achieve such performance alone, but it would require a strong magnetic field. Superconducting magnet technology is well established and is commercially used in numerous ground-based applications for generating strong magnetic fields in the 10–20 T range. The old liquid helium-based superconductors (<10 K) are being replaced by newer high-temperature superconductors (around 100 K). Room-temperature superconducting technology is on the horizon and is assumed to be available in the NASA study of this concept. The major design challenges would be a magnet coil with a current density of 1000 A/mm^2, corresponding electrode erosion, and a mechanical force containment structure. The thermal management of the equipment that handles such high currents is also a challenge.

It is estimated that the MHD accelerator would have an efficiency in the 80%–90% range and only a couple of percent of the system mass. The remaining 98% mass would be primarily in the receiving rectenna. A low-mass rectenna is therefore a critical technology for deploying this concept.

The frequency considered for such a system is from 3 to 300 GHz, with the corresponding wavelengths from 0.10 to 0.001 m. Brandhorst,[2] in a previously cited study, considered two power beaming options, microwave and laser beams. Because of on-orbit aperture limitations, the microwave option was dismissed. For the laser option, 10.6 μm and 1.06 μm wavelengths were considered. The energy conversion system for a 10.6 μm laser was either a thermal engine or a thermo-PV. For the 1.06 μm laser, suitable energy conversion would be direct bandgap PV cells giving excellent

conversion efficiency around 50%. Electrothermal propulsion using microwave power is another possible concept that has been studied.

17.9 TETHER POWER PROPULSION

Space tethers are being developed for a wide range of applications, such as electrodynamic propulsion, momentum transfer, formation flying satellites, remote sensing, and space structures. It is a distinctly different propulsion system. It is electrodynamic in principle and uses a long conducting wire moving in the Earth's magnetic field to generate electrical power for propulsion. The power delivered by the tether eventually comes from the incremental decay of the orbit. NASA has experimented with this concept a few times in space. If further development proves to be successful, it can transfer satellites from one orbit to another and even power missions to the outer planets with a suitable source of primary power, nuclear or solar.

In its working principle, electrons floating in space are made to flow in a long conductor from the spacecraft. This constitutes an electric current. A conductor carrying current I moving in a magnetic field of density $\boldsymbol{B}$ generates mechanical force per unit length equal to $I \times \boldsymbol{B}$ in the direction that is perpendicular to both $\boldsymbol{B}$ and I. This force, known as the Lorentz force, works as a motoring force that can raise or lower the payload orbit depending on the current flowing toward or away from the Earth.

The tether can also be used for power generation. Experimental and theoretical work using very large high-voltage structures in a simulated LEO plasma has shown that substantial currents may couple between such structures and the surrounding ionospheric plasma. A long-tethered satellite system (TSS) would behave as a power generator if the induced $V \times \boldsymbol{B}$ voltage in a long conducting tether moving in the Earth's magnetic field was allowed to drive a negative current through an on-board load, providing electrical power at the expense of orbital energy. NASA's tether power generation concept utilizes such electrodynamic characteristics of a conducting tether in the Earth's orbit to generate useful electric power for a number of applications. It has several advantages over conventional power sources. It is 2.5–3 times as efficient as fuel cells in terms of fuel utilization and is not subject to day/night cycles as are solar arrays. The magnitude of the power generated depends on the tether length. As an example, it has been estimated that a current of 5 A through a 100 km tether can produce upwards of 80 kW of power. Accounting for drag and other losses, the system could operate at a net efficiency of 75%.

The concept has been around since the 1960s. In 1993, NASA's Plasma Motor Generator Mission used a tether equipped with a hollow cathode end mass to collect electrons. In 1996, NASA flew another 20 km long, 2.5 mm diameter conducting tether between the space shuttle *Orbiter* and a 500 kg satellite with scientific instruments provided by the Italian Space Agency. This TSS generated over 2 kW of power and 1 A of current. While not a complete success, it provided valuable data for future research and development on this unique concept of bleeding energy from space charges.

The most critical requirement for the tether power system is the availability of tether materials with the required strength, conductivity, insulation, and protection from adverse effects of the space environment, such as radiation. Even with

the availability of such materials, a number of design issues need to be studied in the near term to gain a clear understanding of the technologies necessary for power generation. These issues include advances in high-voltage technology and power-processing equipment. In addition, there are basic questions about phenomenology and design that must be investigated. They are:

- The plasma–electrodynamic interactions affecting return current losses
- High-voltage electronic components and insulation materials
- Hollow cathode current emission technology
- dc tether impedance controller technology
- Passive tether control techniques

The primary focus of the tether research is plasma interactions for power generation. It should also consider plasma interactions related to the system's use as a source of thrust and as an extremely low-frequency antenna system. The concept of the TSS as a generator or motor envisions the ejection of charge from one end of the system and the collection of a compensating current at the other end. The effect of the magnetic field on charged particle collection is considered and shown to be substantial. Specific calculations of charged particle collection would utilize computer codes for geometrically complex objects and well-developed analytical theories of spherical probes, both for the case of unmagnetized plasmas. Without the aid of plasma contactors or large-area collectors, quiescent plasma theory indicates that the effect of the magnetic field would limit the usable power developed in an initial electrodynamic tether mission to about 1 kW. Since the plasma may be turbulent, however, this estimate may be pessimistic. In any case, uncertainties in present knowledge clearly point to a need for a better understanding of probes in magnetized plasmas, including plasmas that are strongly perturbed by the passage of electron beams.

The working of the tether is described as follows:

1. The conducting tether attached to a space object moving in the Earth's magnetic field generates voltage across the wire given by $e = BLV$.
2. Space electrons are attracted to the positively biased far end of the tether.
3. The electrons flowing downward through the tether constitute a current.
4. The current-carrying tether moving in the Earth's magnetic field exerts a drag force given by $F = BIL$, causing the de-orbiting of the space object.
5. A hollow cathode at the near end of the tether emits electrons back into space, completing the electric circuit.

The force will be reversed if a reverse current is applied by a higher voltage than that self-generated in the tether, such as from a solar array. In this case, the orbit of the space object attached to the tether would rise.

The tether forms a unique type of electric circuit, which NASA demonstrated in space with the Plasma Motor Generator in 1993 and the TSS in 1992 and 1996. These missions deployed long, conducting tethers from orbiting spacecraft and generated kilowatts of power. The tether is dragged through the ionospheric plasma, through

which the spacecraft and the tether are traveling at a speed of 7–8 km/s. In so doing, a few kilometers of aluminum wire extracts electrons from the plasma at the end farthest from the payload and carries them to the near end. A specially designed device, known as a hollow cathode emitter, expels the electrons to ensure their return to space. Currents in the plasma complete the circuit.

Ordinarily, a uniform magnetic field acting on a current-carrying loop of wire yields a net force of zero since the force on one side of the loop is canceled by that on the other side, where the current is flowing in the opposite direction. However, since the tethered system is not mechanically attached to the plasma, the magnetic forces on the plasma currents in space do not cancel the forces on the tether, and so the tether experiences a net force.

As the tether cuts across the magnetic field, its bias voltage is positive at the end farthest from the Earth and negative at the near end. This polarization is due to the action of the Lorentz force on the electrons in the tether. Thus, the *natural* upward current flow is due to the (negatively charged) electrons in the ionosphere being attracted to the tether's far end and then returned to the plasma at the near end, aided by the hollow cathode emitter (steps 3–5 above). The hollow cathode is vital. Without it, the wire's charge distribution would quickly reach equilibrium, and no current would flow. The Earth's magnetic field exerts a drag force on the current-carrying tether, decelerating it and the payload and rapidly lowering their orbit. Eventually, they re-enter the Earth's atmosphere (de-orbit).

A key advantage of the electrodynamic tether is that it does not need the spacecraft's on-board power to quickly de-orbit the spacecraft. If the tether were being used to raise rather than lower the orbit, the current would have to be forced in the other direction. The addition of a small PV power source is then necessary. Some of the near-term applications of tether propulsion systems are as follows.

17.9.1 Space Debris Cleanup

Over the past few decades, the space around Earth has become cluttered with debris, which could take years, and in some cases, a century, to fall from orbit. The danger is that old satellites, rocket stages, and trash thrown overboard by early spacecraft could collide with present-day satellites, space shuttles, and space stations. The International Space Station, for example, has to maneuver several times a year to avoid hitting debris, burning up precious fuel each time. NASA and ESA have recommended that national governments require future spacecraft to be self-removed the orbit at the end of their life spans. To do that, a satellite must be loaded with extra propellant, which could add as much as 25% of the satellite's weight. Using a tether to de-orbit would be inherently more mass efficient and reliable. A tether is much lighter and more compact than conventional thrusters and can account for as little as 2% of a satellite's total weight. It has no complex valves, plumbing, or circuitry that must stay operational and leak-free for years. At the end of a satellite's useful life, the tether would unreel, and tether-driven orbital decay would begin. A satellite's orbit, which would otherwise take years to decay naturally, could be deorbited in a few days using a tether.

17.9.2 Orbit Transfer Vehicle

The electrodynamic tether can be attached to an unmanned orbit transfer vehicle (space tugboat) that would carry satellites to different orbits. After being launched into low Earth orbit, the tug would grapple the satellite and maneuver it to a new altitude or inclination. The tug could then lower or raise its own orbit to rendezvous with another satellite and repeat the process. Conceivably, several such orbital reassignments could be performed with high fuel efficiency, making the tug relatively inexpensive to operate. Because plasma density diminishes rapidly with distance from the Earth, the tug could only operate below 2500 km. The lowest usable altitude would be about 250 km, below which the atmosphere would begin to exert too much aerodynamic drag.

17.9.3 Keeping the Space Station Afloat

A structure like the International Space Station is estimated to require 0.5–1.5 tons of propulsion fuel replenished from the Earth for every year of operation. This is to overcome the atmospheric drag, which would cause its altitude to drop by several kilometers per week. The ISS, with an electrodynamic tether, could drastically cut its dependency on fuel. Atmospheric drag exerts a force of up to 1N on the station. NASA has designed a 10 km long, 0.6 mm × 10 mm aluminum ribbon tether capable of delivering 0.5–0.8 N of thrust with less than 10 kW of solar array power needed to reverse the direction of the current in the tether to maintain the orbit. More research is needed before such a tether can be actually deployed on a space station like the ISS. For example, if a micrometeoroid or orbital debris accidentally severs the tether, a mechanism is needed to keep it from recoiling around the station and damaging key components.

17.9.4 Exploring the Outer Planets

Electrodynamic tether technology may be used to propel and power spacecraft exploring the outer planets. Jupiter has an environment particularly favorable to the electrodynamic tether. It has a strong magnetic field, and its mass dictates high orbital velocities. Present Jupiter missions rely on RTGs, but the power available is typically less than 300 W. In theory, the tether could power the craft's instruments and generate thrust at the same time. For a circular orbit close to the planet, tether propulsive forces have been calculated to be as high as 50 N and power levels as high as 1 MW. This level of power can enable high-power instruments and radar. But it also means resolving the high-power conversion, energy dissipation, and tether overheating problems.

REFERENCES

1. Kerslake, T.W. and Gefert, L.P., Solar power system analysis for electric propulsion missions, in *Proceedings of the 34th Intersociety Energy Conversion Engineering Conference*, SAE, 1999, Paper No. 2449.
2. Brandhorst, H.W., Power without wires, a solar electric propulsion concept for space exploration, *IEEE Aerospace and Electronic System*, 16(2), 3–7, February 2001.

FURTHER READINGS

Bailey, S.G., Hepp, A.F., and Raffaelle, R.P. Thin film photovoltaic for space applications, in *Proceedings of the 36th Intersociety Energy Conversion Engineering Conference*, ASME, 2001, Paper No. AT-36.

Beik, O., Patel, M.R. and Talebzadeh, S., Large spacecraft electric propulsion using multiphase generator, in *2023 IEEE Aerospace Conference*, Big Sky, MT, USA, pp. 1–8, 2023.

Cosmo, M.L. and Lorenzini, E.G., *Tethers in Space Handbook*, NASA Handbook, Springfield, VA, December 1997.

Johnson, L., The tether solution, *IEEE Spectrum*, 37(7), 38–43, July 2000.

Laug, K.K. and Holmes, M.R., Paraboloidal thin film inflatable concentrators and their use for power applications, in *Proceedings of the 34th Intersociety Energy Conversion Engineering Conference*, SAE, 1999, Paper No. 2552.

Lineberry, J.T. and Chapman, J.N., MHD Augmentation of rocket engines for space propulsion, in *Proceedings of the 35th Intersociety Energy Conversion Engineering Conference*, AIAA, 2000, Paper No. 3056.

Mohan, N., Undeland, T., and Robbins, W.P., *Power Electronics Converters, Applications and Design*, IEEE and John Wiley & Sons, Hoboken, NJ, 1995.

Patel, M.R., *Spacecraft Power Systems*, 1st Edition, Chapter 26 Superconductors in Space, CRC Press, Boca Raton, FL, 2004.

Patel, M.R., *Spacecraft Power Systems*, 1st Edition, Chapter 27 Microwave Beam Power Satellite, CRC Press, Boca Raton, FL, 2004.

Power, J.L., Microwave electrothermal propulsion for space, *IEEE Transactions on Propulsion in Space*, 40(6), 1179–1191, June 1992.

18 Fuel Cell Power

18.1 INTRODUCTION

The fuel cell converts the chemical energy of a fuel such as hydrogen to dc electricity. Fuel cells may use different fuels and can be used in applications ranging from a few watts for local use to MW-scale power for grid usage. The fuel cell has been used as a power source for space applications. It was first used in a moon buggy and then routinely used to power NASA's fleet of space shuttles (Orbiter) that carried components and crew to the International Space Station and other space service missions.[1] Unlike a battery, the fuel cell does not run out of energy and does not need to be recharged. It keeps producing electricity as long as the fuel is supplied. One can call the fuel cell 'the gas battery.' A typical fuel gas is hydrogen or a hydrogen-rich mixture with an oxidant.

Fuel cells find applications in space missions lasting for a few days to a few weeks where a battery is not practical. It also has a potential use as an auxiliary power source for orbital transfer vehicles. The regenerative fuel cell (RFC) integrated with an electrolyzer unit presents an attractive mass savings for low Earth orbit (LEO) satellites requiring large energy storage. It was a serious candidate to replace the battery in the original version of the International Space Station. The workings of a fuel cell are the reverse of the electrolysis of water. In electrolysis, electricity is passed between two electrodes in water to produce hydrogen and oxygen. In the fuel cell, hydrogen and oxygen are combined to produce electricity and water. The energy conversion is direct from chemical to electrical. Since the process is isothermal, the conversion efficiency is not limited by the Carnot efficiency. This is unlike many chemical-to-thermal-to-mechanical-to-electrical energy converters using steam or internal combustion engines. It skips the usual combustion step of conventional power systems and converts a high percentage of the fuel's available free chemical energy directly into electricity. Its efficiency, therefore, can be about twice that of the thermodynamic converter. It is as high as 65% in some designs and 75%–80% in solid metal oxide fuel cells developed for ground-based power plants. Its superior reliability and lack of noise from moving parts are additional benefits over thermodynamic power generators.

18.2 ELECTROCHEMISTRY OF A FUEL CELL

A fuel cell consists of anode and cathode electrodes separated by a liquid or solid electrolyte. The electrodes are electrically connected through an external load circuit, as shown in Figure 18.1. Hydrogen or a hydrogen-rich mixture is fed to the anode. The hydrogen fuel is combined with the oxygen of the oxidant entering from the cathode port. The hydrogen, however, does not burn as in the internal combustion engine. It splits into hydrogen ions (H^+) and electrons (e^-), and produces electricity

 DOI: 10.1201/9781003344605-22

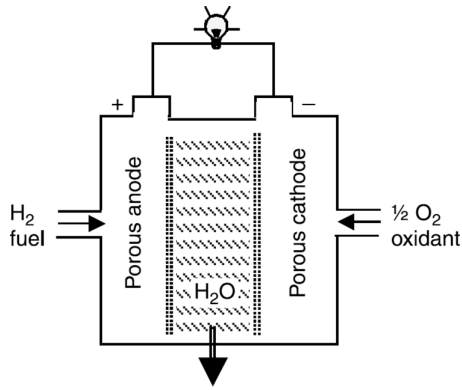

FIGURE 18.1 Fuel cell construction.

by an electrochemical reaction. Water and heat are the byproducts of this reaction if the fuel is pure hydrogen. With natural gas, ethanol, or methanol as the source of hydrogen, as in some ground-based fuel cells, the byproducts include carbon dioxide, traces of carbon monoxide, hydrocarbons, and nitrogen oxides, all of which are negligible.

The hydrogen–oxygen fuel cell consumes hydrogen as fuel, oxygen as an oxidant, and an aqueous acid solution as an electrolyte. Their net reaction is $2H_2 + O_2 = 2H_2O$, and, of course, energy is released in the process. In one type of fuel cell, the electrons flow from the anode and travel through the external circuit to the cathode, powering the electrical load en route. Hydrogen ions migrate through the electrolyte to the cathode, closing the loop. At the cathode, they combine with the oxygen and the incoming electrons from the external circuit to produce water. The kind of ions and the direction in which they migrate vary depending on the type of electrolyte.

The major components and their functions in the fuel cell are:

- The anode (fuel electrode) provides a common interface for the fuel and electrolyte, catalyzes the fuel oxidation reaction, and conducts electrons from the reaction site to the external circuit.
- The cathode (oxygen electrode) provides a common interface for the oxygen and the electrolyte, catalyzes the oxygen reduction reaction, and conducts electrons from the external circuit.
- The electrolyte transports one of the ionic species involved in the fuel and oxygen electrode reactions while preventing the conduction of electrons to avoid a short circuit.
- Other components may also be necessary to seal the cell, provide for gas compartments, and separate one cell from the next in a fuel cell stack.

The fuel cell is thus a static electrochemical device that generates electricity by using a chemical reaction without altering the electrodes or the electrolyte materials. This distinguishes the fuel cell from the electrochemical battery. Unlike a conventional battery, the fuel cell has no electrical energy storage capacity. Hence, it

must continuously supply the reactant and withdraw the reaction products during operation.

18.3 ELECTRICAL PERFORMANCE

The fuel cell basically works as a voltage source with an internal resistance. The electrical potential appears at the terminals of two electrodes involved in the process. The theoretical value of the fuel cell potential is 1.25 V, which matches that of the NiCd and NiH_2 batteries. Multiple fuel cells stack up in series–parallel combinations using heavy graphite pallets for the required voltage and current, just as the electrochemical cells do in the battery. However, as soon as the current is drawn, the voltage drops significantly due to various losses. Because the primary loss mechanism is ohmic loss in the electrodes, the voltage continues to drop with increasing current. The voltage drop is given by

$$V_{\text{drop}} = \alpha + \beta \log_e J \tag{18.1}$$

where J is the current density at the electrode surface, and α and β are constants that depend on temperature and the electrode surface. The theoretical potential difference of 1.25 V between the anode and cathode in the hydrogen–oxygen fuel cell is determined by the difference between the free energy of the reaction product and the fuel and oxidant. This potential is different in different fuel cells, depending on the reactions involved. The electrical performance of a fuel cell is represented by the electrode voltage versus surface current density, commonly known as the polarization curve or the *V–I* curve, as shown in Figure 18.2.

Ideally, a single H_2–O_2 fuel cell could produce 1.25 V dc under ambient conditions. Undesirable ions and products of the intermediate irreversible reactions decrease the cell potential, even at open circuit. Further voltage drops under load result from various irreversible polarizations in the cell, such as:

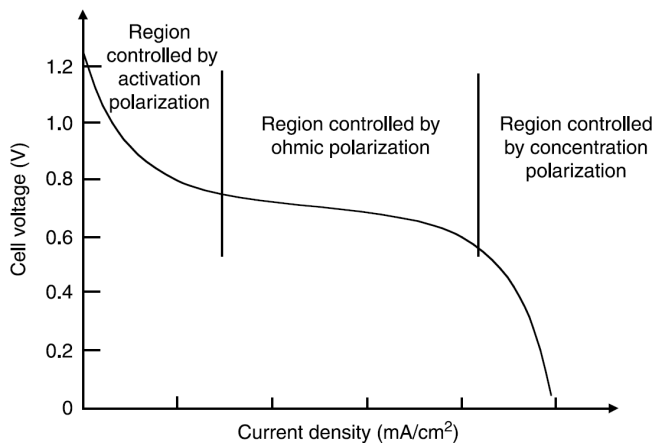

FIGURE 18.2 Fuel cell polarization curve—voltage versus current.

- Resistance polarization, i.e., the electrical resistance of the electrolyte and electrodes
- Concentration polarization, i.e., the accumulation of ions and reaction products and the depletion of consumed ions and reactants in the electrolyte near the electrode surfaces
- Activation polarization, i.e., the reluctance of the fuel and oxidant to undergo reaction at each electrode
- Activation polarization causes energy losses associated with reactions
- All ohmic losses within the cell, i.e., electrodes, current collectors, contacts, and the ionic impedance of the electrolyte
- Concentration polarization causes the energy losses associated with mass transport

The net result of these polarizations is that the practical fuel cell produces between 0.5 and 1.0 V dc at currents of 100–400 mA/cm^2 of cell area. Fuel cell performance can increase by increasing cell temperature and reactant partial pressure. A trade-off exists between achieving higher performance by operating at a higher temperature or pressure and confronting the materials and hardware problems imposed by more severe conditions.

The practical operating range of the fuel cell is controlled by ohmic loss. The *V–I* characteristic in this region is very similar to that of the battery, except that the average discharge voltage is lower. The voltage drops approximately linearly with increasing current and also with time, as shown in Figure 18.3.[2] At any given time, the terminal *V–I* relationship can be expressed as

$$V = V_o - kI \tag{18.2}$$

where V_o = open-circuit voltage and k = constant. The value of k increases and that of V_o decreases with time. The power at any operating point is given by

$$P = VI = (V_o - kI)(V_o - V)/k \tag{18.3}$$

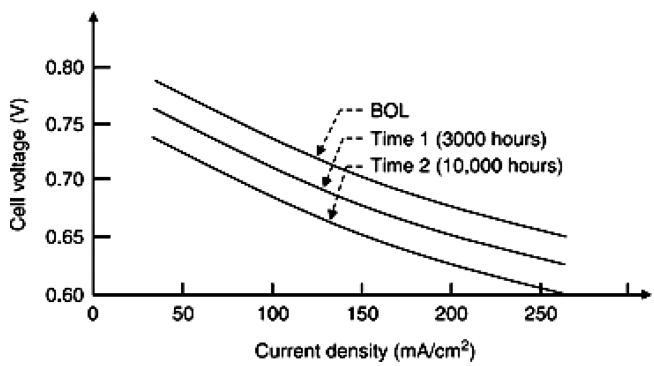

FIGURE 18.3 Fuel cell operating characteristics degrade with time.

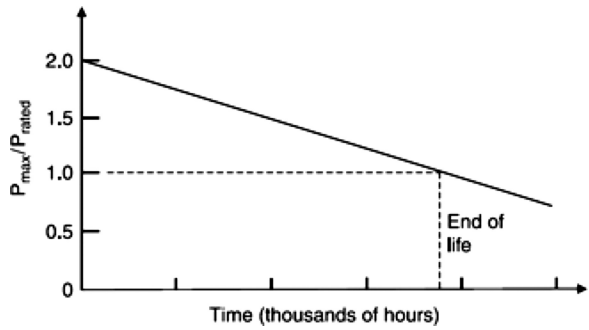

FIGURE 18.4 P_{max}/P_{rated} ratio versus time determines life.

The maximum power is when $dP/dI = 0$, which occurs at $V = ½V_o$, leading to

$$P_{max} = \frac{1}{4} V_0^2 / k \tag{18.4}$$

Unlike the PV cell, the fuel cell does not work in the *use the input energy or lose it* mode. It uses the on-board fuel to generate power. For this reason, the fuel cell is not operated at P_{max} until it approaches the end of its life. It is rather operated at maximum fuel efficiency until the EOL.

Since V_o degrades with time, so does P_{max}. The open-circuit voltage can be expressed as a function of time as

$$V_o(t) = V_o(0) - K_o h \tag{18.5}$$

where h = number of hours since the fuel cell has been in operation. With a voltage-regulating converter between the fuel cell and the load, the life of the fuel cell can be defined as the time it takes for the voltage to decay below the required input voltage, or the P_{max} to fall below the required output power. It can be predicted from the V_o versus time relation. The expected life of the fuel cell is determined as shown in Figure 18.4.[2]

The transient electrical performance model of the fuel cell includes electrochemical, thermal, and mass flow elements that affect the electrical output.[3] Of primary interest is the electrical response of the cell to a load change. To design for the worst-case scenario, the performance is calculated under both constant reactant flow and constant inlet temperature.

18.4 TYPES OF FUEL CELLS

A fuel cell is classified by the types of fuel and electrode materials used in its construction. The space-qualified fuel cell of the future is likely to take advantage of recent advances in commercial fuel cells using extensive ground experience in advanced technologies. The various types available at present are described below.

Solid polymer electrolyte was used in the early manned missions lasting less than a week. Since then, two parallel fuel cell technologies have been developed:

proton exchange membrane (PEM) for *Gemini* and alkaline for *Apollo* missions to the moon. An improved aqueous alkaline technology was also selected for NASA's space shuttle fleet. A lightweight alkaline fuel cell stack has been recently developed by United Technologies for NASA. It is designed to use propellant grade H_2 and O_2 to generate a peak power of 3.5 kW for an average load of 2.2 kW. The specific powers of these units were approximately 110 W/kg for the standard space shuttle fuel cell and approximately 150 W/kg for the lightweight stack.

A high-power shuttle fuel cell stack operating on dedicated cryogenic reactants H_2 and O_2 is designed for a peak power of 12 kW with brief overloads of 15 kW and an average load limited to 4.5 kW for life consideration. The average load has now been increased to 7 kW. The space shuttle does not have batteries. It obtains starting power from the ground before launch and then uses fuel cells after the launch. Each shuttle has three fuel cells generating 30 to 36 V dc power. Some of this power is used in dc form, and some is converted to 400 Hz ac for aircraft-type equipment used in the shuttle. It has 118 kg of dry mass. The output power capability of 12–15 kW gives a specific power of around 100–120 W/kg based on the stack and accessories without power conditioning and gas supplies. Although the electrical startup time is 10–20 min and the shutdown is instantaneous, the whole system requires about 2 h of warm-up time before it can be loaded. The design life for the space shuttle power plant is 5000 h at rated power. It is likely that the life of the shuttle power plant could be increased to 20,000 h (along with higher power capability) with the incorporation of advanced technology items.

The alkaline fuel cell used in the space shuttle combines hydrogen and oxygen to generate electricity, with water as a byproduct. Oxygen enters the cell through the sintered-nickel cathode, where a catalyst produces OH ions and delivers them to the cell's potassium hydroxide electrolyte. The ions drift through the alkaline electrolyte to the anode, where they combine with hydrogen atoms to form water molecules and release electrons, and the electrical power is delivered to the external load. The energy released when 1 kg of cryogenic hydrogen combines with 8 kg of oxygen is about 34,000 Wh. That is 3800 Wh/kg of fuel, excluding the fuel tank and the supporting systems. This amounts to an energy conversion efficiency of about 50%. The byproduct water is used by the crew.

The performance of various types of fuel cells for space applications is compared in Table 18.1. Compared to the PV array, the fuel cell gives much higher power per kilogram. Flexibility is another major advantage, as it does not need sun pointing and

TABLE 18.1
Various Fuel Cell Performance Compared

Fuel Cell Technology	Specific Power (W/kg)	Life, in hours
Alkaline	100–150	~50,000
Solid polymer	100–150	~50,000
Alkaline (space shuttle)	300–400	3000–5000
Lightweight cell under development	600–700	Varies

provides the same power during both day and night. Its disadvantage is that it needs to carry fuel on board.

18.5 REGENERATIVE FUEL CELLS

The fuel cells presented above convert energy one way: from fuel to electricity. They are not designed for the reverse recharging operation. Recharging the fuel cell requires an electrolyzer to decompose the water back into hydrogen and oxygen. The electrolyzer is generally a separate unit from the fuel stack, and the two cannot operate simultaneously. The hydrogen–oxygen RFC has been developed for energy storage in short-term space missions, but has not been used in space yet. The RFC was considered for the International Space Station but was dropped in favor of the NiH_2 battery due to its poor round-trip energy efficiency. However, a high-power, long-term manned mission to the moon or Mars may find the RFC practical. It would use solar energy to produce power and independent electrolysis units for hydrogen and oxygen production. This is advantageous not only for energy storage but also for life support and for auxiliary thrusters as well.

The RFC is based on a hydrogen–oxygen PEM fuel cell and electrolyzer technology. The fuel stacks consist of multiple cells, each with a certain active area operated at 60 psi, 80°C, and a nominal 50 A/m^2 current density. Cells are series–parallel connected and include bypass diodes. The electrolyzer stack consists of multiple cells with certain active areas, operated at 315 psi and with a nominal current density of 20 A/m^2. The hydrogen and oxygen reactants are stored in gaseous form at 3000 psi, while water is stored at 14.7 psi. Hydrogen is contained in Kevlar tanks with 10-mil titanium liners to minimize gas diffusion. Similar tanks are used to contain oxygen and water. The fuel's cell operating temperature is maintained by a radiator using water as the working fluid. The electrical energy efficiency for the electrolyzer is 90% and that of the fuel cell is 60%; thus, the overall round-trip efficiency of the systems is about 54%. The life is estimated to be 10,000 h.

The RFC has a good peak power capability, about 10 times the base power. This may be useful for providing power pulses. The primary disadvantage of RFC is the lack of peripheral pumps and plumbing that can handle fluids reliably over a long mission life in geosynchronous Earth orbit (GEO). Providing redundancy in such a system may incur a significant mass penalty. Other than the reliability issue, the fuel cell is a well-developed technology. It may be possible to service the RFC system for a 5-year LEO mission. In LEO, it has a reasonable specific energy of 5–8 Wh/kg and a round-trip energy efficiency of 60%–70%. Because of the lower efficiency compared to the battery, both the solar array charging power and the thermal cooling requirement would be greater. In high-power GEO applications, mass-optimized RFC units may provide 20–35 Wh/kg. The high specific energy is largely due to the need for only a small electrolyzer unit because of the relatively long recharge time available in GEO. The specific energy, however, is sensitive to various thermal and electrical design requirements.

Proton Energy Systems[4] is currently developing 1–100 kW RFC for LEO and GEO applications. The company has tested 25%–35% dc–dc round-trip efficiency. The efficiency is low, but the specific energy and specific power are high compared

to the battery. At stack level, 300–400 Wh/kg and 70–100 W/kg are possible, including 10% for hydrogen storage. This compares with about 200 Wh/kg with the Li-ion battery.

18.6 RFCs FOR SPACE COLONIES

When human exploration of space grows into colonies on the moon and mars, power systems that last for decades will be required. Small nuclear-based power systems can provide long-term, sustainable power for interplanetary missions and for human habitation in space colonies. However, the system issues related to the use of large nuclear power plants needed to provide large amounts of power for life support are yet to be resolved. These issues include the system integration of all functions of the habitat as well as safety concerns. The RFC provides an alternative with significant advantages. It coincidentally furnishes a backup supply of oxygen and water valuable to the inhabitants in the event of emergencies and unforeseen circumstances. A simple architecture of such a power system is shown in Figure 18.5. It includes the following:

- PV array for power generation during the cyclic daytime periods of approximately 14 Earth days
- Electrolyzer that uses dc electricity from the array and electrochemically converts water into hydrogen, oxygen, and low-grade heat
- Fuel cell stack that electrochemically converts hydrogen and oxygen into dc electricity, water, and low-grade heat during the cyclic night period of approximately 14 Earth days
- Storage tanks for pure water
- High-pressure hydrogen and oxygen tanks
- Automated controls

A preliminary study of a 25 kW power system for a lunar habitat by Voecks[5] compared the KOH alkaline technology with PEM technology for use in both electrolysis and fuel cell units, each with 65% efficiency. The study identified significant advantages associated with the PEM technology for the following reasons:

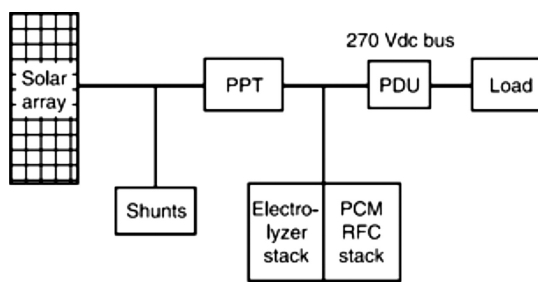

FIGURE 18.5 Power system architecture for a human colony in space (Moon or Mars).

- PEM fuel cells and electrolyzers require less pressure control complexity.
- Containment of the aqueous KOH electrolyte is much more difficult than that of polymeric membrane.

The environment is very demanding, while some aspects are simpler for operating an RFC on the moon compared to on Earth. The moon operation requires the storage of hydrogen, oxygen, and water, whereas the terrestrial operation does not need to store oxygen since air can be fed through the cathode on a one-pass basis. It is easy to maintain the PV power generation schedules on the moon, as the sun time and dark are nearly constant in the lunar month (as is the day, which is 29 days, 12 h, 24 min and 2.9 s on the Earth). On Earth, the seasonal variations and the clouds can make the sunlight vary over a wide range.

18.7 RFCs FOR SATELLITES

The RFC may perhaps replace the battery in satellites, although not in the very near future, because even the efficiency-optimized RFC design has a much lower round-trip energy efficiency than the battery (Table 18.2). Moreover, the radiators and heat pipes required in the RFC system are significant in terms of both mass and integration into the spacecraft design. The protection against single-cell failure using a bypass diode is not practical in the case of the fuel cell. For a space-based radar power system as a hypothetical example, the mass and volume of the fuel cell energy storage alone—not counting the system integration-related mass—are roughly estimated and compared with those using two batteries in Figures 18.6 and 18.7, respectively. This study assumed a mission life of 5 years, an orbital inclination of 90° at various altitude, a power of 20 kW, a discharge time equal to the charge time, giving a duty ratio of 50%, and a battery depth of discharge (DOD) of 25% for NiCd and 35% for NiH_2. It is seen in the figures that the RFC power system results in low mass in low orbits, comparable mass in mid-orbits, and a very large volume in both orbits. In GEO, the RFC would certainly result in much greater mass in almost all cases.

However, when the designs are further developed, the RFC may find applications in high-power spacecraft. For a 10 MW pulse power directed energy weapon platform in LEO as an example mission, Allen[6] reports a conceptual design study comparing the alternative systems, such as the RFC, heat engines, flywheel, and batteries

TABLE 18.2
Round-Trip Energy Efficiency of RFC and Battery

Energy Technology	Round-Trip Energy Efficiency
Nickel cadmium battery	70–80
Nickel hydrogen battery	75–85
Hydrogen–oxygen RFC:	
Mass-optimized design	55–60
Efficiency-optimized design	65–70

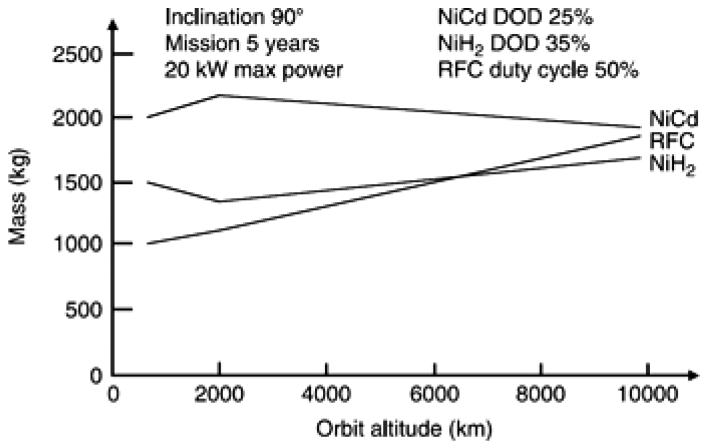

FIGURE 18.6 Alternative energy storage mass for 20 kW space-based radar.

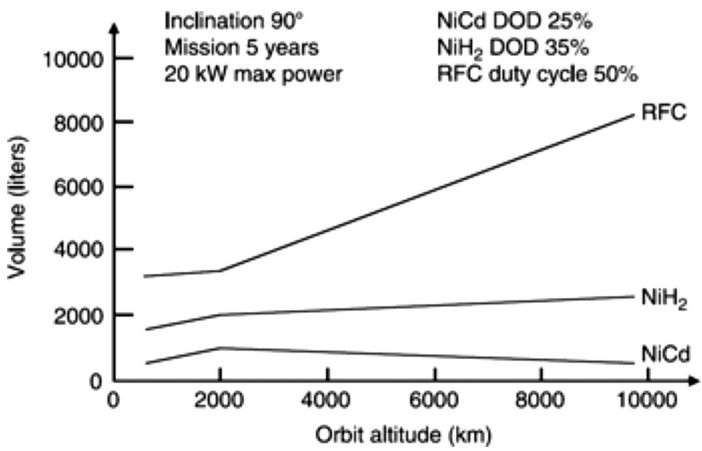

FIGURE 18.7 An alternative energy storage volume for 20 kW space-based radar.

that could be recharged using a PV array. The study concluded that the solid-oxide RFC with PV charge power could deliver the required power with the lowest mass.

RFC, regenerative fuel cell.

REFERENCES

1. Oman, H., Fuel cells power for aerospace vehicles, *IEEE Aerospace and Electronics System Magazine*, 17(2), 35–41, February 2002.
2. Babasaki, T., Take, T., and Yamashita, T., Diagnosis of fuel cell deterioration using fuel cell current-voltage characteristics, in *Proceedings of the 34th Intersociety Energy Conversion Engineering Conference*, SAE, 1999, Paper No. 01-2575.
3. Hall, D.J. and Colclaser, R.G., Transient modeling and simulation of tubular solid oxide fuel cell, *IEEE Power Engineering Review*, July 1998, Paper No. PE-100-EC-004.

4. Barbir, F., Dalton, L., and Molter, T., Regenerative fuel cells for energy storage - Efficiency and weight trade off, in *Proceedings of the 1st International Energy Conversion Engineering Conference*, AIAA, 2003, Paper No. 5937.
5. Voecks, G.E., et al., *Operation of the 25 kW NASA Lewis Research Center Solar Regenerative Fuel Cell Testbed Facility*, NASA Technical Report No. 97295, 1997.
6. Allen, D.M., Multi-megawatts specifications power technology comparison, in *Proceedings of the 36th Intersociety Energy Conversion Engineering Conference*, ASME, 2001, Vol. I, pp. 243–249.

FURTHER READINGS

Burke, K., Fuel cells for space science applications, in *Proceedings of the 1st International Energy Conversion Engineering Conference*, AIAA, 2003, Paper No. 5938.

Hoberecht, M. and Reaves, W., PEM fuel cell status and remaining challenges for manned space flight applications, in *Proceedings of the 1st International Energy Conversion Engineering Conference*, AIAA, 2003, Paper No. 5963.

Perez-Davis, M.E., et al., Energy storage for aerospace applications, in *Proceedings of the 36th Intersociety Energy Conversion Engineering Conference*, ASME, 2001, Vol. I, pp. 85–89.

Sorensen, B., and Spazzafumo, G., *Hydrogen and Fuel Cells: Emerging Technologies and Applications*, 3rd Edition, Academic Press, Elsevier Ltd, Cambridge, MA, 2018.

Index

ac power system 237
Advanced Radioisotope Power System 268
aluminum conductor 155, 292
amplifier 46, 69, 102, 134, 180–182, 226
ancillary components 173
apogee kick motor 7, 14
Apollo-11 250
arcing 53, 56, 163, 168, 172, 178–179
Ariane 20
array drive electronics 73, 173
Arrhenius equation 122
ascent power 70, 115
ascent simulation 204
autumnal equinox 15, 66

backward analysis 70
baffles 14
battery cell voltage monitor 119, 180
battery charge converter 45, 136
battery charge/discharge 62, 68, 100, .196–198, 314
battery charge efficiency 201
battery charge regulation 115
battery circuit model 107, 120–122, 206, 218–220, 232, 263
battery design 111–114, 124, 204
battery design trades 62, 72
battery self-discharge 102, 104, 110, 112, 115
battery, self-heating 110, 121
battery sizing 68
bi-directional DC-DC converter 45, 50, 172
boost converter 14, 139–143
Brayton engine 35, 291
buck converter 136–143
burst power 30, 37, 112, 270, 287–289
bus module 199
BVR bypass diode 58, 92–94, 112–114, 334

cable 20 kHz ac 237, 284
cable R-L-C parameters 151, 154
calibrated step shunt 133
capacitor, ceramic 183, 292–295
capacitor, metalized polypropylene 183
capacitor, tantalum 40, 183, 293
Cassini 254, 262, 267
CEASE sensor 15, 121
charged particle radiation 60, 186
charged particles 41, 58, 94–95, 187–188, 251, 278, 280, 282, 303–304
chemical-dynamic system 37, 289
closed-loop control 315
commercial fuel cells 32, 330
communication and data handling 3–4
communication satellites 52, 199, 202, 212, 221, 297, 305, 308
component models 229, 232
computer program structure 197
conductor materials 155
connector 151–158, 186, 191, 234, 293
control circuit 33, 128, 132, 172, 178, 238, 299
control electronics 5, 69
converter push-pull 142
copper, conductor 155, 158, 270
corona degradation 275–276
cost multipliers, Rule of Ten 71
Cuk converter 143, 149
current meters 173, 181
current regulators 5, 46, 114, 211, 229
current *vs.* voltage *(I-V)* curve 34, 41–54, 80–92, 129, 199–208, 223–228, 250, 263–266
cut-off wavelength 5, 77, 81, 232–237, 252, 320

damage, atomic oxygen 48, 156, 270, 277–278
damage, micrometeoroid 22–23, 58–94, 324
dead-band 196, 211
debris and micrometeoroids 22–23, 58–94
Deepspace-1 303–305
deep space mission 36, 61, 247–312
degradation factors 66–93, 124, 199
deployment controller 173–176
de-spinning operation 14
DET, direct energy transfer 44
dielectric breakdown 239, 275, 285
dual-axis gimbals 60
dynamic stability 225–227

early fault detection 172
Earth orbit classification 6
eclipse 14–19, 33–34, 41–72, 85–91, 99–114, 130–139, 195–208, 216, 281–298, 302–309
eddy currents 191
EED, electro-explosive device 46, 51, 84, 174, 204, 240
electric thruster 298–320
electrochemical cell 42, 99, 328
electronic packaging 186
EMC, Electromagnetic Compatibility 231
EMF, electromotive force 120–121, 231
EMP nuclear threat 238, 258
energy balance 195–209
energy management software 51, 115

energy storage 30–40, 61–68, 99–126
environmental effects 58
EP. electric propulsion 283, 297–320
EQX, equinox 8, 14–18, 65
ESD, electrostatic discharge 28, 39, 44, 83, 231

feedback control loop 138, 225
flexible array 85
flexible harness 162
flexible solar panel 86
flight history 267
Fly-back converter 141
Fourier series 216
Freon 285
full-bridge converter 143
fuel cell 326
fully regulated bus 44, 52, 63, 139
fuse 162
fuzzy logic 206

Galileo 254, 258, 267
Ganymede (Jupiter moon) 254
GEO 239
geomagnetic storm 28
ground power cord 51
ground test 71

Hall-effect thruster 306
Hall-effect transducer 181
harmonic distortion, ripples 217
harness 151
heat radiation 20
HEO, highly elliptical orbit 10
high-frequency ac 211
high-power high-voltage 270
high-power satellites 13, 130
high-temperature components 292
high-voltage DC (HVDC) 283

inductor coupled buck converter 143
Inmarsat 306
inner planets 247
in-space electric propulsion 297
insulation, solid 156
internal impedance 104, 110–112, 120, 206
interplanetary missions 301
inverter 48–50, 127, 143–147
ion thruster 303–313
IPS, ion propulsion system 303
Iridium 268
isolated DC-DC converter 49, 311, 315
ISS, International Space Station 51

Jupiter 253
Jupiter mission 254, 324

Kapton 23, 156, 186, 237, 278
Kelly cosine 87
Kevlar in solar array 292
Kuiper belts 248

large signal analysis 230
large spacecrafts 297
laser initiated deployment 175
launch and ascent power 70, 115
LEO, low earth orbit 10
Libration points 14, 201, 229
life-cycle cost 30, 298
Li-ion battery 35, 62, 105–118
Li-polymer battery 106
load budget, transfer orbit 203
load power profile 63
low-voltage DC (LVDC) 283, 314–315
lunar mission 250

magnetic amplifier 181–182
magnetic damping 12
magnetic field 21
magnetic moment 95
major fuse blow transient 220
Mars 252
maximum power point tracking (MPPT) 47, 49, 311, 313
Maxwell's equations 238
mean solar day 8–9, 15
MEO, mid Earth orbit 6, 238, 305
metalized polypropylene 183
metallic resistance wire 177
meteoroids and debris 22, 58, 94
meteoroids and debris 22, 58, 94

NEP, Nuclear Electric Propulsion 312
Neptune 247
neural network 206
NiCd, nickel cadmium battery 101
NiH_2, nickel hydrogen battery 101
NiMH, nickel metal hydride battery 102
nine-phase (9-phase) 316–320
Nomex 83
northern lights 23
NSSK, N-S station keeping 297
nuclear electric propulsion (NEP) 312–320
nuclear thermal propulsion (NTP) 312
nuclear threat on satellites 28, 37, 238, 258

OBC, on-board computer 173, 196
offsetting from sun 94
Olympus 85
on-orbit environment 20
on-orbit simulation 202
open-loop control 173
operational orbit 195–196

orbit mechanics 10
orbit period 7–21, 41–44, 57–69, 158–159, 195
orbit transfer vehicle 324
outer planets 247, 309, 321–324
output source impedance 216

parabolic concentrator 35
parallel fuses 170
parking orbit 14, 57, 308
partial shunts 129–134
Paschen curves, Paschen voltage breakdown 273
passive rectifier 316–318
PDU, power distribution unit 44–50
Pellon 101
Peltier effect 269
PEM, proton exchange membrane 331
PEMS, power and energy management system 51
penumbra 15–16, 86, 207
performance comparison 308
permanent magnet (PM) 316
pin diodes 242
Pioneer-10, 254
plasma and charged particles 278
plasma arcing 284
plasma contactor 241
platinum 177, 238
Pluto 247, 254, 257–260, 268
plutonium 36, 254, 254, 257–258, 260, 268
polyphase PWM shunt 132
potassium hydroxide (KOH) 101, 331
power conditioning 38–39, 229, 288–331
power conversion 258, 289, 312–324
power converters 135
power electronics 127
power flow analysis 68–69
power losses 69, 93
power management 195
power regulation 42
power system architectures 43
power system functions over life 72
power system level trades 60
power system options 30
power system requirements 57
PPT, peak power tracker 47
primary battery 30
propulsion 5, 297
PRU mode controller 196
PRU, power regulator unit 44–47, 114, 158–163, 176–196
pulse width modulation (PWM) 49–50, 129–133
PV 41, 77

quality of power 216–217

radiation damage 94
radiation shield 187
regenerative fuel cell 326–335
relays 178
Resistojet 302
resonant converter 143
RFC, regenerative fuel cell 326–335
ripple 134
roll spin 203
RPC, remote power controller 171
RPP, repetitive pulse power 287
RTG, radioisotope thermoelectric generator 31–49, 261–269

SAD, solar array drive 45, 162, 173
SA, solar array 41, 62–66, 77, 173, 199, 228, 241
Saturn 247–255
SBR, space-based radar 334–335
self-derived requirements 43
semiconductor devices 127, 170, 188, 230, 255
sensors, thermal control system 5, 17
SEU, single event upset 254
shape memory metal 175
Short-stay mission on Mars 319
shunt control loop 228
shunt dissipator 42–45, 272
shunt mode 128, 230
shunt regulator 46, 128–136, 229
silicon rubber 23, 277
single charge rate 117
single-stage multicouple 260
single-stage unicouple 260
slip ring assembly 33, 174
small signal analysis 230
SOC, state of charge 42, 68–69, 100, 177, 185, 196, 205
solar electric propulsion (SEP) 309–324
solar flare 26–28, 188
solar flux 17, 47–65, 195
solar winds 251
source impedance 211–225
spacecraft level trades 59
spacecraft mass 300
space debris cleanup 323
space shuttle 10, 20, 32, 91, 284, 321, 326, 331
specific energy 332
specific impulse (Isp) 300
specific power and power density 100
spin stabilization 12
sputtering 45, 48
SS, summer solstice 14, 18, 65, 67
SSU, sequential linear shunt 131
stability and bus impedance 221
sublimation 21, 261
sun acquisition 90
sun angle 86
sun intensity 86
sun-regulated bus 207

sunspots 26
sunsynchronous orbit 10
supervisory controller for spacecraft bus 48
switching devices 127

Taylor series 91
TCS, thermal control system 5, 17
TDRS, tracking and data relay satellite 8, 22
TE cooling 128
Teflon, silver 101, 152, 277–288, 308, 311
telemetry and commands 184
temperature compensation 119
temperature extremes 282
tether power 321
TF, Transfer Function 225
thermistor 178
thermocouple 177
thermoelectric cooler 269
thermostats 178
thruster 302
transfer orbit 14
transformer coupled converter 49
transistor BJT, bipolar junction 127
transistor, field effect (FET) 127
transistor, IGBT 127, 144–147, 283
transistor, MOSFET 127

Ulysses 267
umbra 15–16, 86, 207, 251
unfused loads 171
unregulated charging 117
Uranus 247–248

Van Allen radiation belts 232
Venus 247
vibration 289, 291, 316
voltage options 39
voltage regulation and transients 213
voltage source converter (VSC) 144
voltage trades 62
voltage transients 214
Voyager, Jupiter and Saturn 254

wire ampacity 151
wire insulation 153
wound field (WF) 316
WS, winter solstice 14, 18, 65

XIPS, xenon ion propulsion system 304

yaw spin 203

zinc 21